LASER-INDUCED ALIGNMENT AND COULOMB EXPLOSION OF ALKALI DIMERS ON HELIUM DROPLETS

PhD Thesis

Henrik Høj Kristensen
Department of Physics and Astronomy
Aarhus University

July 2024

Revised October 2024

CONTENTS

PREFACE

Minor grammatical errors have been fixed in the printed version of this thesis. In particular, the thesis now contains fewer commas.

The front cover of this book was made with inspiration from the cover of the Master thesis *Laser-induced nonadiabatic alignment dynamics of isolated carbon disulfide dimers* by Mia Overgaard Baatrup.

ACKNOWLEDGMENTS

I am very grateful to Henrik Stapelfeldt. Henrik has been an excellent supervisor and his encouragement and support have been paramount to my development as a researcher.

Over the last four years, I have had the pleasure of working with many great people in the Femtolab group. A huge thanks goes to Lorenz Kranabetter for all the good times we have spent together in the lab. I would also like to thank Simon H. Albrechtsen, my companion during my PhD and many years before that. It has truly been a pleasure, and I have really enjoyed the many hours we have spent together during our studies. I am also grateful to Constant A. Schouder, Adam S. Chatterley, Rico M. P. Tanyag, Albert V. Muñoz, Jacqueline Arlt, Nicolaj Jyde, Jeppe K. Christensen, Flora A. K. Hübschmann, Christoph Stapper, Paul Janssen, Jean Goudot, Christian E. Petersen, and Emil Hansen for the company they have provided in the office and the lab. In addition, I would like to thank the many students who have been part of the group during their Bachelor project or Challenge Track project. I have enjoyed working together with all of you.

Jan Thøgersen deserves special thanks for maintaining the laser systems and for teaching me so much about lasers and optics. Without support from Jan, our research would progress at a much slower pace.

My projects have benefitted from great theoretical support. I would like to thank Robert Zillich, Areg Ghazaryan, Mikhail Lemeshko, and Frank Jensen for all their contributions to the modeling and interpretation of the alignment dynamics of alkali dimers on helium droplets. I am also grateful to Frank for calculating the dicationic potential curves for the alkali dimers. In addition, I would like to thank Ernesto García-Alfonso, Nadine Halberstadt, Manuel Barranco, and Martí Pi for all the simulations they have done to aid the interpretation of the Coulomb explosion dynamics of alkali dimers on helium droplets, in particular concerning the deflections of the alkali ions. I appreciate the many interesting discussions with all of you.

During my PhD, I spent six weeks at Technische Universität Graz in Austria. I want to thank Markus Koch, Michael Stadlhofer, Patricia M. Brugger, Robert Schwarzl, Simon Malacek, and Maximilian Jeindl for making my brief stay very enjoyable.

Finally, I am very grateful to my family for all their support. It truly means a lot to me. My most heartfelt thanks go to my partner Bolette. Your love, support, and encouragement have been endless. Without you, I would never have gotten this far.

SUMMARY

The focal point of this thesis is laser-induced rotation and alignment of alkali dimers on the surface of superfluid helium nanodroplets. I explore this topic with an experimental approach.

In the first experiment, alkali dimers Ak_2 on helium droplets are doubly ionized by an intense femtosecond laser pulse to trigger Coulomb explosion thereby producing pairs of Ak^+ fragment ions. I demonstrate that it is possible to identify whether the dimers were in the $1^1\Sigma_g^+$ state or the $1^3\Sigma_u^+$ state via the kinetic energies of the Ak^+ ions.

Coulomb explosion is then used to probe the time-dependent degree of alignment of Na_2, K_2, and Rb_2 on helium droplets after they have interacted with a nonresonant 1 ps alignment laser pulse. I observe that the dimers rotate and that they align periodically in transient intervals of time. Comparisons with theory reveal that the observations for Na_2 and K_2 in the $1^3\Sigma_u^+$ state and K_2 and Rb_2 in the $1^1\Sigma_g^+$ state are very well described by a 2D rotor model. I argue that the rotational motion of these dimers must, therefore, occur in a plane dictated by the surface of the helium droplet. In contrast, the rotations of Na_2 in the $1^1\Sigma_g^+$ state are closer to that of isolated molecules, indicating a weaker interaction with the droplet surface. Rotational dynamics are not observed for Rb_2 in the $1^3\Sigma_u^+$ state after the initial reaction to the alignment pulse, possibly due to interactions with the droplet.

Furthermore, I also show three other applications of Coulomb explosion in the thesis. The first application is a reconstruction of the distribution of internuclear distances $P(R)$, which I demonstrate for alkali dimers and trimers on helium droplets. Comparisons with calculated ground state vibrational wave functions for the isolated molecules show an overall good agreement for the central positions of the measured $P(R)$ distributions. However, the widths of the distributions are larger than predicted by theory. The second application is the use of Coulomb explosion to measure vibrational motion of alkali dimers on helium droplets. Here, I observe that the alignment pulses also create

DANSK RESUMÉ

Omdrejningspunktet for denne afhandling er laserinduceret rotation og ensretning af alkali dimerer på overfladen af nanodråber af superflydende helium. Jeg undersøger dette emne med en eksperimentel tilgang.

I det første eksperiment dobbeltioniseres alkali dimerer Ak_2 på heliumdråber af en intens femtosekund laserpuls som forårsager Coulomb eksplosion, hvilket producerer par af Ak^+ ionfragmenter. Jeg demonstrerer, at det er muligt at identificere om dimererne var i $1^1\Sigma_g^+$ tilstanden eller $1^3\Sigma_u^+$ tilstanden via Ak^+ ionernes kinetiske energier.

Coulomb eksplosion bruges dernæst til at probe den tidsafhængige grad af ensretning for Na_2, K_2 og Rb_2 på heliumdråber, efter at de har interageret med en ikke-resonant 1 ps ensrettende laserpuls. Jeg observerer, at dimererne roterer, og at de ensrettes periodisk i kortvarige tidsintervaller. Sammenligninger med teori afslører, at observationerne for Na_2 og K_2 i $1^3\Sigma_u^+$ tilstanden samt for K_2 og Rb_2 i $1^1\Sigma_g^+$ tilstanden er meget velbeskrevet af en 2D rotor model. Jeg argumenterer, at den rotationelle bevægelse for disse dimerer derfor må foregå i et plan, der dikteres af overfladen på heliumdråben. I modsætning minder rotationerne for Na_2 i $1^1\Sigma_g^+$ tilstanden mere om det, der ville forventes for isolerede molekyler, hvilket indikerer en svagere interaktion med dråbeoverfladen. Rotationel dynamik observeres ikke for Rb_2 i $1^3\Sigma_u^+$ tilstanden efter den indledende reaktion på den ensrettende puls, muligvis på grund af interaktioner med dråben.

Jeg viser derudover også tre andre anvendelser af Coulomb eksplosion i afhandlingen. Den første anvendelse er rekonstruktion af fordelingen over internuklare afstande $P(R)$, hvilket jeg demonstrerer for alkali dimerer og trimerer på heliumdråber. Sammenligninger med beregnede bølgefunktioner for de vibrationelle grundtilstande for de isolerede molekyler viser en overordnet god overensstemmelse for centerpositionerne af de målte $P(R)$ fordelinger. Dog er bredderne på fordelingerne større end forudset af teorien. Den anden anvendelse er brugen af Coulomb

eksplosion til at måle vibrationel bevægelse for alkali dimerer på heliumdråber. Her observerer jeg, at de ensrettende pulser også skaber vibrationelle bølgepakker i alkali dimererne i $1^3\Sigma_u^+$ tilstandene. Den sidste anvendelse er brugen af Coulomb eksplosion af et lille molekyle, her alkali dimeren, til at probe et nærliggende objekt, i dette tilfælde heliumdråben. Jeg viser at heliumdråben deflekterer Ak^+ ionerne dannet af Coulomb eksplosionen, og at deflektionsvinklerne muligvis kan bruges til at bestemme størrelsen på heliumdråberne. Derudover foreslår jeg, at deflektionerne kan bruges til at bestemme alkali dimerernes lokation på heliumdråben.

LIST OF PUBLICATIONS

The work presented in this thesis has led to the following publications:

(I) *Quantum-State-Sensitive Detection of Alkali Dimers on Helium Nanodroplets by Laser-Induced Coulomb Explosion.*
H. H. Kristensen, L. Kranabetter, C. A. Schouder, C. Stapper, J. Arlt, M. Mudrich, and H. Stapelfeldt. *Phys. Rev. Lett.* **128** (2022), 093201.

(II) *Laser-Induced Coulomb Explosion Imaging of Alkali-Metal Dimers on Helium Nanodroplets.*
H. H. Kristensen, L. Kranabetter, C. A. Schouder, J. Arlt, F. Jensen, and H. Stapelfeldt. *Phys. Rev. A* **107** (2023), 023104.
Selected as Editors' Suggestion.

(III) *Nonadiabatic Laser-Induced Alignment Dynamics of Molecules on a Surface*
L. Kranabetter, H. H. Kristensen, A. Ghazaryan, C. A. Schouder, A. S. Chatterley, P. Janssen, F. Jensen, R. E. Zillich, M. Lemeshko, and H. Stapelfeldt. *Phys. Rev. Lett.* **131** (2023), 053201.

(IV) *Structure Determination of Alkali Trimers on Helium Nanodroplets through Laser-Induced Coulomb Explosion*
L. Kranabetter*, H. H. Kristensen*, C. A. Schouder, and H. Stapelfeldt. *J. Chem. Phys.* **160** (2024), 131101.
* *These authors contributed equally.*

(V) *Laser-induced Coulomb Explosion of Heteronuclear Alkali-Metal Dimers on Helium Nanodroplets*
S. H. Albrechtsen*, J. K. Christensen*, R. M. P. Tanyag, H. H. Kristensen, and H. Stapelfeldt. *Phys. Rev. A* **109** (2024), 043112.
* *These authors contributed equally.*

In addition, several manuscripts are currently being drafted with the working titles:

(VI) *Nonadiabatic laser-induced alignment dynamics of alkali dimers on helium droplet surfaces*
H. H. Kristensen, L. Kranabetter, A. Ghazaryan, C. A. Schouder, F. Jensen, R. E. Zillich, M. Lemeshko, and H. Stapelfeldt.

(VII) *Time-resolved Coulomb explosion imaging of vibrational wave packets in alkali dimers on helium nanodroplets*
N. Jyde, H. H. Kristensen, L. Kranabetter, J. K. Christensen, E. Hansen, M. B. Carlsen, F. Jensen and H. Stapelfeldt.

(VIII) *Coulomb explosion of alkali dimers at the surface of superfluid ^{4}He droplets*
E. García-Alfonso, M. Barranco, M. Pi, H. H. Kristensen, L. Kranabetter, H. Stapelfeldt, and N. Halberstadt.
(Author list and order to be revised)

1

INTRODUCTION

The specific orientation of molecules plays an important role in chemistry. For a reaction to occur, the correct parts of the reacting molecules must meet [1–4]. In some cases, multiple reaction pathways may even be available depending on which parts of the molecules collide with each other. How molecules are oriented also influences the interaction with polarized light [5–7], and is also important in, for example, single-shot diffraction experiments because a randomly oriented ensemble of isolated molecules typically result in weak and less informative signal [8, 9]. For such reasons, it is of strong interest to develop and improve methods that can be used to control the rotation of molecules and manipulate their spatial orientation.

One such method is laser-induced alignment [10–28]. It has been developed for gas-phase molecules over the past three decades and explored and applied in a huge number of works. The principle is to use a laser pulse to confine one or more molecular axes in space for an initially randomly oriented molecule. For a broad selection of gas-phase molecules, it has been demonstrated that the most polarizable axis can be aligned along the polarization axis of a linearly polarized laser pulse. This is termed 1D alignment. If an elliptically polarized laser pulse is used instead, the most and the second most polarizable axes of the molecule can be aligned along the major polarization axis and the minor polarization axis, respectively. This is termed 3D alignment because the least polarizable axis is then automatically aligned perpendicular to the plane of polarization. In my thesis, the focus will entirely be on 1D alignment of a linear molecule.

When the laser pulse is much shorter than the rotational period of the molecule, the pulse "kicks" the molecule into coherent rotation. One result hereof is that the molecules exhibit transient alignment in narrow, periodically spaced intervals termed revivals. This regime is known as nonadiabatic, or impulsive, alignment [12, 16, 20]. In addition to the ability to manipulate the

spatial orientation of molecules, nonadiabatic laser-induced alignment can also provide information about the rotational energy levels and the molecular structure [17, 25, 28–32]. This approach is generally known as rotational coherence spectroscopy [33, 34].

In recent years, laser-induced alignment has been extended to also encompass molecules inside nanodroplets of superfluid helium [32, 35–42]. The droplets act as optically transparent, cryogenic matrices, and facilitate the study of how molecules rotate in an isotropic fluid environment. In a study from my group, the three linear molecules I_2, OCS, and CS_2 were nonadiabatically aligned inside helium droplets using picosecond laser pulses [32]. It was found that the rotational dynamics is essentially that of gas-phase molecules when the rotational energy is kept below the energy of the roton excitation (~ 5 cm^{-1}) in superfluid helium, thus limiting the coupling between the molecules and the surrounding helium environment. However, to model the observed alignment dynamics with a free-rotor model, an effective rotational constant B_{He} 2–5 times smaller than the gas-phase value B_{gas} had to be employed, alongside an effective centrifugal distortion constant D_{He} increased by a factor of $\sim 10^4$ compared to the value of isolated molecules. Inhomogeneous broadening was also included to capture the observed gradual decay in the amplitude of the time-dependent degree of alignment. The effective rotational constants are consistent with the results of a prior experiment where the rovibrational spectrum of OCS in helium droplets was recorded with infrared spectroscopy [43]. The findings have been explained by a shell of nonsuperfluid helium that co-rotates with the molecule, altering the moment of inertia and thereby also the rotational constant [44–47].

In a contrasting experiment, D_2 inside helium droplets was aligned with an intense femtosecond pulse [40]. In this case, the dominant rotational coherence had an energy (179 cm^{-1}) which vastly exceeded the roton energy. Here, the authors found that the rotational constant B_{He} inside the helium droplets was unchanged from that of the gas-phase molecule, illustrating a very weak coupling to the droplets as predicted for this energy regime, where the density of excited states in the helium droplet is low. Furthermore, the rotational energy was much larger than the binding energy of He atoms to the D_2 molecule, so the helium

could not stick and form a co-rotating shell. The authors concluded that D_2 inside helium droplets rotate as if they were in gas phase.

Yet another recent study, this time in bulk liquid helium, demonstrated the viability of laser-induced alignment inside a quantum liquid [42]. The work is focused on the rotation of the helium dimer exciplex He_2^*, a system that repels the nearby superfluid helium and thus resides inside a small empty bubble. In this scenario, the rotations are also observed to be essentially unaffected by the helium environment due to a weak coupling.

A so far unexplored scenario is molecular rotation and alignment on a surface, perhaps because it is difficult to find a good model system. However, it has been established that alkali atoms and clusters thereof can be doped onto the surface of the droplets. These systems have been extensively studied and characterized via spectroscopy, and the vibrational structures of alkali dimers and trimers are now well-known [48–56]. Surprisingly, however, nothing has been learned about the rotational structure of such systems, leaving a gap in the literature. In a publication from 2011 about the vibrational dynamics of Rb_2 in triplet states on helium droplets, Grüner and coauthors remark that they do not see any effect from rotational recurrences, as otherwise predicted by their simulations [57]. The authors speculate that the rotational dynamics of Rb_2 on helium droplets are strongly affected by the presence of the droplet surface. To quote them directly:

> "Due to the surface position of the Rb_2 molecules presumably with the molecular axis being oriented parallel to the surface, we expect the rotation to decompose into weakly perturbed in-plane rotation and strongly hindered out-of-plane rotation which more likely resembles a pendular motion. The latter may efficiently couple to surface modes of the droplets causing fast relaxation."

This is supported by theoretical calculations from Guillon and coworkers in a publication from the same year [58].

To my knowledge, no further investigation of this matter has since been conducted. Strongly motivated by this fact, the overarching goal during my PhD has been to study if it is possible

to rotate and align alkali dimers on helium droplets in the nonadiabatic regime. If this can be achieved, is it then possible to determine the rotational structure of the systems from the measured time-dependent degree of alignment? Additionally, can the alignment dynamics reveal new insight into the coupling between the alkali dimers and the surface of the helium droplets?

Experimentally, I have used two laser pulses in a pump-probe scheme to conduct the investigations. The purpose of the first laser pulse was to start the molecular rotation and alignment dynamics. The second laser pulse has then been used to probe the dynamics, via a technique that is sensitive to the orientation of the dimers. Here, I employed laser-induced Coulomb explosion which prior work on gas-phase alignment has already demonstrated is well-suited for this task [26, 27, 29, 31, 59–61]. The principle of the technique is to rapidly remove several electrons from the molecule, typically via multiphoton absorption from an intense femtosecond pulse, thereby creating a strong internal electrostatic repulsion that leads to fragmentation, or 'explosion', of the charged molecule. This produces several cationic fragments, in my case always alkali ions Ak^+, with velocities that are governed by the structure and orientation of the molecule at the moment the explosion is triggered. By measuring the ion velocities, for example via the 2D velocity map imaging technique, which I have utilized, the molecular orientation can be determined and, sometimes, also the molecular structure.

In a first step toward the goal, I experimentally established that Coulomb explosion imaging creates an opportunity for studying the alkali homonuclear dimers in two different quantum states, namely the singlet ground state $1^1\Sigma_g^+$ and the lowest-lying triplet state $1^3\Sigma_u^+$, which both form on the helium droplets. I have then used this quantum-state-sensitivity to investigate the rotational structure and alignment dynamics of both states, to obtain additional information about the interplay between the molecules and the helium droplet surface.

I have also obtained other results due to the structure sensitivity of the Coulomb explosion technique. I have used it to do a direct structure determination of the homonuclear alkali dimers, in the $1^1\Sigma_g^+$ state and the $1^3\Sigma_u^+$ state, as well as for the homonuclear alkali trimers in the lowest-lying $^4A_2'$ state in a

spin-off experiment. Similar results have also been obtained for heteronuclear alkali dimers in the $1^3\Sigma^+$ state. Additionally, I have extracted the distribution of internuclear separations, commonly also known as wave function imaging, for both the dimer and the trimer systems. In another related experiment, I used timed Coulomb explosion to investigate vibrations induced in the $1^3\Sigma_u^+$ state homonuclear dimers by the alignment pump pulse. Finally, I have devoted a lot of energy to a large project where I have studied deflections in the trajectories of the Ak^+ fragments, due to the presence of the nearby helium droplet, using 3D velocity map imaging enabled by a Tpx3Cam detector. This project is interesting due to prospects of using the deflections to determine the helium droplet size distribution as well as the location of the alkali dimers on the droplets.

The thesis is structured as follows. First, Chapter 2 introduces helium droplets and their properties, after which Chapter 3 gives an overview of the relevant aspects of laser-induced alignment. A thorough description of the experimental apparatus used for all experiments, including helium droplet beam generation, the detection system, and the preparation of the required laser pulses, is presented in Chapter 4. The first experiments with Coulomb explosion imaging of alkali dimers are then covered in Chapter 5. Here, I demonstrate that Coulomb explosion can be used to do a direct structure determination of the homonuclear alkali dimers, enabling quantum-state-sensitive measurements in all the following experiments on the dimers. In this chapter, I also present results for the distributions of the internuclear separations. In Chapter 6 and Chapter 7, I present the Coulomb explosion imaging results for the heteronuclear alkali dimers and the homonuclear alkali trimers, respectively.

The main results on nonadiabatic laser-induced rotation and alignment of alkali dimers are presented and discussed in Chapter 8. Chapter 9 is dedicated to results on vibrational motion of alkali dimers while Chapter 10 discusses the work on the deflection of Ak^+ fragments during the Coulomb explosion process. Chapter 11 wraps up the thesis in an overall conclusion and presents my outlook on future possible experiments. At the very end, the appendix provides additional details and data for select parts of the shown work.

2

HELIUM DROPLETS

The purpose of this chapter is to give a more in-depth introduction to superfluid helium droplets. The droplets and their properties have been the subject of a large amount of studies, and many interesting details could be brought up. I will however limit the description here to the aspects most necessary for the experiments presented in this thesis. Readers interested in additional details are referred to reviews in the literature [45, 62–69].

First, I will describe some of the fundamental properties of superfluid helium. Following that, the principles of helium droplet formation are covered before I explain how the droplets can be doped with atoms and molecules. Finally, I will go into detail about the formation of alkali dimers and trimers on the helium droplets, the systems I have been studying.

2.1 Fundamental properties of superfluid helium

^{4}He has the remarkable property that it can turn into a superfluid liquid, also known as liquid helium II, as illustrated in the phase diagram in Fig. 2.1. This transition occurs when helium is cooled down to a temperature below 2.18 K, known as the λ-point [70]. ^{3}He also has a superfluid phase, but this transition occurs at a much lower temperature of 3 mK [45]. However, ^{3}He is very scarce on Earth and rarely used for experiments. In this thesis, "helium" therefore always refers to ^{4}He.

In superfluid helium, particles that move at a velocity below $v_\mathrm{L} = 58$ m/s will experience the fluid as frictionless. This limit is known as the Landau velocity. The lack of interaction arises from the fact that there are no elementary excitations in the superfluid helium that can couple to such slowly moving particles [72, 73].

Three other properties are also interesting to highlight here. The first is the very high heat conductivity of superfluid helium [65]. Due to this, helium is very good at cooling down

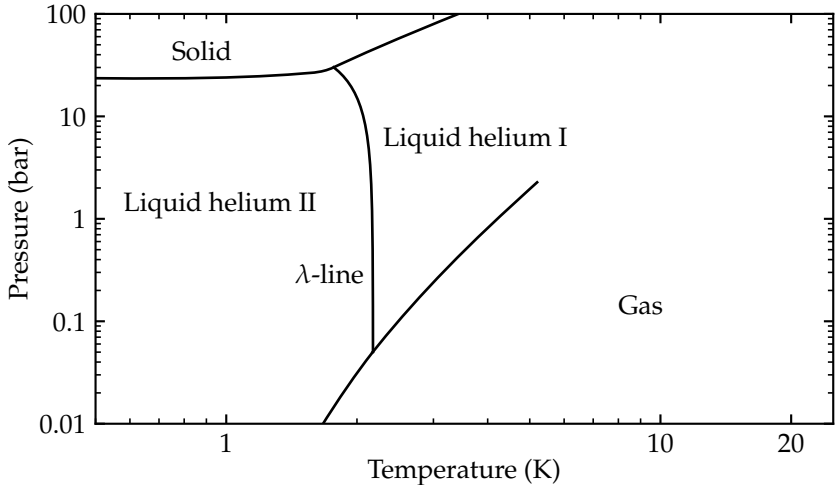

Figure 2.1: Phase diagram for ^{4}He. When helium is cooled enough to cross the λ-line it transitions to the superfluid phase, liquid helium II. The phase transition lines have been plotted via tabulated functions and values in [71].

atoms and molecules solvated in the liquid. This makes superfluid helium very interesting as a matrix for spectroscopic studies of very cold atoms and molecules. The second property is the fact that helium is optically transparent over a large span of wavelengths, ranging from far UV and all the way to IR [45]. As a result, atoms and molecules in superfluid helium can conveniently be studied with standard spectroscopic tools. The last property, which is somewhat related to the prior, is the very high ionization potential of helium, I_p = 24.6 eV [74]. When doing spectroscopy, the intensity of the laser will typically not be high enough to strip such a tightly bound electron from the helium. The helium therefore typically remains uncharged in the experiments.

It is tempting to put atoms and molecules into a bath of superfluid helium to facilitate the study of the cooled systems in the superfluid environment. Unfortunately, doing so will lead to aggregation of the foreign atoms and molecules on the container walls of the bath, because the interactions with those are much stronger than with the superfluid helium. This issue can however be avoided entirely by forming free droplets of the superfluid helium [45].

2.2 Helium droplet formation

Droplets of helium can be formed by a free jet expansion into a vacuum [45, 66, 69]. This is commonly done in the subcritical expansion regime, where a gas of helium cooled to around 10–25 K is expanded into a vacuum through a small micrometer-sized nozzle at a stagnation pressure of 20–80 bar. This adiabatically cools the helium gas, which initiates cluster growth as the helium gas propagates forward in the expansion beam. At some point, the helium atoms cease to collide in the beam and the clustering stops. The formed droplets of helium then cool through evaporative cooling, further reducing the temperature of the helium droplets by evaporation of individual helium atoms bound to the droplet by an energy of around 5 cm^{-1}. The droplets equilibrate at a temperature of 0.37 K, at which point the helium has transitioned to its superfluid state, see Fig. 2.1 [45, 64–66]. This droplet temperature has been experimentally verified via rotational spectroscopy of SF_6 molecules in the droplets [75].

The size of the formed helium droplets follows a log-normal distribution [65, 66]. In the subcritical expansion regime, the mean size of the helium droplets can span from a size of around 2000 to 20000 helium atoms depending on the expansion conditions, as shown in Fig. 2.2. The sizes are known from experiments where the helium droplets were scattered on a secondary molecular beam [76, 77]. If the temperature of the nozzle is reduced it will increase the droplet size. Similarly, the droplets become bigger if the stagnation pressure of the helium is increased. The width of the droplet size distribution is approximately the same as the mean size, a characteristic of the experimentally measured log-normal distributions, so large variations in size can be present for individual droplets in an experiment [69].

It is also possible to form helium droplets in the supercritical regime [45, 64, 69]. In this case, the helium is initially cooled to a lower temperature, so it condenses into normal liquid helium I prior to the expansion into vacuum. The helium is again further cooled during the expansion and droplets are created via fragmentation of the liquid jet. The final droplets formed in this process are much larger than those created in the subcritical regime, as also shown in Fig. 2.2. On the small side, the droplets

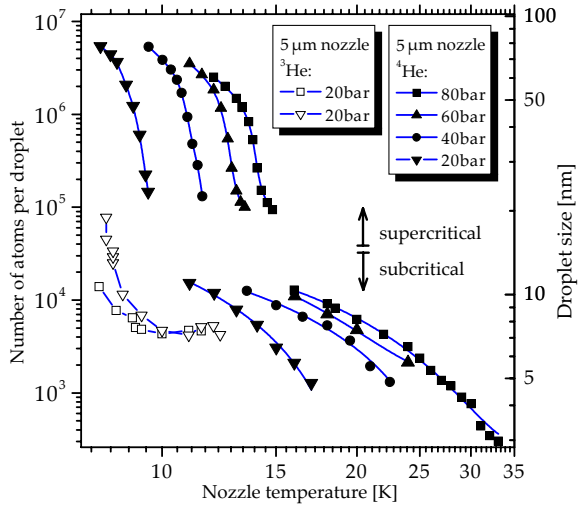

Figure 2.2: Mean size of helium droplets formed with various expansion conditions. Droplets formed in the supercritical regime are vastly bigger than those formed in the subcritical regime (note the logarithmic y-axis). Figure from [64]. Reproduced with minor adaptions with permission. © IOP Publishing. All rights reserved.

contain around 10^5 helium atoms, while the biggest droplets that have been formed contain on the order of 10^{11} atoms [78, 79].

The droplets are generally spherical[1], and their radius can be calculated as [45, 81]

$$R = 2.22N^{1/3}\text{Å}, \tag{2.1}$$

where N is the number of helium atoms in the droplet. According to this formula, the radius of the droplets created in the subcritical regime ranges from 3–6 nm, while those made in the supercritical regime span from 10–1000 nm.

2.3 Doping with foreign species

In 1990 it was demonstrated for the first time that helium droplets can be doped with foreign atoms via a collisional pickup process [82]. This has since been shown for a wide variety of atoms

1 At least in the subcritical regime. For very large droplets, angular momentum may distort the droplet shape [79, 80].

and molecules, including the alkali metals [45, 63, 83]. The standard way of doping helium droplets is by passing them through a gas where the droplets collide with individual atoms or molecules. In practice, this typically takes place in a doping cell or oven designed for the purpose. The probability p_k of sequentially picking up k dopants approximately follows Poisson statistics [65]

$$p_k = \frac{(n\sigma l)^k}{k!}\exp(-n\sigma l), \tag{2.2}$$

with n being the number density of the gas, σ the pickup cross-section and l the length of the pickup region. Whenever the helium droplet picks up a dopant, it cools the dopant down to the 0.37 K temperature of the droplet. In this process, the helium droplet must get rid of the excess energy from the dopant. Once again this happens via evaporation of helium atoms, which reduces the size of the helium droplet and thereby also the probability of picking up additional dopants. For atoms, small molecules, and complexes this effect is usually not very large, so Eq. 2.2 remains a good approximation, especially for large helium droplets [65].

It is instructive to show an example of the pickup probabilities for a chosen set of parameters. I have therefore calculated the probability of picking up k dopants for a droplet consisting of $N = 10000$ helium atoms that pass through a 2-cm long doping cell with a vapor of gas at pressure P. For the calculations, the pickup cross-section σ was approximated as

$$\sigma = 15.5N^{2/3}\text{Å}^2, \tag{2.3}$$

as suggested in the literature for a helium droplet with a uniform density close to that of bulk liquid helium [65]. The number density n was calculated using the ideal gas law, assuming a volume of 10 cm^3 and a temperature of 120 °C (393 K).

Figure 2.3 illustrates the calculated probabilities. It is apparent from this figure that it is impossible to select a doping pressure where only one specific amount of dopants is picked up by the droplets. In fact, at the pressure where the probability of picking up one dopant is largest, a significant amount of the droplets will pick up two dopants and some may pick up even more. Thus, by

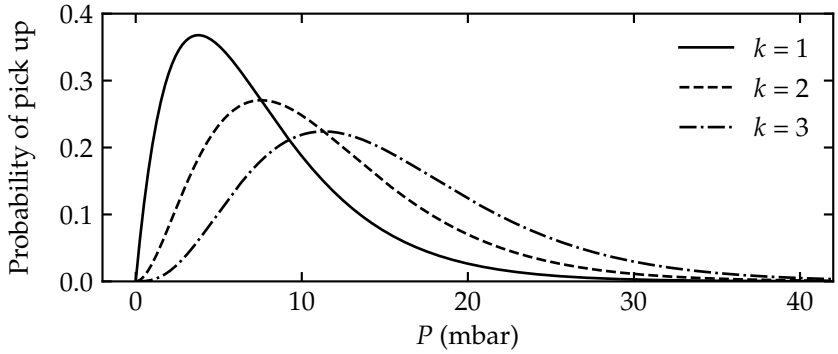

Figure 2.3: Exemplified plot of the probabilities for a helium droplet to pick up k dopants. The values used to calculate the probabilities are given in the text.

regulating the doping pressure it is possible to select the most likely amount of dopants, but there will always be a presence of droplets doped with a different amount. Since the probabilities depend on the cross-section, and thus the droplet size, the large experimental spread in helium droplet sizes will also lead to a mix of doping conditions.

In some experiments, droplets carrying the wrong amount of dopants can lead to unwanted background signals. The optimal doping conditions may therefore not always be those that, for example, maximize the probability of picking up two dopants, but instead a compromise where the unavoidable background signals are kept at a manageable level. This is the case for the experiments I have conducted, where droplets doped with a single alkali atom are never of interest but lead to background signals which can become problematic if not handled.

2.3.1 *Formation of alkali clusters*

The vast majority of dopants picked up by helium droplets will be embedded in the droplet interior. However, the alkali atoms, and clusters thereof, deviate in this regard. This is due to a combination of two interactions: the very weak van der Waals attraction between the alkali atom and the helium atoms. The other is the repulsive Pauli interaction between the paired electrons in the helium and the weakly bound outer electron of the alkali atoms.

As a result, the equilibrium position turns out to be at the surface where the alkali sits over a small dimple in the helium droplet [62, 84].

The alkali dimers and trimers are not doped directly onto the droplets but instead formed by bonding during cold collisions, on the droplet surface, of two or three alkali atoms that were sequentially picked up by the helium droplets [62, 85]. These systems have been experimentally confirmed to reside on the surface via spectroscopic studies using both pulsed and continuous lasers, with the primary methods being resonance-enhanced multiphoton ionization (REMPI) and laser-induced fluorescence [48, 62, 86–95]. Theoretical calculations have furthermore indicated that the alkali dimers lie parallel to the surface plane of the droplets [58, 84, 96, 97].

As briefly mentioned in Chapter 1, the alkali dimers are known to form in two states on the droplets depending on the pairing of the spin of the electrons, namely the singlet ground state $1^1\Sigma_g^+$ and the lowest-lying triplet state $1^3\Sigma_u^+$. This is known from the beforementioned spectroscopic studies that confirm the surface position of the alkalis [48, 89, 90, 92, 98]. The $1^1\Sigma_g^+$ state dimers are covalently bound whereas the $1^3\Sigma_u^+$ state dimers are bound by weak van der Waals forces. Taking Na_2 as an example, the binding energy of the $1^1\Sigma_g^+$ state is 5943 cm^{-1} (0.74 eV), which is significantly more than the 161 cm^{-1} (20 meV) binding energy of the $1^3\Sigma_u^+$ state [99]. This can also be seen from the potential curves of Na_2, see Fig. 5.1.

Upon formation of the alkali dimers on the droplet surface, the binding energy is released and dissipated to the helium which heats up. This leads to evaporation of a number of helium atoms until all excess energy has been carried away, such that the droplet maintains its temperature of 0.37 K. Returning to the example of Na_2, the formation of a $1^1\Sigma_g^+$ state dimer will therefore result in the evaporation of almost 1200 helium atoms since evaporation of one helium atom from the droplet requires 5 cm^{-1}. In sharp contrast, only around 30 helium atoms will evaporate if the dimer forms in the $1^3\Sigma_u^+$ state [99]. Thus, the evaporation process is, presumably, more turbulent when $1^1\Sigma_g^+$ state dimers are formed.

The helium evaporation following the release of binding energy

has been used to explain an interesting phenomenon. In the vast amount of work conducted on alkali dimers on helium droplets, the dimers have almost exclusively been in the $1^3\Sigma_u^+$ state. The reason is that the $1^1\Sigma_g^+$ state dimers are formed but often desorb alongside the evaporation of helium atoms initiated by the release of the large binding energy[2] [57, 98, 99, 101, 102]. For $1^3\Sigma_u^+$ state dimers, the evaporation is so gentle and limited that the dimers are preserved on the droplets. Hence, the $1^3\Sigma_u^+$ state dimers become more accessible. This stands in contrast to gas phase at higher temperatures, where essentially only the $1^1\Sigma_g^+$ state dimers are available because the $1^3\Sigma_u^+$ state dimers fragment immediately due to their low binding energy [99]. The high abundance of the $1^3\Sigma_u^+$ state is in fact one of the primary reasons that people have studied the alkali dimers so much on helium droplets.

In the scenario where three alkali atoms are picked up by the droplet, they will eventually meet and form a trimer on the surface [51–53, 56]. By the same arguments as before, trimers in the weakly bound quartet state $^4A_2'$ are preserved on the droplets because the released binding energy is rather small, for example 850 cm^{-1} for Na_3 (see the potential curve in Fig. 7.1). If the trimers instead form in the much more strongly bound doublet state $^2B_2$, vast amounts of helium are again expelled by the droplet. Once more using Na_3 as the example, the binding energy is around 8000 cm^{-1} [52]. While some $1^1\Sigma_g^+$ state alkali dimers are generally present on the droplet surface, the $^2B_2$ state trimers have, to my knowledge, never been observed, presumably because they always desorb [56].

2 For Li_2, which has the largest binding energy of the alkali dimers [100], it appears that desorption always occurs for the $1^1\Sigma_g^+$ state. To this date, the $1^1\Sigma_g^+$ state has never been observed experimentally on helium droplets.

3

LASER-INDUCED ALIGNMENT

In this chapter, I cover the relevant theory about laser-induced alignment of linear molecules. I am not going to derive any of the theory myself, but will instead focus on establishing the core concepts and terminology needed for the later interpretation of the experimental results.

First, I will discuss the principles of nonadiabatic alignment and show a simulation of the time-dependent alignment dynamics of a molecule in gas phase. Next, I show how the rotational structure of the molecule can be retrieved from a spectral analysis of the alignment trace. Finally, a brief introduction to adiabatic alignment is given.

3.1 Nonadiabatic alignment

The cycle-averaged potential energy of a rigid linear molecule in the electric field of a nonresonant linearly polarized laser pulse is described by the dynamic Stark interaction [10, 12, 18]

$$V(t) = -\frac{E^2(t)}{4}\left[(\alpha_{\parallel} - \alpha_{\perp})\cos^2\theta + \alpha_{\perp}\right]. \tag{3.1}$$

Here, $E(t)$ is the envelope of the electric field and θ is the angle between the internuclear axis of the molecule and the polarization axis of the laser pulse, while $\alpha_{\parallel}$ and $\alpha_{\perp}$ are the parallel and perpendicular components of the molecular polarizability, respectively. From Eq. 3.1 it can be inferred that the potential energy is lowest for $\theta = 0$ and $\theta = \pi$ (since $\alpha_{\parallel} > \alpha_{\perp}$ for linear molecules [10]), i. e., when the internuclear axis of the molecule is aligned parallel to the polarization axis of the laser pulse.

In the nonadiabatic alignment regime, where the rotational period of the molecules is much longer than the duration of the laser pulse, the molecules can classically be considered frozen while the interaction lasts. However, the electric field will exert a torque $\tau \propto -\sin(2\theta)$ on the molecules, setting them into

rotation afterward [20]. The angular velocities of the molecules will depend on the initial angle θ, and as a result, the angular distribution of the molecules will become more narrow shortly after the interaction, that is, the molecules become more aligned. Since the molecules continue to rotate, the increase in the degree of alignment for the molecular ensemble quickly disappears again [28].

To understand why the molecules will transiently realign in periodic intervals, as briefly mentioned in Chapter 1, a quantum mechanical treatment is necessary. A useful first step is to solve the time-dependent rotational Schrödinger equation for a rigid linear molecule irradiated by a nonadiabatic, nonresonant alignment pulse [28],

$$i\hbar\frac{\partial\psi(t)}{\partial t} = \left[\frac{B\hat{J}^2}{\hbar^2} + V(t)\right]\psi(t), \tag{3.2}$$

where $\hat{J}^2$ denotes the squared angular momentum operator, $V(t)$ describes the interaction with the laser pulse as given by Eq. 3.1, and $B = \hbar^2/2I$ is the rotational constant of the molecule [103, p. 343], with I being the moment of inertia. B is often expressed in units of both energy (typically in wavenumbers $\tilde{\nu} = E/hc$) and frequency ($\nu = E/h$), so I will not explicitly convert the units throughout the thesis, however, the units should be clear from the context. The general solution to the Schrödinger equation in Eq. 3.2 is a coherent rotational wave packet [20, 28, 104, 105]

$$|\psi(t)\rangle = \sum_{JM} C_{JM}(t)\,|JM\rangle e^{-iE_J t/\hbar}. \tag{3.3}$$

In this expression, $|JM\rangle$ are the rotational eigenstates of the field-free linear rotor (equivalent to the spherical harmonics Y_J^M) with J being the rotational quantum number and M the projection of J on an axis parallel to the laser polarization axis [28]. Meanwhile, C_{JM} is the expansion coefficients and E_J is the rotational energies associated with the different J-states of the molecule

$$E_J = BJ(J+1). \tag{3.4}$$

The time-dependent degree of alignment for the found wave packet can now be determined by calculating $\langle\cos^2\theta_{2D}\rangle(t)$, a

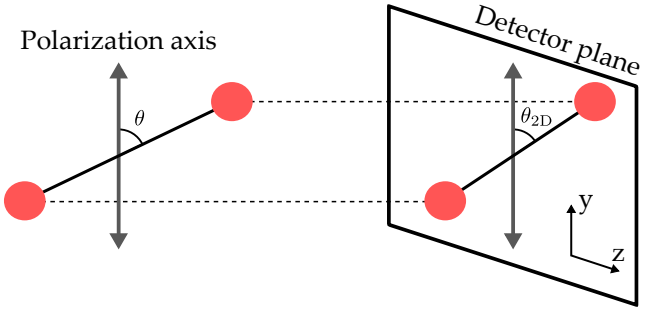

Figure 3.1: The angle θ_{2D} between the projections of the alignment pulse polarization axis and the internuclear axis of the molecule can be observed directly in experiments with 2D velocity map imaging.

measure commonly used in experiments with 2D velocity map imaging [18]. Here, $\langle\cdot\rangle$ denotes the expectation value and θ_{2D} is the observed angle between the internuclear axis of the molecule and the polarization axis of the alignment pulse after a projection onto a 2D plane, see Fig. 3.1. For perfectly aligned molecules $\langle\cos^2\theta_{2D}\rangle = 1$, while $\langle\cos^2\theta_{2D}\rangle = 0$ corresponds to perfectly anti-aligned molecules (alignment perpendicular to the polarization axis) and $\langle\cos^2\theta_{2D}\rangle = 0.5$ corresponds to randomly aligned molecules. Note that $\langle\cos^2\theta_{2D}\rangle \geq \langle\cos^2\theta\rangle$ so the degree of alignment determined via the 2D projection overestimates the degree of alignment in 3D [106].

As an illustrative example, I have calculated a $\langle\cos^2\theta_{2D}\rangle(t)$ trace for Na_2 in the $1^3\Sigma_u^+$ state with the Alignment Calculator program [106] made by former group member Anders Aspegren Søndergaard. This molecule has a rotational constant $B = 1.65$ GHz [107], and the static polarizabilities $\alpha_\parallel = 73.3$ Å^3 and $\alpha_\perp = 41.2$ Å^3 [108]. The polarizability anisotropy, which determines the strength of the interaction with the laser pulse, is, therefore, $\Delta\alpha = \alpha_\parallel - \alpha_\perp = 32.1$ Å^3. I assumed that the dimers were initially populated in different rotational states according to the Boltzmann distribution at a temperature of 0.37 K, weighted by the 5 to 3 abundance ratio of the even and odd J states resulting from nuclear spin statistics [103, p. 349]. For the alignment pulse, I used a duration of 1 ps and an intensity of 5×10^{10} W/cm^2. Note here that such a high intensity can only be used because

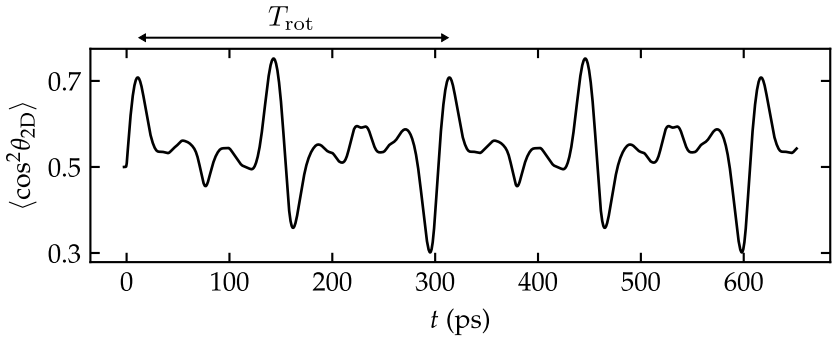

Figure 3.2: Simulation of the nonadiabatic alignment dynamics for gas-phase Na_2 in the $1^3\Sigma_u^+$ state at a temperature of 0.37 K. The pulse parameters are given in the text.

the interaction is nonresonant, which limits unwanted processes such as electronic excitation or ionization of the molecules. This is crucial for the experiments on alignment of the alkali dimers that I will show in Chapter 8 because the alkali metals have very low ionization potentials.

Figure 3.2 shows the result of the calculation. The alignment trace exhibits a transient increase in the degree of alignment promptly after the molecules have interacted with the laser pulse, as also predicted with the classical description earlier. Due to a phase mismatch in the rotational wave packet, the obtained degree of alignment is limited [18]. After a full rotational period defined as $T_{\mathrm{rot}} = 1/2B$, the molecules realign because all phase factors in Eq. 3.3 have evolved by multiples of 2π. This is known as a *full revival*. *Half revivals* also show up halfway in between the full revivals, and here the maximally obtained degree of alignment is higher than for the full revivals. Note that the degree of alignment drops below 0.5 (anti-alignment) immediately after the half revival, while the order is reversed at the full revivals, where the degree of alignment first dips below 0.5 and then increases to a value far above. Finally, *quarter revivals* are observed at $T_{\mathrm{rot}}/4$ and $3T_{\mathrm{rot}}/4$ due to the nuclear spin statistics weights which skew the populations in the even and odd J states [14, 20, 28, 29].

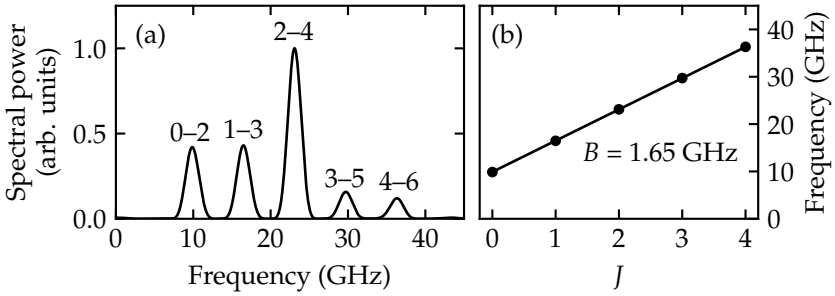

Figure 3.3: (a) Spectral analysis of the simulated alignment trace for Na_2 in the $1^3\Sigma_u^+$ state (Fig. 3.2). The observed frequencies can be ascribed to the coupling between the J and $J' = J + 2$ rotational states, as annotated above each peak (labeled as J–J'). (b) Central positions of the frequency peaks in (a) as a function of the assigned J quantum numbers. A fit with Eq. 3.5 is shown, enabling the determination of the rotational constant.

3.2 Spectral analysis

Information about the rotational energies of the Na_2 molecules is encoded in the frequencies that make up the alignment trace in Fig. 3.2. To illustrate this, I have made a spectral analysis by calculating the Fast Fourier Transform (FFT) of the alignment trace, see Fig. 3.3(a)[3]. The spectrum reveals that the alignment trace is comprised of several distinct frequencies that are equally spaced from each other. These arise from coherences between the J and $J' = J + 2$ rotational states in the rotational wave packet[4] [25, 28, 29]. Knowing this, the J quantum numbers can be assigned to each peak in Fig. 3.3(a). Note also that the populations in the peaks are modulated by the nuclear spin statistics weights.

From the rotational energies, see Eq. 3.4, one can calculate that

3 Before calculating the FFT the data has first been corrected for a constant detrend (subtraction of the mean), then multiplied by a Hamming window, and finally zero-padded. This approach has been used for all FFT spectra shown in this thesis. Readers are referred to reference [109] for an overview of these concepts.

4 When calculating the matrix elements $\langle\psi(t)|\cos^2\theta_{2D}|\psi(t)\rangle$ for the wave packet in Eq. 3.3, the terms where $\Delta J = J' - J \neq 0$ or 2 cancel out. For $\Delta J = 0$, the time-dependence cancels out, so these couplings only result in a constant offset [20].

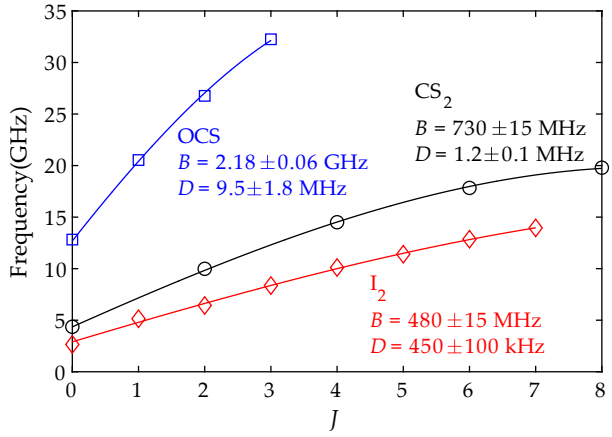

Figure 3.4: Fits with the nonrigid linear rotor model, Eq. 3.7, to the observed frequencies for the J and $J+2$ coherences for nonadiabatic alignment of I_2, OCS, and CS_2 inside helium droplets. Figure from [32]. Reproduced with minor adaptions with permission. Copyright 2024 by the American Physical Society.

the frequencies associated with the J and $J+2$ coherences are given as

$$\nu_{J,J+2} = B(4J+6). \tag{3.5}$$

To obtain the rotational constant, a linear fit using Eq. 3.5 can now be made to the frequencies in Fig. 3.3(a) as a function of the assigned J values, see Fig. 3.3(b). With this strategy, the rotational energy levels of the molecule can be determined.

As mentioned in Chapter 1, experiments on nonadiabatic alignment of I_2, OCS, and CS_2 inside helium droplets were previously conducted in my group. In this study, the rotational energies were found to be those of nonrigid linear rotors [32]

$$E_J = BJ(J+1) - DJ^2(J+1)^2. \tag{3.6}$$

The J and $J+2$ coherences thus gave rise to frequencies at

$$\nu_{J,J+2} = B(4J+6) - D(8J^3+36J^2+60J+36). \tag{3.7}$$

Fits with this nonlinear function were then used to extract the effective B_{He} and D_{He} constants for the molecules inside the helium droplets, as shown in Fig. 3.4.

3.3 Adiabatic alignment

Molecules can also be aligned adiabatically by a laser pulse with a duration that is much longer than the rotational period of the molecule [11, 12, 14, 28, 110–115]. In this scenario, the molecules can no longer be considered frozen while the interaction, still given by Eq. 3.1, lasts. When the interaction is turned on slowly, the induced torque will cause the molecules to start aligning along the polarization axis and the achieved degree of alignment will follow the envelope of the pulse intensity profile. The degree of alignment reaches its maximum at the peak intensity of the pulse and then starts to decrease again as the intensity drops. If the turn-off of the interaction is also slow enough, the molecules ultimately return to their original randomly oriented states after the interaction is gone.

In the quantum mechanical picture, the process can be understood as an adiabatic perturbation of the rotational eigenstates of the initially field-free molecule. As the interaction slowly ramps up, the eigenstates transition to those of the field-perturbed molecule, called *pendular states*, which represents molecules undergoing libration around the polarization axis of the laser field. In these states, the degree of alignment is increased. When the interaction strength slowly decreases again, the molecules return to their original rotational field-free eigenstates [28, 111].

An advantage of adiabatic alignment is that it can be used to align molecules more strongly than with a single nonadiabatic alignment pulse. In addition, a high degree of alignment can be maintained for a long time by using a sufficiently long laser pulse. This is very useful when experiments are to be done on aligned samples of molecules. However, the disadvantage is that the molecules are perturbed by the presence of the alignment laser field, which can, for example, lead to unwanted ionization and fragmentation of excited state molecules [116]. In contrast, with nonadiabatic alignment, the molecules periodically align under field-free conditions but only for brief periods that may be too short for some experimental purposes [28].

A third option is to induce alignment with a temporally truncated pulse. In this scenario, the interaction is adiabatically switched on and then rapidly switched off again when peak

alignment has been reached [39, 117–123]. This prepares the molecules in a set of pendular states that are then projected back on the rotational eigenstates of the field-free molecule, thereby creating a rotational wave packet that will lead to periodic revivals of the alignment. Wave packets formed in this way are comprised of fewer populated J states than those created by nonadiabatic alignment pulses (with the same pulse fluence), but the phase relationships are improved which can lead to stronger alignment during the revivals [123].

4

EXPERIMENTAL SETUP

The experiments I have conducted require a fairly extensive laboratory setup. In this chapter, I will give a detailed overview of the used equipment and the overall setup, before I dig into the actual experiments in the following chapters.

Figure 4.1 shows a graphic illustration of the alignment experiment with Ak_2 on the surface of helium droplets, to be discussed later. Conducting such an experiment involves multiple steps. First, the helium droplet beam has to be generated. The droplets must then be doped with the alkali dimers before the dimers are then pumped and probed using laser pulses. Finally, the Ak^+ fragments produced by the laser-induced Coulomb explosion must be detected. Generally, all the experiments I have done are conducted in this fashion, albeit with some changes to the wavelength and polarizations of the laser pulses. In some of the experiments, only the probe pulse is used.

As a brief note, it should be mentioned that the experiments presented in Chapter 6 and Chapter 10 were done on a separate, but very similar setup to the one I will now present. I will not describe this other setup here, but a detailed description from 2017 is available in the literature [125]. It has been upgraded somewhat since then to enable experiments with alkali metals and generally has the same capabilities as the setup I have primarily used.

4.1 The helium droplet machine

The helium droplet machine consists of four vacuum chambers, see Fig. 4.2. For the helium droplet experiments, three of those chambers are used: the helium droplet source chamber (I), the doping chamber (II), and the target chamber (III). The last chamber is a secondary source chamber (IV) containing a pulsed Even-Lavie valve that can be used for gas-phase experiments. A small chamber between the doping chamber and the target cham-

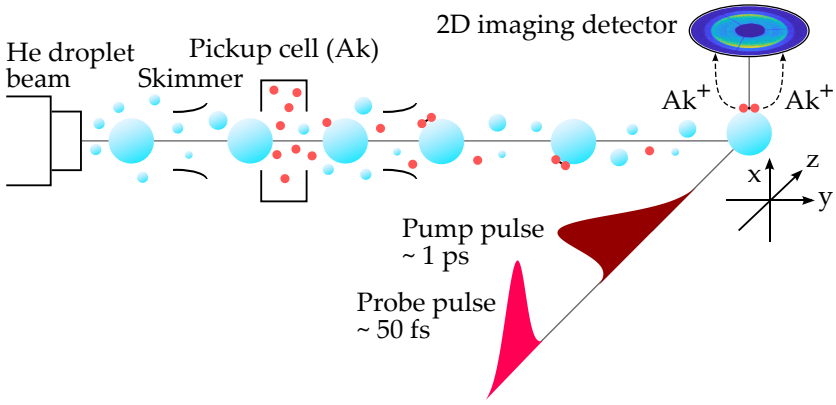

Figure 4.1: Sketch of the experiment conducted to study the rotational dynamics of Ak_2 on helium droplets. First, the helium droplets are formed and doped with the alkali dimers, and then the systems are exposed to the pump pulse and the subsequent probe pulse, producing pairs of Ak^+ fragments to be detected. Own work, adapted from [124].

ber was in place until spring 2023, see Fig. 4.2. This chamber only contained a liquid nitrogen cold trap and was removed to reduce the path length in the experiment. For all presented experiments performed on this machine, with the exception of that presented in Section 11.2, the cold trap was still in place.

Each chamber is evacuated using attached turbo pumps. Turbo pumps cannot pump directly to atmospheric pressure and the exhausts are therefore connected to pipes ("backing lines"). These pipes are pumped down to $\sim 10^{-3}$ mbar by backing pumps, which can pump directly to the atmosphere. Some of the turbo pumps are connected to the same backing line, as the backing pumps can pump large volumes per second. The pumping speeds for both the turbo pumps and the backing pumps are listed in Table 4.1[5].

The chambers are separated by pneumatic gate valves, which can be used to isolate the chambers from each other. Relays monitor the status of the turbo pumps and also receive information

5 The pump setup has changed a bit over time due to breakdowns, pump maintenance, and removal of the small chamber with a cold trap, which also had its own small turbo pump (Leybold Turbovac 361, 400 l/s). The pumping specifications given here are correct at the moment of writing and differ a bit from that given in [126].

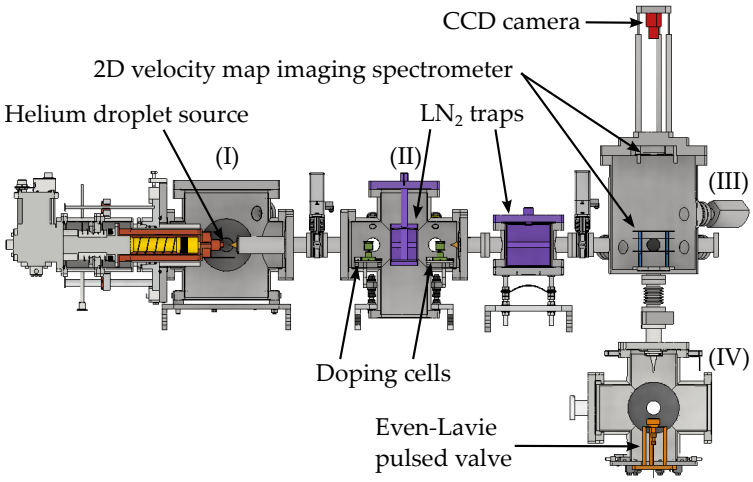

Figure 4.2: The helium droplet machine, consisting of a helium droplet source chamber (I), a doping chamber (II), a target chamber (III), and an occasionally used secondary source chamber (IV). A small chamber (removed in spring 2023) with a cold trap is located between the doping chamber and the target chamber. A flight tube, located above the target chamber, is not shown. Figure adapted from [126].

Chamber	Turbo pump	Pump speed (l/s)
Source (I)	Pfeiffer HiPace 2300	1900
Doping (II)	Pfeiffer TMU 521	520
Target (III)	Pfeiffer HiPace 700	685
EL (IV)	Pfeiffer HiPace 700	685
Backing	**Backing pump**	**Pump speed (m^3/h)**
Source (I)	Edward Booster EH500 and Edward E2M80	400
Doping (II)	Pfeiffer Duo 65	70
Target (III) and EL (IV)	Leybold Trivac D16B	16

Table 4.1: Pumping speeds for the turbo pumps connected to the different chambers, and for the backing pumps.

about the pressure in the chambers and backing lines. If the turbo pumps fail, or if the pressure rises above predetermined threshold values, the relays close the gate valves that surround the chamber where the incident occurred, thus isolating it from the rest of the machine.

The pressures in the chambers are monitored by Vacom ATMION ATS40C pressure gauges. These are attached to a port on the outside of each chamber and utilize a combination of a Pirani gauge and a hot cathode gauge to measure the pressure. The hot cathode gauge (a Bayard-Alpert ion gauge) measures the pressure by emitting electrons that ionize the surrounding gas molecules. The formed ions are collected on a wire and the current they produce is measured. This works for pressures down to around 10^{-11} mbar. For pressures above 10^{-1} mbar, the gauge is at risk of burning out very quickly. Thus, the ATMION automatically switches to the Pirani gauge when reaching this threshold. Pirani gauges are based on the principle that the pressure of a gas can be measured via the heat loss of a thin wire. This heat loss is primarily driven by convection and heat conductance through the gas. As this does not work properly once the gas becomes too dilute, Pirani gauges are only used for low vacuum [127].

For the backing lines, only Pirani gauges (InstruTech CVM211 Stinger and Kurt Lesker KJL275808LLMB) are used, since the low vacuum encountered here is well within their working range.

4.1.1 *Helium droplet source chamber*

The continuous helium droplet beam is created in the helium droplet source chamber. In all my experiments, the droplets are formed via subcritical expansion (see Section 2.2), that is, by expanding a cold gas of helium at high pressure into a vacuum through a small nozzle. I will now explain how this is done in practice.

First, 99.999% purity helium gas is sent through a 2-m long copper pipe with a diameter of 1/16 inch. The pipe is wrapped around both the first and the second stage of a coldhead attached to a closed cycle cryostat (Sumitomo Heavy Industries, RDK-415D). At the end of the pipe, the helium has been cooled down to around 4 K, which is too low for the subcritical expansion. It

is therefore necessary to reheat the helium slightly. This is done by heating the nozzle assembly, which is mounted at the tip of the coldhead, where the helium passes through before finally reaching the nozzle. A set of heating resistors (Farnell MHP35 470F) are directly mounted on the nozzle assembly alongside a temperature probe (a silicon diode, Lake Shore DT-670B-CU). These are connected to a temperature controller (Lake Shore 335), which automatically regulates the heating to maintain the desired temperature. Since heat radiation from the surrounding parts of the vacuum chamber can affect the temperature of the nozzle assembly, it is covered with a copper heat shield. The helium, now reheated to the desired working temperature, is finally expanded into the vacuum chamber through a platinum nozzle with a 5-μm diameter (PLANO, 0.6 mm thickness with 2 mm diameter) [126].

The experiments conducted on this machine have been done with a stagnation pressure of 25 bar and nozzle temperatures ranging from $T_{\text{nozzle}} = 10.5$–16 K. Outside this temperature range, the signal levels in the experiments tend to either become uncontrollably large (big droplets) or too weak to measure (small droplets)[6]. I estimate that the mean size of the helium droplets generated with these expansion conditions varies from ~ 4000 to ~ 18000 helium atoms (see Fig. 2.2).

4.1.2 *Doping chamber*

The helium droplet beam enters the doping chamber through a small 1-mm skimmer (Beam Dynamics, Model 2), see Fig. 4.2. This chamber has two aluminum guiding rails attached to the bottom. A doping cell can be mounted on each rail. The doping cells can either be ovens, used for solid samples, or gas cells. For the work presented in this thesis, only the ovens have been utilized and solely for alkali metals.

The ovens are made of stainless steel and consist of a socket, a detachable crucible, and a lid for the crucible. Technical drawings of the doping chamber with the oven assembly in place are

6 The weak signals with small droplets can perhaps be remedied by improving the droplet flux (via different nozzle designs) and the detection efficiency in the experiment.

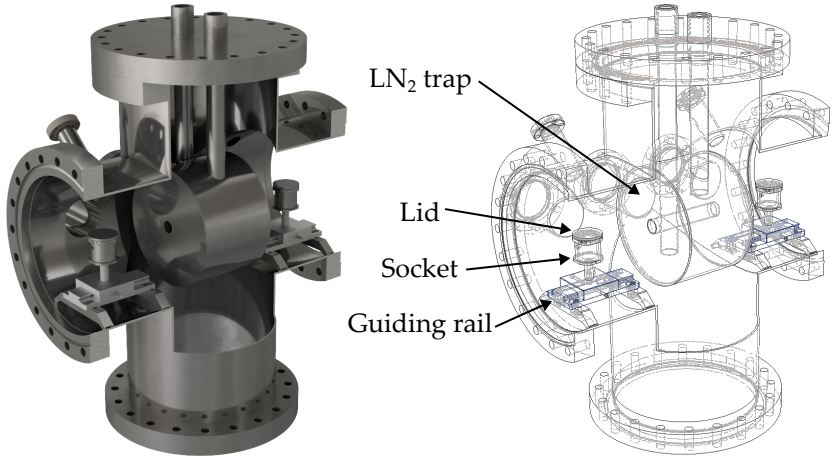

Figure 4.3: Technical drawings of the doping chamber, courtesy of Lorenz Kranabetter. Two oven setups can be fit into the chamber, one on each side of the LN_2 coldtrap. See the text for details.

shown in Fig. 4.3. Physical pictures of the oven and crucible can also be seen in Fig. 4.4(a) and (b). Two 3-mm holes have been drilled through the sides of both the sockets and the crucibles such that the helium droplet beam can pass directly through. Having a detachable crucible makes it easy to change samples. After removing the crucible and loading it with a new sample (see Section 4.2), it can simply be dropped back into the socket which is still mounted on the guiding rail in the chamber. Small grooves have been cut into the socket, such that the crucible locks correctly into place with the holes for the helium droplet beam lining up. Thus, no realignment of the equipment is necessary.

A Kapton wire is wrapped around the socket of each of the two ovens. By sending an appropriate current through these wires, the ovens can individually be resistively heated to a desired temperature. This heating process is monitored and controlled by PID controllers (Eurotherm 3216) outside the chamber via a set of thermocouples. Both the thermocouples and wires for the current enter the chamber via a feed-through mounted on a side port. The current, controlled by the PID controllers, is delivered by a standard power supply (Aim-TTi CPX400DP).

By heating the ovens, the vapor pressures of the alkalis in the

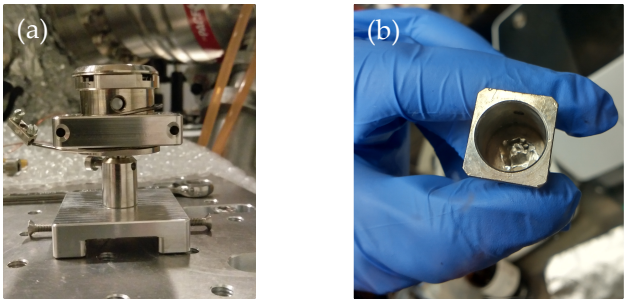

Figure 4.4: (a) Side view of the oven. The 3-mm hole for the helium droplet beam is visible on the front. (b) Detachable crucible loaded with a potassium sample, before being covered with anhydrous *n*-hexane.

crucibles increase. When the helium droplets pass through the ovens, they can collide with the atoms in the vapor and pick them up, as previously explained in Chapter 2. By adjusting the oven temperatures, the doping conditions can be controlled such that some of the droplets pick up two or three alkali atoms, which then form the dimers or trimers. For experiments on homonuclear alkali oligomers only one oven is used, while both ovens are in use for heteronuclear alkali oligomers such that the droplets can pick up atoms of first one species and then the other species afterward. Table 4.2 lists temperatures that I have commonly used when doing measurements on the various alkali homonuclear dimers and homonuclear trimers. As the temperatures are always optimized before conducting the experiments to get proper signal levels, quite some variation may be present in the actual values. Note also that due to the Poisson pickup statistics, the listed operating temperatures will not result in exclusive doping with dimers or trimers (see Section 2.3).

A consequence of the oven design where the helium droplets pass through via holes in the sides is that some alkali atoms will manage to escape. The atoms will only exit the oven if they fly along the same axis as the helium droplet beam. Thus, an effusive beam of gas-phase alkali atoms will also unavoidably be present in the experiments. There are possible alternative oven designs that can mitigate the presence of such an effusive beam[7],

7 One possible design is to let the helium droplet beam pass over the top of an

	Operating temperature (°C)	
Alkali	Dimers	Trimers
Li	425	–
Na	170	200
K	120	150
Rb	100	120
Cs	80	100

Table 4.2: Common operating temperatures for experiments with focus on a particular alkali homonuclear dimer or homonuclear trimer. Note that these values can vary quite a lot based on other aspects of the experiment.

but none have been tested or implemented in our group.

The doping chamber also contains a liquid nitrogen filled cold trap located between the two ovens, see Fig. 4.2 and Fig. 4.3. The cold trap is shaped like a torus, where the droplet beam can pass through the center. The cold trap primarily helps reduce the amount of residual gas-phase atoms and molecules in the chamber, which may unintentionally be doped onto the droplets. The cold trap thus helps maintain a clean droplet beam. Since the cold trap is lined up such that it does not block the droplet beam, it will not efficiently block the effusive beam of alkali atoms that escape the oven that is positioned before the cold trap in the beam direction.

Before entering the target chamber, the doped droplet beam passes through a 2-mm skimmer (Beam Dynamics, Model 2) and into a small chamber containing just a liquid nitrogen cold trap. This cold trap captures parts of the droplet beam and the effusive beam that are diverging. Since this small chamber adds extra length to the droplet beam path, it will reduce the wanted signal levels due to the beam divergence. As already mentioned, it was therefore removed in spring 2023.

oven with a long slit along the droplet beam axis. The alkali atoms can then exit through the slit and cross the droplet beam perpendicularly, thereby enabling pick up.

4.1.3 *Target chamber*

After traveling through another 2-mm skimmer (Beam Dynamics, Model 2), the droplet beam enters the target chamber (see Fig. 4.2). This chamber contains the velocity map imaging (VMI) spectrometer used for all the experiments and the multichannel plate (MCP) detector system (see details in Section 4.3). Inside the spectrometer, the droplet beam is intersected perpendicularly by the laser pulses used for the given experiment. The laser pulses enter the chamber via a window with an anti-reflection coating for 400 nm and 800 nm, mounted on a port on the side of the chamber.

A feed-through with ports for SHV cables (rated for 15 kV) is mounted on the side of the chamber. These ports make it possible to connect the electrostatic plates in the VMI spectrometer to a voltage supply. The top of the chamber also has a set of feed-throughs for SHV cables (rated for 5 kV), such that the MCP detector system can be connected to the voltage supply as well.

A μ-metal cylinder surrounds the VMI setup to shield against external magnetic fields. This is critical when doing measurements on electrons, but less so when measuring ions as I have done in all my experiments.

4.1.4 *Secondary source chamber*

The secondary source chamber is located underneath the target chamber, see Fig. 4.2. This chamber hosts a pulsed Even-Lavie valve (EL-7-4-2015-HRR, HT, 1 kHz) used for gas-phase experiments [128, 129]. For the work presented in this thesis, the valve has been used to produce molecular beams of I_2. These beams have then been used for calibration experiments (see Section 10.1.2 and Appendix A).

The Even-Lavie valve can be used for both liquid and solid samples as well as gasses. Liquid samples can be put onto some glass microfiber filter paper and solid samples, I_2 for example, can be wrapped up inside the filter paper. The filter paper with the sample is placed inside a small cylindrical tube in the center of the valve assembly. Vaporized atoms or molecules from the sample can then be co-expanded into the vacuum chamber with

a carrier gas, typically helium at high pressure, in a supersonic expansion [130]. If needed, the valve can be heated to increase the vapor pressure of the sample. The valve is typically operated at 200 Hz, creating a pulsed molecular beam that enters the target chamber and the VMI spectrometer from below. Inside the spectrometer, the beam can be crossed perpendicularly with appropriately timed laser pulses to probe the atoms or molecules. For corrosive samples, like I_2, the sample should be removed after use and the valve thoroughly cleaned.

4.2 Sample preparation

To avoid the rapid oxidation that happens when alkalis are exposed to oxygen, and the risk of explosions if they come in contact with water[8], the samples are stored and handled in an inert argon atmosphere inside a glove box. To load a new sample, the detachable crucible from the oven is brought into the glove box and a small spoonful of the chosen alkali is scooped up with a spoon and put into the crucible, see Fig. 4.4(b). The crucible is then filled with anhydrous *n*-hexane (an inert liquid) to prevent the sample from getting into contact with air later in the process, before storing it in a small jar with a lid on. As the jar is closed inside the glove box it will be filled with argon, serving as an additional layer of protection against air. Finally, the closed jar is taken out of the glove box and transported to the lab where the crucible (still containing anhydrous *n*-hexane) can be dropped into the oven socket in the vacuum chamber. The lid for the crucible is then put on before the chamber is closed again and pumped down to $\sim 10^{-9}$ mbar. When the pressure drops the n-hexane quickly evaporates, leaving an isolated alkali sample ready to use.

The first time a newly inserted alkali sample is used in the lab it is often necessary to heat the sample to a higher temperature than otherwise needed during daily operation (see commonly used temperatures in Table 4.2) before any appreciable amount of alkali ions can be observed. This could indicate that a thin

8 Interestingly, the explosion is in part driven by a Coulomb explosion between alkali cations that are created in the outer layer by rapid transfer of electrons from the alkali atoms to the water [131].

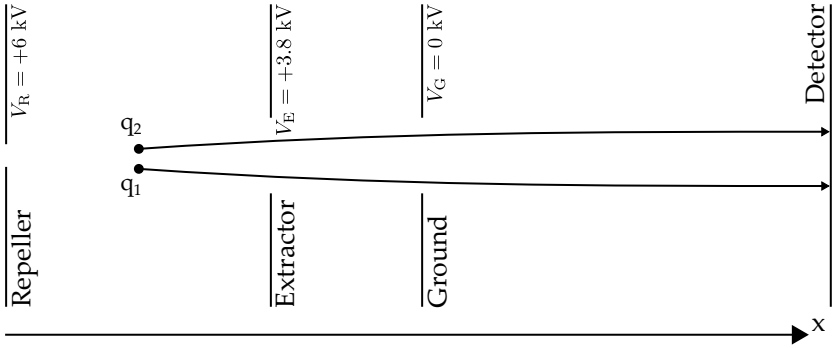

Figure 4.5: Illustration of the VMI spectrometer, consisting of the repeller, the extractor, and the ground electrodes. The spectrometer maps charged particles created in the interaction region onto a position-sensitive detector. The hit location is determined by the velocity of the particle.

layer of alkali-metal oxide has managed to form on the sample surface, even after taking all the precautions to avoid it. Typically, heating the sample an additional 20 degrees Celsius or so for a while will be enough to make the signal appear, after which the temperature can be lowered again.

For alkali samples that have been stored for a long time in the glove box (or if the glove box has been temporarily out of order), a beginning layer of oxidation may also have begun to form. This is seen as a white crust, which should be avoided when scooping up the alkali. If the crust is colorful (for example yellow), this is a sign of superoxides which are extremely explosive and may detonate when, e. g., digging a spoon into it [132, 133]. A careful inspection of the sample is thus always a good idea before working with it.

4.3 Detection system

4.3.1 *Velocity map imaging*

In all experiments presented in this thesis, the basic observables are the velocities of various ions. These velocities are measured by using a VMI spectrometer in conjunction with a position-sensitive detector.

The VMI spectrometer is based on the original Eppink-Parker design [134]. It consists of three circular electrodes named repeller (R), extractor (E), and ground (G), see the drawing in Fig. 4.5. In the experiments, the ions of interest will be generated in the center between the repeller and the extractor, where the helium droplet beam (or the molecular beam from the Even-Lavie valve) is crossed by the laser pulses. A static inhomogeneous electric field, created by applying voltages to the repeller and the extractor plates, can now be used to focus the ions on a detector a given distance away. Eppink and Parker demonstrated that by appropriately choosing the electrode voltages, velocity map imaging can be obtained, where ions with the same initial velocity are projected onto the same position on the detector screen [134]. Effectively, this corresponds to a projection of the 3D velocity sphere (a Newton sphere) onto a 2D plane, where the radial distance r in the projected image is proportional to the transverse (radial) velocity of the ions. The kinetic energy associated with the transverse velocity can thus be expressed as

$$E_{\mathrm{Tr}} = cr^2, \tag{4.1}$$

where c is a calibration constant. It is however of limited use to only know the energy associated with the transverse velocity. Fortunately, the 3D velocity distribution can be reconstructed mathematically via an inverse Abel transform if the projected image has cylindrical symmetry [135]. The total kinetic energies of the ions, only available as a distribution after the inverse Abel transform, are then proportional to the radial component $\mathcal{R}$ in the 3D velocity distribution [134]

$$E_{\mathrm{kin}} = k\mathcal{R}^2, \tag{4.2}$$

where k is a calibration constant, which can be determined by recording a velocity map image of ions with known kinetic energies (see Appendix A). For our setup, the VMI conditions are obtained with repeller and extractor voltages V_{R} = +6000 V and V_{E} = +3800 V. The ground plate is kept at V_{G} = 0 V to create a field-free region before the detector.

Two position-sensitive MCPs ($\sim$ 40-mm active diameter, El Mul Technologies B050V), stacked in Chevron configuration [136] with $-$600 V on the front MCP and +1200 V on the back MCP, are used

to detect the ions. The MCPs are located at the top of a flight tube, which is mounted on top of the target chamber (not sketched in Fig. 4.2). When the ions hit a channel in the MCP stack, an avalanche of electrons is released. These electrons are accelerated toward a phosphor screen (El Mul Technologies Scintimax P47) kept at +4000 V, where they impinge and create a fluorescent dot. The time-of-flight (ToF) of the ions are related as

$$t \propto \sqrt{\frac{m}{qV_{\mathrm{R}}}}, \tag{4.3}$$

where m is the mass of the ion and q is the charge [134], leading to a whole distribution of different arrival times for the various ions created in the experiments.

A CCD camera (Allied Vision Prosilica GE680), operating at 100–200 Hz, is used to record frames of the phosphor screen with a 401×401 pixel resolution, thereby recording the locations the ions are mapped to. The low frame rate creates an issue because the camera shutter is open for so long that signals from ions with different masses will be collected into one frame with no way to separate the signals afterward. It is therefore necessary to gate the detector such that it is only sensitive to the wanted ions. This can be done by keeping the front MCP at 0 V and then only lowering the voltage to -600 V in the short time window where the ions of interest arrive. This makes the MCP insensitive outside the window since a voltage difference of $\sim$ 1800 V is needed for normal operation. As different ions can have the same mass-to-charge ratio m/q, the gating cannot always be used to isolate a single ion species fully.

Each detected ion hit will be seen as a cluster of pixels lighting up. The clusters are identified via the DBSCAN clustering algorithm [137] and then centroided to obtain a final value for the location. Since the lasers used for the experiments run at 1 kHz (see Section 4.4), one frame recorded by the camera will contain ions from 5 to 10 laser shots. By stacking many frames, a full 2D VMI image can be constructed.

Toward the end of my PhD, we installed a Tpx3Cam detector as a replacement for the CCD camera. The Tpx3Cam has a time resolution of 1.6 ns which makes it possible to record VMI images for different ion species at the same time without having to gate

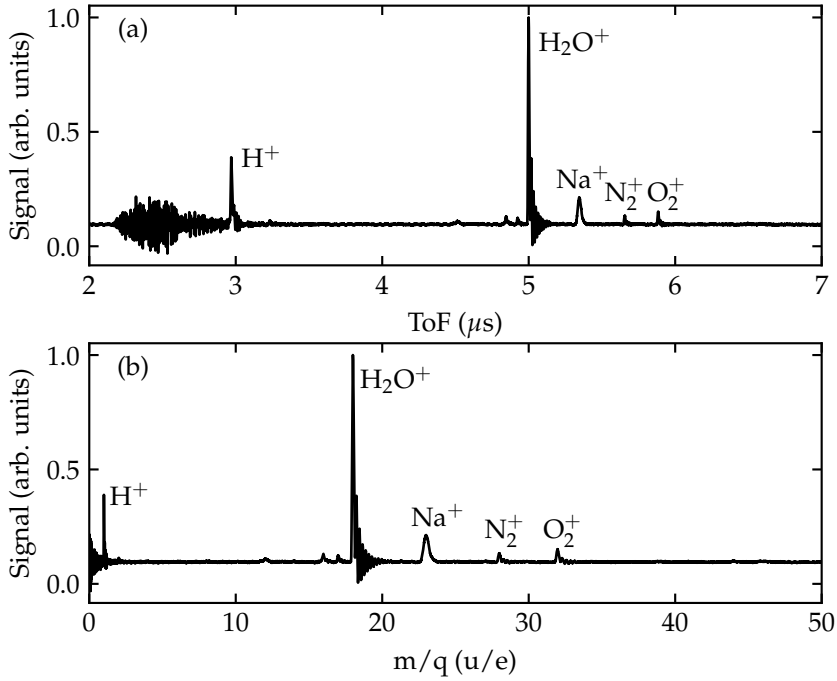

Figure 4.6: (a) ToF spectrum for a measurement on Na_2 where Na^+ ions were created. Peaks for H^+ and H_2O^+ are always present due to residual gas in the chamber, and can be used to calibrate the spectrum. (b) Calibrated ToF spectrum showing the m/q ratios for the different peaks. This enables identification of the various formed ions and confirms that the Na^+ ions are indeed formed in the experiment.

the detector and even enables a direct determination of the full 3D velocities of the ions [138]. This creates many new opportunities for experiments, some of which will be explored in Chapter 6 as well as in Chapter 10, where a more thorough introduction to the Tpx3Cam will also be presented.

4.3.2 *ToF mode*

The detection system can also be run in a ToF mode where the arrival times of ions at the detector are recorded. This is a useful tool for identifying the ions present in the experiment and for setting up the gate window for the detector. To enable ToF mode, the front MCP and the phosphor screen must be grounded. The

voltage on the back MCP is then set to 1800 V to make the detector sensitive. Via capacitative decoupling of the voltage, the fluctuations in the voltage on the back MCP, caused by the arrival of the ions, can be measured and displayed on an oscilloscope.

Figure 4.6(a) shows an example of a ToF measurement recorded for an experiment on Na_2, in which Na^+ ions were created. Most of the present peaks arise from the ionization of residual atoms and molecules in the target chamber, especially H_2O. These peaks can be used to calibrate the entire ToF spectrum via Eq. 4.3, such that the m/q ratios of the other peaks can be determined, see Fig. 4.6(b). In the calibrated spectrum, a peak lies at $m/q = 23$ u/e, demonstrating that sodium is present in the experiment and that Na^+ ions are formed. The electronics controlling the detector gating can now be configured such that the detector is only active for the ToF interval that contains the Na^+ ions.

4.4 Optical setup

The femtosecond laser pulses in the experiments originate from a Ti:Sapphire tabletop laser system (Solstice Ace, Spectra-Physics) seeded by an 80 MHz laser oscillator (MaiTai, Spectra-Physics). The pulses are generated at a 1 KHz repetition rate with a pulse energy of 7 mJ and are spectrally broad ($\sim$ 50 nm at FWHM) with a central wavelength of 800 nm. The pulse duration is on the order of 50 fs (FWHM). A beam splitter is used to split the pulses into two arms: one that will be used for the probe pulses and one that will be used for the pump pulses. In the following paragraphs, I describe the beam paths in each of the two arms. An overview of the general optical setup is also presented in a sketch in Fig. 4.7.

To set the alkali dimers into rotational motion, I need a nonresonant pump laser pulse. 1300 nm is a good choice of wavelength since the energy of a single photon is then lower than the energy gap to the nearest excited states (see Section B.3 for some of the potential curves) [139–142]. Pulses with that wavelength can be created from the 800 nm pulses in the pump arm via an optical parametric amplification (OPA) system (TOPAS Prime, Spectra-Physics). The generated 1300 nm pulses have a pulse duration of approximately 50 fs which is too short for the experiments, in

particular because it typically results in a high intensity which can ionize the alkali dimers. It is therefore necessary to temporally stretch the 1300 nm pulses to a more appropriate duration of around 1 ps. To achieve this, the pulses are sent through a prism stretcher (see details in Section 4.4.1). After stretching, the beam is guided toward the target chamber. To obtain spatial overlap with the probe beam, the pump beam is transmitted through a dichroic overlap mirror and then aligned through a set of irises in front of the chamber. Finally, it is focused to a spot size $\omega_0 \sim 100$ μm at the intersection with the helium droplet beam by a planoconvex (f = +300 mm) lens. To adjust the pulse energy for the experiment, a combination of a polarizer and a half-wave plate is used before stretching the pulses, thereby also partly reducing the self-focusing effects that may occur when passing the initially short pulse through the thick glass prisms in the stretcher. The transmission axis of the polarizer is always set to horizontal (p-polarization) to minimize the transmission losses when passing through the stretcher. This is also the polarization used for the final experiments.

The pulses in the probe arm are already very suitable for the experiments and only require a minimum of manipulation. To enable a time overlap for the pump and the probe pulses at the target chamber, the probe beam is sent through a delay line to compensate for the beam path the pump beam must traverse inside the OPA and the prism stretcher. The detour includes passing through a motorized delay stage, such that the final time delay between the pump and the probe pulses can be carefully adjusted and scanned in the experiments. The probe beam is then reflected on the dichroic overlap mirror and carefully overlapped with the pump beam. Ultimately, the beam is focused to a spot size $\omega_0 \sim 50$ μm at the helium droplet beam by the lens. It is vital that the spatial overlap of the pump and the probe is still preserved at the focus such that the pumped molecules are also the ones that are eventually probed in the experiments. To achieve this overlap, the focused beams can be redirected (via an insertable mirror in front of the chamber) toward a small pinhole, and the beams aligned for maximum throughput. Before starting the experiments, a half-wave plate and a thin-film polarizer at the beginning of the probe arm are used to set the desired probe

power. A second half-wave plate, positioned toward the end of the beam path, can be used to choose the polarization for the experiment.

In some of the experiments, probe pulses centered at 400 nm are used. These pulses are made via second-harmonic generation by passing the 800 nm probe pulses through a beta barium borate (BBO) crystal, cut for a phase matching angle at 29.2°, which can be placed into the setup.

4.4.1 *Pulse stretching*

A broadband laser pulse can be stretched by adding group delay dispersion (GDD)[9], or, in other words, by chirping the laser pulses such that some frequency components arrive earlier than others, thus extending the duration of the pulse. Adding positive GDD corresponds to up-chirping the pulse (red light arrives before blue light), while negative GDD down-chirps the pulse (blue light arrives before red light). For some pulse with an initial pulse duration τ_0, the pulse duration after accumulating some amount of GDD can be calculated as [143, p. 48]

$$\tau = \tau_0 \sqrt{1 + \left(\frac{4 \ln(2) \times \mathrm{GDD}}{\tau_0^2} \right)^2}. \tag{4.4}$$

Propagation through a material typically adds some positive GDD (for materials with normal dispersion). In contrast, the angular dispersion that can be obtained with prisms and gratings can be used to add significant amounts of negative GDD to a pulse. Often, prisms and gratings are used to recompress pulses by counteracting the positive GDD added by passing through various optical elements in a setup, thus balancing the chirp. In my case, however, I will use them to introduce large amounts of negative GDD to the pump pulses, thereby down-chirping them, to stretch the pulses to an appropriate duration. Note that the chirp itself is not a problem in the experiments, since the pump pulses are nonresonant. Thus, the actual temporal distribution of wavelengths in each pulse is unimportant.

9 Also known as second-order dispersion, calculated as $\frac{\mathrm{d}^2\phi}{\mathrm{d}\omega^2}$ where ϕ is the phase accumulated by a plane wave propagating through a dispersive medium [143, p. 48].

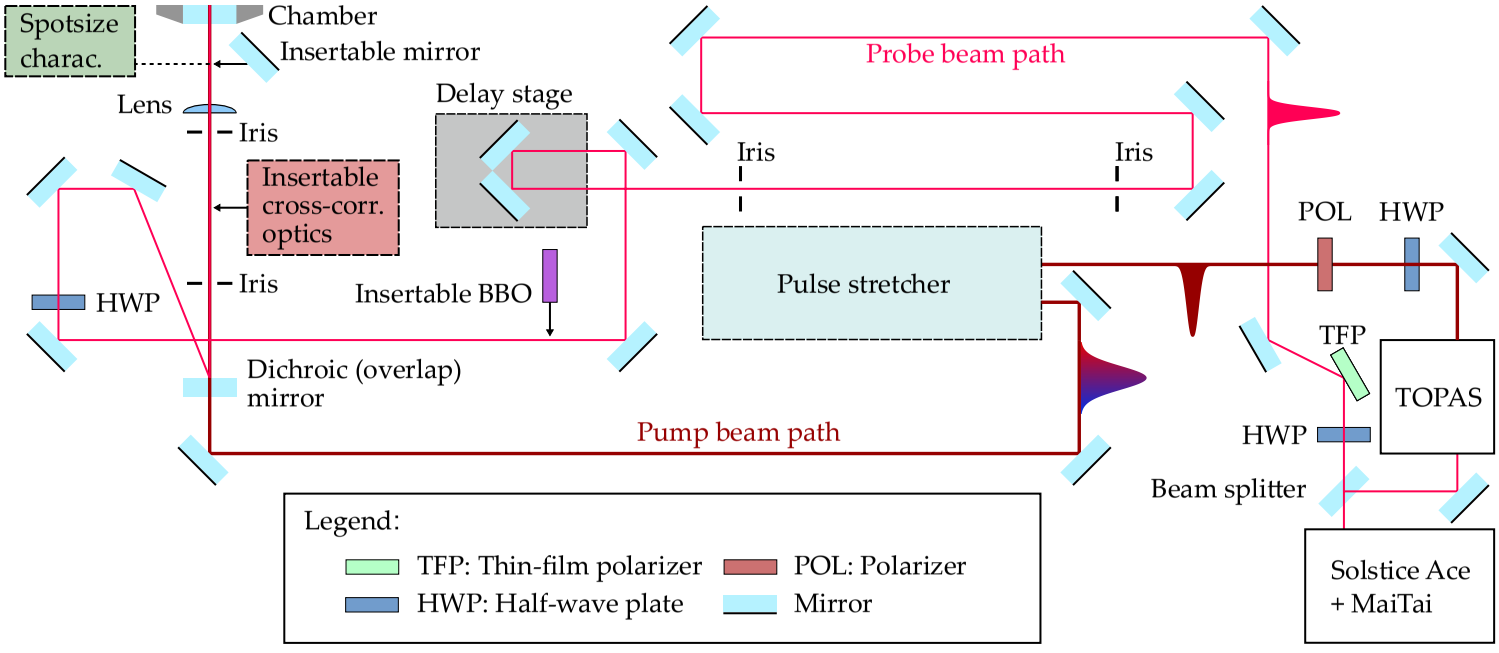

Figure 4.7: Sketch of the general optical setup for the probe beam path and the pump beam path. The used pulse stretcher has mostly been a prism stretcher, but a grating stretcher can be used as a replacement to make longer pump pulses.

To create 1300 nm pulses with a duration of around 1 ps, the pulses are sent through a prism pair, see Fig. 4.8. In such a setup, the blue wavelengths have a shorter optical path length than the red wavelengths, thereby giving rise to the wanted pulse stretching. Figure 4.8 may appear to suggest the opposite, but the red wavelengths travel through more glass than the blue wavelengths, which adds a significant contribution to the optical path length. The prisms are angled such that the beam enters at the Brewster angle and exits at the same angle, leading to minimal losses for a horizontally polarized beam. During setup, this angle is identified as the angle leading to the minimum deviation in the beam path with respect to the entering beam. While propagating through the glass in the prisms some positive GDD is accumulated. The amount of GDD can be calculated by looking up the amount of group velocity dispersion (GVD) for the specific glass type and multiplying with the path length L in the material [143, p. 49],

$$\mathrm{GDD}_{\mathrm{material}} = \mathrm{GVD}_{\mathrm{material}} \times L. \tag{4.5}$$

The (negative) GDD contribution from the angular dispersion when passing through the prism pair is given as

$$\mathrm{GDD}_{\mathrm{angular}} = -\frac{2l\lambda^3}{\pi c^2}\left(\frac{\mathrm{d}n}{\mathrm{d}\lambda}\right)^2 \quad \text{(single pass)}, \tag{4.6}$$

where l is the distance between the prisms, λ is the wavelength, and n is the wavelength-dependent refractive index of the prism material [144, pp. 26–28, 143, pp. 81–82][10].

After the first pass through the prism pair, the pulses are spatially chirped. This chirp can be removed by passing the pulses through the prism pair one more time, which will also double the added negative GDD. Thus, a retro-reflector is placed after the prism pair to redirect the beam upwards and then back into the prisms again. Moving the beam upwards makes it possible to separate the output beam from the input beam after exiting the stretcher.

10 Be aware that reference [144] for unexplainable reasons choose to call GDD for GVD, which deviates from the established terminology and only serves to confuse people.

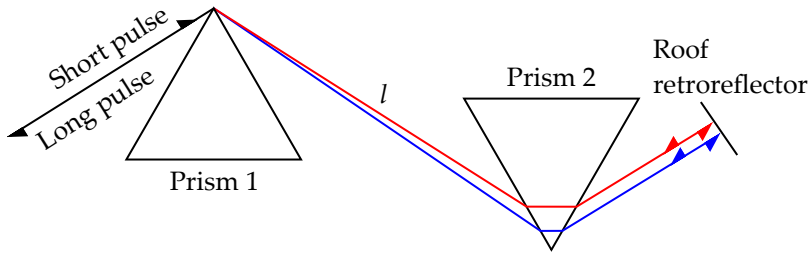

Figure 4.8: Sketch of the prism stretcher used to down-chirp and stretch the pump pulses. A roof retroreflector is used to reflect the beam directly back through the prims a second time to stretch the pulses even further and eliminate spatial chirp.

The used prisms are made of SF10 glass. SF10 is only moderately dispersive at 1300 nm with a GVD of 62.166 fs^2/mm and a chromatic dispersion $dn/d\lambda = -0.018536\ \mu m^{-1}$ [145]. For a double pass through the prism pair, with an estimated average total path length through the glass material of 30 mm[11], one can use Eq. 4.4, 4.5, and 4.6 to calculate that the prisms must be separated by 1.9 m to achieve the desired pulse duration of around 1 ps. Longer pulse durations would require an even larger separation between the prisms, which quickly becomes impossible because the beam expands too much after the first prism to fit onto the second. To make pulses longer than around 1 ps, it is therefore necessary to use a grating stretcher instead, which is extremely dispersive at high wavelengths. Such a grating stretcher is essentially a drop-in replacement for the prism stretcher in the optical setup, see Fig. 4.7.

I designed and built a grating stretcher using a pair of volume phase holographic transmission gratings[12] (Wasatch Photonics, HD 1145 l/mm, 1310 nm), to enable long-pulse alignment experiments. The setup is sketched in Fig. 4.9. To get optimal transmission through the gratings, the 1st order diffraction is used (Littrow configuration). The GDD accumulated from the

11 The path length is different for the various wavelength components, but the deviations are too small to be of interest here.

12 These gratings are neat because they have no etched grooves but instead use modulation of the refractive index in the glass material. As a result, they can in principle be cleaned without damaging the component.

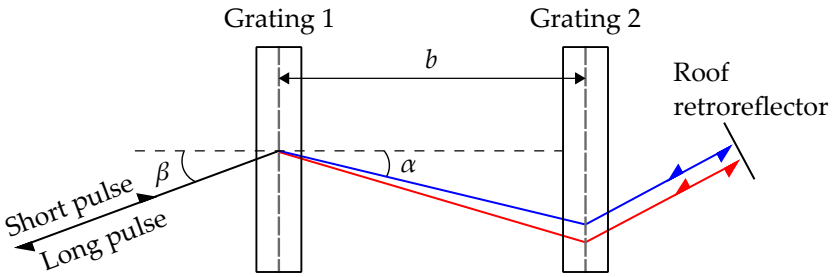

Figure 4.9: Sketch of the grating stretcher, which is much more dispersive than a prism stretcher. As for the prism stretcher, a double pass is used to eliminate spatial chirp and add additional GDD.

angular dispersion for a single pass through the grating pair is given by

$$\mathrm{GDD}_{\mathrm{angular}} = -\frac{b\lambda^3}{2\pi c^2 d^2 \cos^3(\alpha)} \quad \text{(single pass)}, \tag{4.7}$$

where b is the separation between the two gratings, d is the grating constant, and α is the diffraction angle [144, pp. 24–26]. The GDD is again negative here, because the optical path length is shortest for the blue light, and even more so than for the prisms, since blue light diffracts at a smaller angle than red light. The gratings are optimized such that the diffraction angle α is the same as the angle of incidence $\beta = 48.6°$. As for the prisms, a small amount of positive GDD is accumulated while propagating through the grating material (6-mm thickness). However, the GDD from the angular dispersion is so large that the contribution from the material may as well be neglected. To avoid spatial chirp, a double pass through the grating pair is used in the same way as for the prism stretcher.

Due to the 35 × 45 mm dimension of the used gratings, the maximum pulse duration that can be obtained with this setup, while still fitting the beam nicely onto the second grating, turns out to be around 200 ps. In that configuration the gratings are only separated by around 10 cm, demonstrating the very strong angular dispersion obtained when using gratings for stretching pulses with large wavelengths.

4.4.2 *Beam characterization*

The pulse duration of the stretched pump pulse is characterized by an optical cross-correlation [146, pp. 209–213]. To make the cross-correlation, I do sum frequency generation with the pump and the probe pulses via critical phase-matching (type I) in a BBO crystal (100–200 μm thickness) [146, pp. 39–43]. The crystal is inserted into the path of the overlapped pump and probe beams before the target chamber. A fake window, identical to the one at the entrance of the target chamber, is placed before the crystal to emulate the conditions inside the chamber. The position of the delay stage in the 800 nm beam path is now adjusted until the pump and the probe arrive simultaneously in the crystal. If the phase-matching criteria are fulfilled, the photons from the probe (800 nm) and pump (1300 nm) will then be mixed to create photons at 495 nm, a visible green color. In practice, it is usually necessary to rotate the crystal while scanning the delay stage position to create the green light, since both the timing and the crystal angle must be correct for the process to take place[13].

After the crystal, the green light must be separated from the original beams. I do this with a prism, thus spatially separating the different color components. The green light can then be recorded with a commercial grating spectrometer (Avantes AvaSpec-3648). To obtain the temporal profile of the pump pulse, the delay stage is moved in steps, thereby shifting the delay between the two pulses. The spectrometer is used to integrate the signal, which is larger for better temporal overlap, at each stage position. The integration is done across the wavelength spectrum and the time interval used for the measurement. This produces a convolution of the two temporal pulse profiles. Since the pump pulse duration is much larger than the duration of the probe, the convolution is a sufficiently accurate estimate of the pump pulse profile.

An example of a recorded cross-correlation is presented in Fig. 4.10(a). By fitting a Gaussian curve to the data, the pulse duration and t_0, the stage position where the pulses arrive simul-

13 Rotating the crystal is only required because the crystal I use is cut for second-harmonic generation of 800 nm light, not sum-frequency generation with 800 nm and 1300 nm where the phase matching angle is different.

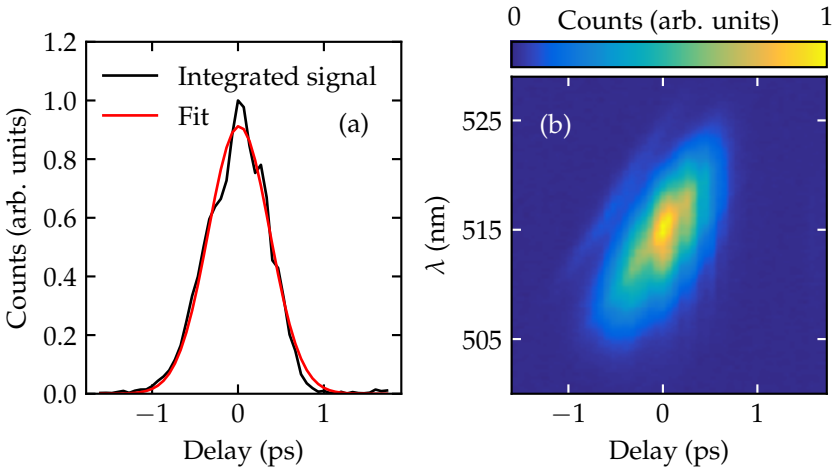

Figure 4.10: (a) Integrated signal for the sum frequency generated beam in the cross-correlation with the pump and probe, shown in black. The Gaussian fit used to extract the pulse duration, here 840 fs, is shown in red. The fit has been used to define t_0 and the delay axis. (b) Spectrogram from the same cross-correlation as in (a). The wavelength increases as a function of the delay, showcasing the down-chirp of the stretched pump pulse.

taneously (zero delay) in the experiment, can be extracted. Figure 4.10(b) shows a spectrogram from the cross-correlation. The down-chirp introduced to the pump pulse in the prism stretcher is directly visible here. Notice that the dominant wavelength is around 515 nm, not the predicted 495 nm, so it seems that the mixed wavelengths are not exactly 800 nm and 1300 nm but rather nearby wavelengths present in the broadband pulses. This is of no consequence to the cross-correlation and the extracted values.

To characterize the spot size of the focused pump and probe beams, the beams are intercepted by a mirror after the focusing lens in front of the target chamber and guided toward a 5 μm slit. By scanning the slit across the focused beams and integrating the transmitted light signal on a photodiode, the spatial characteristics can be measured, and the spot size extracted via a Gaussian fit. Recently, we have acquired beam profilers (Femtoeasy LP6.3 with UV window and Duma Optronics BeamOn HR 1") that allow for quick and quite reliable measurements of the spatial

pulse profiles.

The peak intensities of the Gaussian laser pulses are calculated as

$$I = \frac{4\sqrt{\ln 2}}{\pi^{3/2}} \frac{E_{\text{pulse}}}{\omega_0^2 \tau}, \tag{4.8}$$

where E_{pulse} is the pulse energy, τ is the pulse duration (FWHM), and ω_0 is the beam radius, that is, the spatial distance from the center of the beam spot and out to where the intensity has dropped by a factor of $1/e^2$ [147]. This formula has been used to calculate all intensities stated throughout the thesis.

5

QUANTUM-STATE-SENSITIVE DETECTION OF ALKALI DIMERS ON HELIUM DROPLETS

In this chapter, I present results from Coulomb explosion imaging of homonuclear alkali dimers on helium droplets. First, an in-depth introduction to the laser-induced Coulomb explosion method will be given. Next, the details of the experiment are presented. I will then show how Coulomb explosion can be used to identify whether the dimers were in the $1^3\Sigma_u^+$ state or the $1^1\Sigma_g^+$ state. In addition, I also show how covariance analysis can be used to corroborate the identification. Toward the end of the chapter, I extract the distribution of internuclear distances for the alkali dimers in both spin states and compare the findings to theoretical predictions.

The results to be shown are important because they establish Coulomb explosion of the alkali dimers on helium droplets as a probing technique that provides information about both the orientation of the dimers and their structures. In particular, the Coulomb explosion technique makes it possible to separate the signal from dimers in the $1^1\Sigma_g^+$ state and in the $1^3\Sigma_u^+$ state. This enables quantum-state-sensitive measurements throughout all my experiments on the alkali dimers.

5.1 Laser-induced Coulomb explosion of Ak_2

The principle of the method is to use an intense femtosecond pulse to double ionize the alkali dimers via multiphoton absorption. To illustrate this process, Fig. 5.1(a) shows the relevant potential curves for Na_2. As described in Section 2.3.1, Na_2 can form in both the $1^3\Sigma_u^+$ state and the $1^1\Sigma_g^+$ state on the helium droplets. Essentially only the respective vibrational ground states of the dimers will be populated because the droplets cool them down to the droplet temperature of 0.37 K [92, 99]. When the dimers are double ionized by the laser pulse, the wave functions are projected onto the repulsive Na_2^{2+} potential curve. Only a

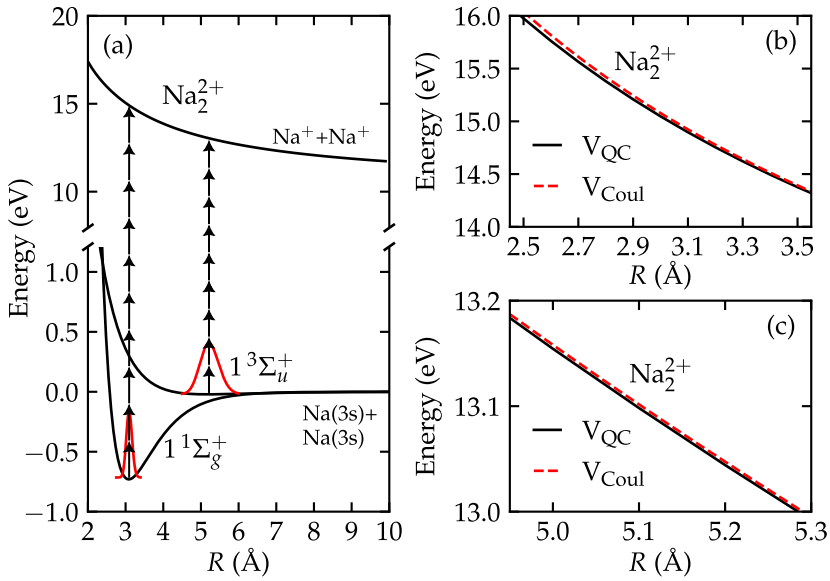

Figure 5.1: (a) Potential energy curves for Na_2 in the $1^3\Sigma_u^+$ state [107], the $1^1\Sigma_g^+$ state [139], and $V_{QC}(R)$ for $Na_2{}^{2+}$. The red curves illustrate the square of the ground state wave functions. The vertical black arrows (not to scale) depict the nine (ten) photons at 800 nm used to trigger Coulomb explosion of Na_2 in the $1^3\Sigma_u^+$ ($1^1\Sigma_g^+$) state. (b) and (c) Zoomed-in views of the calculated $Na_2{}^{2+}$ potential $V_{QC}(R)$ and the Coulomb potential $V_{Coul}(R)$ around the equilibrium distance of the $1^1\Sigma_g^+$ state (b) and the $1^3\Sigma_u^+$ state (c). Own work, adapted from [126].

single curve exists for $Na_2{}^{2+}$, because all valence electrons have been removed, leaving a closed-shell system. In the repulsive potential, the systems immediately begin to fragment into a pair of Na^+ ions due to the electrostatic repulsion, thereby converting the potential energy into kinetic energy.

As I will elaborate on below, the $Na_2{}^{2+}$ potential is to a good approximation given by the Coulomb potential

$$V_{\text{Coul}}(R) = 14.4\ \text{eV}/R[\text{Å}], \tag{5.1}$$

where R is the internuclear distance. The pair of Na^+ ions created by Coulomb explosion of Na_2 will share the available Coulomb energy evenly due to momentum conservation, and therefore end up with kinetic energies $E_{\text{kin}} = V_{\text{Coul}}(R)/2$. For a dimer starting

from the equilibrium distance R_{eq} = 3.08 Å of the $1^1\Sigma_g^+$ state [139], each ion will get an energy of E_{kin} = 2.34 eV. Meanwhile, Coulomb explosion for dimers in the $1^3\Sigma_u^+$ state will result in E_{kin} = 1.39 eV, as dictated by the larger equilibrium distance R_{eq} = 5.17 Å [107]. If the kinetic energies of the Na^+ fragments are measured, the internuclear distance of the parent dimers can be retrieved via Eq. 5.1. I will use this to determine the distribution of internuclear separation $P(R)$ for the dimers.

The Coulomb potential has previously been used as an approximation for the dicationic potential in studies on Coulomb explosion of diatomic molecules and molecular dimers [148–152]. For the alkali dimers, this approximation should be especially valid due to the closed-shell structure of Ak_2^{2+}. To assess how much the Coulomb potential deviates from the actual potential, Frank Jensen from Aarhus University has done a quantum chemistry calculation at the CCSD(T) level for Na_2^{2+} [124]. The found potential, $V_{QC}(R)$, is plotted alongside $V_{Coul}(R)$ in Fig. 5.1(b) at R-values around the equilibrium distance for the $1^1\Sigma_g^+$ state of Na_2. Figure 5.1(c) shows a similar plot for the equilibrium distance of the $1^3\Sigma_u^+$ state. The two potentials lie very close in energy with a difference of 27 meV at R_{eq} for the $1^1\Sigma_g^+$ state, and 3 meV at R_{eq} for the $1^3\Sigma_u^+$ state. Thus, the Coulomb potential can with good accuracy be used to determine the internuclear separation from the kinetic energies of the Na^+ ions. Additional calculations by Frank Jensen point to the same conclusion for the other alkali dimers [153].

Such a good agreement should however not be taken for granted. Consider for example Coulomb explosion of the argon dimer Ar_2. In this case, the removal of two electrons leads to an open-shell structure that can fragment via multiple channels [152]. Due to this, the Coulomb approximation breaks down and the kinetic energies of the formed Ar^+ fragments cannot be uniquely related to a single internuclear distance R. The problem can be remedied by removing all the valence electrons to once again end up with a closed-shell structure. Such a highly charged state can possibly be created using ultrashort intense x-ray pulses at free-electron laser facilities [154].

A final point I want to address here is whether more highly-charged states than Na_2^{2+} can be formed by multiphoton absorp-

tion. To answer this question, it is necessary to look at the ionization potential of Na. The valence electron is bound by 5.14 eV and can therefore be stripped from the atom by absorption of a few photons from an intense 800 nm laser pulse. However, the energy required to remove a second electron, this time from a closed shell, is 47.3 eV [74]. It is not feasible to deliver so much energy to the system with the laser pulses I have used. At most one electron will therefore be stripped from each of the Na atoms constituting the dimer, thereby forming the Na_2^{2+} state and initiating the Coulomb explosion. Similar arguments can be made for the other alkali dimers.

5.2 Experimental setup

Figure 5.2 illustrates the experiment, which I will now present. First, the droplets were doped with alkali dimers by sequential pick up of two alkali atoms in a heated oven that contained either Li, Na, K, Rb, or Cs (see operating temperatures in Table 4.2). Next, the doped droplet beam was then crossed by a laser beam consisting of intense $\sim$ 50 fs linearly polarized pulses inside the VMI spectrometer to trigger the Coulomb explosion of the dimers, and the velocities of the fragments recorded. Li_2, Na_2, and Rb_2 were probed with pulses centered at 800 nm, while 400 nm was used for K_2. Cs_2 was probed using the nonstretched 1300 nm output from the TOPAS. The used intensities varied from 1×10^{13} to 3×10^{14} W/cm^2 [see annotated values in Fig. 5.3(a2)–(e2)]. In the experiments with Li_2 and Na_2 the nozzle temperature was 11 K, giving slightly larger droplets than for the experiments with K_2, Rb_2, and Cs_2 where a temperature of 12 K was used.

5.3 Results

Figure 5.3(ai)–(e1) show a series of 2D velocity map images of the Ak^+ ions recorded in the experiments while gating the detector such that only the most abundant isotope is observed. All the ion images have a central region with no signal, due to a small metal disk, referred to as the *beam block*, placed in front of the detector. The purpose of the beam block is to prevent ions with low kinetic energy from hitting the detector. These ions can be created by

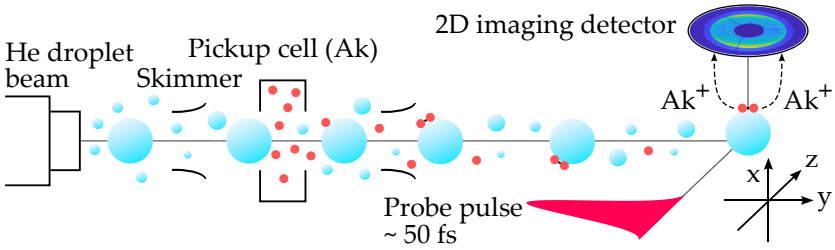

Figure 5.2: Illustration of the experiment. The droplets were doped with two alkali atoms to form Ak_2. The probe pulses were then used to trigger Coulomb explosion, producing pairs of Ak^+ fragments which were detected with the 2D imaging setup.

ionization of Ak atoms in the effusive beam and from ionization of single Ak atoms doped onto the helium droplets. Due to their low velocities, they would hit the detector in a small area, which can quickly cause burn damage. By blocking them, the signal levels on the remaining parts of the detector can be increased. Three radial stripes with no signal are also present in the images. These are due to the thin supporting rods that the beam block is mounted on. In Fig. 5.3(a1)–(c1) and (e1), part of the center has furthermore been digitally cut to remove the remaining parts of ions with low kinetic energy that hit the detector around the edge of the beam block, thereby improving the visual contrast in the images.

Several channels are visible in the ion images outside the blocked centers in the regions marked by the annotated white rings in Fig. 5.3(a1)–(e1). The inner channel in each image lies between the solid ring and the dashed ring. The next channel, termed the outer channel, lies between the dashed and dot-dashed rings. This channel is not present in the Li^+ image, see Fig. 5.3(a1). A third channel is visible in the K^+, Rb^+, and Cs^+ images, Fig. 5.3(c1)–(e1), outside the dot-dashed rings. These channels are the topic of Chapter 7 and will be ignored for now.

5.3.1 *Energy analysis*

To help identify the origin of the Ak^+ ions in the inner and outer channels it is useful to determine their kinetic energies. As men-

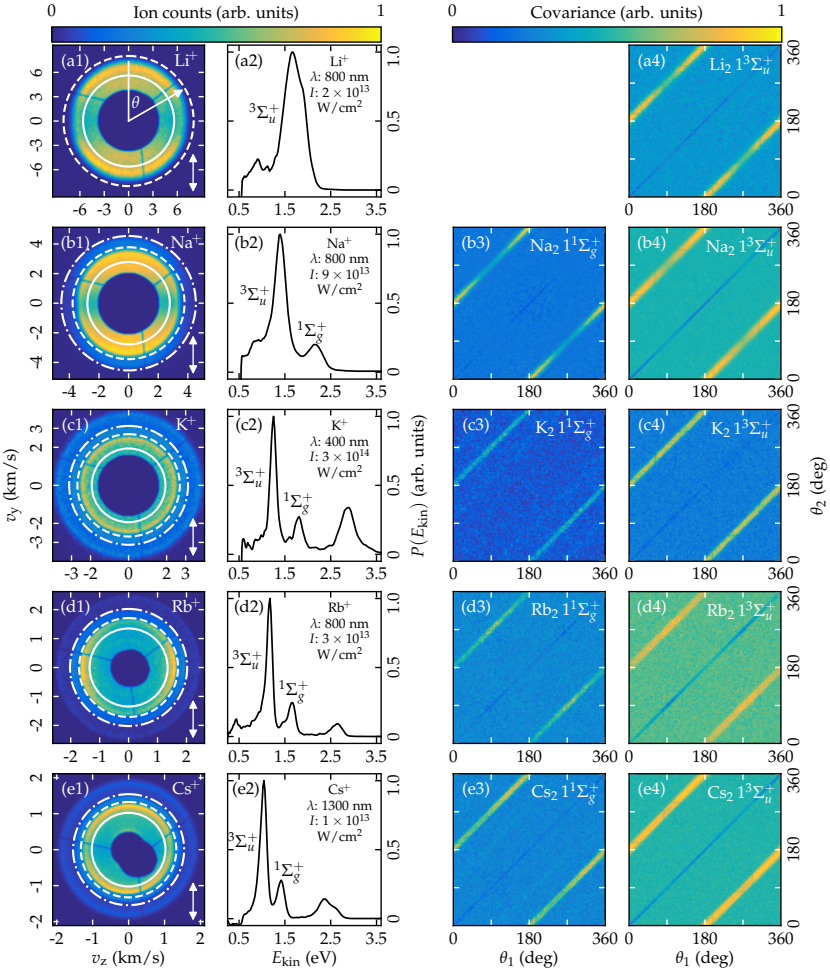

Figure 5.3: (a1)–(e1) 2D velocity map images of Ak^+ ions. The polarization axis of the laser pulses is indicated by the white arrows in the lower right corners. The regions between the annotated white rings contain ions from the $1^3\Sigma_u^+$ and the $1^1\Sigma_g^+$ channels (see the text). (a2)–(e2) Kinetic energy distributions $P(E_{\mathrm{kin}})$ for the ion images in (a1)–(e1). (b3)–(e3) [(a4)–(e4)] show angular covariance maps for the ions in the $1^1\Sigma_g^+$ [$1^3\Sigma_u^+$] channels. The experiments were conducted with nozzle temperatures T_{nozzle} = 11 K for the data in (a) and (b) and 12 K for the data in (c)–(e). Own work, adapted from [126]. Visual errors in the signal levels in panels (a1)–(e1), (b3)–(e3), and (a4)–(e4) have been corrected compared to the original figure, of no consequence to the interpretation.

tioned in Section 4.3.1, the energies of the ions are related to their radial velocity components in the 3D velocity distribution. The radial velocity distribution $P(\mathcal{R})$ can be obtained via an inverse Abel transform of the ion images if they are cylindrically symmetric. The requirement is fulfilled here, because the polarization axis of the laser pulses lies in the plane of the detector, as annotated with the white arrows in the lower right corner of Fig. 5.3(a1)–(e1). This creates a symmetry because the laser field imposes a preferred ionization direction in the images, which is either parallel or perpendicular to the polarization axis due to resonance effects (see Section B.1).

I use the *polar onion peeling* algorithm for the inverse Abel transform [135]. This algorithm first determines the contribution from the ions at the outer edge of the image, and then subtracts this from the inner parts. It then moves one step inward and repeats the process until it has worked its way through the entire image, thereby reconstructing the full 3D velocity distribution from which the radial velocity distribution $P(\mathcal{R})$ can be extracted. By using this approach, the center part screened by the beam block does not affect the retrieved distribution for the parts of the image that contain the signal of interest. With $P(\mathcal{R})$ at hand, the kinetic energy distribution $P(E_{\text{kin}})$ can now be obtained by applying Eq. 4.2. Since this is a transformation of a probability distribution, the distribution must be multiplied by the appropriate Jacobian elements to conserve the probabilities [155, p. 119],

$$P(E_{\text{kin}}) = P(\mathcal{R}) \left| \frac{\mathrm{d}\mathcal{R}}{\mathrm{d}E_{\text{kin}}} \right| = P(\mathcal{R}) \frac{1}{2k\mathcal{R}}. \tag{5.2}$$

The found $P(E_{\text{kin}})$ distributions are shown in Fig. 5.3(a2)–(e2). Each distribution features several peaks, except for the Li^+ ions where only one peak is observed, see Fig. 5.3(a2). The central positions of the peaks associated with the inner and the outer channels in the ion images can now be compared with the expected energy releases for Coulomb explosion of the alkali dimers. To do so, I fit a Gaussian curve to each of the peaks to determine their central positions. For Na_2, see Fig. 5.3(b2), I find that the peaks associated with the two channels lie centered at 1.39 eV and 2.15 eV. I estimate that the uncertainty on these values, primarily arising from the fitting procedure and the finite energy

resolution of the spectrometer, is less than 50 meV. The central positions match the expected energy release for Na_2 in the $1^3\Sigma_u^+$ state and the $1^1\Sigma_g^+$ state, 1.39 eV and 2.34 eV respectively. I therefore ascribe the ions in the peak at 1.39 eV to Na^+ fragments produced during Coulomb explosion of Na_2 in the $1^3\Sigma_u^+$ state. Likewise, the ions in the 2.15 eV peak are then ascribed to the $1^1\Sigma_g^+$ state dimers. I will further corroborate these assignments with covariance analysis in Section 5.3.2.

Table 5.1 presents an overview of the found peak positions for the different alkali dimers. As for Na_2, the uncertainty on the peak positions is estimated to be less than 50 meV. Note that for some of the dimers, multiple isotopologues are present in the experiment, but this will only lead to very minor uncertainties in the energies (see the discussion in Section 5.3.3). The table also shows the expected kinetic energy release for the $1^3\Sigma_u^+$ state and the $1^1\Sigma_g^+$ state dimers, based on equilibrium distances from the literature. In all cases, the energy of the ions in the inner channel agrees well with the expected energy, according to the Coulomb potential (see Eq. 5.1), for ions from the corresponding $1^3\Sigma_u^+$ state dimer. Similarly, the energies for the outer channels match the expectation for the $1^1\Sigma_g^+$ states. The origin of the ions in all the peaks can therefore be identified. Note that for Li_2 only the $1^3\Sigma_u^+$ state is observed, which is consistent with the literature [95, 99].

5.3.2 *Twofold covariance analysis*

To strengthen the interpretation that the two channels in the ion images, Fig. 5.3(a1)–(e1), contain ions from Coulomb explosion of the $1^1\Sigma_g^+$ state and $1^3\Sigma_u^+$ state dimers, I have conducted a twofold covariance analysis of the data. Covariance is used as a statistical tool to investigate the correlation between fragments. It has frequently been used to identify and study fragments that originate from Coulomb explosion of molecules in gas phase [26, 156–165] and inside helium droplets [26, 125, 161, 166, 167]. The principle is as follows.

In the experiments, distributions of events of various random variables are recorded in each camera frame[14]. This includes the

14 Note here that each camera frame contains data from 10 consecutive probe pulses, as mentioned in Section 4.3.1. Ideally, a distribution is measured for

	Peaks in $P(E_{\text{kin}})$ (eV)		$\frac{1}{2}E_{\text{Coul}}(R_{\text{eq}})$ (eV)	
	Inner	Outer	$1^3\Sigma_u^+$	$1^1\Sigma_g^+$
Li_2	1.69	–	1.73	2.69
Na_2	1.39	2.15	1.39	2.34
K_2	1.25	1.80	1.26	1.83
Rb_2	1.16	1.65	1.19	1.71
Cs_2	1.03	1.41	1.14	1.55

Table 5.1: Central positions of the $P(E_{\text{kin}})$ peaks in Fig. 5.3(a2)–(e2) associated with the inner and the outer channels in the ion images, Fig. 5.3(a1)–(e1). For comparison, theoretical kinetic energies for Ak^+ ions formed in Coulomb explosion of the alkali dimers are also listed, based on equilibrium distances for the $1^3\Sigma_u^+$ state and the $1^1\Sigma_g^+$ state taken from the literature [107, 108, 142]. The uncertainty on the experimental peak positions is estimated to be less than 50 meV.

angular distribution of ions in the image, the radial distribution of ions, the distribution of pixels that events are observed at, and so on. Mathematically, a chosen distribution can be denoted as X_i, where i is a label for the i'th camera frame. The distribution can be evaluated at a specific value x, to determine how many times an event was observed at that value in that particular camera frame. The covariance between two values from two distributions (which may be the same) is then calculated for a large sample of data as [156]

$$\text{cov}(x, y) = \langle XY \rangle - \langle X \rangle \langle Y \rangle, \tag{5.3}$$

where the terms $\langle X \rangle$ and $\langle XY \rangle$ are given as

$$\langle X \rangle = \frac{1}{N} \sum_{i=1}^{N} X_i(x), \tag{5.4}$$

$$\langle XY \rangle = \frac{1}{N} \sum_{i=1}^{N} X_i(x) Y_i(y), \tag{5.5}$$

each probe pulse, but that was not possible here due to the limited trigger rate of the CCD camera.

with N being the number of camera frames. The first term in Eq. 5.3 models the probability of measuring one ion with value x and another with value y within the same camera frame. Meanwhile, the second term models the probability of measuring one ion with value x independently of another ion with value y in the same camera frame and serves to correct the statistical measure for random coincidences. In total, Eq. 5.3 expresses how likely it is to observe x and y together in a frame, compared to the uncorrelated case where x and y are randomly observed.

The emission angles θ, see definition in Fig. 5.3(a1), of the Ak^+ ions released in Coulomb explosion of the $1^1\Sigma_g^+$ state and the $1^3\Sigma_u^+$ state dimers should be correlated with a 180° difference, since the ions must be ejected back to back as demanded by momentum conservation. Similarly, momentum conservation dictates an even sharing of the released Coulomb energy between the two ions, so their radial velocities v_r in the ion image must be equal in magnitude. I can check if these criteria are fulfilled for the channels associated with the $1^1\Sigma_g^+$ state and the $1^3\Sigma_u^+$ state dimers by calculating cov(θ,θ) ("the angular covariance") and cov(v_r,v_r) ("the radial covariance") for all the possible values of θ and v_r, and then displaying the results as covariance maps. In practice, the events are collected in bins of manageable sizes before doing the calculation (for example bins of 1° for the emission angles), to reduce the computation time.

Figure 5.3(b3)–(e3) and (a4)–(e4) show the angular covariance maps calculated for the ions in the channels associated with the $1^1\Sigma_g^+$ state and $1^3\Sigma_u^+$ state dimers in Fig. 5.3(a1)–(e1). Since the maps show the covariance, and thus the correlations, between the emission angles, an autocorrelation line on the diagonal of the map will be present because each event always correlates with itself. The diagonal is therefore filtered out. Each covariance map reveals two diagonal lines with $\theta_2 = \theta_1 \pm 180°$. This demonstrates that the ions are correlated with a relative emission angle of 180°, as expected for Coulomb explosion, similar to previous works [125, 166, 167]. Note that the modulations in the covariance along the two diagonal lines are due to anisotropies in the emission directions of the fragment Ak^+ ions (see Section B.1).

The angular covariance lines in Fig. 5.3(b3)–(e3) and (a4)–(e4) have a significant transverse width. For instance for Rb_2, the width is 19° for the channel ascribed to the $1^3\Sigma_u^+$ state, and

14° for the channel ascribed to the $1^1\Sigma_g^+$ state. This is much wider than what is typically observed for Coulomb explosion of a diatomic molecule in gas phase. As an example, in a study on gas-phase I_2 the width of the angular covariance lines was reported to be around 1° [125]. The large widths observed here for the alkali dimers indicate that the trajectories of the recoiling Ak^+ fragments are influenced by the helium droplets. I investigate this in Section 10.2.

The radial covariance maps are calculated for the distributions of v_r in the $1^3\Sigma_u^+$ state and $1^1\Sigma_g^+$ state channels in the upper half and the lower half of the ion images in Fig. 5.3(a1)–(e1). Splitting the images in halves is mostly a matter of preference, but one advantage here is that it removes the autocorrelation contribution along the diagonal, since the events are no longer matched up with themselves. This is important, as the real signal should lie on the diagonal if pairs of Ak^+ fragments with the same radial velocities are present. Figure 5.4 display the radial covariance maps calculated for the Na^+ ions in the channels associated with $1^3\Sigma_u^+$ state and $1^1\Sigma_g^+$ state Na_2 in Fig. 5.3(b1). For each channel, a clear island is present in the radial covariance map. The islands demonstrate that the Na^+ ions in the channels are created pairwise with the same radial velocities, and thereby support the assignment of these channels to Coulomb explosion of Na_2, again similar to previous work in the literature [161]. The radial covariance maps for the channels in the other ion images, Fig. 5.3(a1) and (c1)–(e1), show similar correlations and are left out due to the strong similarity to the plots shown for Na_2 in Fig. 5.4.

Overall, the twofold covariance analysis corroborates that the channels in the ion images indeed contain Ak^+ ions that originate from Coulomb exploded $1^1\Sigma_g^+$ state and $1^3\Sigma_u^+$ state alkali dimers. With this established, various types of analysis of the Ak^+ ions originating from Coulomb explosion of the $1^1\Sigma_g^+$ state and the $1^3\Sigma_u^+$ state dimers can now be conducted. It is a key point here that measurements for both spin states are done simultaneously in the lab, and that the contributions from the different states can then be separated afterwards. This makes it possible to obtain quantum-state-sensitive results, with the same experimental conditions, in a straightforward manner.

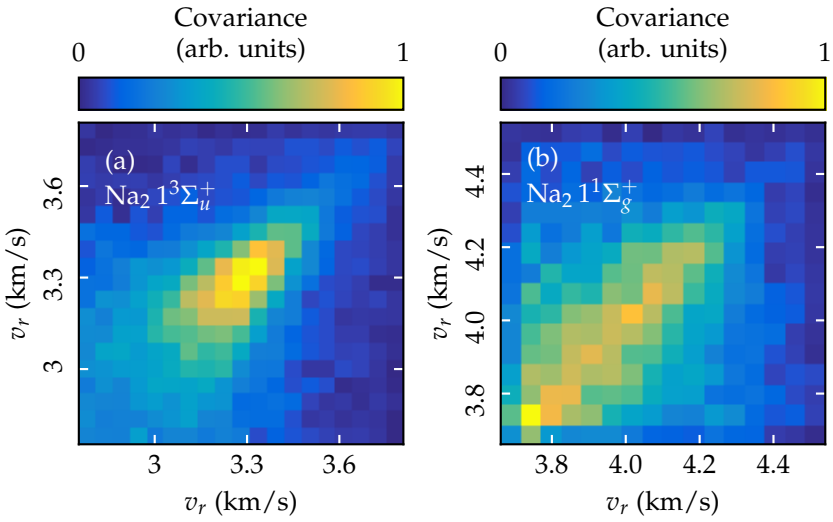

Figure 5.4: (a) and (b) Radial covariance maps for the Na^+ ions in the $1^3\Sigma_u^+$ channel (a) and the $1^1\Sigma_g^+$ channel (b) in Fig. 5.3(b1).

5.3.3 *Wave function imaging of Ak_2*

I will now demonstrate that the distribution of internuclear distances can be determined for the alkali dimers, similar to what has previously been shown in the literature for other diatomic systems [149–151, 168]. I will do this via the one-to-one correspondence between the kinetic energy of the recorded Ak^+ ions and the internuclear distance R of the dimers, for both the $1^3\Sigma_u^+$ states and the $1^1\Sigma_g^+$ states. The idea is to transform the distribution of kinetic energies $P(E_{\text{kin}})$ [from Fig. 5.3(a2)–(e2)] into the distribution of internuclear distances $P(R)$ by applying the probability transformation [152]

$$P(R) = P(E_{\text{kin}}) \left| \frac{\mathrm{d}E_{\text{kin}}}{\mathrm{d}R} \right| = P(E_{\text{kin}}) \left| \frac{1}{2} \frac{\mathrm{d}V(R)}{\mathrm{d}R} \right| . \tag{5.6}$$

Though I argued earlier that the Coulomb potential is a good approximation for the Ak_2^{2+} potentials, I will here use the potentials that Frank Jensen determined with the quantum chemistry calculations, since I have them available. When applying the above equation, I therefore set $V(R) = V_{\text{QC}}(R)$.

The results are shown by black curves in Fig. 5.5(a)–(e) for the different alkali dimers. The figure also shows the theoretical

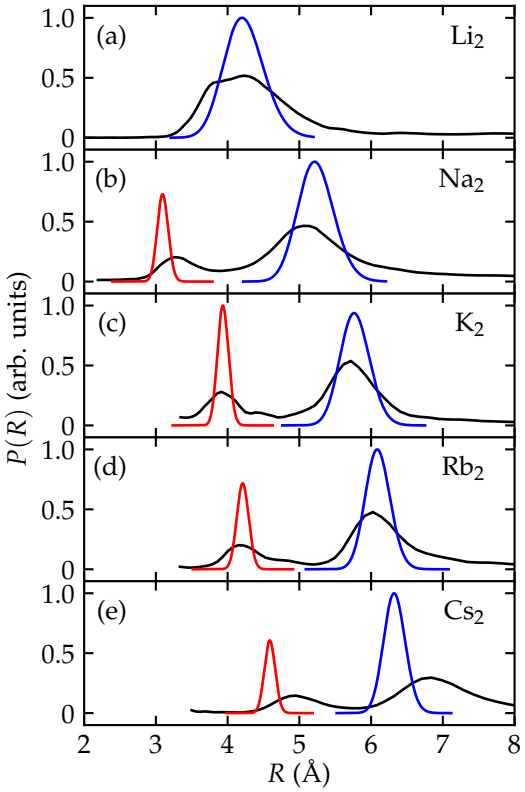

Figure 5.5: $P(R)$ distributions for the alkali dimers, calculated from the $P(E_{\mathrm{kin}})$ distributions presented in Fig. 5.3(a2)–(e2). The red curves depict the theoretically calculated $|\Psi(R)|^2$ distributions for isolated $1^1\Sigma_g^+$ state dimers, while the blue curves are for the $1^3\Sigma_u^+$ state dimers. Own work, adapted from [126].

$|\Psi(R)|^2$ distributions for the vibrational ground state of the $1^3\Sigma_u^+$ state and the $1^1\Sigma_g^+$ state dimers with blue and red curves, respectively. I calculated those distributions by solving the stationary vibrational 1D Schrödinger equation for the isolated dimers via available potential curves from the literature [107, 139–142]. To enable a direct comparison between the experimental results and the theory, I have normalized the theoretical distributions to the same area as the corresponding experimental peaks. First, I extracted the experimental areas for the $1^3\Sigma_u^+$ and the $1^1\Sigma_g^+$ states simultaneously by fitting the $P(R)$ distributions with a sum of two Gaussians. With this approach, the fit had to take the overlap

	Central position (Å)		FWHM (Å)	
	$P(R)$	$\lvert\Psi(R)\rvert^2$	$P(R)$	$\lvert\Psi(R)\rvert^2$
Na_2 $1^1\Sigma_g^+$	3.32	3.10	0.7	0.18
K_2 $1^1\Sigma_g^+$	3.96	3.94	0.8	0.18
Rb_2 $1^1\Sigma_g^+$	4.25	4.21	0.8	0.19
Cs_2 $1^1\Sigma_g^+$	4.97	4.59	0.8	0.18
Li_2 $1^3\Sigma_u^+$	4.22	4.22	1.2	0.65
Na_2 $1^3\Sigma_u^+$	5.13	5.22	1.4	0.58
K_2 $1^3\Sigma_u^+$	5.73	5.77	0.9	0.48
Rb_2 $1^3\Sigma_u^+$	6.09	6.09	0.9	0.41
Cs_2 $1^3\Sigma_u^+$	6.90	6.32	1.3	0.35

Table 5.2: Central positions and widths (FWHM) of the experimentally determined $P(R)$ distributions, alongside theoretical values for the $\lvert\Psi(R)\rvert^2$ distributions calculated using potentials from the literature. See the text for a discussion of the uncertainties. Own work, adapted from [126].

between the two peaks into account. Next, the areas found by the fit were individually used to normalize the related $\lvert\Psi(R)\rvert^2$ distributions. In the case of Li_2, I only used a single Gaussian for the fit.

By visual inspection of Fig. 5.5, it is clear that the experimental $P(R)$ distributions are wider than those predicted by the theory. To investigate this quantitatively, I have compiled a list of the widths (FWHM) for both the theoretical and the experimental distributions, extracted via Gaussian fits. This is presented in Table 5.2. The experimental widths for the $1^1\Sigma_g^+$ states are observed to be about 4 times larger than the corresponding $\lvert\Psi(R)\rvert^2$ distribution. In contrast, the widths are only about 2 times larger for the $1^3\Sigma_u^+$ states, except for Cs_2 where the width is about 4 times larger.

The experimental distributions are also observed to be shifted with respect to $\lvert\Psi(R)\rvert^2$ for some of the systems, as seen in Ta-

ble 5.2 where the central positions of the distributions are listed. For Li_2, K_2, and Rb_2 the shifts are below 0.05 Å for both spin states. In contrast, quite substantial shifts are observed for Na_2 and Cs_2. The $1^3\Sigma_u^+$ states are shifted with 0.09 Å and 0.58 Å, respectively, while the $1^1\Sigma_g^+$ states are shifted by 0.22 Å and 0.38 Å. Note here that the shift in energy for Na_2 in the $1^1\Sigma_g^+$ state is about twice as large as the shift for Cs_2 in the $1^1\Sigma_g^+$ state. This can be inferred from Table 5.1. The reason that the observed shift in $P(R)$ turns out to be larger for Cs_2 is due to the shape of the $Ak_2{}^{2+}$ potentials. For larger internuclear distances, the potentials become more flat, and as a result, any shift in the energy translates to a larger shift in the perceived internuclear distance. The equilibrium distance becomes larger when going to the heavier alkalis, so for Cs_2 a small energy shift will affect $P(R)$ more than the same energy shift would for the lighter alkalis.

There are multiple factors, which can affect the observed $P(R)$ and lead to deviations from the $|\Psi(R)|^2$ distributions. The first factor is nuclear motion in transiently excited electronic states of Ak_2 and $Ak_2{}^+$ during the ionization process, which can lead to shifts of $P(R)$. The ~ 50 fs duration of the probe pulses might not be short enough to avoid that such motion can occur. It is difficult to say which exact electronic states there is a possibility of populating, so I will not attempt to make any estimates of the precise shifts. Depending on the potentials, the shifts may be toward higher R-values or lower R-values. How big the shifts become will depend on the shape of the potential, but also the mass of the system. The effect will therefore most likely be largest for the lighter systems and could be a part of the explanation for the shifts in $P(R)$ observed for Na_2. For Cs_2, which also exhibited large shifts in $P(R)$, the effect should be small due to the very high mass. It is therefore possible that those shifts are primarily caused by other factors.

Motion in electronically excited states can also give rise to some of the broadening observed for $P(R)$. Again it is difficult to make quantitative estimates without knowing the involved potentials. I will however remark that a straightforward way to investigate such broadening, and also the beforementioned shifts, would be to shorten the probe pulses, thereby limiting the time in which the nuclear motion can occur. In addition, Franck-Condon

factors associated with the transitions can possibly also affect the observed $P(R)$ to some extent.

Interaction between the helium droplet and the recoiling Ak^+ fragments is another factor that can influence the results. As I will show in Chapter 10, the Ak^+ fragments are affected by an attraction to the helium which makes their trajectories bend. Possibly, this can lead to a small loss of kinetic energy. In particular, Cs_2 may be strongly affected by this, because the interactions with the droplets are larger for slowly moving fragments (see discussion in Section 10.2). Furthermore, if a dimer does not lie completely flat on the surface[15], one fragment might be slowed down by the helium, causing the other fragment to take a larger portion of the available Coulomb energy. Such interactions can lead to both broadening and shifts of $P(R)$.

The next factor is the energy resolution of the VMI spectrometer, which I have loosely estimated to be at most 100 meV, based on the widths of peaks in $P(E_{\text{kin}})$ for the photodissociation experiment on I_2 used for the energy calibration (see Appendix A for details on the calibration). The width of the $P(R)$ distributions will be influenced by this resolution, in particular for the heavier alkalis, where the equilibrium distances are larger and the Ak_2^{2+} potentials thus more flat. The estimated resolution can explain up to around 15% of the observed width for Rb_2 and Cs_2. Other students in the group are actively working on a new spectrometer design, which will hopefully improve the energy resolution and thereby enable better measurements.

A final minor factor is the presence of isotopologues in the experiment. If a dimer consists of two different isotopes of the same alkali, the Coulomb energy will not be equally shared due to momentum conservation. The effect will be largest for $^6Li^7Li$, where the relative mass difference is around 15%. The abundance of this dimer is however only around 13% [169], so it will not contribute much to the $P(E_{\text{kin}})$ distribution and thus also not to the $P(R)$ distribution. Note that since the detector is only gated on the most abundant isotope, only the $^7Li^+$ fragments

15 Figure 8.6 shows the distribution of orientations with respect to the surface for Na_2, K_2, and Rb_2 in both the $1^3\Sigma_u^+$ states and the $1^1\Sigma_g^+$ states. While it is most likely to find the dimers parallel to the surface, the distributions are quite broad, illustrating that the dimers may also be found at an angle to the surface.

are observed, which receive less energy than $^{6}Li^{+}$. For $^{39}K^{41}K$ (12% abundance) the relative mass difference is lower and will therefore not cause any significant broadening. Similar is the case for $^{85}Rb^{87}Rb$ even though the abundance is fairly significant (around 37%). Na and Cs are isotope pure, so isotopologues play no role in the discussion of Na_2 and Cs_2. In experiments with the new Tpx3Cam detector that has been mounted on the setup, it is possible to disentangle the contributions from the various isotopologues entirely. This will be demonstrated in a study of the heteroalkali dimers in Chapter 6.

5.4 Conclusion

In conclusion, I have demonstrated that Coulomb explosion can be used to identify homonuclear alkali dimers on helium droplets in both the $1^3\Sigma_u^+$ state and the $1^1\Sigma_g^+$ state. The identification was done via the kinetic energy of the fragment Ak^+ ions, which differ depending on the spin state of the dimer due to the different internuclear distances. Twofold covariance analysis revealed that the Ak^+ fragments were formed in pairs with matching velocities but ejected in opposite directions, as expected for Coulomb explosion of a diatomic molecule, thereby corroborating the identification. In addition, I determined the distribution of internuclear distances for the alkali dimers in the $1^3\Sigma_u^+$ state and the $1^1\Sigma_g^+$ state. This was done via the unique one-to-one correspondence between the kinetic energy of the Ak^+ ions and the initial internuclear distance, as dictated by the Ak_2^{2+} potential curves. The distributions were found to be broader than the theoretically expected $|\Psi(R)|^2$ by a factor of 2–4. Small shifts along the internuclear distance coordinate were also observed, in particular for Na_2 and Cs_2. I highlighted transient nuclear motion in electronically excited states of Ak_2 and Ak_2^+, the interaction between the recoiling Ak^+ ions and the helium, and the resolution of the spectrometer as primary factors that might affect the observed results.

6

COULOMB EXPLOSION IMAGING OF HETERONUCLEAR ALKALI DIMERS ON HELIUM DROPLETS

I will now present results that have been obtained in our lab for Coulomb explosion imaging of heteronuclear alkali dimers on helium droplets. The experiments were conducted by Simon H. Albrechtsen, Jeppe K. Christensen, and Rico M. P. Tanyag, while I assisted with parts of the experimental analysis (mostly that to be presented in Section 6.2.2) and following interpretation of the results. I include these results in my thesis because they provide additional perspectives to what I presented for the homonuclear alkali dimers in Chapter 5. Large parts of the analysis to be presented are identical to what was done for the homonuclear dimers, and I will therefore keep the explanations rather brief and primarily focus on the new aspects. Since the laser-induced Coulomb explosion principle was already introduced for the alkali dimers in Section 5.1 it will be skipped entirely here.

In brief, a description of the experimental setup will be given, after which I demonstrate that the heteronuclear alkali dimers can be experimentally identified via Coulomb explosion. The use of coincident filtering to clean the data from contaminating signals, originating from an unavoidable presence of homonuclear dimers on the droplets, is then discussed. Finally, the distribution of internuclear separations is determined for the heteronuclear alkali dimers and compared to theory.

6.1 Experimental setup

These experiments were conducted on the other helium droplet machine in the lab. A description of this machine has been published in the past [125], and the setup has since then been equipped with two doping ovens of the same type as described in Section 4.1.2, which are needed for the experimental investigations done here.

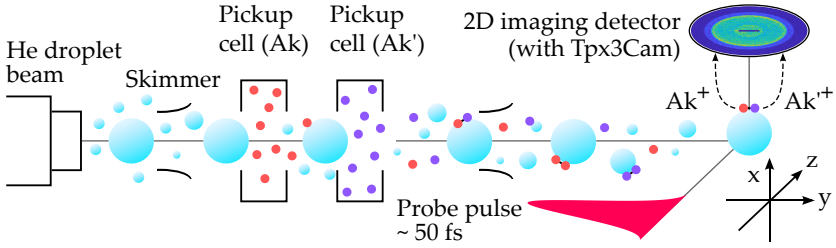

Figure 6.1: Sketch of the experiment. First, the droplets were doped with two species of alkali, Ak and Ak', to form heteronuclear alkali dimers. Next, Coulomb explosion of the dimers was triggered by an intense femtosecond pulse. The velocities of the Ak^+ and Ak'^+ fragments were recorded simultaneously with a 2D VMI spectrometer equipped with a Tpx3Cam detector.

The helium droplets were doped with one alkali atom Ak in the first oven, and then subsequently one atom of another alkali species Ak' in the second oven, as illustrated in Fig. 6.1. The two atoms then formed an AkAk' dimer on the surface of the droplet [99, 101]. However, in some cases, a droplet would manage to pick up either two Ak atoms or two Ak' atoms since the doping probabilities follow Poisson statistics as explained in Section 2.3. As a result, Ak_2 and Ak'_2 were also formed on some droplets. To trigger the Coulomb explosions via double ionization, the dimers were then probed by linearly polarized laser pulses with a $\sim$ 50 fs pulse duration, centered at a wavelength of 800 nm and with an estimated intensity of 1.3×10^{14} W/cm^2.

In this experiment, the velocities of the formed ion fragments were recorded with a 2D VMI spectrometer equipped with a Tpx3Cam detector. The Tpx3Cam has sufficient time resolution to enable simultaneous measurement of ions with different m/q values and entirely removes the need to gate the detector (see Chapter 10 for an in-depth introduction to the Tpx3Cam) [138, 170–172]. This feature was used in the present experiment to record ion images for Ak^+ and Ak'^+ at the same time. Note that the ion images not only contain contributions from Coulomb explosion of the AkAk' dimers but also Coulomb explosion of Ak_2 and Ak'_2.

Different expansion conditions were used to form the helium droplets in this experiment, compared to the settings given in Section 4.1.1. The nozzle temperature was set to 16 K while the

stagnation pressure of the helium was set to 50 bar. For this helium droplet machine, these parameters are expected to create droplets with a mean size of $\sim$ 10000 helium atoms (see Fig. 2.2).

6.2 Results

Results have been obtained for two different heteronuclear alkali dimers. In one case, the droplets were doped with Li and K to form LiK, and in the other case, the droplets were doped with Na and K to form NaK. I will focus on the experiments with LiK and only treat the results with NaK at the end of the chapter.

Figure 6.2(a1) and (b1) show 2D velocity images of $^7Li^+$ and $^{39}K^+$ ions recorded simultaneously with the Tpx3Cam. No beam block was used for these measurements, but a small rectangular part of the image centers have been digitally cut to remove the otherwise dominating effusive signal. The images contain signals from dissociative ionization of dimers at small radii, and then multiple channels of interest at larger radii.

The kinetic energy distributions $P(E_{\mathrm{kin}})$ for the ions, obtained via Abel inversion and calibration, are displayed in Fig. 6.2(a2) and (b2). The $P(E_{\mathrm{kin}})$ distributions contain new peaks not seen in the distributions shown previously for the experiments with only the homonuclear dimers $^7Li_2$ and $^{39}K_2$, see Fig. 5.3(a2) and (c2). For $^7Li^+$ the new peak shows up centered at 2.38 eV, while the new peak for $^{39}K^+$ lies at 0.42 eV. The peaks at 1.69 eV for $^7Li^+$ and 1.23 eV for $^{39}K^+$ match the kinetic energy releases previously observed from Coulomb explosion of $^7Li_2$ and $^{39}K_2$ in the $1^3\Sigma_u^+$ state (see Table 5.1), indicating that the homonuclear dimers are indeed still formed on the droplets in these experiments also[16].

According to the literature, the equilibrium distance of $^7Li^{39}K$ in the $1^3\Sigma^+$ state is R_{eq} = 4.97 Å [173]. If a Coulomb explosion is triggered by forming $(^7Li^{39}K)^{2+}$ at this internuclear separation, the fragment $^7Li^+$ ion receives a kinetic energy of 2.46 eV in the

16 A very faint peak is also present at 1.70 eV for $^{39}K^+$. This matches the energy expected for Coulomb explosion of $1^1\Sigma_g^+$ state K_2, see Table 5.1. It is unclear why so few $1^1\Sigma_g^+$ state dimers are present in this measurement series compared to the results shown previously in Fig. 5.3(c2). Note however that the probe wavelength is different, which may change the intensity needed to saturate the Coulomb explosion probing probability of the $1^3\Sigma_u^+$ state and the $1^1\Sigma_g^+$ state dimers.

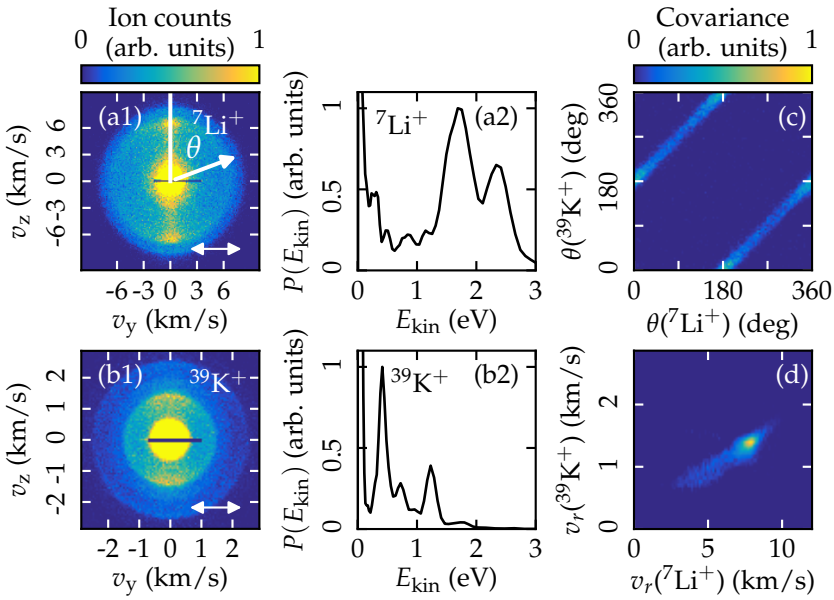

Figure 6.2: Simultaneously recorded 2D velocity map images for $^7Li^+$ (a1) and $^{39}K^+$ (b1). The probe polarization axis is indicated by the white arrows in the lower right corners. The kinetic energy distribution is shown in (a2) for the $^7Li^+$ ions and in (b2) for the $^{39}K^+$ ions. (c) Angular covariance map between the $^7Li^+$ and $^{39}K^+$ ions in the kinetic energy ranges that correspond to Coulomb explosion of $1^3\Sigma^+$ state $^7Li^{39}K$. (d) Radial covariance map between the $^7Li^+$ and $^{39}K^+$ ions. Own work, inspired from [174].

Coulomb approximation, while the $^{39}K^+$ ion receives 0.44 eV as required to conserve momentum. These energies are in good agreement with the new peaks that show up in the $P(E_{kin})$ distributions when doping the droplet with both Li and K. The peak at 2.38 eV in Fig. 6.2(a2) and the peak at 0.42 eV in Fig. 6.2(b2) are therefore ascribed to Coulomb explosion of $^7Li^{39}K$ in the $1^3\Sigma^+$ state.

To corroborate the identification of the dimers, twofold covariance analysis (see Section 5.3.2) is once more useful. First, angular and radial covariance maps are calculated for the $^7Li^+$ ions associated with $1^3\Sigma_u^+$ state $^7Li_2$ [the 1.69 eV peak in Fig. 6.2(a2)]. The results of the calculations look like the angular covariance map shown in Fig. 5.3(a4) and the radial covariance maps in Fig. 5.4 (only shown for Na_2), and I have therefore excluded the figures.

Likewise, for the $^{39}K^+$ ions from $1^3\Sigma_u^+$ state $^{39}K_2$ [the 1.23 eV peak in Fig. 6.2(b2)], the angular covariance map matches that shown in Fig. 5.3(c4) and the radial covariance map again looks like that obtained for Na_2, see Fig. 5.4. The correlations thus support that those $^7Li^+$ and $^{39}K^+$ ions originate from $^7Li_2$ and $^{39}K_2$.

Now, to strengthen the identification of ions from Coulomb explosion of $^7Li^{39}K$ in the $1^3\Sigma^+$ state, the angular covariance map between the $^7Li^+$ ions in the $P(E_{kin})$ peak at E_{kin} = 2.38 eV, Fig. 6.2(a2), and the $^{39}K^+$ ions in the peak at E_{kin} = 0.42 eV, Fig. 6.2(b2), is calculated. The resulting covariance map is displayed in Fig. 6.2(c). A clear 180° correlation is present in the emission directions of the $^7Li^+$ and $^{39}K^+$ ions, similar to that seen for the homonuclear dimers in Fig. 5.3(b3)–(e3) and (a4)–(e4). This indicates that they are created pairwise and ejected back to back as expected for Coulomb explosion of $^7Li^{39}K$. A radial covariance map calculated between all the $^7Li^+$ and $^{39}K^+$ ions, presented in Fig. 6.2(d), also reveal a correlation between $^7Li^+$ ions with a radial velocity of around 8.1 km/s (E_{kin} = 2.38 eV) and $^{39}K^+$ ions with a radial velocity of around 1.4 km/s (E_{kin} = 0.42 eV). This supports that these channels contain the ion signal from Coulomb explosion of $^7Li^{39}K$.

6.2.1 *Coincident filtering*

Since the contributions from $^7Li_2$ and $^{39}K_2$ overlap the signal from $^7Li^{39}K$ in the $P(E_{kin})$ distributions, it is not possible to determine the distribution of internuclear separations for $^7Li^{39}K$ from the raw energy distributions. Therefore, a way to separate the signals in the data analysis must first be established.

One solution is to use a coincident filter. The idea is to look for pairs of Ak^+ and Ak'^+ ions, created within the same probe pulse, that fulfill the momentum conservation criteria sufficiently well, that is, they must have momentum of equal magnitude but in opposite directions within some tolerance. In practice, it can be decomposed into two criteria: one that their emission directions must be related by close to 180° and the other that the difference in the magnitude of their momenta in the detector plane must be close to zero. Ions that do not fulfill the criteria are discarded. To isolate the heteronuclear dimer signal, the filter

Ak^+	Ak'^+	θ_{tol}	p_{tol} (u·km/s)
$^7Li^+$	$^7Li^+$	15°	9.1
$^7Li^+$	$^{39}K^+$	20°	9.1
$^{39}K^+$	$^7Li^+$	20°	23.4
$^{39}K^+$	$^{39}K^+$	15°	23.4

Table 6.1: Combinations of filter tolerances used when filtering the Ak^+ data by checking for coincident partner ions Ak'^+. The filter tolerances are based on the transverse widths of the covariance lines in the angular and radial covariance maps, see Fig. 6.2(c) and (d).

should look for $^7Li^+$ ions with a matching $^{39}K^+$ ion partner, while the homonuclear dimer signal would be isolated by looking for $^7Li^+$ with a $^7Li^+$ partner or $^{39}K^+$ with a $^{39}K^+$ partner.

The filters can be expressed mathematically as[17]

$$-\theta_{tol} < \left|\theta_1(Ak^+) - \theta_2(Ak'^+)\right| - 180° < \theta_{tol} \tag{6.1}$$

$$\left|m_{Ak^+} v_r(Ak^+) - m_{Ak'^+} v_r(Ak'^+)\right| < p_{tol}, \tag{6.2}$$

where Ak^+ is the ion species for which the signals are currently being separated, Ak'^+ is the partner ion species for the filter, and m_{Ak^+} and $m_{Ak'^+}$ are the masses. All the filter tolerances for the different combinations of Ak^+ and Ak'^+ are listed in Table 6.1.

Figure 6.3 shows the $P(E_{kin})$ distributions for $^7Li^+$ and $^{39}K^+$ without the filters and after applying filters to isolate the contribution from $^7Li_2$, $^{39}K_2$, and $^7Li^{39}K$. In Fig. 6.3(a2) the filter has been used to isolate the $^7Li_2$ contribution in the $^7Li^+$ data. The resulting $P(E_{kin})$ distribution can then be compared to the $P(E_{kin})$ distribution obtained after applying the filter to a measurement in which only homonuclear dimers were formed [akin to that shown in Fig. 5.3(a2)], shown in red. The agreement is excellent, demonstrating that the filter can be used to isolate the homonuclear dimer contribution. Similarly, it works well for the isolation of the $^{39}K_2$ contribution in the $^{39}K^+$ data, see Fig. 6.3(b2). If the filter is instead used to isolate the contributions from $^7Li^{39}K$, the

17 The form used here is different but equivalent to the form used in the published paper [174].

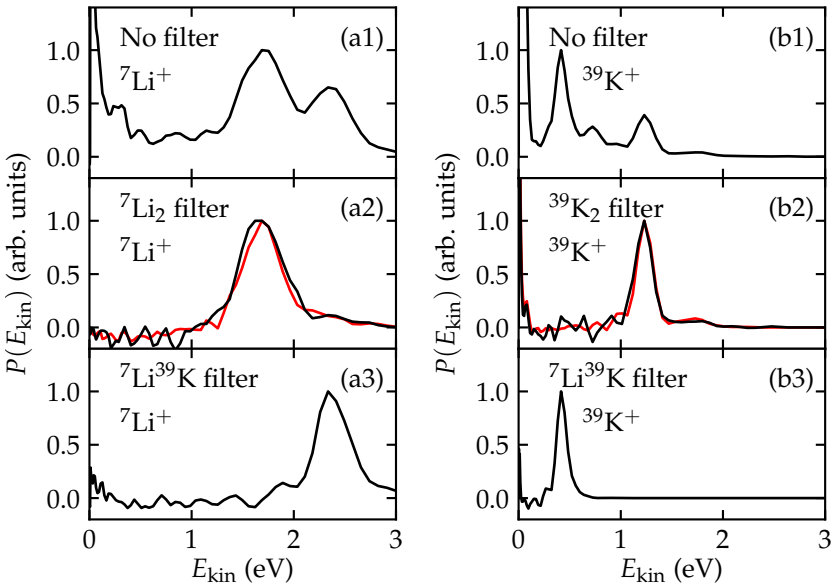

Figure 6.3: Kinetic energy distribution $P(E_{kin})$ for $^{7}Li^{+}$ (a1) and $^{39}K^{+}$ (b1) ions extracted from the 2D velocity map images in Fig. 6.2(a1) and (b1). (a2) and (a3) [(b2) and (b3)] $P(E_{kin})$ distributions for the $^{7}Li^{+}$ [$^{39}K^{+}$] ions after filtering the data with the homonuclear and heteronuclear dimer filters as annotated on the panels. The red curves in (a2) and (b2) show $P(E_{kin})$ distributions for $^{7}Li_2$ (a2) and $^{39}K_2$ (b2) obtained from a measurement series where only homonuclear dimers were formed on the droplets. Own work, inspired from [174].

peaks associated with the homonuclear dimers are filtered out and only the peaks at 2.38 eV for $^{7}Li^{+}$ and 0.42 eV for ^{39}K remain, as illustrated in Fig. 6.3(a3) and (b3). In this way, $P(E_{kin})$ distributions that only contain the signal from the heteronuclear alkali dimers can be obtained and subsequently used to determine the distribution of internuclear separations, as presented in the next section.

6.2.2 *Wave function imaging of AkAk'*

The procedure for extracting the distribution of internuclear separations $P(R)$ for the heteronuclear alkali dimers is similar to the one used for the homonuclear alkali dimers in Section 5.3.3.

In the present case, I will use the Coulomb potential $V_{\mathrm{Coul}}(R)$ to connect the kinetic energies of the $^{7}Li^{+}$ and $^{39}K^{+}$ fragments to R. To do so, the released Coulomb energy E_{Coul} must first be determined, which can be done starting from the kinetic energy E_{kin} of either the $^{7}Li^{+}$ ions or the $^{39}K^{+}$ ions. Ideally, the determined Coulomb energy, and thus also the determined $P(R)$, should be the same no matter which of the ions form the basis for the calculation.

In practice, I use two subsequent transformations to retrieve $P(R)$ from the isolated $P(E_{\mathrm{kin}})$ distributions associated with $^{7}Li^{39}K$ [see Fig. 6.3(a3) and (b3)]. The first is the conversion from E_{kin} to E_{Coul}, which is done via the equations

$$E_{\mathrm{Coul}} = \kappa E_{\mathrm{kin}} \tag{6.3}$$

and

$$P(E_{\mathrm{Coul}}) = P(E_{\mathrm{kin}}) \left| \frac{\mathrm{d}E_{\mathrm{kin}}}{\mathrm{d}E_{\mathrm{Coul}}} \right| = \frac{1}{\kappa} P(E_{\mathrm{kin}}). \tag{6.4}$$

Here, κ = 1+7/39 when doing the calculation for the $^{7}Li^{+}$ ions and κ = 1+39/7 when doing it for the $^{39}K^{+}$ ions, as dictated by momentum conservation. The next transformation is then from E_{Coul} to R via the Coulomb potential, where $P(E_{\mathrm{Coul}})$ transforms as

$$P(R) = P(E_{\mathrm{Coul}}) \left| \frac{\mathrm{d}V_{\mathrm{Coul}}(R)}{\mathrm{d}R} \right|. \tag{6.5}$$

The results found via these transformations are presented in Fig. 6.4(a), together with the theoretical $|\Psi(R)|^2$ distribution which I calculated by solving the stationary vibrational 1D Schrödinger equation for the isolated $1^{3}\Sigma^{+}$ state dimer via a potential from the literature [173]. The heights of both the experimental results and $|\Psi(R)|^2$ have been normalized to unity to make the curves comparable. Normalization of the areas does not work so well here, because the result obtained via the $^{7}Li^{+}$ ions has a significant shoulder towards lower R-values, see Fig. 6.4(a). It is thus difficult to define the part of the peak for which the area should be calculated.

Table 6.2 presents an overview of both the central positions and the widths for $P_{\mathrm{Li}}(R)$ and $P_{\mathrm{K}}(R)$, the distributions determined from the $^{7}Li^{+}$ ions and $^{39}K^{+}$ ions respectively, and for $|\Psi(R)|^2$.

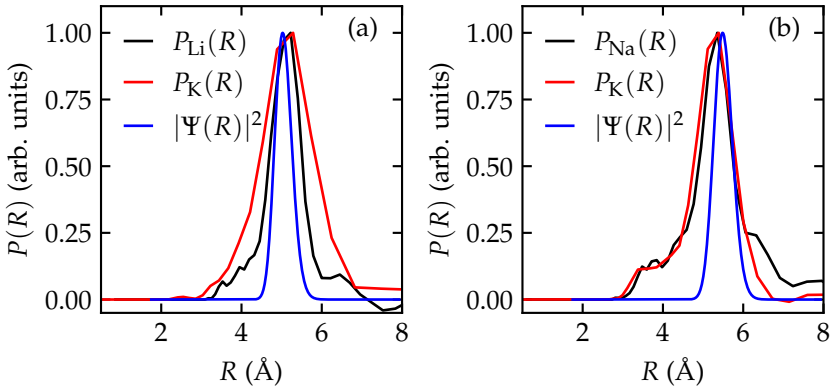

Figure 6.4: (a) Experimental $P(R)$ distributions for $^{7}Li^{39}K$ extracted from the $^{7}Li^{+}$ kinetic energies (black) and the $^{39}K^{+}$ energies (red), in comparison to the theoretical $|\Psi(R)|^2$ distribution for an isolated $^{7}Li^{39}K$ dimer (blue). (b) Similar to (a) but for $^{23}Na^{39}K$, where the experimental $P(R)$ distributions were extracted from the $^{23}Na^{+}$ and the $^{39}K^{+}$ kinetic energies. Own work, inspired from [174].

The centers for $P_{Li}(R)$ and $P_K(R)$ are observed to lie within 0.1 Å of the value for $|\Psi(R)|^2$ and are thus in good agreement with theory. Concerning the widths, quite some discrepancy is observed. The width is found to be 3 times larger for $P_K(R)$ compared to $|\Psi(R)|^2$. However, $P_{Li}(R)$ is only about twice as wide as $|\Psi(R)|^2$, and thus also more narrow than $P_K(R)$.

The explanation for the difference in widths for $P_{Li}(R)$ and $P_K(R)$ is found in Eq. 6.3. In that equation, $P(E_{kin})$ is multiplied by κ to determine the released Coulomb energy based on the kinetic energy of the ions. $P(E_{kin})$ is, however, broadened and shifted by the same mechanisms that were discussed for the homonuclear alkali dimers in Section 5.3.3, that is, transient motion in electronically excited states, interactions between the Ak^{+} fragments and the helium droplets, and the energy resolution of the detection setup. When multiplying by κ, the broadening and shifts are amplified. Since κ is much bigger when doing the transformation for the $^{39}K^{+}$ ions than for the $^{7}Li^{+}$ ions, the width of $P_K(R)$ is expected to be affected significantly more by broadening than $P_{Li}(R)$, consistent with the observations.

Results were also obtained for $^{23}Na^{39}K$ in the $1^{3}\Sigma^{+}$ state. The initial identification of the dimers was done in the same way as for $^{7}Li^{39}K$, that is, via the kinetic energies of the $^{23}Na^{+}$ and

	Central position (Å)	FWHM (Å)
$^{7}Li^{39}K\ 1^{3}\Sigma^{+}$		
$P_{Li}(R)$	5.10	0.86
$P_{K}(R)$	5.14	1.5
$\lvert\Psi(R)\rvert^2$	5.04	0.50
$^{23}Na^{39}K\ 1^{3}\Sigma^{+}$		
$P_{Na}(R)$	5.33	0.92
$P_{K}(R)$	5.28	1.1
$\lvert\Psi(R)\rvert^2$	5.50	0.55

Table 6.2: Central positions and widths (FWHM) of the experimentally determined $P(R)$ distributions for $^{7}Li^{39}K$ and $^{23}Na^{39}K$ alongside theoretical values for the $|\Psi(R)|^2$ distributions calculated using potentials from the literature [173, 175].

$^{39}K^{+}$ ions and via covariance analysis. I will not go through the details, but the ion images, kinetic energy distributions, and covariance images between the $^{23}Na^{+}$ and $^{39}K^{+}$ ions can be found in Appendix C. In this case, it is also necessary to use coincident filtering to clean the $^{23}Na^{+}$ and $^{39}K^{+}$ $P(E_{kin})$ distributions, see Fig. C.2, before determining $P(R)$. Having done that, $P(R)$ can be determined via Eq. 6.3, 6.4, and 6.5, with κ = 1+23/39 when $P(E_{kin})$ for $^{23}Na^{+}$ is used and κ = 1+39/23 when $P(E_{kin})$ for $^{39}K^{+}$ is used.

Figure 6.4(b) presents the results for $^{23}Na^{39}K$, alongside $|\Psi(R)|^2$ calculated by solving the Schrödinger equation for the isolated molecule with a potential from the literature [175]. The central positions and widths of these distributions are also listed in Table 6.2. Small shifts of around 0.2 Å are observed in the central positions for both $P_{Na}(R)$ and $P_{K}(R)$ with respect to $|\Psi(R)|^2$. The width of $P_{K}(R)$ is only a bit larger than that found for $P_{Na}(R)$, and the widths of both distributions are about 2 times larger than the width of $|\Psi(R)|^2$. Here the mass difference between ^{23}Na and ^{39}K is smaller than between ^{7}Li and ^{39}K, so it is expected that the widths of $P_{Na}(R)$ and $P_{K}(R)$ are more similar, just as observed.

Finally, it is interesting to note that $P_{\mathrm{Li}}(R)$ extracted for $^{7}\mathrm{Li}^{39}\mathrm{K}$ is the experimental distribution of internuclear separation which is closest to the width of the corresponding $|\Psi(R)|^2$ distribution, taking the results for both the homonuclear alkali dimers (see Table 5.2) and the heteronuclear alkali dimers (see Table 6.2) into account. An even better system for accurate determination of $P(R)$ could be $^{7}\mathrm{Li}^{85}\mathrm{Rb}$, or maybe even $^{7}\mathrm{Li}^{133}\mathrm{Cs}$, where the large mass difference would give a κ value very close to 1 for the $^{7}\mathrm{Li}^{+}$ fragments, thereby further reducing the influence from broadening of $P(E_{\mathrm{kin}})$ on the retrieved $P(R)$ distribution.

6.3 Conclusion

In this chapter, I have shown results from Coulomb explosion imaging of the heteronuclear alkali dimers $^{7}\mathrm{Li}^{39}\mathrm{K}$ and $^{23}\mathrm{Na}^{39}\mathrm{K}$. Using a Tpx3Cam detector, 2D velocity map ion images were recorded simultaneously for the $^{7}\mathrm{Li}^{+}$ and $^{39}\mathrm{K}^{+}$ ion fragments in the experiment with $^{7}\mathrm{Li}^{39}\mathrm{K}$, and likewise simultaneously for $^{23}\mathrm{Na}^{+}$ and $^{39}\mathrm{K}^{+}$ in the experiment with $^{23}\mathrm{Na}^{39}\mathrm{K}$. The ion images were unavoidably contaminated with ions from homonuclear alkali dimers that also formed on the droplets during the experiments. A combination of twofold covariance analysis and an analysis of the kinetic energy of the fragments enabled the identification of $^{7}\mathrm{Li}^{39}\mathrm{K}$ and $^{23}\mathrm{Na}^{39}\mathrm{K}$ dimers in the $1^{3}\Sigma^{+}$ state, despite the contaminated $P(E_{\mathrm{kin}})$ distributions. Via coincidence filtering, the contributions from the heteronuclear alkali dimers were isolated in the $P(E_{\mathrm{kin}})$ distributions and then used to retrieve the distribution of internuclear separations $P(R)$ for $^{7}\mathrm{Li}^{39}\mathrm{K}$ and $^{23}\mathrm{Na}^{39}\mathrm{K}$. Only minor shifts on the order of 0.1–0.2 Å were observed for the central positions of the experimentally determined $P(R)$ distributions compared to the theoretical $|\Psi(R)|^2$. Meanwhile, the widths of the determined $P(R)$ distributions were broader than the theoretical predictions by a factor of 2–3.

7

STRUCTURE DETERMINATION OF ALKALI TRIMERS ON HELIUM DROPLETS

In this chapter, I show the results from experiments on Coulomb explosion imaging of homonuclear alkali trimers on the surface of helium droplets. In the first section, I will give a brief introduction to the theoretically predicted structures of the alkali trimers and briefly recap the laser-induced Coulomb explosion method. Next, the experimental details are presented. Via a combination of threefold covariance analysis of the fragment ion ejection directions and an analysis of the kinetic energies of the ions, I then show that the alkali trimers Na_3, K_3, and Rb_3 on the droplets have an equilateral triangular structure consistent with the $^4A_2'$ state. In addition, the internuclear distances of the trimers are retrieved, something which, to my knowledge, has not been done directly before. I also present results for Coulomb explosion of Cs_3. Finally, under the assumption of fixed bond angles the distributions of internuclear separations $P(R)$ for Na_3, K_3, and Rb_3 are determined and compared to theoretical predictions.

7.1 Laser-induced Coulomb explosion of Ak_3

The alkali trimers can form in two quantum states on the helium droplets, namely the $^4A_2'$ state and the $^2B_2$ state. Theory predicts that the $^4A_2'$ state of the trimers has an equilateral triangular structure with D_{3h} symmetry [51, 54], while the $^2B_2$ state has an obtuse triangular structure with C_{2v} symmetry. As an example, the structures for the two spin states of Na_3 are shown in Fig. 7.1(a) and (b). The $^4A_2'$ state has the lowest binding energy and is therefore expected to be preserved on the droplets after the formation process, as previously explained in Section 2.3.1. For the low-spin state, $^2B_2$, the released binding energy is much larger, which is expected to lead to immediate desorption from the droplet again.

Figure 7.1(c) shows the potential curve for the $^4A_2'$ state of Na_3.

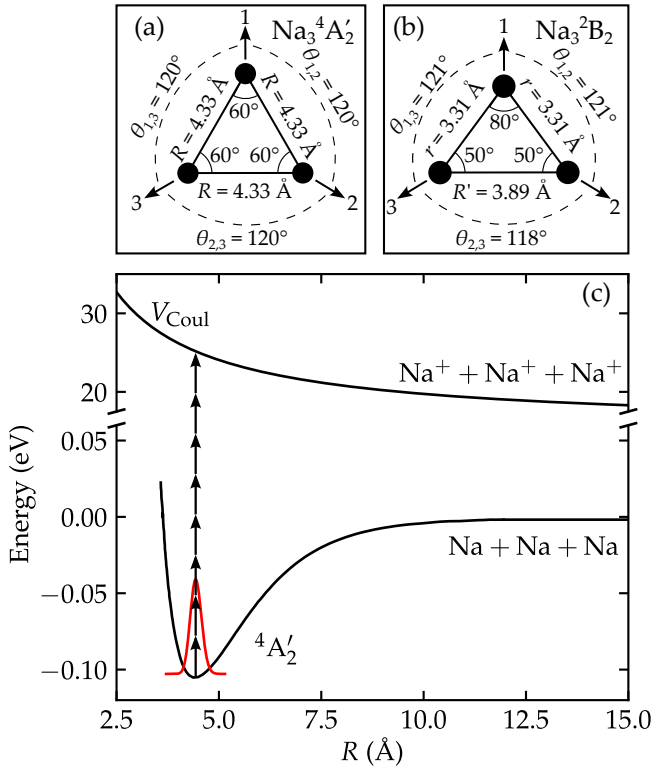

Figure 7.1: Sketch of (a) Na_3 in the $^4A_2'$ state [176] and (b) the $^2B_2$ state [177]. For reference, the atoms are labeled 1, 2, and 3. The emission directions of the Na^+ ions produced during Coulomb explosion are visualized by the annotated arrows and the angles between neighboring fragments are indicated by θ. (c) Potential curve for Na_3^{3+}, here approximated as the Coulomb potential $V_{Coul}(R)$, and extrapolated potential for the $^4A_2'$ state [51]. The red curve illustrates the square of the vibrational ground state wave function. The vertical black arrows (not to scale) depict the eight 400 nm photons used to trigger Coulomb explosion of Na_3. Own work, adapted from [178].

Similar to the dimers, the droplets cool the trimers down to the droplet temperature of 0.37 K [179]. The trimers on the droplets are therefore essentially only populated in the vibrational ground state. By removal of three electrons via multiphoton absorption of photons from an intense femtosecond probe pulse, Na_3^{3+} is formed. Again there is only one potential curve associated with

this state due to the closed shell structure, similar to the earlier presented cases with double ionization of the alkali dimers. It can therefore be approximated by the available Coulomb energy in the system, $V_{\text{Coul}}(R) = 3/R$ (in atomic units), for a given bond length R in the equilateral triangular structure[18]. The internal electrostatic repulsion then makes the ion fragment immediately in a Coulomb explosion, producing three Na^+ fragments. The potential energy is shared equally between the three ions, so the kinetic energy of each ion after the Coulomb explosion is[19]

$$E_{\text{kin}} = V_{\text{Coul}}(R)/3 = 14.4 \text{ eV}/R[\text{Å}]. \tag{7.1}$$

The strategy in the experiments is, completely analogous to the experiments on the dimers, to record the velocity of the fragment ions and use a combination of the ejection directions and the kinetic energies to identify the Coulomb exploded trimers and assign their quantum states.

7.2 Experimental setup

Figure 7.2 shows a sketch of the experiment. The helium droplets were doped with three alkali atoms of the same species, either Na, K, Rb, or Cs, which then formed alkali trimers Ak_3 on the surface (see operating temperatures for the doping oven in Table 4.2). The doped droplet beam then entered the VMI spectrometer where the trimers were probed with a laser beam of intense, linearly polarized $\sim$ 50 fs pulses that triggered Coulomb explosion. Finally, the velocities of the formed Ak^+ fragments were recorded with the 2D VMI spectrometer.

For K_3 and Rb_3, the results I will show are from the same experiments presented in Chapter 5, where strong signals from the trimers were also present. In the case of Na_3, the experiment was conducted with a nozzle temperature of 11 K, and the wavelength

18 One could make a quantum chemistry calculation of the Na_3^{3+} potential, as done for Ak_2^{2+} in Chapter 5, but the correction to the energies is estimated to be smaller than other uncertainties in the experiment and therefore neglected.

19 Equation 7.1 is correct if the fragments have the same mass. This is the case for Na_3 and Cs_3 since Na and Cs are isotope pure. For K_3, and Rb_3, multiple isotopologues may play a role in the experiments, making it necessary to modify Eq. 7.1 as explained in Section 7.3.2.

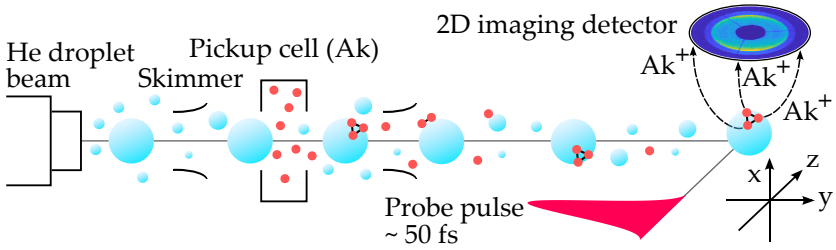

Figure 7.2: Sketch of the experiment conducted to investigate the structure of Ak_3 on helium droplets. The trimers were first formed by picking up three alkali atoms on the droplets, and then Coulomb exploded by a beam of intense femtosecond laser pulses. The created Ak^+ ions were detected with the 2D VMI spectrometer. Own work, adapted from [178].

of the probe pulses was centered at 400 nm with an estimated intensity of 1.5×10^{13} W/cm^2. A series of measurements with different nozzle temperatures, in the range from 10.5 to 15 K, was conducted for Cs_3. Of these, the measurement at 12 K was also already shown in Chapter 5. All Cs_3 measurements were done with a wavelength of 1300 nm and an estimated intensity of 1×10^{13} W/cm^2.

7.3 Results

Figure 7.3(a1)–(d1) show the 2D velocity map images obtained for the various Ak^+ ions in the experiments while gating on the $^{23}Na^+$, $^{39}K^+$, $^{85}Rb^+$, and $^{133}Cs^+$ ions. The centers of the images are screened by the beam block (see Section 5.3). Outside the screened areas, three channels are present. The channels between the annotated white rings are those ascribed to the $1^3\Sigma_u^+$ state and $1^1\Sigma_g^+$ state Ak_2 dimers, as explained in Section 5.3. I will now focus on the outermost channel in the images, which lies outside the annotated dot-dashed rings.

7.3.1 *Threefold covariance analysis*

The first step in my analysis of the Ak^+ ions in the outermost channels in the ion images, Fig. 7.3(a1)–(d1), is to look for correlations in the emission angles of the ions. For this purpose, I

employ a threefold covariance analysis. It is a direct extension of twofold covariance analysis (see Section 5.3.2) which has been used to investigate correlations between three fragment ions in gas-phase experiments [160, 163, 164, 180–182].

Mathematically, the threefold covariance is defined as [160]

$$\begin{aligned}\mathrm{cov}(x,y,z) = \langle XYZ\rangle &- \langle XY\rangle\langle Z\rangle - \langle XZ\rangle\langle Y\rangle \\ &- \langle YZ\rangle\langle X\rangle + 2\langle X\rangle\langle Y\rangle\langle Z\rangle,\end{aligned} \tag{7.2}$$

where, as for the twofold covariance, $\langle X\rangle$, $\langle XY\rangle$, and $\langle XYZ\rangle$ are given as

$$\langle X\rangle = \frac{1}{N}\sum_{i=1}^{N} X_i(x), \tag{7.3}$$

$$\langle XY\rangle = \frac{1}{N}\sum_{i=1}^{N} X_i(x)Y_i(y), \tag{7.4}$$

$$\langle XYZ\rangle = \frac{1}{N}\sum_{i=1}^{N} X_i(x)Y_i(y)Z_i(z). \tag{7.5}$$

The $\langle XYZ\rangle$ term in Eq. 7.2 is a measure for the probability of measuring three ions with values x, y, and z, associated with some distribution, within the same camera frame. The remaining terms describe the probabilities for measuring either three ions where two are correlated or three uncorrelated ions.

While the extension from twofold to threefold covariance seems straightforward, one complication does arise. If the number of ions recorded in each camera frame follows a Gaussian distribution, the threefold covariance becomes zero even if the ions are correlated. This is however not the case for a Poissonian distribution of ions per frame, which is the statistical distribution normally observed in photoionization experiments. In fact, for a Poissonian distribution, the threefold covariance can be interpreted in the same way as the twofold covariance [183]. Due to this, it is important to conduct the experiment with stable parameters, since fluctuations in probe pulse intensity, doping conditions for the droplet beam, etc., can alter the Poissonian distribution of ions to a Gaussian distribution.

Representing threefold covariance can be done in a useful 2D format by creating recoil-frame covariance images in pixel

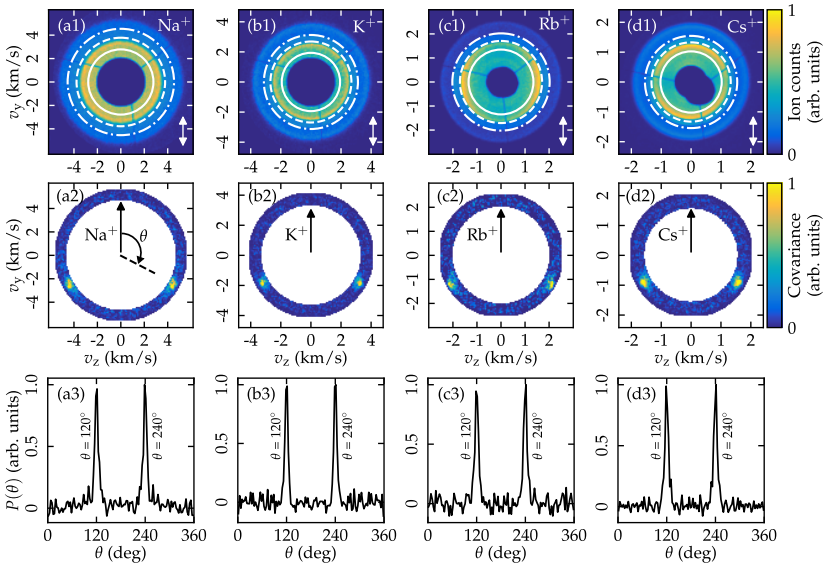

Figure 7.3: (a1)–(d1) 2D velocity map images of Ak^+ ions. The polarization axis of the laser pulses is indicated by the white arrows in the lower right corners. The regions between the annotated white rings contain ions from the $1^3\Sigma_u^+$ and the $1^1\Sigma_g^+$ channels of Ak_2 (see Section 5.3), while the channels outside the dot-dashed rings contain ions from Ak_3. (a2)–(d2) Threefold covariance images calculated for the ions within the Ak_3 channel in the 2D velocity map images. Note that the covariance images have been oversaturated to improve the visual contrast. (a3)–(d3) Angular distributions $P(\theta)$ for the covariance images shown in (a2)–(d2). Annotations on the figures show the central positions of the two peaks. The FWHM of the peaks is 11°, except for (b3) where the FWHM is 9°. Own work, adapted from [178].

space [158, 159, 163, 181]. The idea is to select one Ak^+ ion recorded in each camera frame as the 'reference ion', and then calculate the threefold covariance between the Ak^+ ions within that camera frame in the recoil frame of the selected reference ion[20]. This is then repeated with a new ion selected as the reference ion until all possible permutations for the data in that frame

20 It is possible to not only select a reference ion but also constrain the recoil direction of a second ion. Doing so can make it possible to separate contributions from different enantiomers of a molecule and to retrieve information about molecular conformations [181].

have been treated. In this way, a series of individual covariance images for each camera frame is obtained. The final step is to rotate the covariance images for all the camera frames such that the reference ions lie along the same vector, and then sum all the images together into one final recoil-frame covariance image.

In practice, calculating the recoil-frame threefold covariance images can be quite difficult. It is necessary to use large, nested for-loops to iteratively add the contributions from the various terms in Eq. 7.2 to the final result. This is very slow, so I have written a program in C++ to handle it. The program is based on Fortran code provided by James Pickering, a former PhD student in the group. I have adapted parts of the code to my needs and implemented further optimizations to speed up the overall computation time.

Figure 7.3(a2)–(d2) show the recoil-frame threefold covariance images for the ions in the outermost channel in each of the images in Fig. 7.3(a1)–(d1). The images indicate that two partner Ak^+ ions are likely to show up in two isolated islands in the recoil frame of the reference Ak^+ ion. The locations of the ions can be determined by integrating the covariance images along the radial direction, thereby obtaining the angular distribution $P(\theta)$ of the covariance. Each of the $P(\theta)$ distributions, presented in Fig. 7.3(a3)–(c3), exhibit two large peaks that correspond to the two islands in the covariance images. The central positions of these peaks are at 120° and 240°, as also annotated in Fig. 7.3(a3)–(c3). From this I interpret that the Ak^+ ions in the outermost channel are correlated with two other Ak^+ ions, all ejected with an angle of 120° between neighboring Ak^+ ions. From symmetry arguments, this is what one would expect to observe for the previously discussed Coulomb explosion process of Ak_3 in the equilateral triangular $^4A_2'$ state, see Fig. 7.1(a). My observations are therefore consistent with alkali trimers in the $^4A_2'$ state residing on the helium droplets. It turns out, however, that Coulomb explosion, again via triple ionization, of alkali trimers in the $^2B_2$ state leads to very similar ejection angles, even though the structure of the $^2B_2$ state trimers are obtuse, as illustrated for Na_3 in Fig. 7.1(b). This was determined via classical trajectory calculations carried out by Constant Schouder [178]. The calculations reveal that for Na_3 and Cs_3 the angles between the neighboring

ejected fragments are 121° and 118°. Similarly, the angles are 121° and 117° for K_3 and Rb_3. These angles are all very close to those observed in the experiments. Distinguishing between ions originating from Coulomb explosion of $^4A_2'$ state and $^2B_2$ state alkali trimers will require a better resolution since the small deviations in the ejection angles lie within the 11° FWHM of the peaks in Fig. 7.3(a3), (c3), and (d3), and the 9° FWHM of the peaks in Fig. 7.3(b3). On its own, the threefold covariance analysis cannot rule out one or the other spin state, but it supports that the Ak^+ ions in the outermost channel indeed come from alkali trimers.

7.3.2 *Energy analysis for Na^+, K^+, and Rb^+*

The second step in my analysis of the Ak^+ ions in the outermost channels is to study their kinetic energies. As explained in Section 5.3, the distribution of kinetic energies $P(E_{kin})$ can be determined for the ions in each of the ion images in Fig. 7.3(a1)–(d1) via Abel inversion and application of a calibration. Figure 7.4 presents the obtained $P(E_{kin})$ distributions.

I will first discuss the results for the Na^+, K^+, and Rb^+ data sets, for which three peaks are present in the $P(E_{kin})$ distributions, see Fig. 7.4(a)–(c). The two peaks that lie at the lowest energies in each distribution were ascribed to the $1^3\Sigma_u^+$ state and $1^1\Sigma_g^+$ state dimers discussed in Chapter 5. The last peak in each distribution (marked with vertical dashed lines in Fig. 7.4), which lie at significantly higher energies than the dimer peaks, are the ones associated with the outermost channels in the ion images and therefore the ones of interest for the current discussion.

In the $P(E_{kin})$ distribution for Na^+, Fig. 7.4(a), the peak to be identified lies at 3.10 eV (found by a Gaussian fit). This is close to the kinetic energy E_{kin} = 3.33 eV that each Na^+ ion would receive from Coulomb explosion of Na_3 in the $^4A_2'$ state if it is initiated at the equilibrium distance R_{eq} = 4.33 Å [176]. For Na_3 in the $^2B_2$ state, the classical trajectory calculations reveal that Coulomb explosion would produce one Na^+ ion with E_{kin} = 4.3 eV [this is fragment 1 in Fig. 7.1(b)], and two Na^+ ions [fragments 2 and 3 in Fig. 7.1(b)] with E_{kin} = 4.0 eV. These energies are in poor agreement with the experimental peak. From these arguments, and corroborated by the threefold covariance analysis, I identify

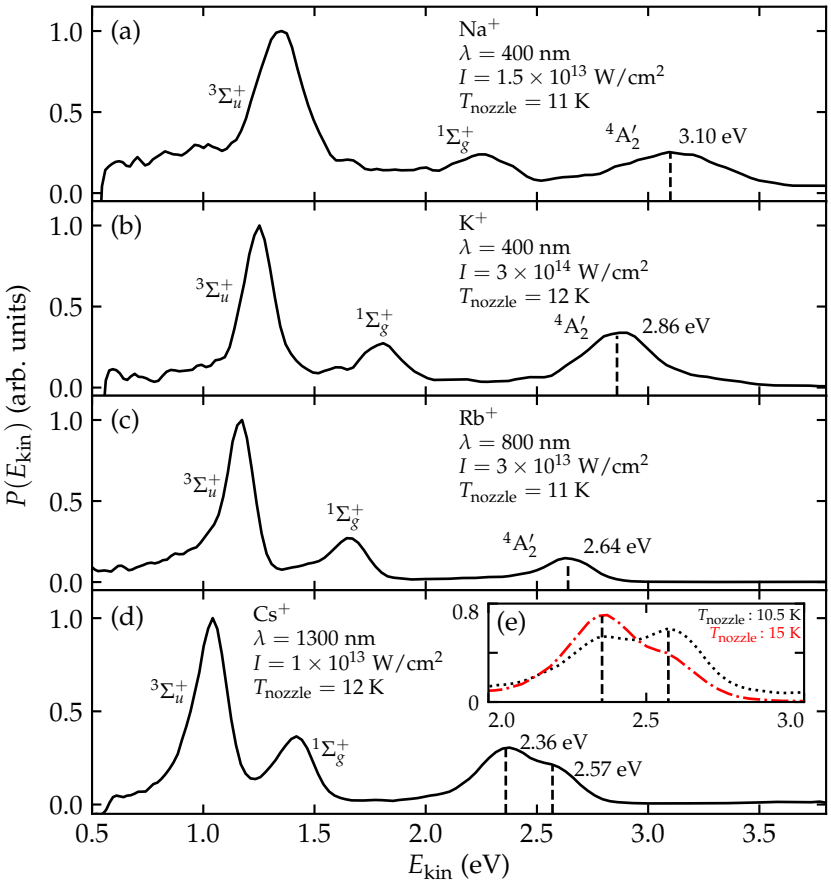

Figure 7.4: $P(E_{\text{kin}})$ distributions for Na^+, K^+, Rb^+, and Cs^+ obtained from the 2D velocity map images in Fig. 7.3(a1)–(d1). (e) Excerpt of the Cs^+ $P(E_{\text{kin}})$ distribution ascribed to Cs_3 for measurements with T_{nozzle} = 10.5 K (black dotted line) and T_{nozzle} = 15 K (red dot-dashed line, upscaled by a factor 10). The vertical dashed lines are used to mark the centers of the peaks associated with Ak_3. Own work, adapted from [178].

the peak at 3.10 eV [and thus the Na^+ ions in the outermost channel in Fig. 7.3(a1)] as ions that originate from Coulomb explosion of Na_3 in the $^4A_2'$ state.

For K^+, Fig. 7.4(b), the peak at 2.86 eV matches Coulomb explosion of K_3 in the $^4A_2'$ state, which would produce three K^+ ions with E_{kin} = 2.85 eV when the fragmentation starts from a distance of R_{eq} = 5.05 Å [54]. Coulomb explosion of the $^2B_2$ state trimer in its equilibrium configuration [54], would produce K^+

ions with a kinetic energy of 3.5 and 3.2 eV, which does not match my observation. Similarly, 2.62 eV would be expected for Rb_3 in the $^4A_2'$ state, while 3.0 and 3.2 eV would be expected for the $^2B_2$ state [54]. Also here, the $^4A_2'$ state matches the experimental observation of 2.64 eV for the Rb^+ peak in Fig. 7.4(c). Therefore, I conclude that K_3 and Rb_3 form in the $^4A_2'$ state on the droplets, and that Coulomb explosion of these is the origin of the ions in the outermost channel in Fig. 7.3(b1) and (c1).

I can now utilize the correspondence between the energy release and the initial internuclear distances to retrieve experimental values for the equilibrium internuclear distances R_{eq} for the $^4A_2'$ state trimers. For Na_3, which is isotope pure, this can be done via Eq. 7.1, but for K_3 and Rb_3 the presence of different isotopologues must be taken into account. The abundance ratios for the various isotopologues are presented in Table 7.1. The effect of the isotopologues is most pronounced for K_3, where the relative mass difference between the two isotopes of K (^{39}K and ^{41}K) is larger than for Rb (^{85}Rb and ^{87}Rb), leading to the largest difference in the momentum sharing during Coulomb explosion. For $^{39}K^{39}K^{41}K$, the isotopologue with the second largest abundance (17.6%) for K_3, the kinetic energy obtained for the $^{39}K^+$ ions during Coulomb explosion can be derived from momentum considerations and is given as

$$E_{kin} = \frac{3}{2 + \frac{39}{41}} \frac{14.4\ \text{eV}}{R[\text{Å}]}, \tag{7.6}$$

which replaces Eq. 7.1. These $^{39}K^+$ ions will therefore have 50 meV more kinetic energy than $^{39}K^+$ ions from Coulomb explosion of $(^{39}K)_3$, calculated at the equilibrium distance. However, only about 13% of the $^{39}K^+$ ions detected in the experiment will come from $^{39}K^{39}K^{41}K$ (since it only produces two $^{39}K^+$ fragments), so the contribution to the observed $^4A_2'$ state peak in Fig. 7.4(b) is minor. For Rb_3 the deviations in the kinetic energy of the $^{85}Rb^+$ fragments are smaller, but $(^{85}Rb)_3$ is not the most abundant isotopologue. It does however still produce the majority of the observed $^{85}Rb^+$ ions in the $^4A_2'$ state peak in Fig. 7.4(c), making up 52% of the signal. One way to handle these isotope effects is to treat it as an uncertainty in the energy and then apply Eq. 7.1 which holds for the majority of the ions observed from

K_3	Abundance (%)	Rb_3	Abundance (%)
$(^{39}K)_3$	81.2	$(^{85}Rb)_3$	37.6
$^{39}K^{39}K^{41}K$	17.6	$^{85}Rb^{85}Rb^{87}Rb$	43.5
$^{39}K^{41}K^{41}K$	1.27	$^{85}Rb^{87}Rb^{87}Rb$	16.7
$(^{41}K)_3$	0.0305	$(^{87}Rb)_3$	2.15

Table 7.1: Abundances for the different isotopologues of K_3 and Rb_3. The values are based on the isotope abundances of K and Rb [169]. Note that Na_3 and Cs_3 are isotope pure.

the trimers. Some uncertainty from the spectrometer itself is also present, and likewise for the fitting routine used to determine the central positions of the peaks in $P(E_{\text{kin}})$. Overall, I estimate the total uncertainty on the center of the experimental peaks to be around 100 meV.

The retrieved equilibrium distances R_{eq} for Na_3, K_3, and Rb_3, after taking the uncertainties into account, are presented in Table 7.2. The table also provides theoretical values for R_{eq} found in the literature. The agreement between the experiments and the theoretical values is good, especially for K_3 and Rb_3 where the found values of R_{eq} lie within 0.1 Å of the predictions. In the case of Na_3, a shift of 0.2–0.3 Å is observed compared to the calculations. Such a shift was likewise also observed for Na_2 in Chapter 5, where I ascribed it to internuclear motion in transiently excited states during the probing process. I believe the cause for the shift is the same here for Na_3. It is a light system, so within the 50 fs probe pulse duration, some internuclear motion can occur in Na_3, Na_3^+, and Na_3^{2+} potentials. For K_3 and Rb_3, the larger masses will cause motion in transiently excited states to be slow, such that only very small shifts can occur within the 50 fs, leading to a better agreement between the experimental observations and the predictions in the literature.

7.3.3 *Energy analysis for Cs^+*

I now turn my attention to the measurements on cesium. The $P(E_{\text{kin}})$ distribution for the Cs^+ ions in Fig. 7.3(d1) are presented

	$P(E_{\mathrm{kin}})$ peak (eV)	R_{eq} (Å)
Na_3	3.10 ± 0.10	4.65 ± 0.15
Na_3 Theory	–	4.33, 4.41
K_3	2.86 ± 0.10	5.03 ± 0.18
K_3 Theory	–	4.95, 5.05
Rb_3	2.64 ± 0.10	5.45 ± 0.22
Rb_3 Theory	–	5.35, 5.50, 5.31, 5.45

Table 7.2: Central positions of the $P(E_{\mathrm{kin}})$ peaks, Fig. 7.4(a)–(c), associated with $^4A_2'$ state alkali trimers, and the corresponding R_{eq} values. Also given are R_{eq} values found in the literature for the various trimers [51, 54, 176, 184, 185]. Own work, adapted from [178].

in Fig. 7.4(d). Multiple peaks are present in the distribution, of which two peaks contain ions from Coulomb explosion of $1^3\Sigma_u^+$ state and $1^1\Sigma_g^+$ state Cs_2, as identified in Section 5.3. At kinetic energies around 2.5 eV, a double peak structure that corresponds to the ions in the outermost channel in Fig. 7.3(d1) is observed. I have fitted a sum of two Gaussians to the peaks to find their central positions, 2.36 and 2.57 eV. The threefold covariance analysis, see Fig. 7.3(d2) and (d3), indicates that the peaks contain ions that can be associated with Coulomb explosion of Cs_3, though it cannot distinguish between the $^4A_2'$ state and the $^2B_2$ state. I have also performed the threefold covariance calculations separately for the ions in each of the two overlapping peaks, but the resolution still hinders any further identification. Note that Cs is isotope pure, so the presence of two peaks cannot be explained by isotopologue effects.

To investigate the two peaks further, and in particular to test if some of the ions can originate from $^2B_2$ state Cs_3, a series of measurements were conducted for Cs_3 with different nozzle temperatures in the range between 10.5 and 15 K. The motivation for doing this was that the quartet-to-doublet ratio of Cs_3 on the droplets should vary with the droplet size if both states are present. This has been theoretically predicted [102], and I have also observed such a droplet size dependence for the triplet-to-singlet ratio for the alkali dimers (see Section B.2).

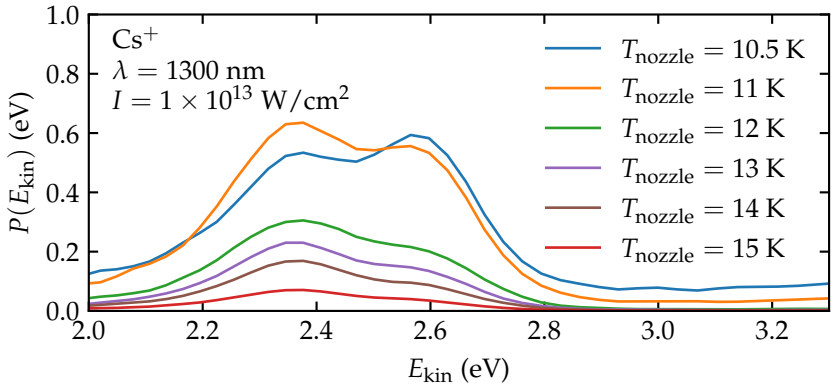

Figure 7.5: $P(E_{\text{kin}})$ distributions for Cs^+ ions obtained for various nozzle temperatures. The plot is zoomed in on the part of the distribution associated with the outer channel in the ion images [see T_{nozzle} = 12 K image in Fig. 7.3(d1)]. An upscaled plot of the curve for T_{nozzle} = 15 K is shown in the inset in Fig. 7.4(d).

The obtained $P(E_{\text{kin}})$ distributions are presented in Fig. 7.5. For the measurement with T_{nozzle} = 15 K, where the mean droplet size is estimated to be around 5000 helium atoms, the peak at 2.36 eV dominates [see also upscaled plot in the inset of Fig. 7.4(d)]. This suggests that the peak at 2.36 eV contains ions from Coulomb explosion of Cs_3 in the $^4A_2'$ state since the $^4A_2'$ state trimers should be preserved much better on small droplets than $^2B_2$ state trimers. However, the energy deviates from the expected kinetic energy of 2.59 eV that each Cs^+ ion would obtain from Coulomb explosion of Cs_3 starting from the predicted equilibrium distance R_{eq} = 5.56 Å of the $^4A_2'$ state [176]. The expected kinetic energy instead matches the other observed peak at 2.57 eV. As the nozzle temperature is decreased, creating larger droplets, the peak at 2.57 eV becomes more dominant, and at T_{nozzle} = 10.5 K, it is larger than the peak at 2.36 eV. This is not expected if the peaks arise from both $^4A_2'$ state and $^2B_2$ state trimers, since there should be a higher amount of $^4A_2'$ state trimers than $^2B_2$ state trimers on the droplets at all droplet sizes. On a final note, Coulomb explosion of Cs_3 initiated at the equilibrium configuration of the $^2B_2$ state [186] would produce two Cs^+ ions with E_{kin} = 2.8 eV and one Cs^+ ion with E_{kin} = 3.0 eV, according to the classical trajectory

simulations[21]. The difference in these fragment energies is similar to the 0.21 eV difference between the central peak positions of 2.36 and 2.57 eV in the experiment, but the 2:1 formation ratio of the fragments does not properly match the ratios between the two peaks in $P(E_{\mathrm{kin}})$ observed for the various nozzle temperatures in Fig. 7.5. To conclude, the current data is not sufficient to determine the quantum states of Cs_3 present in the experiment.

7.3.4 *Wave function imaging of Ak_3*

As a last thing in this chapter, I will once more discuss wave function imaging, this time for the alkali trimers. In Section 5.3.3 and Section 6.2.2 it was demonstrated for the alkali dimers that the distribution of internuclear separations $P(R)$ can be extracted directly from the kinetic energies of the Ak^+ fragments. The matter is, however, more complicated for the trimers because they can stretch asymmetrically, such that the three bond lengths are not identical. The internuclear wave function $\Psi(R_1, R_2, R_3)$ therefore depends on all three bond lengths, which are not directly available in the experiment. To move forward, it is necessary to make an assumption that simplifies the problem. Following the procedure used in published studies on wave function imaging of Ne_3 and Ar_3 via Coulomb explosion [150], I assume that the bond angles are fixed, such that the trimers are in an equilateral structure at all times and can only undergo symmetric stretching. When this assumption is applied, the wave function can be expressed in one coordinate as $\Psi(R)$. $P(R)$ can now be calculated as

$$P(R) = P(E_{\mathrm{kin}}) \left| \frac{\mathrm{d}E_{\mathrm{kin}}}{\mathrm{d}R} \right| = P(E_{\mathrm{kin}}) \left| \frac{1}{3} \frac{\mathrm{d}V_{\mathrm{Coul}}(R)}{\mathrm{d}R} \right|, \tag{7.7}$$

where the expression for E_{kin} from Eq. 7.1 was used.

The resulting $P(R)$ distributions for Na_3, K_3, and Rb_3 are shown in Fig. 7.6(a)–(c) alongside theoretical predictions for $|\Psi(R)|^2$. I calculated $|\Psi(R)|^2$ by solving the stationary vibrational 1D Schrödinger equation for the isolated $^4A_2'$ state trimers

21 Due to degeneracy there are two doublet states for Cs_3 that are very close to each other in energy. The fragment energies for Coulomb explosion of the acute triangular $^2A_1$ state at the equilibrium distance [186] is E_{kin} = 2.61 eV and 2.89 eV, which does not match the experimental results.

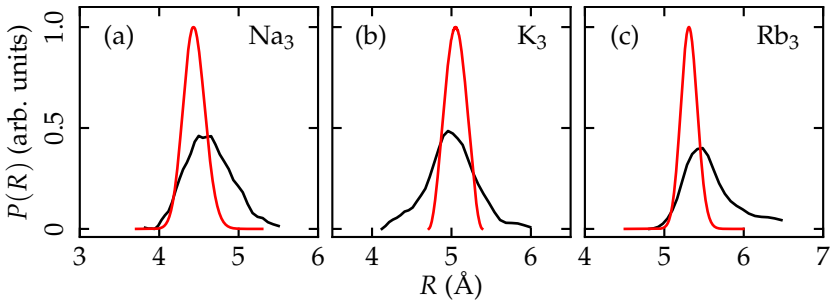

Figure 7.6: Distributions of internuclear separations $P(R)$ (black) for $^4A_2'$ state Na_3, K_3, and Rb_3, obtained via a transformation of the experimental $P(E_{kin})$ distributions in Fig. 7.4(a)–(c), and a subtraction of a flat background. The red curves show the $|\Psi(R)|^2$ distributions calculated for the isolated $^4A_2'$ state trimers. Own work, adapted from [178].

via potentials found in the literature [51, 184, 187]. The area of the $P(R)$ distributions and the corresponding $|\Psi(R)|^2$ distributions are normalized to the same value, after an initial flat background subtraction for $P(R)$, to make them comparable. Via Gaussian fits I have determined the FWHM of the $P(R)$ distributions to be 0.8 Å, 0.6 Å, and 0.4 Å for Na_3, K_3, and Rb_3, respectively. This should be compared to a FWHM of 0.3 Å for the theoretical distributions for Na_3 and K_3, and a FWHM of 0.2 Å for Rb_3. The widths of the experimental $P(R)$ distributions are thus 2–3 times larger than the widths of the theoretical distributions, a ratio similar to what I obtained for the alkali dimers in Section 5.3.3 and Section 6.2.2.

I believe the observed $P(R)$ distributions are wider than the corresponding theoretical $|\Psi(R)|^2$ distributions due to the same factors listed for the alkali homonuclear dimers in Section 5.3.3. To be brief, the first factor is transient nuclear motion in electronically excited states, which is expected to influence Na_3 most, as also mentioned in Section 7.3.2. The second and third factors are the limited resolution of the detection setup and the presence of different isotopologues. The last factor is the attractive force between the formed Ak^+ ions and the helium, which will depend on how the trimers are oriented at the surface. To my knowledge, the orientation of the trimers has not been studied. I assume that the plane of each trimer lies roughly parallel to the surface

plane since the trimers in the $^4A_2'$ state are essentially just three distant Ak atoms that barely remain bound to each other. Each of the atoms that make up the trimer therefore most likely hovers roughly equally far from the droplet surface. If that is indeed the case, the ejected Ak^+ ions will rarely collide with the helium, but the attractive force toward the helium will still deflect the Ak^+ trajectories a bit and potentially cause the fragments to lose some kinetic energy. The effect should however be smaller than for the dimers because the Ak^+ fragments have larger velocities when produced by Coulomb explosion of the trimers. This results in less interaction with the droplet (see discussion in Section 10.2).

7.4 Conclusion

In summary, I have shown that Coulomb explosion imaging can be used to identify Na_3, K_3, and Rb_3 residing on helium droplets. Via a combination of threefold covariance analysis of the fragment Ak^+ ions and an analysis of the fragment kinetic energies, the trimers were found to be in the $^4A_2'$ state with an equilateral triangular structure. The equilibrium bond distances were determined to be 4.65±0.15 Å for Na_3, 5.03±0.18 Å for K_3, and 5.45±0.22 Å for Rb_3. This is in good agreement with theoretical predictions for K_3 and Rb_3, while a shift of around 0.3 Å is observed for Na_3 compared to expectations. The shift was ascribed to transient nuclear motion in excited states. Distributions of the internuclear separations $P(R)$ were additionally obtained under the assumption that the bond angles were fixed. I found the width of the distributions to be 2–3 times larger than for the corresponding theoretical $|\Psi(R)|^2$ distributions. I listed the resolution of the detector setup, the interaction between the helium and the fragment Ak^+ ions, and once again nuclear motion in electronically excited states as factors that may influence the found results.

Finally, measurements were also done with cesium. Here, the threefold covariance analysis supported that three Cs^+ fragments pairwise correlated by 120° in the emission angle were formed, consistent with Cs_3 in the $^4A_2'$ state. However, two peaks were present in the kinetic energy distribution of the Cs^+ fragments, and they could not be assigned unambiguously to specific quantum states of Cs_3.

8

ALIGNMENT AND ROTATIONAL DYNAMICS OF ALKALI DIMERS ON HELIUM DROPLETS

The topic of this chapter is the experiments on nonadiabatic alignment of homonuclear alkali dimers on the surface of helium droplets. I explained the fundamental details of laser-induced alignment in Chapter 3 and will therefore start directly with a description of the experimental details in the first section of this chapter. Following that, I present the results for both the $1^1\Sigma_g^+$ states and the $1^3\Sigma_u^+$ states of Na_2, K_2, and Rb_2. The rotational dynamics of the dimers are found to be strongly influenced by the presence of the helium droplet surface. Finally, a theoretical model is developed and compared with the experimental measurements to facilitate an in-depth interpretation and to retrieve information about the rotational energy levels.

8.1 Experimental setup

A sketch of the alignment experiment is presented in Fig. 8.1. Helium droplets were first doped with either Na_2, K_2, or Rb_2 (see operating temperatures for the doping oven in Table 4.2). The droplets were created with a nozzle temperature of $T_{\text{nozzle}} = 11$ K for Na_2 and Rb_2 while $T_{\text{nozzle}} = 12$ K was used for K_2.

Inside the VMI spectrometer, the doped droplets were then crossed by two beams of focused laser pulses. The first beam contained the alignment pump pulses and was used to set the dimers into rotation. To enable nonadiabatic alignment, a nonresonant wavelength of 1300 nm was used, and the pulse duration was adjusted to ~ 1 ps with a prism stretcher (see Section 4.4). The pump pulses were linearly polarized parallel to the detector plane. After an adjustable delay t, the dimers were irradiated by linearly polarized laser pulses from the second beam. These pulses had a duration of ~ 50 fs and were used to probe the alkali dimers by triggering Coulomb explosion into two Ak^+ fragments. Once again, the detector was gated such that the velocities were

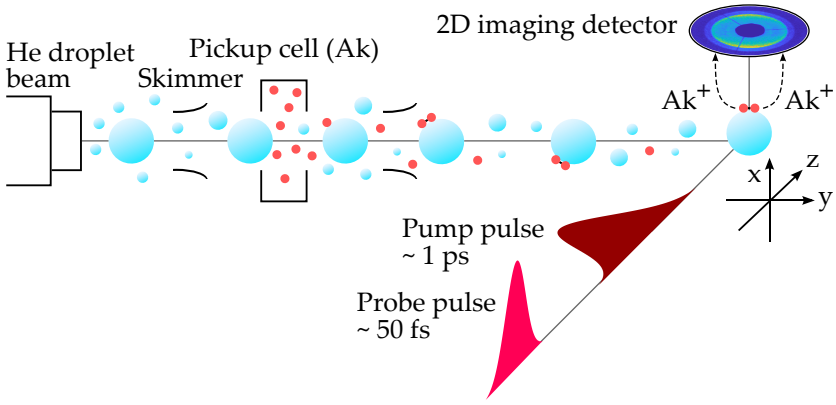

Figure 8.1: Sketch of the experiment conducted to study nonadiabatic alignment dynamics of Ak_2 on helium droplets. Na_2, K_2, and Rb_2 were individually doped onto the droplets and set into rotation by a nonresonant pump pulse. A delayed probe pulse was used to trigger Coulomb explosion of the dimers, forming Ak^+ ions that were detected with the 2D imaging setup. Own work, adapted from [124].

only measured for the most abundant isotopes $^{23}Na^+$, $^{39}K^+$, and $^{85}Rb^+$.

To avoid unwanted influence from anisotropies in the emission directions of the Ak^+ ions caused by the ionization process, see Section B.1, the probe pulses were polarized along an axis perpendicular to the detector plane. Furthermore, as mentioned in Section 4.4, the focused spot size of the probe beam was adjusted to around half of the focused spot size for the alignment beam. This was done to ensure that the probed molecules had been rather uniformly pumped by the alignment pulses.

The intensities of the alignment pulses were kept moderate to avoid premature ionization of the alkali dimers, see Table 8.1. The table also lists the used probe pulse intensities and wavelengths. Note that while the signal from the $1^3\Sigma_u^+$ state and the $1^1\Sigma_g^+$ state of the dimers can be recorded simultaneously, as demonstrated in Chapter 5, the optimal pulse conditions for conducting the experiments are not necessarily the same for both states. For this reason, separate measurements have been conducted for the $1^3\Sigma_u^+$ state and the $1^1\Sigma_g^+$ state of Na_2 and K_2 to obtain the results.

	I_{pump} (10^{10} W/cm^2)	I_{probe} (10^{13} W/cm^2)	λ_{probe} (nm)
Na_2 $1^3\Sigma_u^+$	5.0	0.5	800
Na_2 $1^1\Sigma_g^+$	6.7	7.1	800
K_2 $1^3\Sigma_u^+$	2.6	2.9	800
K_2 $1^1\Sigma_g^+$	4.2	9.3	400
Rb_2 $1^3\Sigma_u^+$	3.4	3.5	400
Rb_2 $1^1\Sigma_g^+$	3.4	3.5	400

Table 8.1: Pulse intensities and probe wavelengths used for the experiments on nonadiabatic alignment of Ak_2.

8.2 Results

Figure 8.2(a) shows a 2D velocity map image of K^+ ions recorded in a measurement with K_2 where only the probe pulses were used. As for the earlier presented results, the center is screened by the beam block. The image contains two channels with K^+ ions from Coulomb explosion of K_2 in the $1^3\Sigma_u^+$ state and the $1^1\Sigma_g^+$ state. Annotated white rings mark the location of the channels, with the $1^3\Sigma_u^+$ channel being between the solid and the dashed ring and the $1^1\Sigma_g^+$ channel between the dashed and the dot-dashed ring (see identification in Section 5.3). The angular distributions of K^+ ions in both channels are isotropic, as expected when probing randomly oriented dimers.

An example of a 2D velocity map image of K^+ ions measured using both the alignment pulse and the probe pulse is displayed in Fig. 8.2(b). The timing of the probe pulses was adjusted such that the dimers were probed 10 ps after the alignment pulses had set them into rotation. In this image, the majority of the ions in both channels are coming out in a direction close to the polarization axis of the alignment pulse. As the ion fragments recoil along the internuclear axis during the Coulomb explosion process, this indicates that the dimers have been aligned.

The use of crossed polarization axes for the alignment pulses and the probe pulses results in a lack of cylindrical symmetry in

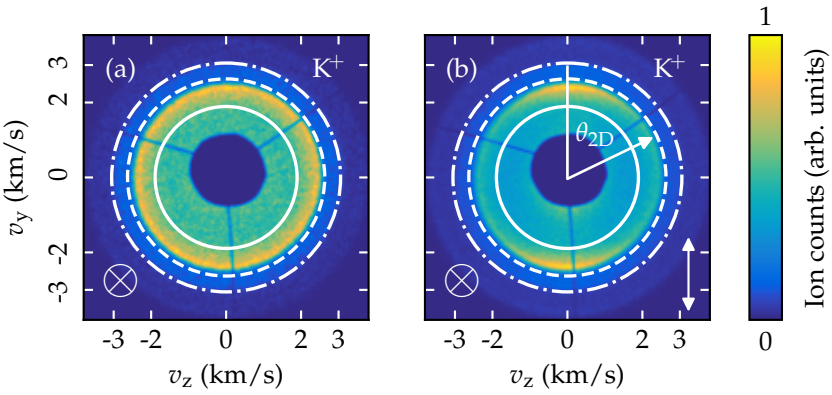

Figure 8.2: 2D velocity map images of K^+ ions (a) recorded with the probe pulse only and (b) recorded with the alignment pulse and the probe pulse, using a probe delay of 10 ps. The polarization directions of the probe pulses (⊗) and the alignment pulses (↕) are depicted at the bottom corners of the images. Annotated white rings mark the regions that contain ions from the $1^3\Sigma_u^+$ and the $1^1\Sigma_g^+$ channels of K_2 (see Section 5.3).

the ion images. As a direct consequence, the ion images cannot be Abel inverted to reconstruct the angular distribution of the ions in 3D [24]. This leads to a potential problem with signal leakage since some ions from Coulomb explosion of the $1^1\Sigma_g^+$ state dimers will be projected onto locations inside the region associated with the $1^3\Sigma_u^+$ state dimers. However, the number of $1^1\Sigma_g^+$ state dimers present in the experiment is generally 3–5 times lower than the number of $1^3\Sigma_u^+$ state dimers. This can be deduced from the areas of the $P(E_{\text{kin}})$ peaks in Fig. 5.3(b2)–(d2), which were recorded under quite similar experimental conditions (see also the detailed discussion in Section B.2). The influence of signal leakage in the present experiments is therefore expected to be minor. In future experiments, the issue may be circumvented entirely by directly measuring the 3D velocities of the ions, thereby removing the need for Abel inversions. Such 3D imaging is investigated in Chapter 10, although not in relation to alignment.

8.2.1 *Experimental alignment dynamics for Na_2, K_2, and Rb_2*

The alignment dynamics were measured by recording a sequence of ion images with various probe delays. For Na_2 and K_2 in

the $1^1\Sigma_g^+$ state, the probe delay was scanned from $t = -20$ ps to $t = 600$ ps, while a range from $t = -20$ ps to $t = 1200$ ps was used for Rb_2 in the $1^1\Sigma_g^+$ state and for all the $1^3\Sigma_u^+$ state measurements. The step size ranged from 1 ps to 5 ps. To characterize the degree of alignment, $\langle\cos^2\theta_{2D}\rangle$ is now calculated for the ions in the $1^3\Sigma_u^+$ and $1^1\Sigma_g^+$ channels in each ion image, with θ_{2D} defined as shown in Fig. 8.2(b).

Figure 8.3(a2)–(c2) show the determined alignment traces $\langle\cos^2\theta_{2D}\rangle(t)$ for the $1^1\Sigma_g^+$ state dimers with black curves, while Fig. 8.4(a1)–(c1) show the results for the $1^3\Sigma_u^+$ state dimers, again using black curves. Minor corrections have been made to the alignment traces (apart from Na_2 in the $1^3\Sigma_u^+$ state and K_2 in the $1^1\Sigma_g^+$ state) such that $\langle\cos^2\theta_{2D}\rangle = 0.5$ before the interaction with the alignment pulse and such that the interaction starts at $t = 0$ ps[22]. This is done to ease later visual comparison with theoretical calculations.

To start with, I will narrow down the scope and focus on the case of Na_2 in the $1^3\Sigma_u^+$ state, displayed in Fig. 8.4(a1). In this trace, the degree of alignment starts at a value around 0.5 for delays $t < 0$ and then rapidly increases to a maximum value of 0.66 at $t = 6$ ps. This increase in the degree of alignment takes place after the interaction with the 1 ps alignment pulse and thus demonstrates field-free alignment, as expected in the nonadiabatic regime (see Section 3.1). Following the prompt alignment peak, the trace oscillates with a gradually decreasing amplitude and with multiple revival structures appearing in regular intervals. Qualitatively, the observed trace differs from the simulation shown in Fig. 3.2 for alignment of gas-phase Na_2 in the $1^3\Sigma_u^+$ state, a simulation done with the experimentally used laser parameters. In addition to the decay in amplitude, the revivals appear to be delayed and the phase of the half revivals is opposite, that is, the degree of alignment first rapidly decreases and then sharply increases, in contrast to what is observed in the gas-phase simulation. The shapes of the oscillations in the experimental trace also do not fully match what has been found previously for linear molecules inside helium droplets [32].

22 The offsets in the delay presumably arose due to slight inaccuracies in the cross-correlations performed to determine $t = 0$ ps. It is unclear why some of the traces had a slight offset in the degree of alignment.

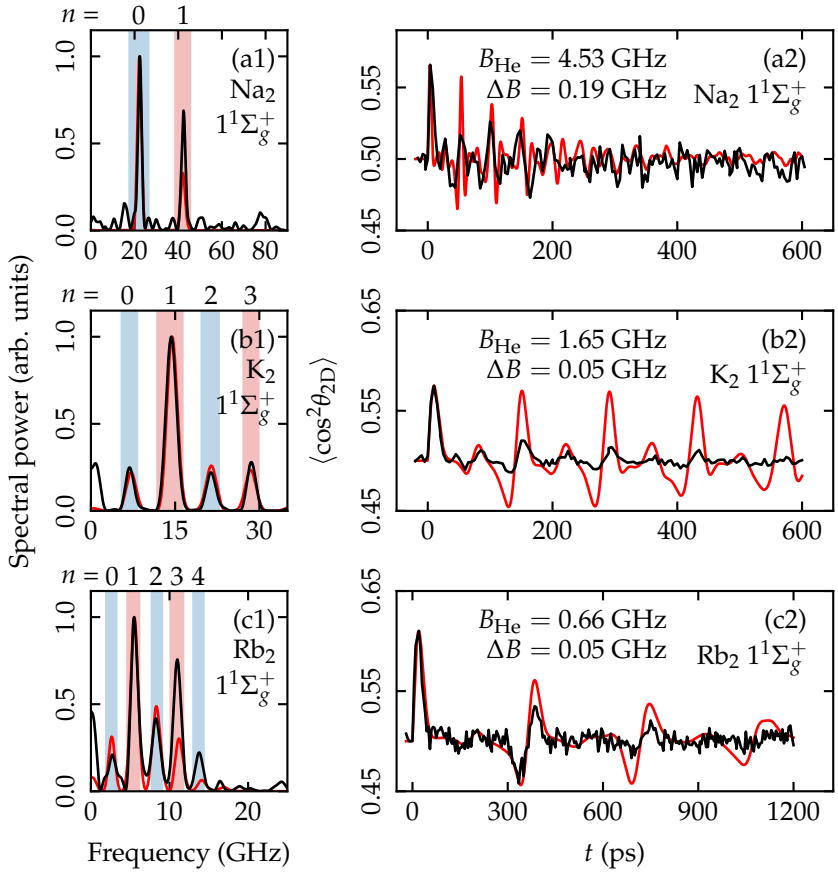

Figure 8.3: (a2)–(c2) Alignment traces for Na_2, K_2, and Rb_2 in the $1^1\Sigma_g^+$ state. The black curves show the experimental data and the red curves show the calculated traces obtained using the 3D model with V_{He}, including inhomogeneous broadening. (a1)–(c1) FFT spectra for the corresponding traces in (a2)–(c2). The peaks are assigned numbers n given above each panel and marked with colored stripes (blue: even n, red: odd n). The calculated traces were made by Areg Ghazaryan (private communication).

The alignment trace for K_2 in the $1^3\Sigma_u^+$ state, Fig. 8.4(b1), exhibits the same qualitative features as just explained for Na_2. For Rb_2 in the $1^3\Sigma_u^+$ state, Fig. 8.4(c1), the prompt alignment peak is observed but there are no clear dynamics or revivals in the rest of the trace. Finally, the traces for the $1^1\Sigma_g^+$ states also do not qualitatively resemble what is typically observed for align-

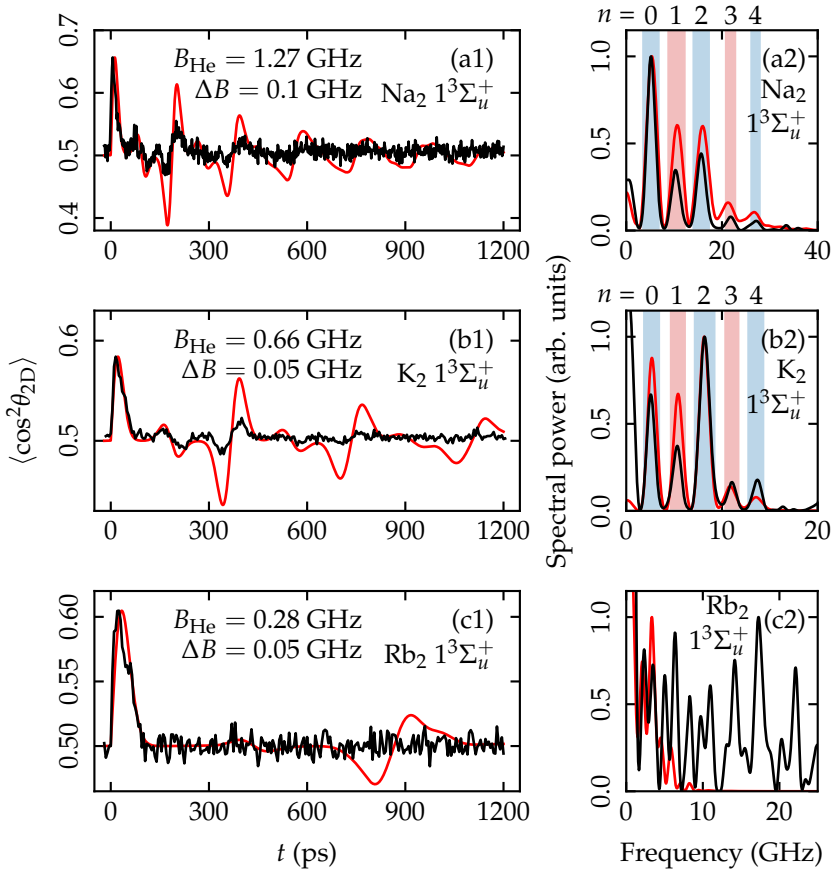

Figure 8.4: Similar to Fig. 8.3. (a1)–(c1) Alignment traces for Na_2, K_2, and Rb_2 in the $1^3\Sigma_u^+$ state. (a2)–(c2) FFT spectra for the corresponding traces in (a1)–(c1). The peaks for Na_2 and K_2 are assigned numbers n while only noise is observed for Rb_2. The calculated traces were made by Areg Ghazaryan (private communication).

ment in gas-phase [15, 17, 25, 29] or in helium droplets [32], see Fig. 8.3(a2)–(c2). However, the $1^1\Sigma_g^+$ traces do contain clear revival features and a prompt alignment peak, which for Rb_2 is in sharp contrast to the observation for the $1^3\Sigma_u^+$ state.

To investigate the frequency content in the alignment traces, I have calculated the FFT spectra, see Fig. 8.3(a1)–(c1) for the $1^1\Sigma_g^+$ states and Fig. 8.4(a2)–(c2) for the $1^3\Sigma_u^+$ states. Each spectrum shows distinct peaks, except for Rb_2 in the $1^3\Sigma_u^+$ state, Fig. 8.4(c2), where the spectrum is filled with noise. I have labeled the dis-

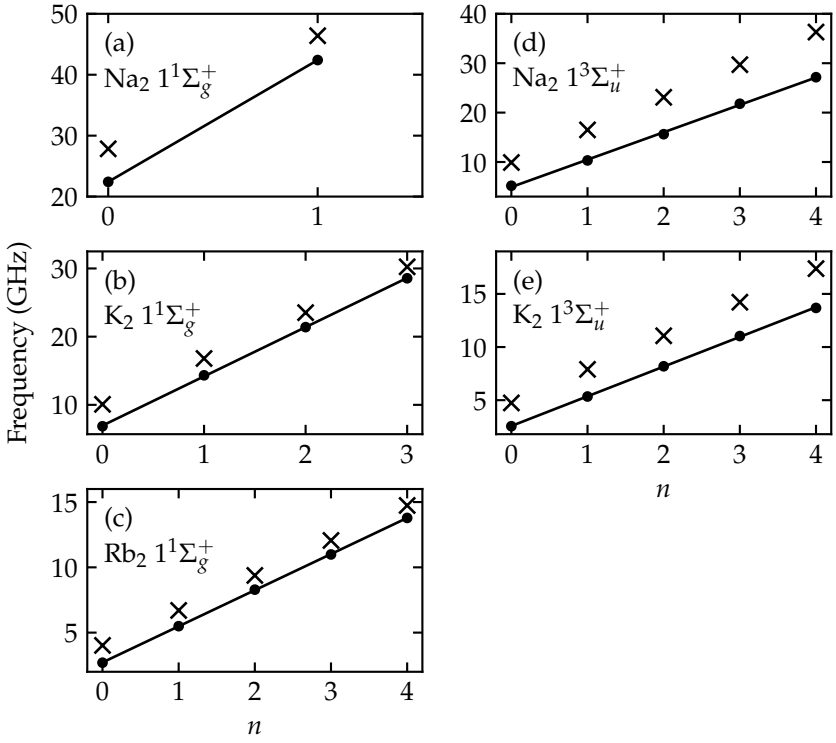

Figure 8.5: Central frequencies, shown with black dots, of the FFT spectra peaks in Fig. 8.3(a1)–(c1) and Fig. 8.4(a2)–(b2) as a function of the assigned n. The black lines show linear fits to the data points. In addition, the gas-phase frequencies $(4J+6)B_{\text{gas}}$ with $J = n$ is shown with crosses. The used B_{gas} values are listed in Table 8.2.

tinct peaks with integer values n, starting from zero for the peak at the lowest frequency in each measurement, as shown with the annotated values above the panels in Fig. 8.3(a1)–(c1) and Fig. 8.4(a2)–(b2). The central positions of the peaks lie on almost perfectly straight lines when plotted as a function of n, as illustrated in Fig. 8.5 with black dots. This is supported by linear fits, shown with black lines, that follow the data points very accurately.

If the alkali dimers rotate like isolated molecules, the frequencies that make up the alignment trace are given by

$$\nu_{J,J+2} = B(4J + 6), \tag{8.1}$$

as explained in Section 3.2. The black crosses in Fig. 8.5 show

	B_{He} (GHz)	B_{gas} (GHz)	B_{gas}/B_{He}
Na_2 $1^1\Sigma_g^+$	4.53 ± 0.02	4.64	1.02 ± 0.01
K_2 $1^1\Sigma_g^+$	1.65 ± 0.02	1.68	1.02 ± 0.01
Rb_2 $1^1\Sigma_g^+$	0.66 ± 0.02	0.67	1.02 ± 0.03
Na_2 $1^3\Sigma_u^+$	1.27 ± 0.02	1.65	1.30 ± 0.02
K_2 $1^3\Sigma_u^+$	0.66 ± 0.02	0.79	1.20 ± 0.04
Rb_2 $1^3\Sigma_u^+$	-	0.32	-

Table 8.2: Experimentally found B_{He} values retrieved via fits with the 3D model including $V_{He}(\Theta)$. Also shown are B_{gas} values calculated for the most abundant isotopologue of each dimer via equilibrium distances R_{eq} from the literature [107, 108] and the ratios B_{gas}/B_{He}. B_{He} is excluded for Rb_2 in the triplet state because a value cannot be reliably assigned, see Section 8.2.5. The stated uncertainties for B_{He} have been qualitatively estimated, see the discussion in Section 8.3, and propagated to B_{gas}/B_{He}.

the frequencies expected for this model, calculated via the gas-phase rotational constants B_{gas} listed in Table 8.2. For Na_2 and K_2 in the $1^3\Sigma_u^+$ state, Fig. 8.5(d)–(e), the model deviates strongly from the experimental observation, in particular with respect to the slope of the line. Judging from the data points at $n = 0$, the constant offsets in the experimental frequencies are also reduced compared to what is predicted by the model. In the case of the $1^1\Sigma_g^+$ state dimers, Fig. 8.5(a)–(c), the observed frequencies follow lines with slopes that lie close to those given by the models, but still with offsets toward lower frequencies. The spectral analysis thus corroborates that the alignment dynamics observed for the alkali dimers are not accurately described by normal gas-phase rotation for linear molecules. Note finally that the linear relationships for the measured frequencies differ from what was seen for linear rotors inside helium droplets (see Fig. 3.4), where the large effective centrifugal distortion constants D_{He} gave rise to nonlinear spectra.

8.2.2 *Theoretical modeling of alignment traces*

To get a better understanding of the observed dynamics, it is useful to develop a theoretical model. This has been done in collaboration with Frank Jensen from Aarhus University, Robert Zillich from the Johannes Kepler University in Linz, and Areg Ghazaryan and Mikhail Lemeshko from the Institute of Science and Technology Austria. The main goal is to solve the time-dependent rotational Schrödinger equation for the Hamiltonian

$$H = \frac{B\hat{J}^2}{\hbar^2} - \frac{E^2(t)}{4}\left[(\alpha_\parallel - \alpha_\perp)\cos^2\theta + \alpha_\perp\right] + V_{\mathrm{He}}(\Theta). \quad (8.2)$$

I previously showed the first two terms in Section 3.1, where I described how they can be used to model laser-induced alignment of isolated linear molecules. The third term, $V_{\mathrm{He}}(\Theta)$, is an effective static mean-field potential for the alkali dimer at the surface of the helium droplet, with Θ describing the angle between the surface normal and the internuclear axis of the dimer [see Fig. 8.9(a)] [58].

As a first step toward the goal, Frank Jensen made CCSD(T) level calculations of the Ak_2–He potentials for the alkali dimers in both the $1^3\Sigma_u^+$ state and the $1^1\Sigma_g^+$ state [188]. These potentials were then used in the next set of calculations, carried out by Robert Zillich, where $V_{\mathrm{He}}(\Theta)$ was determined for the different alkali dimers in both quantum states. The strategy applied by Robert was to first determine the angular distribution $P(\Theta)$ of the alkali dimers on the surface of a thin helium film using *path integral Monte Carlo* simulations. Next, the $V_{\mathrm{He}}(\Theta)$ potentials were extracted from the $P(\Theta)$ distributions [58, 188]. In the case of $1^3\Sigma_u^+$ state Rb_2, the Rb_2–He and $V_{\mathrm{He}}(\Theta)$ potentials, as well as the $P(\Theta)$ distribution, were already available from the literature, and thus not calculated here [58]. All the angular distributions and the effective potentials are shown in Fig. 8.6. For all the dimers, $P(\Theta)$ peak at $\Theta = \pi/2$, corresponding to an orientation parallel to the surface of the droplet.

With $V_{\mathrm{He}}(\Theta)$ at hand, it is now possible to solve the Schrödinger equation for the Hamiltonian in Eq. 8.2 with pulse parameters equal to those used in the experiments (see Section 8.1 and Table 8.1). This part of the calculations was handled by Areg

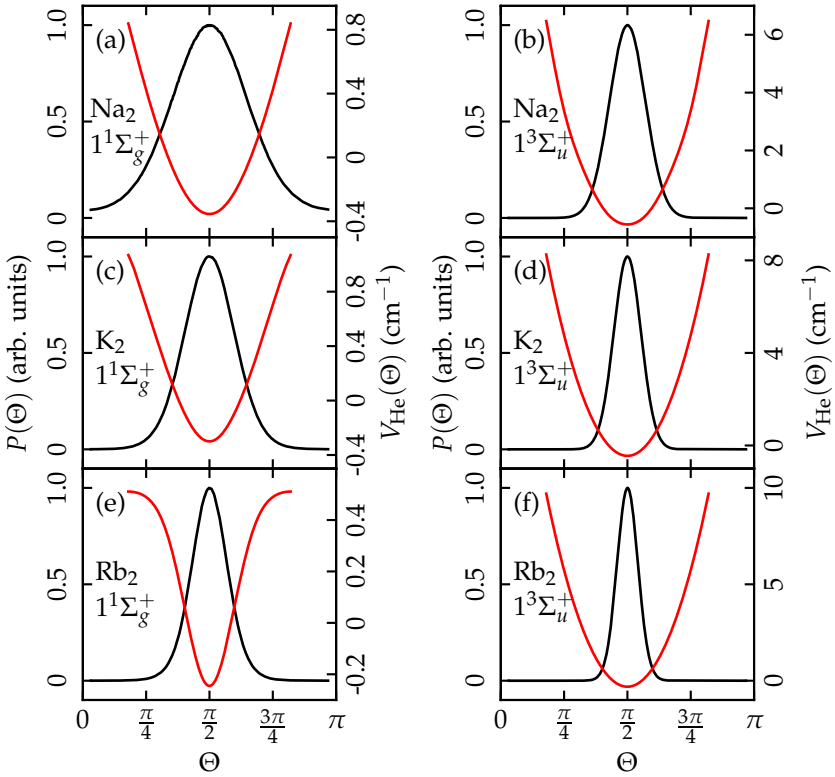

Figure 8.6: Calculated angular distributions $P(\Theta)$ (black) for Na_2, K_2, and Rb_2 in the $1^1\Sigma_g^+$ state and the $1^3\Sigma_u^+$ state on the surface of helium droplets. Θ denotes the angle between the surface normal and the internuclear axis of the dimer. The red curves show the determined $V_{He}(\Theta)$ potentials for the different systems. The calculations were made by Robert Zillich with support from Frank Jensen (private communication).

Ghazaryan with support from Mikhail Lemeshko. The static polarizabilities for the alkali dimers were taken from the literature [108], while an effective rotational constant B_{He} was used instead of B and treated as a free parameter to be determined by the best fit to the experimental results. In addition, inhomogeneous broadening of the rotational frequencies, arising from the different droplet sizes present in the experiment [189–191], was included as a Gaussian distribution of B_{He} values. The FWHM of this distribution, ΔB, was also treated as a free parameter. The inhomogeneous broadening will lead to dephasing (that is, the phase components in the wave packet drift apart), which has

previously been demonstrated as a necessary ingredient in the modeling of alignment dynamics for molecules inside helium droplets [32].

In the calculations, the dimers are assumed to reside on the droplet at a location where the surface plane is parallel to the detector plane, that is, the calculations are not averaged over all the possible dimer locations on the surface. This is a simplification, but it is somewhat justified because the experimental alignment traces were retrieved for the Ak^+ ions in the identified $1^3\Sigma_u^+$ state and $1^1\Sigma_g^+$ state channels in the ion images, see Fig. 8.2(a). These ions have the largest transverse velocities of the Ak^+ ions produced in Coulomb explosion of the $1^3\Sigma_u^+$ state and $1^1\Sigma_g^+$ state dimers. Thus, the ions should primarily originate from dimers that were lying quite parallel to the detector plane prior to Coulomb explosion[23].

Temperature effects were taken into account by thermal averaging of the calculated $\langle \cos^2 \theta_{2D} \rangle$ values according to the Boltzmann factors for the systems at the droplet temperature of 0.37 K. The even and odd abundances of J states due to nuclear spin statistics are also included in the calculations. For K_2 and Rb_2, multiple isotopologues are present in the experiment, even though we gate on the most abundant isotopes in the experiment ($^{39}K^+$ and $^{85}Rb^+$). In the case of K_2, both $^{39}K_2$ and $^{39}K^{41}K$ are therefore taken into account, weighted by their abundance ratios, and similarly both $^{85}Rb_2$ and $^{85}Rb^{87}Rb$ are included for Rb_2. Note that the abundances of odd and even J states for $^{39}K^{41}K$ and $^{85}Rb^{87}Rb$ are not affected by nuclear spin statistics because the dimers are no longer completely symmetric.

For all the simulations, with the exception of those on Na_2 in the $1^3\Sigma_u^+$ state, focal volume averaging (FVA) has not been included, that is, the spatial intensity profiles of the alignment pulses and the probe pulses have not been taken into account [192]. The spatial dependence tends to smear out the finer details in alignment traces and to reduce the obtained degree of alignment. However, the effect of FVA is expected to be minor in this work

23 Note that the dimers can lie parallel to the detector plane without being at a position on the droplet where the surface plane is parallel to the detector plane. The contributions from all such positions are neglected with the used model.

because the spot sizes of the alignment pulses were around twice as large as those of the probe pulses, leading to a quite uniform alignment pulse intensity in the probed region. This is supported by the calculations on Na_2 in the $1^3\Sigma_u^+$ state, where including FVA only changed the simulated alignment traces insignificantly.

Finally, the calculated $\langle\cos^2\theta_{2D}\rangle(t)$ traces are normalized such that the degree of alignment at the maximum of the prompt alignment peak is the same as that observed in the corresponding experiments. This is done to make it easier to compare the traces qualitatively. Note that the calculated traces would generally reach higher degrees of alignment than the experiment. I believe the primary reason for this is non-axial recoil during the Coulomb explosion process producing the Ak^+ fragments. As observed from the widths of the angular covariance lines in Fig. 5.3(b3)–(e3) and (a4)–(e4), the angle between the ejected Ak^+ ions often deviates significantly from 180°. The result is that the observed degree of alignment is reduced. It has previously been shown that it is possible to deconvolve the nonaxial recoil effect from the experimentally observed degree of alignment by utilizing the information obtained from the angular covariance maps [193]. This has, however, not been attempted for the results presented here.

8.2.3 *Theoretical results for K_2*

I will first treat the theoretical results for K_2, starting with the $1^1\Sigma_g^+$ state. Figure 8.7(a2) presents the calculated alignment trace (red curve) that was found to describe the experimental measurement (black curve) most accurately. The calculation was done with B_{He} = 1.65 GHz, a minor reduction compared to the gas-phase value B_{gas} = 1.68 GHz (see Table 8.2) [108], and ΔB = 0.05 GHz. By visual inspection, the predicted locations of the revivals appear to match those observed in the experiment. Note also that the applied inhomogeneous broadening creates a slow decrease in the degree of alignment, as can be inferred from a visual comparison of the calculation in Fig. 8.7(a2) and the calculation in Fig. 8.7(b2), which was done with the same B_{He} value but without broadening.

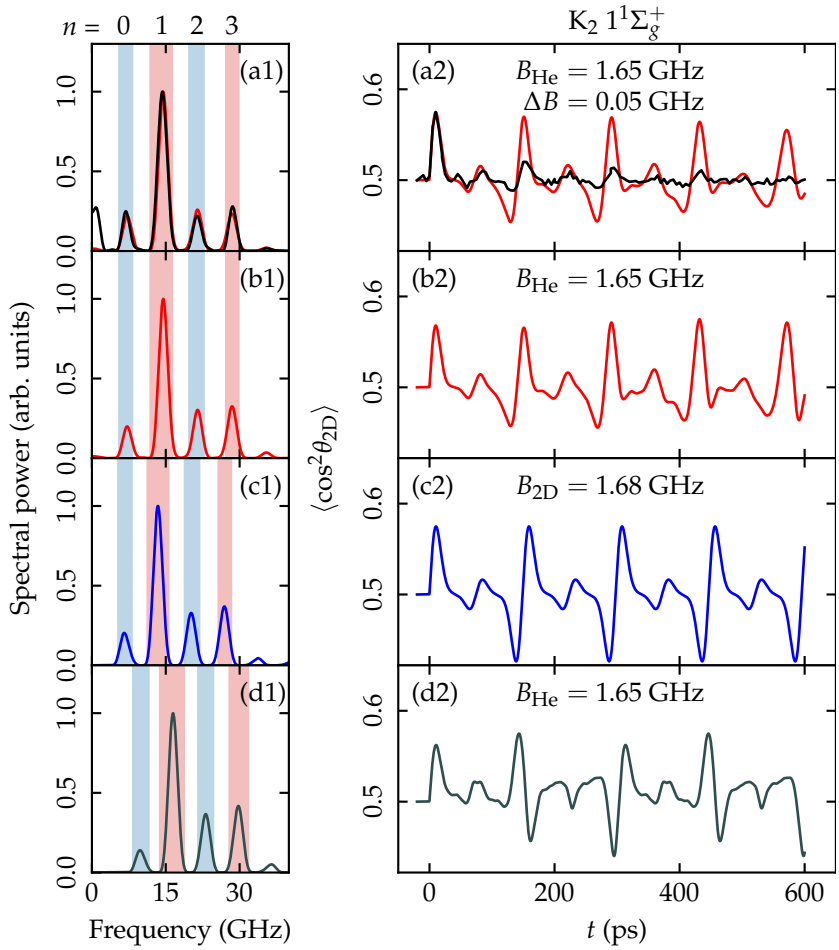

Figure 8.7: (a2) Experimental alignment trace (black) for K_2 in the $1^1\Sigma_g^+$ state and calculated alignment trace (red) using the 3D model with $V_{He}(\Theta)$ including inhomogeneous broadening. (b2) Calculation for the 3D model with $V_{He}(\Theta)$ without inhomogeneous broadening. (c2) and (d2) Calculations for the 2D model and the 3D model, respectively. (a1)–(d1) FFT spectra for the alignment traces in (a2)–(d2). The peaks are assigned numbers n given above panel (a1) and marked with colored stripes (blue: even n, red: odd n). The calculated traces were made by Areg Ghazaryan (private communication).

The theoretical model does not fully capture the measured gradual decay in the degree of alignment. Increasing ΔB will lead to a faster decay but will also gradually broaden the revival

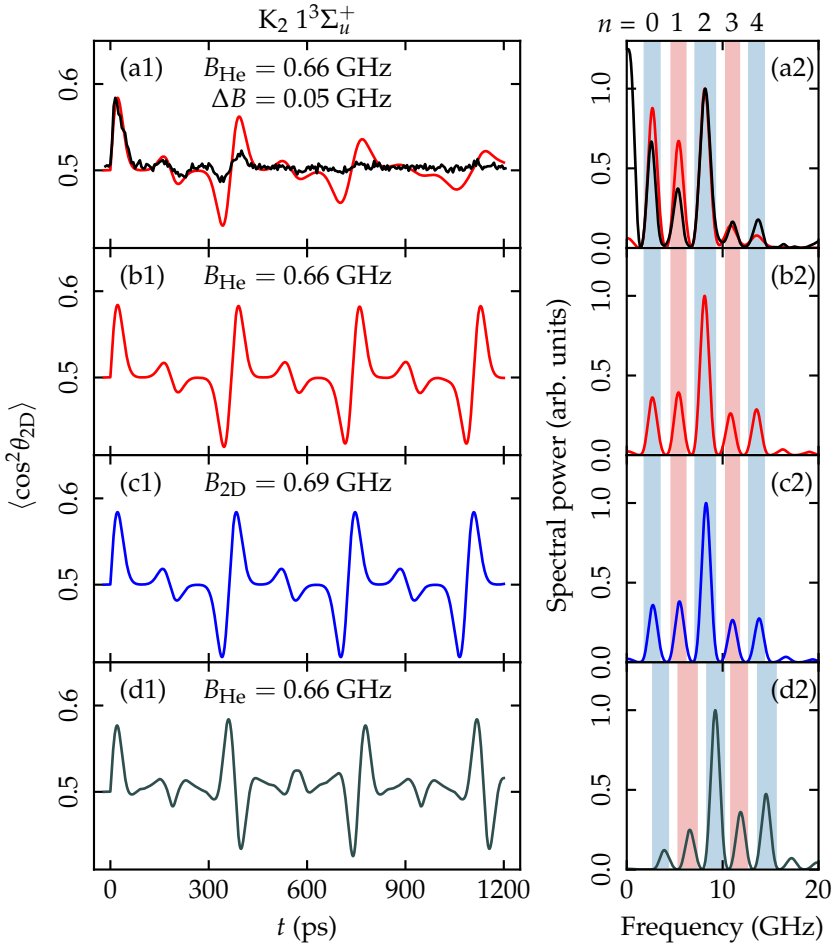

Figure 8.8: Similar to Fig. 8.7 but for K_2 in the $1^3\Sigma_u^+$ state. The alignment traces are shown in (a1)–(d1) while (a2)–(d2) show the respective FFT spectra. The calculated traces were made by Areg Ghazaryan (private communication).

features, causing the positions of the minima and maxima to shift in a way that cannot be accounted for by selecting another value for B_{He}. As a consequence, changing ΔB will not improve the overall agreement with the measurement. This indicates that homogeneous broadening may also play a role in the experiment. I will discuss this in more detail in Section 8.3.

Figure 8.7(a1) shows the frequency spectra for the experimental and the theoretical trace in Fig. 8.7(a2). The height of the tallest peak in each spectrum has been normalized to unity. Both the

central positions and the relative amplitudes of the peaks are in agreement for the two spectra, showing that the model captures the essential rotational dynamics.

At this point, it is instructive to consider the effect of the $V_{\mathrm{He}}(\Theta)$ potential. Figure 8.6(c) shows that the potential forces the dimers to lie mostly parallel to the surface plane. The consequence is that rotational motion out of the plane is restricted. As mentioned in Chapter 1, this is what Grüner and coworkers speculated in an earlier publication, although for Rb_2 [57]. To test this interpretation, the alignment dynamics have also been calculated for a 2D rotor model by solving the time-dependent Schrödinger equation [194]. Once again, an effective rotational constant B_{2D} was employed and treated as a free parameter to be determined by the best fit.

Figure 8.7(c2) presents the calculated 2D trace. In this case, B_{2D} = 1.68 GHz gave the best match with the measured trace. This rotational constant is equal to B_{gas} and thus corresponds to completely unhindered rotation in the surface plane. A comparison with the trace in Fig. 8.7(b2) shows that the 2D alignment dynamics are qualitatively very similar to those obtained with the 3D model including $V_{\mathrm{He}}(\Theta)$, at least for the first 300 ps. However, the rotations are too slow in the 2D model, as seen from the positions of the minima and maxima which show up increasingly late as time progresses. The FFT spectrum in Fig. 8.7(c1) likewise shows that the rotational frequencies in the 2D model are lower than for the 3D model with $V_{\mathrm{He}}(\Theta)$, Fig. 8.7(b1), although the relative heights of the peaks are very similar. In principle, the issue could be solved by increasing B_{2D}, but it does not seem plausible that the rotational constant for the dimer on the droplet is larger than for the isolated molecule.

The reason that the rotations are too slow with the 2D model, even though $B_{2D} > B_{\mathrm{He}}$, can be explained with a classical argument. Consider a dimer rotating in 2D around the normal $\hat{\mathrm{n}}$ of the surface plane, see Fig. 8.9(a). The rotational constant $B_{\hat{\mathrm{n}}}$ associated with rotation around $\hat{\mathrm{n}}$ is in this case equal to B_{2D}. In contrast, if the dimer is tilted out of the surface plane but still rotates around $\hat{\mathrm{n}}$, see Fig. 8.9(b), then the value of $B_{\hat{\mathrm{n}}}$ will increase because the moment of inertia for the rotation is decreased. As a

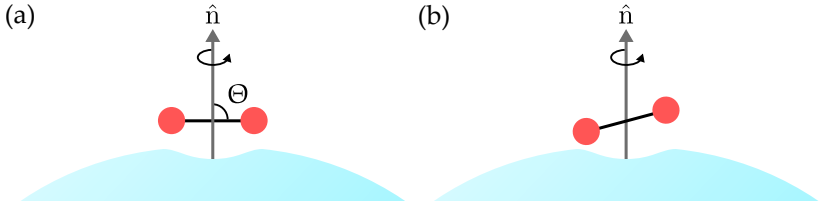

Figure 8.9: (a) Sketch of a dimer undergoing 2D rotation in the surface plane ($\Theta = \pi/2$) around an axis $\hat{n}$ normal to the surface. (b) A dimer rotating in 3D around $\hat{n}$. The rotational constant $B_{\hat{n}}$ of the dimer with respect to $\hat{n}$ is larger for the situation in (b) compared to that in (a).

result, $B_{\hat{n}} > B_{2D}$. The observed rotations will thus be faster for the 3D model with $V_{He}(\Theta)$, where the dimer is allowed to fluctuate out of the surface plane, compared to the 2D model, even if the same rotational constant is used for both calculations. B_{2D} must therefore be increased to compensate, but in the present case, the rotations are still too slow for $B_{2D} = B_{gas}$.

Finally, the alignment dynamics have been calculated for the isolated dimer in 3D, that is, excluding the $V_{He}(\Theta)$ potential, see Fig. 8.7(d2). The calculation was done using the previously found B_{He} value. Qualitatively, the trace resembles neither the measured trace nor those calculated with the other models. Additionally, the frequency spectrum illustrated in Fig. 8.7(d1) also deviates from the other spectra in Fig. 8.7(a1)–(c1). Evidently, the observations cannot be described by the rotation of isolated molecules.

I will now discuss the results for K_2 in the $1^3\Sigma_u^+$ state. Using the 3D model with the respective $V_{He}(\Theta)$ potential, see Fig. 8.6(d), the alignment dynamics have been calculated. Once again, the simulated trace is in good qualitative agreement with the measured trace, see Fig. 8.8(a1). In particular, the minima and maxima line up quite well. The effective rotational constant was found to be $B_{He} = 0.66$ GHz, which deviates from $B_{gas} = 0.79$ GHz [107], while $\Delta B = 0.05$ GHz. Note that increasing ΔB would again model the observed decay in $\langle \cos^2 \theta_{2D} \rangle$ better, but result in worse agreement with respect to the positions of the revivals.

Figure 8.8(b1) shows the alignment trace obtained for the $1^3\Sigma_u^+$ state when excluding the inhomogeneous broadening. This trace

is almost identical to the trace obtained with the 2D model[24], see Fig. 8.8(c1), and vastly different from that obtained with the gas-phase 3D model, displayed in Fig. 8.8(d1). Considering that the $P(\Theta)$ distribution for the $1^3\Sigma_u^+$ state, Fig. 8.6(d), is more narrow than for the $1^1\Sigma_g^+$ state, it is not surprising that the 2D model agrees so well with the 3D model including $V_{\mathrm{He}}(\Theta)$.

A spectral analysis supports the observations, see Fig. 8.8(a2)–(c2). The positions of the frequency spectra are quite consistent throughout, but the relative height of the peaks from the calculations do not fully match those from the experiment. However, the 3D model with $V_{\mathrm{He}}(\Theta)$ and inhomogeneous broadening does give a better agreement than when the broadening is excluded, as seen by comparison of Fig. 8.8(a2) and (b2).

8.2.4 *Theoretical results for Na_2*

The theoretical treatment of Na_2 follows the same strategy as for K_2. For Na_2 in the $1^3\Sigma_u^+$ state, the rotational dynamics are again well-described by a 2D rotor model. This agrees with expectations since the $P(\Theta)$ distribution, see Fig. 8.6(b), is very similar to those for K_2 shown in Fig. 8.6(c) and (d). The best fit with the 3D model including $V_{\mathrm{He}}(\Theta)$ is illustrated with the red curve in Fig. 8.4(a1) and gives $B_{\mathrm{He}} = 1.27$ GHz and $\Delta B = 0.1$ GHz. As for K_2 in the $1^3\Sigma_u^+$ state, B_{He} deviates noticeably from the gas-phase value, here $B_{\mathrm{gas}} = 1.65$ GHz [107].

Na_2 in the $1^1\Sigma_g^+$ state breaks the pattern. This dimer has a much wider $P(\Theta)$ distribution, Fig. 8.6(a), than all the other dimers. As a consequence, the qualitative features of alignment traces calculated with the 2D rotor model (not shown) no longer match the features in the measured trace shown in Fig. 8.3(a2). Nonetheless, including $V_{\mathrm{He}}(\Theta)$ in the 3D calculation once more results in a trace that agrees well with the measurement, see the red curve in Fig. 8.3(a2). This is corroborated by the fre-

24 Keen-sighted readers may notice that the minima and maxima in Fig. 8.8(c1) are shifted to slightly earlier times compared to Fig. 8.8(b1). This is because the 3D model with $V_{\mathrm{He}}(\Theta)$ was fitted to the experimental data with the inhomogeneous broadening included. Removing the broadening causes the minima and maxima to shift a small amount. As a result, it does not line up perfectly with the 2D trace, which was fitted directly to the measurement.

quency spectra presented in Fig. 8.3(a1). From the fit, the values B_{He} = 4.53 GHz and ΔB = 0.19 GHz are obtained. While B_{He} is close to B_{gas} = 4.64 GHz [108], ΔB is by far the largest amount of inhomogeneous broadening observed for any of the alkali dimers in the experiments. Overall, the rotational dynamics of Na_2 in the $1^1\Sigma_g^+$ state are closer to that of isolated linear molecules compared to the other alkali dimers, but the rotations are still affected by the droplet surface.

8.2.5 *Theoretical results for Rb_2*

Figure 8.3(c2) presents the results for Rb_2 in the $1^1\Sigma_g^+$ state, calculated with the 3D model including $V_{He}(\Theta)$ using B_{He} = 0.66 GHz and ΔB = 0.05 GHz. This system primarily lies in the surface plane, as seen from the $P(\Theta)$ distribution in Fig. 8.6(e), and is therefore also described very well by a 2D rotor model (not shown). The found B_{He} is very close to B_{gas} = 0.67 GHz [108] and ΔB = 0.05 GHz, similar to the results for K_2.

Concerning Rb_2 in the $1^3\Sigma_u^+$ state, the lack of alignment dynamics after the prompt alignment peak in the measurement [Fig. 8.4(c1)] makes it impossible to fit calculated traces to the data reliably. Fortunately, Robert Zillich and coworkers have previously calculated the effective rotational constant for this dimer at a helium surface to be B_{He} = 0.28 GHz [58], which is slightly lower than B_{gas} = 0.32 GHz [107]. Using this B_{He} and ΔB = 0.05 GHz, the same amount of inhomogeneous broadening as for Rb_2 in the $1^1\Sigma_g^+$ state and K_2, an alignment trace has been calculated with the 3D model, again including $V_{He}(\Theta)$. The result is shown in Fig. 8.4(c1) with the red curve. Remarkably, the calculation predicts that $\langle\cos^2\theta_{2D}\rangle$ remains very close to 0.5 from t = 100 ps and out to t = 700 ps where the calculated degree of alignment dips before the half revival. The apparent lack of alignment dynamics in the measured trace may therefore fit well into the overall picture. Presumably, the half revival is not observed experimentally due to the same mechanisms that cause the gradual decay in the degree of alignment for the other alkali dimers. It is interesting to note that alignment dynamics are still observed for Rb_2 in the $1^1\Sigma_g^+$ state around the time scale of the missing half revival for the $1^3\Sigma_u^+$ state, as seen by comparing Fig. 8.3(c2) and Fig. 8.4(c1). This might indicate that the mecha-

nisms causing the gradual decay happen on a faster time scale for $1^3\Sigma_u^+$ state Rb_2 than for $1^1\Sigma_g^+$ state Rb_2.

It should be stressed that the results here cannot provide completely reliable values for B_{He} and ΔB for Rb_2 in the $1^3\Sigma_u^+$ state. If ΔB is chosen sufficiently large, the revivals will always be washed out in the calculated alignment trace and thus resemble the experimental observation. In addition, the calculation is not very sensitive to the chosen value for B_{He} because there are no experimental revivals to compare to. The findings presented here thus merely demonstrate that the experimental observation is consistent with the model if the values for B_{He} and ΔB follow the trends for Rb_2 in the $1^1\Sigma_g^+$ state and K_2 in both quantum states.

8.3 Discussion

To assess how precisely B_{He} can be determined via the fits with the 3D model including $V_{He}(\Theta)$, a series of alignment traces have been calculated with slight changes to B_{He}. From these calculations, I qualitatively estimate that B_{He} can be determined with a precision of 0.02 GHz. Larger variations result in noticeable disagreement between the measurements and the calculated alignment traces, especially with respect to the central positions of the frequency peaks revealed by spectral analysis. The estimated uncertainty is also denoted in Table 8.2 where the found B_{He} values are listed for convenience.

Table 8.2 show the B_{gas}/B_{He} ratios for all the dimers except Rb_2 in the $1^3\Sigma_u^+$ state where B_{He} could not be properly determined. The ratios are significantly smaller than the ratios of 2–6 observed for linear molecules inside helium droplets [32]. This indicates that the alkali dimers interact much more weakly with the droplets than molecules embedded inside the droplets do. While the ratios for Na_2 and K_2 in the $1^3\Sigma_u^+$ state show approximately a 20% reduction in B compared to gas phase, the ratios for the $1^1\Sigma_g^+$ state dimers only deviate with about 2%. Note that the uncertainties on the ratios denoted in Table 8.2 were found by simple propagation of the uncertainty in B_{He} and do not take the possible uncertainties in the B_{gas} values from the literature into account. The uncertainties given here may therefore be slightly understated.

The primary shortcoming of the developed 3D model including $V_{\mathrm{He}}(\Theta)$ and inhomogeneous broadening is that it does not fully capture the gradual decay in the degree of alignment observed in the experiments. As mentioned previously, this indicates that the rotational wave packets may also be subject to significant homogeneous broadening in the form of decoherence (loss of phase) and loss of population in the excited rotational states [46, 195]. This is in stark contrast to the observations for nonadiabatic alignment of molecules inside helium droplets, where it was only necessary to include inhomogeneous broadening to model the alignment dynamics [32]. It is unclear why the case is different for molecules at the surface. Likewise, it is currently not understood why the inhomogeneous broadening appears to be more significant for Na_2 than for K_2 and Rb_2, in particular for the $1^1\Sigma_g^+$ state.

With the current experimental scheme, it is not possible to distinguish between the homogeneous and inhomogeneous broadening effects. However, rotational echo experiments can perhaps be used to investigate the broadening effects more closely [196, 197]. The principle of the rotational echo method is to use two consecutive alignment pulses spaced by some delay to create echoes (revival-like structures) in the degree of alignment. Echoes formed in this way will occur at regular time intervals that can be controlled via the delay between the two alignment pulses. The technique has previously been used to study collisional effects for rotational dynamics of molecules in a gas [198, 199]. Rotational echoes are also particularly useful in cases where the alignment signal has decayed before any prominent revivals have been observed because the experiment can be tailored to create echoes at much earlier times than the revivals. It would therefore be interesting to apply this technique to Rb_2 in the $1^3\Sigma_u^+$ state where only the prompt alignment peak was observed. If such rotational echo experiments can be successfully conducted, it might reveal insight into the coupling between the rotation of the alkali dimers and the ripplon and phonon excitations of the helium droplets [64, 200]. Additionally, it would be interesting to record the alignment dynamics of the alkali dimers for various droplet sizes to test how much the droplet sizes affect the inhomogeneous broadening.

8.4 Conclusion

In conclusion, I have shown that homonuclear alkali dimers can be set into rotation and aligned on the surface of helium droplets. The rotational dynamics deviate from those observed for linear molecules in gas phase and inside helium droplets, indicating that the rotations are affected by the presence of the helium surface. Comparisons with theoretical calculations reveal that the surface potential causes Na_2 and K_2 in the $1^3\Sigma_u^+$ state to undergo 2D-like rotation in the surface plane with rotational constants that are only slightly reduced from the gas phase values, $B_{gas}/B_{He} = 1.30 \pm 0.02$ and 1.20 ± 0.04 respectively. Similar is observed for the $1^1\Sigma_g^+$ states of K_2 ($B_{gas}/B_{He} = 1.02 \pm 0.01$) and Rb_2 ($B_{gas}/B_{He} = 1.02 \pm 0.03$). To my knowledge, these measurements are the first time-resolved measurements of 2D molecular rotation ever.

For Na_2 in the $1^1\Sigma_g^+$ state, the surface potential does not fully confine the dimer to the surface plane. As a result, the rotational dynamics are closer to what is observed for isolated linear molecules. Here, $B_{gas}/B_{He} = 1.02 \pm 0.01$. The alignment trace for Rb_2 in the $1^3\Sigma_u^+$ state exhibits a prompt alignment peak but no clear oscillations or revivals afterward. This might be due to interactions with the helium droplets. As a result, it has not been possible to make proper comparisons to the model for this system.

In contrast to linear molecules inside helium droplets, inhomogeneous broadening of the rotational constants cannot alone describe the observed decay in the degree of alignment for any of the studied dimers. This invites further experimental studies to obtain a better understanding of the broadening mechanisms involved in the rotational dynamics of the alkali dimers on the droplets.

9

VIBRATIONS OF ALKALI DIMERS ON HELIUM DROPLETS

This chapter is dedicated to my exploration of vibrational wave packets in homonuclear alkali dimers on helium droplets, induced by the alignment pulses used for the nonadiabatic alignment experiments presented in Chapter 8. People have already studied vibrational wave packets for the alkali dimers on droplets before, and the dynamics are by now fairly well understood [90, 91, 201–203]. However, since vibrations can affect the rotations of molecules it is interesting to assess whether vibrational dynamics are present under the experimental conditions used in the study of the rotational dynamics of the alkali dimers.

I will first explain how the dynamic Stark effect can lead to the formation of vibrational wave packets in the alkali dimers. After that, I show experimentally that the vibrations can be detected via timed Coulomb explosion. The results are from my early experimental investigations on Rb_2 which were obtained before the project was handed over to Nicolaj Jyde from our group. The following analysis is kept on a rudimentary level. It mainly aims to identify the level of vibrational excitation and to address whether the vibrations may influence the simultaneous rotational dynamics.

9.1 Inducing vibrational motion via the dynamic Stark effect

In Chapter 3, I explained how a nonresonant laser pulse can set the alkali dimers into rotation via the dynamic Stark interaction. I, however, neglected an important detail which is that the polarizabilites of the alkali dimers depend on the internuclear separation R [204]. Taking this into account, the interaction can now be written as

$$V(R,t) = -\frac{E^2(t)}{4}\left\{[\alpha_{\parallel}(R) - \alpha_{\perp}(R)]\cos^2\theta + \alpha_{\perp}(R)\right\}. \quad (9.1)$$

The R-dependence turns out to be quite significant for the

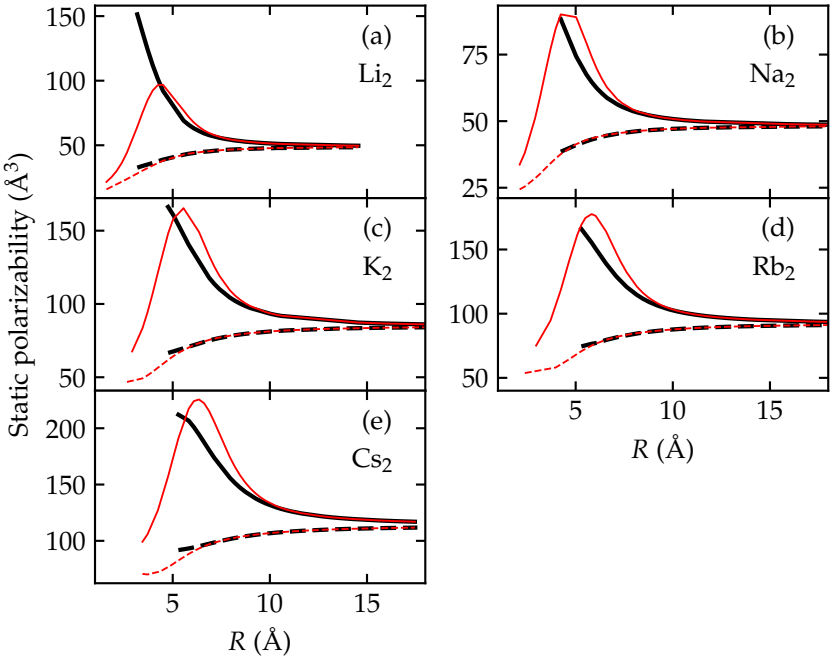

Figure 9.1: Parallel (fully drawn) and perpendicular (dashed) static polarizabilities for the alkali dimers in the $1^3\Sigma_u^+$ state (black) and the $1^1\Sigma_g^+$ state (red). Based on tabulated values from the literature [108].

alkali dimers, as can be inferred from Fig. 9.1 which shows $\alpha_\parallel(R)$ and $\alpha_\perp(R)$ using data found in the literature [108]. As a direct consequence, the interaction with the alignment pulse will distort the potential curve of the dimers along the R-coordinate, shifting the minimum of the potential to a new position. This will set the dimer into vibrational motion when the nuclei start shifting due to the forces in the new potential. An illustration of this is shown in Fig. 9.2 for Rb_2 in the $1^3\Sigma_u^+$ state. If the duration of the interaction with the alignment pulse is shorter than the vibrational period of the dimer and the shift in energy is larger than the gap between vibrational states, it is possible to create a vibrational wave packet that remains after the interaction switches off [204, 205].

If the alkali dimers in the nonadiabatic alignment experiments (see Chapter 8) are vibrating after being subjected to the ~ 1 ps pulse used to induce alignment, it should be reflected in the

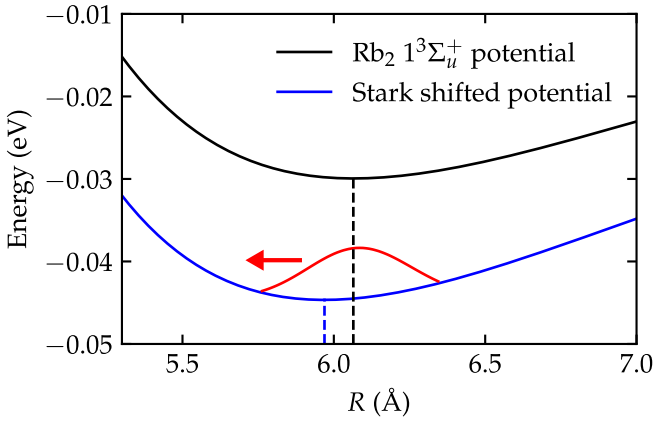

Figure 9.2: Potential energy curve for Rb_2 in the $1^3\Sigma_u^+$ state (black) [107] and for the Stark shifted $1^3\Sigma_u^+$ state potential (blue), calculated for a perfectly aligned dimer ($\cos^2\theta = 1$) and an assumed intensity of 5×10^{10} W/cm^2. The black and blue dashed lines mark the minima of the unperturbed potential and the Stark-shifted potential, respectively. The shift starts vibrational motion, as indicated for the sketched wave function shown in red.

kinetic energies of the Ak^+ ions produced in the Coulomb explosions. This follows from the fact that the released Coulomb energy is dictated by the distance between the two Ak^+ ions at the instant they are formed. The nonadiabatic alignment experiment is therefore conducted again, but this time with the probe pulse polarization in the detector plane as illustrated in Fig. 9.3. This is done to obtain the required cylindrical symmetry in the ion images such that the Abel inversion routine can be applied and $P(E_{\text{kin}})$ extracted. The fundamental idea is then to observe if the positions of the $1^3\Sigma_u^+$ state and $1^1\Sigma_g^+$ state peaks in $P(E_{\text{kin}})$ change as a function of the delay between the alignment pulse and the probe pulse.

9.2 Experimental setup

A beam of helium droplets was created with the nozzle temperature set to $T_{\text{nozzle}} = 12$ K, then doped with Rb_2, and finally intersected by the pump and probe beams inside the VMI spec-

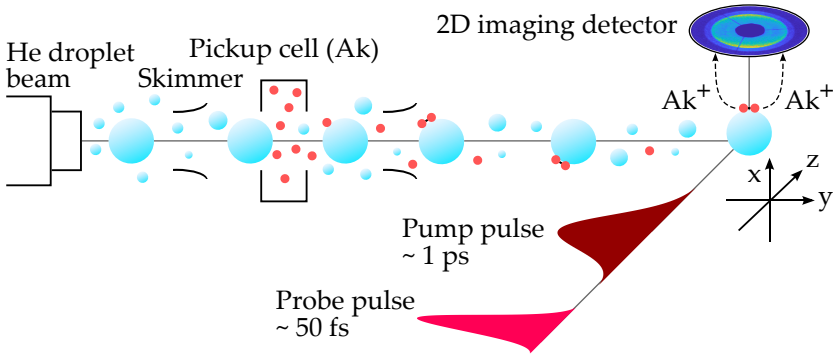

Figure 9.3: Sketch of the experiment conducted to investigate vibrations of Ak_2 on He droplets. The pump pulse starts vibrations in the dimers, alongside the rotations (see Chapter 8), which are then probed with an intense $\sim$ 50-fs pulse. Own work, adapted from [124].

trometer. For the pump, the 1300 nm pulses were used. These pulses were stretched to a duration of 0.8 ps with the prism stretcher and had an intensity of 5×10^{10} W/cm^2. The 800 nm pulses were again used for the probe, with a pulse duration of $\sim$ 50 fs and an intensity of 7×10^{13} W/cm^2. Both the pump and the probe pulses were linearly polarized parallel to the detector plane. As the vibrational dynamics of Rb_2 are much faster than the rotational dynamics, the experiment was conducted with a step size of 250 fs for the pump-probe delay, which is much shorter than the step size that was used while recording the alignment traces. Once again, the detector was gated on the most abundant isotope, $^{85}Rb^+$.

9.3 Results

The pump-probe delay was scanned from t = 0 ps to t = 100 ps. The result of the scan is a series of Rb^+ VMI images, which can all be individually Abel inverted to extract the $P(E_{\text{kin}})$ distribution for the Rb^+ ions at each time step, giving results similar to that shown in Fig. 5.3(d2). A Gaussian function is then fitted to the $P(E_{\text{kin}})$ peak associated with the $1^3\Sigma_u^+$ state of Rb_2 to determine the central peak position E_{peak} for the given pump-probe delay. Finally, the E_{peak} values are converted to internuclear distances

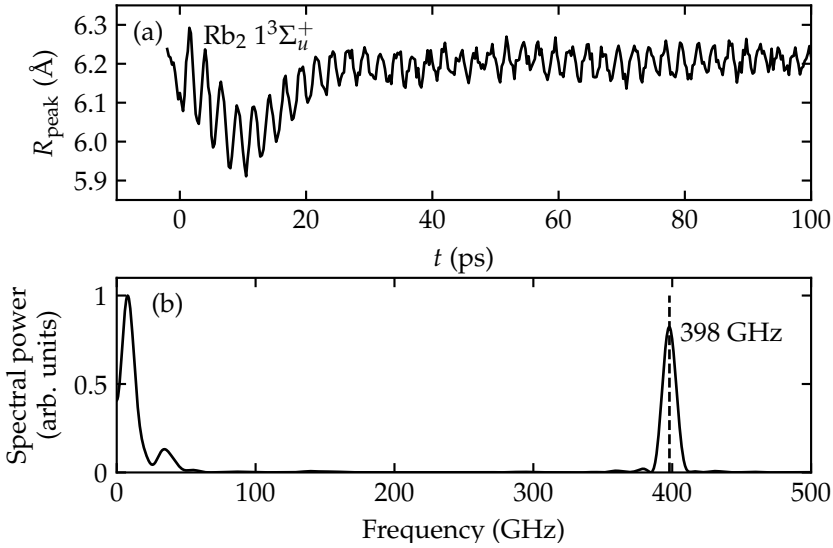

Figure 9.4: (a) Vibrational trace recorded for Rb_2 in the $1^3\Sigma_u^+$ state, derived from the central position of the $1^3\Sigma_u^+$ peak in the $P(E_{kin})$ distributions for Rb^+ as a function of the pump-probe delay t. (b) FFT of the trace in (a), showing one dominant frequency at 398 GHz.

R_{peak} by applying Coulomb's law.

The R_{peak} values are presented as a function of the pump-probe delay in Fig. 9.4(a). The curve exhibits a clear rapidly oscillating structure, which indicates that the $1^3\Sigma_u^+$ state dimers are indeed set into vibration by the alignment pulse. In this particular measurement series the determined pump-probe overlap time t_0 was a bit off [not corrected in Fig. 9.4(a)], so unfortunately no data was recorded where the probe pulse arrived before the pump pulse. Other measurements (not shown), however, clearly demonstrate that the oscillations in R_{peak} start when the alignment pulse irradiates the dimers.

During the first 20 ps, R_{peak} undergoes a large shift from around 6.2 Å to 6.0 Å, while the fast oscillations are occurring. The shift coincides in time with the prompt alignment peak seen in the alignment trace in Fig. 8.4(c1), suggesting that it may be due to some alignment-dependent probing effect. Nothing further is known about this shift at the moment of writing. The rapid oscillations have an amplitude of around 0.12 Å at the beginning

of the trace, which quickly diminishes to an amplitude of around 0.04 Å after about 20 ps. The driving mechanism behind this quick loss of amplitude is also not understood at the moment but is presumably due to some coupling to the droplet. For the rest of the trace, the amplitude remains somewhat constant with no significant decay.

To identify the vibrational levels populated in the wave packet, I have made a spectral analysis of the vibrational trace, see Fig. 9.4(b). Only a single prominent peak is observed in the frequency spectrum. According to a Gaussian fit, the peak is centered at 398 GHz, which corresponds to a vibrational period of 2.51 ps. This fits the vibrational period of 2.52 ps for a wave packet consisting of $v = 0$ and $v = 1$ in isolated $1^3\Sigma_u^+$ state Rb_2, according to my solutions to the stationary vibrational 1D Schrödinger equation using a potential curve for the dimer from the literature [107]. The result also matches the vibrational period of 2.50 ps previously reported for the $v = 0$–1 coherence in $1^3\Sigma_u^+$ state Rb_2 on helium droplets measured using photoionization spectroscopy [201]. Based on this, I conclude that the nonadiabatic alignment pulses used to set the dimers into rotation on the helium droplet surfaces also create vibrational wave packets.

I also analyzed the $1^1\Sigma_g^+$ state channel in the Rb^+ VMI images. In this case, no oscillations are observed, indicating that only the $1^3\Sigma_u^+$ state dimers are set into vibration by the alignment pulse. The vibrational period for a wave packet in the $1^1\Sigma_g^+$ state consisting of $v = 0$ and $v = 1$ is only 0.572 ps according to my calculations for the isolated dimer, again obtained by solving the Schrödinger equation with a potential from the literature [142]. Since the 0.8 ps pulse duration of the alignment pulse is longer than the vibrational period, the $1^1\Sigma_g^+$ state dimers can adiabatically follow the change in the potential caused by the laser field, leaving them in their original state after the field switches off. This explains why no vibrations are present for the $1^1\Sigma_g^+$ state dimers.

Similar measurements (not shown) on Na_2 and K_2 have been conducted in the group. The findings in these experiments are the same as for Rb_2. Vibrational wave packets, again only containing significant population in $v = 0$ and $v = 1$, can be created in the

$1^3\Sigma_u^+$ state dimers due to the interaction with the alignment pulse. However, the vibrations are faster since Na_2 and K_2 are lighter than Rb_2. To more efficiently create the wave packets the pulse duration was therefore decreased to ~ 0.6 ps for these measurements. As for Rb_2, the observed vibrational periods of the wave packets match that expected for the isolated dimers. This was also the conclusion in previous experiments on vibrational wave packets of Na_2 and K_2 (in the $1^1\Sigma_g^+$ state) on helium droplets [90, 91]. Concerning the $1^1\Sigma_g^+$ states of Na_2 and K_2, the vibrational periods are still much shorter than the used pulse duration, so wave packets are not formed.

9.4 Discussion

The observed vibrations for the $1^3\Sigma_u^+$ state dimers are interesting in the context of the rotational dynamics presented in Chapter 8. It is striking that the dimers vibrate with essentially the gas-phase frequencies, in stark contrast to the rotations which are strongly affected by the droplet surface, see Fig. 8.3(a2)–(c2) and Fig. 8.4(a1)–(c1). Furthermore, the rotational wave packets were observed to decay rather quickly, especially for Rb_2, which does not appear to be the case for the vibrations. People have speculated that perhaps the vibrating alkali dimers desorb from the helium droplets within a few picoseconds and therefore vibrate as isolated molecules [90, 91, 201–203]. This can however be excluded in the experiments shown here since the vibrations take place at the same time as the strongly affected rotations. It thus appears that the vibrational motion for some reason couples much weaker to the droplet than the rotational motion but the explanation is not clear at the moment.

It is also interesting to address whether the vibrational motion of the $1^3\Sigma_u^+$ state dimers significantly affects the rotational frequencies. Upon excitation from $v = 0$ to $v = 1$, the internuclear separation in the dimers changes due to the anharmonicity of the $1^3\Sigma_u^+$ state potentials [107]. This affects the moment of inertia and thus also the rotational constant B. For Rb_2 in the $1^3\Sigma_u^+$ state, the change in the value of B is only 1% [201], so this will not

have any pronounced effect on the rotations[25]. The difference should likewise be small for Na_2 and K_2 in the $1^3\Sigma_u^+$ state where we know that we also only excite $v = 1$. If the alignment pulse could excite the dimers to higher-lying vibrational states, things would change. Again using Rb_2 in the $1^3\Sigma_u^+$ state as the example, the value of B for a dimer excited to $v = 5$ would be reduced by around 7% compared to $v = 0$ [201]. A difference that large would definitely be noticeable in the rotational dynamics, but fortunately the alignment pulse does not excite such high-lying vibrational states.

Since the full $P(E_{\text{kin}})$ distributions of the Ak^+ ions are recorded for each pump-probe delay in the experiments, it is possible to do time-resolved wave function imaging of the vibrational wave packet by applying the steps presented in Section 5.3.3. Such a reconstruction of $P(R,t)$ for a vibrational wave packet has previously been demonstrated via timed Coulomb explosion imaging of H_2^+ and D_2^+ vibrations [149, 206], and also via timed electron diffraction for vibrations in I_2 [207]. Ideally, the distributions obtained from our measurements can then be compared to simulations of the vibrational wave packet motion obtained by solving the Schrödinger equation for the dimers and their interaction with the alignment pulse. This analysis, including the theoretical simulations, is handled by Nicolaj Jyde, and I will therefore not present the results here.

9.5 Conclusion

To conclude, I have shown that vibrational wave packets can be formed in $1^3\Sigma_u^+$ state Rb_2 on the surface of helium droplets by the same nonresonant laser pulses used to align the dimers nonadiabatically. A wave packet consisting of a superposition of $v = 0$ and $v = 1$ was measured by timed Coulomb explosion and found to oscillate with a period matching that expected for the isolated molecule. In addition, the amplitude of the vibrations exhibited no significant decay on the time scale of the measurement. An analysis of Rb_2 in the $1^1\Sigma_g^+$ state found no vibrations,

25 Admittedly, this is a somewhat bad example since we do not observe any rotational dynamics for Rb_2 in the $1^3\Sigma_u^+$ state in our experiments after the prompt alignment peak [see Fig. 8.4(c1)].

indicating that the pulse durations are too long to excite those dimers vibrationally. Measurements done by others in the group show that the conclusions for Rb_2 also apply to Na_2 and K_2 on helium droplets.

For Rb_2 in the $1^3\Sigma_u^+$ state, excitation to $v = 1$ only changes the rotational constant by 1%. The vibrational dynamics are therefore of no significant consequence to the simultaneous rotational dynamics. Similarly, the effect for Na_2 and K_2 in the $1^3\Sigma_u^+$ state must be small.

10

3D VELOCITY MAP IMAGING OF ALKALI IONS

To enable the next generation of ion imaging experiments, the CCD camera used for recording the hits on the MCP has been replaced with a Tpx3Cam detector toward the end of my PhD studies. The 1.6 ns time resolution of the Tpx3Cam detector makes it possible to record velocity map images simultaneously for ions with different mass-to-charge ratios, making it a significant upgrade to the old CCD camera. Additionally, the time resolution is sufficient to enable 3D velocity map imaging of the ions. This removes the need for Abel inversions and vastly increases the amount of information that can be extracted from the experiments, including the future possibility of directly determining the degree of alignment $\langle \cos^2 \theta \rangle$ without the 2D projection.

In this chapter, I will first give a brief introduction to the Tpx3Cam detector and show how 3D imaging can be obtained, including necessary corrections to the raw data from the Tpx3Cam. After that, I will present results from static Coulomb explosion of alkali dimers on helium droplets, the same experiment as in Chapter 5 but this time recorded with the Tpx3Cam. The data, now in 3D, reveal a deflection in the Ak^+ trajectories due to interaction of the recoiling Ak^+ ions with the helium droplets. I find that the deflections in particular depend on the fragment velocities and the size of the helium droplets. In an attempt to extract the droplet size distribution from the deflection measurements, the results are compared to TDDFT calculations. Finally, I demonstrate that the Ak^+ deflections enable studies of the parent alkali dimers' locations on the helium droplets, paving the way for location-resolved studies of Ak_2 dynamics on droplets.

10.1 Principle of the Tpx3Cam detector

The Tpx3Cam detector is an event-based detector, where each pixel in the 256×256 pixel grid acts as an independent sensor [171]. Instead of reading out the status of each pixel at given

time intervals, like an ordinary camera, it only registers the x and y positions of pixels that are triggered, as well as the time they get triggered (called the *time-of-arrival*, ToA) and for how long (called the *time-over-threshold*, ToT). Commonly, ToA is just called ToF since the only difference is a small constant offset due to the response time of the MCP stack and the phosphor screen. As the following sections become somewhat technical, I will adhere to the accurate terminology and call it ToA, before later switching back to calling it ToF.

The 1.6 ns time resolution of the electronics makes it possible to separate hits from ions with different mass-to-charge ratios based on their different ToA [138, 170–172, 208]. With the Tpx3Cam, it is therefore no longer necessary to gate the MCP since all the different ions are recorded at once and then separated in the analysis afterward. This was utilized in the experiment with the heteroalkali dimers in Chapter 6.

The ToA of the ions is, however, not only determined by their mass-to-charge ratios but also by their velocities. If the ions formed in the experiments are created with some velocity in the direction toward the detector, their ToA will be slightly reduced. Meanwhile, if the ions initially fly away from the detector, their ToA will be slightly increased because the ions must first turn around in the extraction field, before heading to the detector. It has recently been demonstrated that if the ToA is determined precisely enough, then it is possible to extract the component of the velocity that lies perpendicular to the detector plane, that is, the v_x velocity component that is normally lost in 2D velocity map imaging (see coordinate system in Fig. 10.7) [172, 182, 209, 210]. In a few cases, this has even been achieved for electrons [211, 212].

Unfortunately, the ToA value read out from the Tpx3Cam is not accurate enough from the get-go to do 3D imaging. To understand why this is, it is necessary to look at how the pixels respond to being hit by light. The pixels work as constant threshold discriminators, which means that the pixels register an event once the signal from the light crosses the threshold value, see Fig. 10.1. The crossing time is what is registered as the ToA. However, no matter how strong the signal is, the rise time is the same, and as a consequence, two signals starting at the same time can be

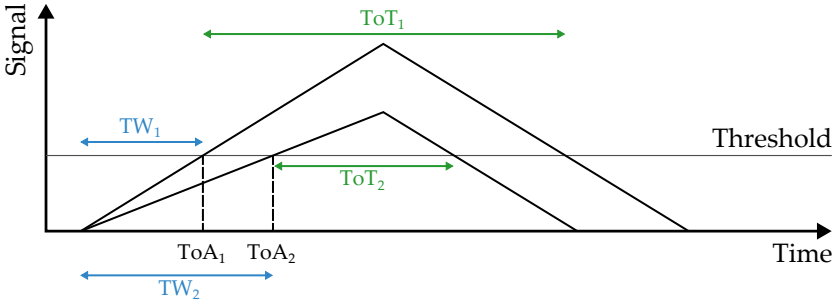

Figure 10.1: Sketch illustrating the time-walk effect for two different signals. A larger signal has a longer ToT but a smaller time-walk (TW). Figure inspired from [138, 213].

registered as having different ToA. The difference in the detected ToA and the true ToA, which is when the light starts to appear at the pixel, is known as the *time-walk* [138, 213]. As shown in Fig. 10.1, the size of the time-walk is smaller for pixel events with higher signal levels.

It turns out that while the rise time of the signal is always the same, the discharge is happening at a constant rate. Thus, an event with a high signal level will keep the pixel triggered for longer than an event with a low signal level, see Fig. 10.1. This leads to a correlation between the registered ToT values and the size of the time-walk, which can be exploited to make corrections that drastically improve the ToA values [138, 213].

10.1.1 *Demonstration of ToA corrections*

Since the time-walk effect is due to the pixel response itself, it is independent of the studied ion species. ToA correction curves can therefore be determined using any ion signal available in the experiments. We typically use the strong H_2O^+ signal that is always present due to ionization of residual H_2O in the vacuum chamber.

Figure 10.2(a) shows a 2D histogram, represented as a color map, for the pairs of ToA and ToT values in the range that corresponds to the H_2O^+ signal. The figure clearly illustrates that events with a high ToT value tend to have an earlier ToA, as expected due to the time-walk effect. As a first step toward a

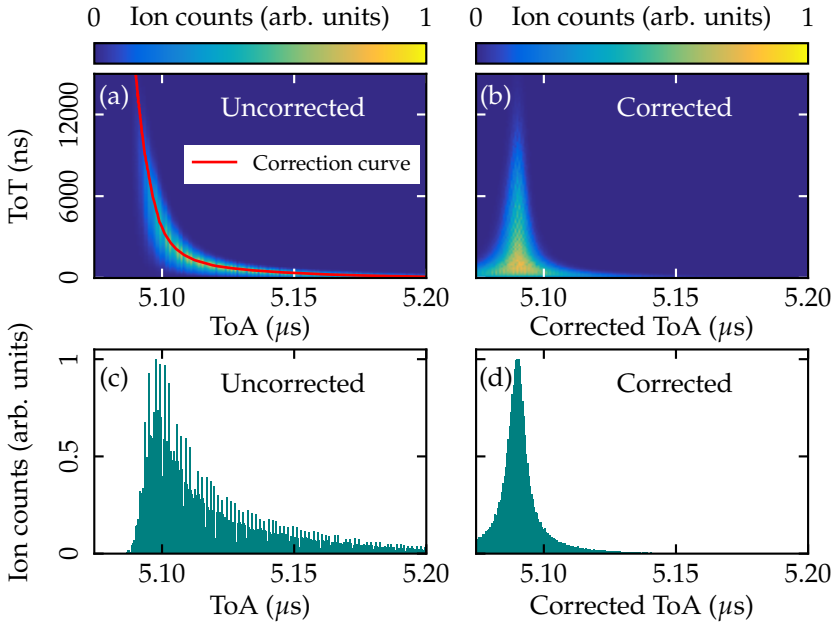

Figure 10.2: Example of a precorrection of raw data from the Tpx3Cam. (a) 2D histogram, visualized as a color map, for the pairs of ToA and ToT values in the raw data that are associated with H_2O^+, illustrating a clear dependency due to time-walk. The red curve shows the determined precorrection curve. (b) 2D histogram of the H_2O^+ data after correcting the raw values in (a) with the correction curve. (c) and (d) 1D histograms of the raw and corrected ToA data for H_2O^+. The uneven stripes in (c) appear due to uneven binning of the raw data.

correction, the mean ToA is found for each ToT bin in the data. Those mean values make up the correction curve, which is also shown in Fig. 10.2(a). Since the time-walk effect is smallest for the bin with the highest ToT values in the data, the mean ToA for that bin is assumed to be the true mean ToA. To correct the data in the other ToT bins, the ToA values of the individual events must be shifted by the difference between the mean ToA for the corresponding ToT bin (represented by the correction curve) and the assumed true mean ToA. Doing so gives the result shown in Fig. 10.2(b), where the mean ToA in each ToT bin now all lie at the same value. I will refer to this correction as the *precorrection* because it is done before any other processing of the

raw data. Figure 10.2(c) and (d) show 1D histograms of the ToA data before and after the precorrection. After the correction, the peak is much more symmetric and narrow, which better reflects what is expected for ions created from residual H_2O. Note that only one correction curve is determined and used to correct the measurements from all the pixels. In principle, the response may vary from pixel to pixel, but this is hard to accommodate for in my experiments since the signal is generally quite unevenly distributed across the detector, causing a lack of useful signal in some regions.

In the next paragraphs, I will demonstrate that the precorrection alone is unfortunately not enough to get rid of the time-walk effect in our data. The reason for this is due to the next step in the overall data analysis. Whenever an ion hit is registered by the Tpx3Cam, a group of pixels will register the signal, in the same way as for the CCD camera (see Section 4.3.1). The precorrected data must therefore be centroided, which is done in two steps. First, the clusters of pixels related to the same ion hit are identified with the DBSCAN algorithm [137]. Next, the averages of the x, y, and ToA values for the pixels in the clusters are found, using the ToT values as weights, since the ToT gives a measure for the intensity of the light that hits the pixel. It is not clear what is the most meaningful way to assign a single ToT value to the clustered hit. Currently, the highest ToT value present in the cluster is used.

Figure 10.3(a) displays a 2D histogram of the ToA and ToT values for the now centroided data. Once again, a systematic dependency is observed between the ToA and ToT values. The dependency can be removed again by doing a second round of corrections, referred to as the *postcorrection*, in the same way as for the precorrection, see Fig. 10.3(b). Why the postcorrection becomes necessary is uncertain, but it has also been observed by another group in the scientific community [172].

The distribution of ToA values, after this routine of precorrecting, centroiding, and then postcorrecting the data, is shown in Fig. 10.3(d). The peak is very symmetric, and the resolution is now high enough to make 3D velocity map imaging feasible. As mentioned earlier, the corrections are due to the pixel response, and the correction curves obtained for H_2O^+ can therefore be

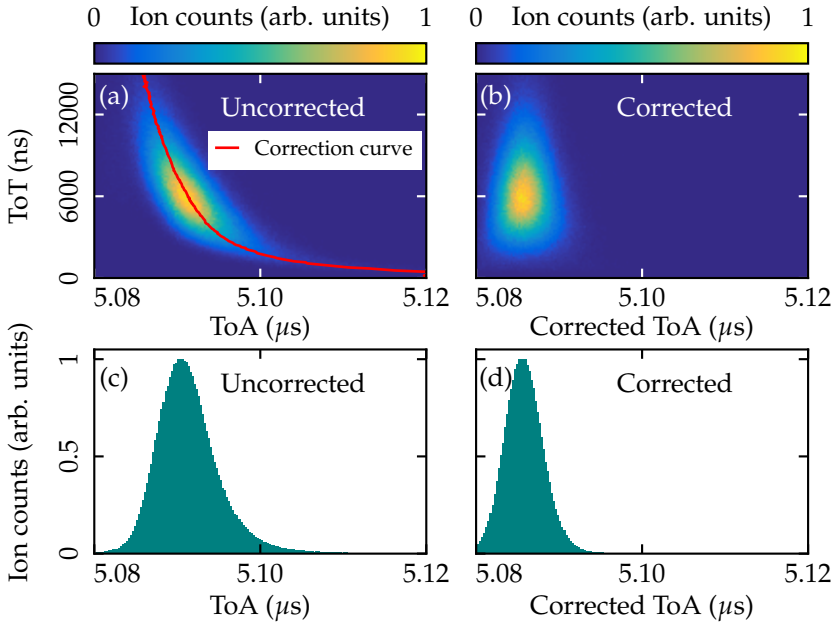

Figure 10.3: Example of a postcorrection of already precorrected and centroided data from the Tpx3Cam. (a) 2D histogram, visualized as a color map, for the pairs of ToA and ToT values in the H_2O^+ data, illustrating that some time-walk effect has re-emerged after centroiding the precorrected data. The red curve shows the determined postcorrection curve. (b) 2D histogram of the data after postcorrecting the data in (a) with the postcorrection curve. (c) 1D histogram of the precorrected and centroided ToA data. (d) Postcorrected version of the data in (c).

used to correct all the data acquired with the Tpx3Cam, including the signal from Ak^+ ions. The correction curves are usually redetermined from day to day to make them as accurate as possible, in case there is any fluctuation in the pixel response over longer time periods.

10.1.2 *Conversion from ToF to v_x*

I will now return to the ordinary use of ToF instead of ToA, to emphasize the physics in the experiments again.

As briefly mentioned earlier, the ToF of each ion contains information about their v_x velocity component, that is, their velocity

along the ToF-axis. The task is now to establish a relationship between the ToF values and the values of v_x, so a calibration must be made. To do this, a ToF spectrum must be recorded for ions with a known velocity in the v_x direction. I achieve this via an experiment with Coulomb explosion of gas-phase I_2, as detailed in the following.

A molecular beam of gas-phase I_2 is created with the Even-Lavie valve (see Section 4.1.4). The beam is then crossed in the center of the VMI spectrometer by a laser beam consisting of linearly polarized, intense $\sim$ 50-fs pulses centered at 800 nm. The pulses multiply ionize I_2, leading to Coulomb explosion into I^++I^+ or I^++I^{2+}. The atomic iodine ions are detected with the VMI spectrometer using the Tpx3Cam. In this experiment, the ionization probability is much higher when the internuclear axis of I_2 is parallel to the laser polarization axis. Thus, the ejection direction of the ions can, to some extent, be controlled by selecting the polarization axis. I exploit this to first record a velocity map image where the ions are primarily ejected in the detector plane, and then an image where the ions are primarily ejected perpendicular to the detector plane, along the ToF-axis.

Figure 10.4(a) and (b) show the 2D velocity map images for I^+ ions recorded with the probe polarization parallel and perpendicular to the plane. No beam block was mounted in front of the detector for these measurements because I^+ ions with large v_x velocity components will land close to the center of the image. A strong unwanted signal was however present in a confined region in the center. I have therefore removed the data in a small square region from the images and the further analysis.

The ToF distributions of the I^+ ions that constitute the images are shown in Fig. 10.4(c) and (d), respectively. The angular anisotropy of ejected I^+ ions is clearly visible in Fig. 10.4(a) and the ToF distribution, Fig. 10.4(c), follow a bell-shaped distribution. When the polarization is rotated the ion image becomes more isotropic, as shown in Fig. 10.4(b), but the ToF distribution, Fig. 10.4(d), splits into six peaks. These peaks have previously been assigned in the literature as I^+ ions from the I^++I^{2+} Coulomb explosion channel [annotated as (2), indicating the charge of the partner iodine fragment], the I^++I^+ Coulomb explosion channel [annotated as (1)], and various dissociative channels [annotated

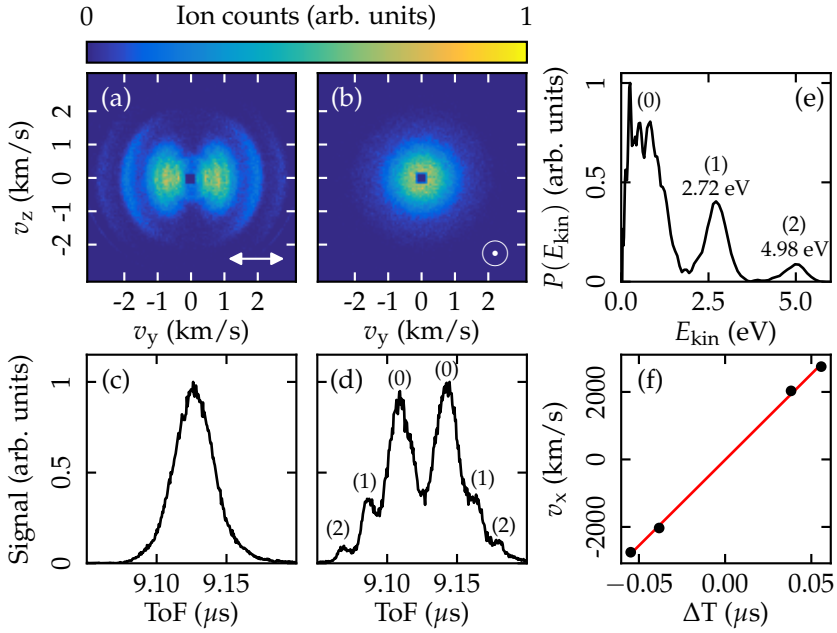

Figure 10.4: (a) and (b) 2D velocity map images of I^+ ions recorded with the probe polarized in the plane (a) and perpendicular to the plane (b). The polarizations are also indicated with the annotated white ↔ and ⊙ symbols. (c) and (d) ToF distributions for the I^+ ions in the ion images in (a) and (b). (e) $P(E_{kin})$ distribution for the ions in (a). (f) Linear fit to obtain a relationship between the v_x velocities of the ions and their ToF values relative to the center of the distribution in (c). The peaks in (d) and (e) are labeled with the charge of the partner iodine fragment.

as (0)] [214]. The ions with ToF values lower than the mean ToF are the ones ejected toward the detector (positive v_x), while the ions with a ToF larger than the mean are ejected away from the detector (negative v_x).

To enable the assignment of velocities to the ToF peaks in Fig. 10.4(d), the $P(E_{kin})$ distribution of the ions in Fig. 10.4(a) is determined via a standard 2D calibration [see Appendix A]. The obtained $P(E_{kin})$ distribution, shown in Fig. 10.4(e), exhibits three peaks. By symmetry, these can also be assigned to the dissociative channels and the Coulomb explosion channels. From the central positions of the Coulomb explosion peaks, the velocities of the I^+ ions are calculated. A calibration fit is then made

to these velocities as a function of the associated ToF-shifts ΔT with respect to the center of the distribution in (c), which should correspond to I^+ ions with $v_x = 0$. This is shown in Fig. 10.4(f). I use a linear fit since SIMION simulations that I have conducted indicate that this should be appropriate for our specific VMI setup. Other groups have also studied this and likewise found that the calibration curve is to a good approximation linear [211].

Finally, using classical laws of motion it is possible to show that the velocity of the ions only matters for the ToF in the region between the repeller and the extractor. One can also calculate that the shift in ToF, due to the v_x velocity, scales with m/q. When the found calibration is applied to other ions, it must therefore be scaled accordingly.

To showcase the viability of the calibration, I have used it to determine the v_x velocities of the I^+ ions and plotted the 3D velocity map images, see Appendix D. The images demonstrate that the v_x velocity component is properly retrieved when using the found calibration function. I have not estimated how the temporal resolution, and thus the resolution of v_x, compares to the spatial resolution. It is, however, known from the literature that the temporal resolution is generally at least an order of magnitude worse, especially for light ions [172]. Because of this, it is still better to Abel invert the ordinary 2D images if one wants to accurately determine for example the distribution of kinetic energies $P(E_{kin})$ of the fragments. Nonetheless, actually knowing the 3D velocity of the individual fragments, even if somewhat less precise for the v_x component, is still a major advantage that enables many new experiments. In the next sections, I will demonstrate how it can be used to extract even more information from my Coulomb explosion experiments.

10.2 Deflections of Ak^+

In the vast amount of studies done in the last few decades on Coulomb explosion of molecules, there has been a clear trend: The Coulomb explosion technique has been used to obtain information about the probed molecules themselves. I will stray from this course now, and investigate a different question: Can Coulomb explosion of a molecule be used to study the properties

of a different object in the vicinity of the molecule?

I therefore return to the static Coulomb explosion measurement of homonuclear Ak_2 on helium droplets that I already presented in Chapter 5. This is an example of exactly such a scenario, where a small molecule is probed next to a much larger helium droplet. There, I found that the widths of the angular covariance lines were much larger than what is typically observed for Coulomb explosion of diatomic systems in gas-phase. Briefly, I mentioned that this indicated an interaction with the droplet, which affected the direction of the ejected Ak^+ ions. I will now describe why these deviations arise, and show how it can be more quantitatively investigated with the Tpx3Cam.

The moment an Ak^+ ion is formed at the surface of a helium droplet, it will experience an attractive force that will pull the ion toward the droplet interior. This is known both theoretically and from experiments [94, 215–218], including a recent result from our group where the solvation process of a single Na^+ ion on a helium droplet was studied in a time-resolved experiment [219]. The consequence of this attractive force in my Coulomb explosion experiments on Ak_2 is that as the two Ak^+ ions repel each other they simultaneously both get pulled toward the surface of the droplet, as illustrated in Fig. 10.5. Because Coulomb explosion proceeds very quickly, the Ak^+ fragments however leave the vicinity of the droplet before they hit the surface and start solvating. The result is a deflection of the trajectories of the Ak^+ fragments, which explains the broad lines in the angular covariance maps in Fig. 5.3[26]. It should be noted immediately that the scenario will depend on the orientation of the dimer on the surface. If the dimer stands at a large angle on the surface, one Ak^+ ion will recoil into the droplet, changing the outcome. However, as known from Fig. 8.6, the dimers typically lie quite parallel to the surface, especially for K_2 and Rb_2. These are the systems I will be focusing on in this section.

The deflection of each Ak^+ ion should depend on how long

26 Due to the way the emission angles of the Ak^+ fragments are determined in the ion images, the deflections will lead to a symmetric broadening of the angular covariance lines. Additionally, since the deflections make it less likely to observe two Ak^+ ions with 180° difference in the emission angle, the covariance should be lower along the middle of the angular covariance lines. This is visible to the trained eye in Fig. 5.3(d4) for Rb_2 in the $1^3\Sigma_u^+$ state.

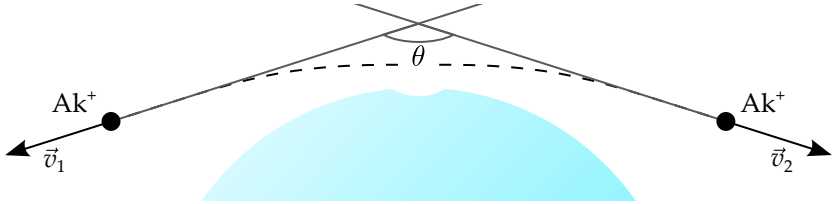

Figure 10.5: Illustration of the deflection of Ak^+ ions created from Coulomb explosion of Ak_2 at the surface of a helium droplet, assuming the dimer was sitting parallel to the surface. θ denotes the final angle between the velocity vectors $\vec{v}_1$ and $\vec{v}_2$. The trajectories of the ions are marked with dashed lines.

the ion interacts with the nearby helium environment. If the droplet is large, it will take longer for the recoiling ions to fly far enough away tangentially to leave the influence of the droplet potential, compared to a smaller droplet. Similarly, faster ions will be influenced by the droplet for a shorter time duration than slower ions. As a consequence, Ak^+ ions created from Coulomb explosion of a $1^1\Sigma_g^+$ state dimer should deflect less than Ak^+ ions from the corresponding $1^3\Sigma_u^+$ state dimer, because the energy release, and thus the velocities of the fragments, are larger for the $1^1\Sigma_g^+$ state dimers. Furthermore, Ak^+ ions from the lighter alkali dimers will generally have larger velocities than Ak^+ ions from the heavier alkali dimers due to the lower mass of the fragment ions, but also because the released Coulomb energy is lower for the heavier dimers, see Table 5.1. Based on these factors, the deflections should therefore be most pronounced for the heavier alkalis. The strength of the attractive force exerted on the ions, however, depends on the alkali species, and will also impact the deflections. The depth of the $V_{Ak^+–He}$ potentials increases when going to lighter alkalis [218], which will typically lead to a larger force and thereby a much larger acceleration due to the lighter mass. In addition, the lighter alkalis sit closer to the helium droplet surface than the heavier alkalis, and the $1^1\Sigma_g^+$ state dimers sit closer than the $1^3\Sigma_u^+$ state dimers. This can be inferred from Fig. 10.6 which shows the perpendicular distance between the alkali dimers and the surface (with an unknown offset), calculated by Robert Zillich in relation to the calculations

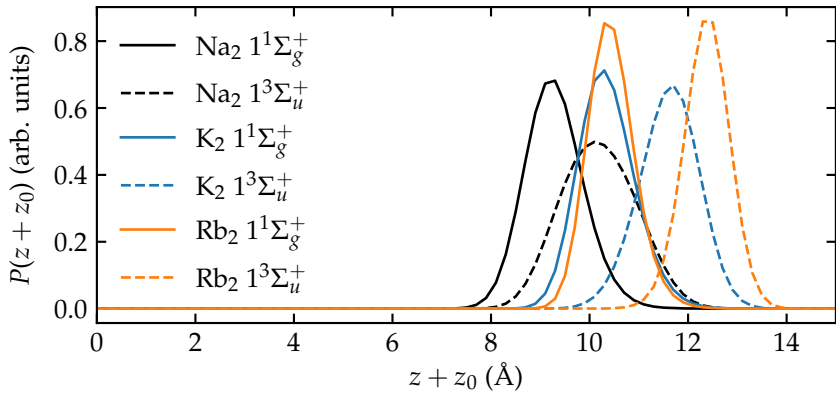

Figure 10.6: Center of mass distributions of the alkali dimers as a function of the perpendicular distance $z + z_0$ from the surface of the helium droplet, with z_0 being an unknown offset. z_0 is the same for all dimers, enabling relative comparison. The calculations were done by Robert Zillich (private communication).

he made for the modeling of Ak_2 rotations on the droplets (see Section 8.2.2). These additional factors point to larger deflections for lighter alkalis than for the heavy alkalis, and can potentially somewhat balance the effects of the different velocities from the Coulomb explosions.

In itself, it is interesting to investigate how the various factors influence the deflections and I will do so. However, perhaps most interesting of all is whether the deflections of a pair of Ak^+ ions can be used to estimate the size of the droplet the parent dimer resided on. If so, the droplet size distribution present in the experiments can potentially be extracted from a distribution of deflection angles obtained from many Ak^+ ions. This would be an innovative application of the Coulomb explosion technique since the Coulomb explosion of Ak_2 is then used to probe the size of the nearby droplet. Finding good ways to determine the experimental droplet size distribution is also something the helium droplet community has struggled with for many years, making the possible results even more interesting.

To investigate the deflections thoroughly, the static Coulomb explosion measurements are repeated, this time with the Tpx3Cam detector, such that the 3D velocity of the Ak^+ ions can be recorded. Figure 10.7 illustrates the experiment once again. This was done

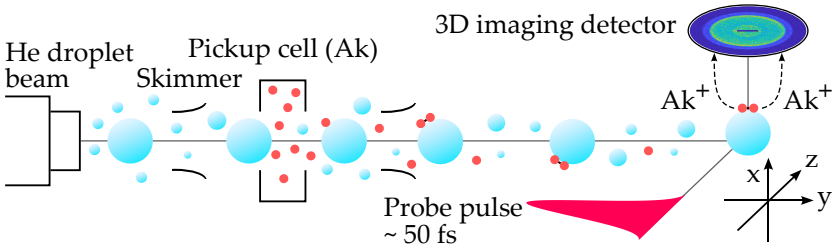

Figure 10.7: Sketch of the repeated experiment with static Coulomb explosion of Ak_2 residing on the surface of helium droplets, this time done with 3D imaging via the Tpx3Cam. Own work, adapted from [124].

on the machine that was also used for the heteroalkali dimer experiments presented in Chapter 6. The stagnation pressure of the helium was set to 50 bar, and the nozzle temperature varied from 14 to 22 K, producing droplets with an estimated mean size of 4000–10000 He atoms (see Fig. 2.2). The droplets were doped with either K_2 or Rb_2 using samples heated to 90 °C and 65 °C, respectively. As for the experiments shown in Chapter 5, the dimers were probed with a $\sim$ 50 fs pulse linearly polarized in the detector plane, centered at 400 nm for K_2 and at 800 nm for Rb_2. The intensity was 1×10^{14} W/cm^2 for the 400 nm pulses and 2×10^{14} W/cm^2 for the 800 nm pulses. Note that the ion images were recorded without the beam block to enable the measurement of ions with large v_x velocity components, as also discussed for the calibration experiment with I_2 in Section 10.1.2. Jeppe Kjædegaard Christensen kindly conducted the measurements to be shown while I was on secondment.

The first step in the treatment of the recorded data is to perform the pre- and postcorrection routines explained in Section 10.1.1. After that, the v_x velocities of the Ak^+ ions can be determined from the individual ToF values by applying the calibration function (see Section 10.1.2), such that all three velocity components of the ions are known. To retrieve information about the deflections, it is now necessary to identify pairs of Ak^+ ions that originate from the same parent dimer. I therefore first isolate the ions that come from either $1^3\Sigma_u^+$ state dimers or $1^1\Sigma_g^+$ state dimers, based on the kinetic energies of the individual ions which are directly available from the 3D velocities. Next, I apply a coincident filter

to the isolated data, akin to what was done in the analysis of the heteroalkali dimers in Section 6.2.1. This time, however, the filtering is based on the kinetic energies of the fragments, instead of directly on the velocity components of the ions. This is crucial to avoid biasing the results because I do not know how much the ion trajectories will be affected by the deflections, or in which direction in space. I can therefore not make any claims about which directions partner ions should move in. The energies should still be similar though, since the interaction with the droplet is quite symmetrical for two fragments that originate from a parent dimer residing (roughly) flat at the surface. Finally, the angle θ between the 3D velocities of identified pairs of Ak^+ ions is determined by taking the inner product of the two vectors. Since the value of interest is how much the Ak^+ are deflected away from their unperturbed trajectories, I will in the following parts use the term *deflection angle* to refer to $180° - \theta$, that is, the deviation in angle from perfect axial recoil.

Figure 10.8(a1)–(a5) shows the distribution of deflection angles for pairs of Rb^+ ions from $1^3\Sigma_u^+$ state Rb_2, measured for different nozzle temperatures. The corresponding distributions from $1^1\Sigma_g^+$ state dimers are shown in Fig. 10.8(b1)–(b5). To obtain these results, I used quite a large energy tolerance of 200 meV for the filtering. A more narrow tolerance could be used, but it also comes with a risk of discarding real ion pairs, if there are scenarios where the ion energies are vastly different. I have analysed the data with different tolerances and the results are generally quite robust with no big deviations for smaller or larger tolerances. To estimate the number of false ion coincidences that pass through the filter, one can look at the number of counts at the deflection angles far from where the main part of the distributions in Fig. 10.8 are located. False coincidences should have no correlation in the angles, and therefore be evenly distributed across all θ values. As the measured distributions go nicely to essentially 0, with the amplitude of the noise level below 2% of the number of counts at the most observed deflection angles, the number of false coincidences is very small.

To characterize the distributions in Fig. 10.8, I fit with a log-normal curve with the general form [220]

$$f(x) = \frac{1}{x\delta N}\exp\left[-\frac{(\ln x - \mu)^2}{2\delta^2}\right], \tag{10.1}$$

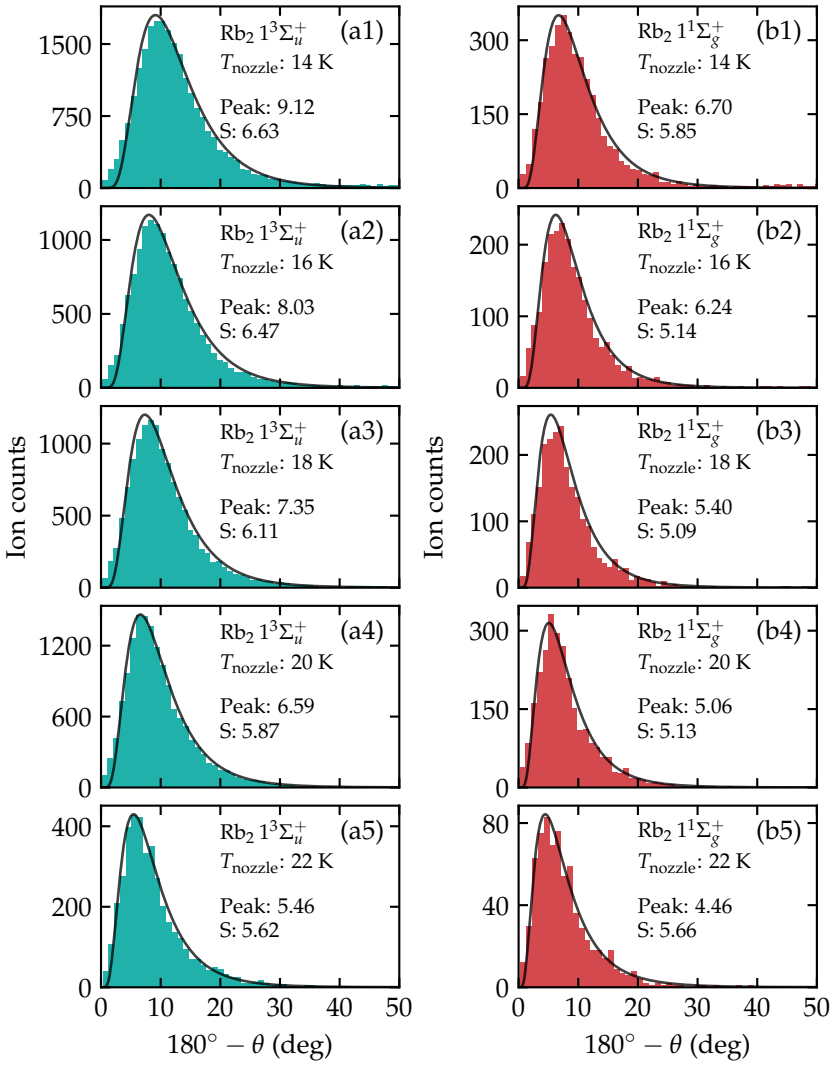

Figure 10.8: (a1)–(a5) Distributions of the deflection angles, defined as $180° - \theta$, for pairs of Rb^+ ions from Rb_2 in the $1^3\Sigma_u^+$ state on droplets formed with various nozzle temperatures (see annotations on panels). The black lines illustrate log-normal distributions fitted to the data. The peak positions and the standard deviations S of the distributions are annotated on the panels. (b1)–(b5) Same as for (a1)–(a5), but this time for Rb^+ ions from Rb_2 in the $1^1\Sigma_g^+$ state.

where $x = 180° - \theta$ and N, μ, and $\delta > 0$ are parameters to be determined by the fit. The found fits are shown with black lines in Fig. 10.8, and generally capture the shape of the distributions

very well. The position of the peak (also known as the *mode*) can be calculated as [220]

$$x_{\max} = \exp\left(\mu - \delta^2\right), \tag{10.2}$$

and the standard deviation as

$$S = \exp\left(\mu + \frac{\delta^2}{2}\right)\sqrt{\exp\left(\delta^2\right) - 1}. \tag{10.3}$$

The peak positions and the standard deviations extracted from the fits are annotated on the panels in Fig. 10.8. Several trends can be observed in these values. First of all, when the nozzle temperature is increased, and the mean droplet sizes thereby decreased, the peak positions shift to lower values. This makes sense, since smaller droplets lead to a shorter interaction time between the droplet and the Rb^+ ions, resulting in less deflection. When the mean droplet size becomes smaller, the width of the droplet size distribution also decreases (see Section 2.2). As a consequence, the width of the deflection distributions, here characterized by the standard deviation, should also decrease. This is observed for the $1^3\Sigma_u^+$ state results in Fig. 10.8(a1)–(a5). For the $1^1\Sigma_g^+$ state results, Fig. 10.8(b1)–(b5), the widths do not monotonically decrease, but fluctuate a bit. This might be due to slightly poor fits not fully capturing the shape of the distributions. Especially the fits in Fig. 10.8(b3) and (b4) appear to be a bit off, as they do not capture the peak positions very accurately.

Direct comparisons between the $1^3\Sigma_u^+$ state results and the corresponding $1^1\Sigma_g^+$ state results recorded with the same nozzle temperature show that the distributions are wider and peak at larger deflections for the Rb^+ ions from $1^3\Sigma_u^+$ state Rb_2. This matches the expectations since the velocities are lower for Rb^+ ions originating from the $1^3\Sigma_u^+$ state dimers, so these should deflect more.

I have also conducted the analysis for the experiments with K_2, here using an energy tolerance of 200 meV for the coincident filter. Figure 10.9(a1)–(a5) and (b1)–(b5) presents the results for the $1^3\Sigma_u^+$ state dimers and the $1^1\Sigma_g^+$ state dimers, respectively. Once more, log-normal distributions have been fitted to the data to determine the peak positions and the standard deviations. The

fits reveal the overall same trends that were observed for Rb_2. The K^+ fragments deflect more when coming from the $1^3\Sigma_u^+$ state than from the $1^1\Sigma_g^+$ state, and the deflections are reduced when the droplets become smaller. For the $1^3\Sigma_u^+$ state the width of the distribution again becomes smaller when the nozzle temperature is increased from 14 to 18 K. At higher temperatures, no further difference in width is observed, even though the peaks still shift toward smaller deflections. Some change is also observed for the widths of the distributions for the $1^1\Sigma_g^+$ state, but similar to the case for Rb_2 there is no clear trend.

To summarize the results and make comparisons between the deflections for K_2 and Rb_2, the peak positions are plotted as a function of the nozzle temperature in Fig. 10.10(a), and the standard deviations likewise in Fig. 10.10(b). The peak positions lie at larger angles for Rb_2 in the $1^3\Sigma_u^+$ state and the $1^1\Sigma_g^+$ state, compared to the K_2 counterparts. This is what one would predict if the differences in fragment velocities play a larger role than the variations in V_{Ak^+-He}, resulting in larger deflections for the heavier alkalis. Somewhat surprisingly though, the widths of the distributions are significantly larger for K_2 than for Rb_2. This does not harmonize with the fact that the distributions peak at larger angles for Rb_2. Why this is the case is currently not entirely clear, but one possibility could be that the K^+ ions are more likely to collide with the helium because K_2 lies less parallel to the surface compared to Rb_2, as shown in Fig. 8.6(d) and (f). Such collisions might change the trajectories of the ions, leading to much broader distributions.

A brief investigation of the influence of the doping pressure has also been done for K_2. The experiment was repeated for three different nozzle temperatures with the sample heated to 80 °C instead of the previous 90 °C. Only small fluctuations were observed for the peak positions and the standard deviations, indicating that the doping pressure is a noncrucial parameter. The additional data points are also shown in Fig. 10.10. Interested readers can find the actual distributions in Appendix D.

I will now investigate if the deflection distributions can be used to determine the size of the droplets. For this purpose, Rb_2 in the $1^3\Sigma_u^+$ state should be a good candidate. It lies very parallel to the surface [see Fig. 8.6(f)], thus making the deflections for

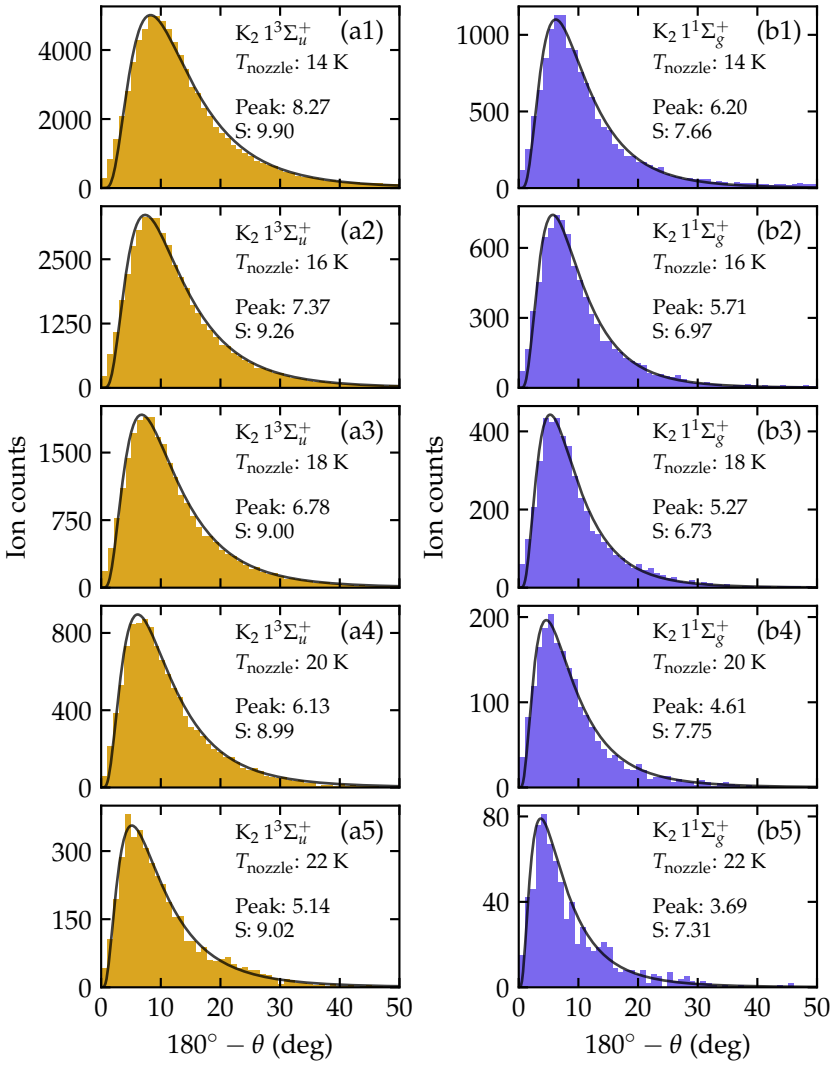

Figure 10.9: (a1)–(a5) Distributions of the deflection angles, defined as $180° - \theta$, for pairs of K^+ ions from K_2 in the $1^3\Sigma_u^+$ state on droplets formed with various nozzle temperatures (see annotations on panels). The black lines illustrate log-normal distributions fitted to the data. The peak positions and the standard deviations S of the distributions are annotated on the panels. (b1)–(b5) Same as for (a1)–(a5), but this time for K^+ ions from K_2 in the $1^1\Sigma_g^+$ state.

pairs of Rb^+ fragments more symmetrical, and reducing the risk of a direct collision with the helium due to the dimer standing at

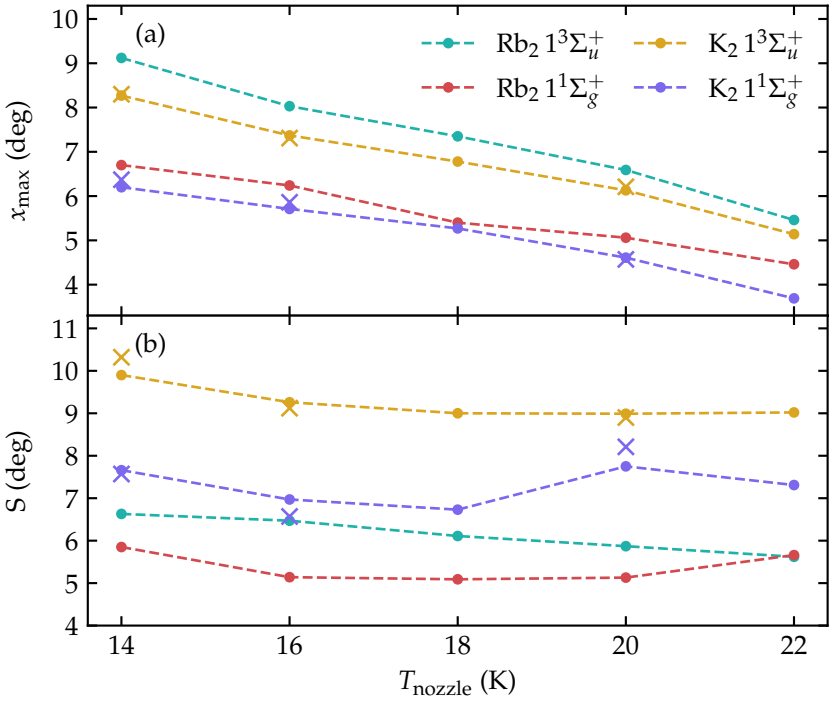

Figure 10.10: (a) Peak positions x_{max} for the deflection distributions in Fig. 10.8 and Fig. 10.9, as a function of the nozzle temperature. (b) Standard deviations S for the deflection distributions. Additional data points for K_2, recorded at a lower vapor pressure ($T_{oven} = 80$ °C compared to $T_{oven} = 90$ °C), are marked with $\times$-symbols.

an angle on the surface. Additionally, the deflection distribution changed in a clear pattern when the droplet size distribution was varied, as shown in Fig. 10.8(a1)–(a5).

There is, however, no way to extract the size directly from the experimental data, so to progress we need theoretical predictions to establish a relationship between the deflections and the droplet sizes. Such theoretical endeavors have been undertaken by Ernesto García-Alfonso and Nadine Halberstadt from the University of Toulouse together with Manuel Barranco and Martí Pi from the University of Barcelona. Using *time-dependent density functional theory* (TDDFT), they have made simulations of the trajectories of Rb^+ fragments originating from Coulomb explosion of $1^3\Sigma_u^+$ state Rb_2 residing parallel to the surface of a

helium droplet. The simulations were done for various droplet sizes, ranging from 50 to 20000 helium atoms. Such TDDFT simulations are computationally heavy, and generally considered unfeasible for droplet sizes above 5000 helium atoms. To enable the simulation of larger droplets, they optimized the starting configuration with the full set of calculations and then treated the helium density as frozen for the actual simulation of the dynamics. This strategy appears to be robust, as it can reproduce the outcome of the full TDDFT calculations for the smaller droplets.

Figure 10.11 presents the theoretically predicted deflections for the different droplet sizes. The magnitude of the deflections changes rapidly for droplet sizes up to around 5000 helium atoms. After that, it almost stagnates, with only a slow increase in the deflection when going toward even larger droplet sizes. Overall, the simulations only predict a deflection of up to around 6° for the treated droplet sizes. This is significantly less than what I observed for a large part of the distributions for Rb_2, where values up to around 30° are present. The mean droplet sizes in the experiments should not be larger than around 10000 helium atoms for the lowest nozzle temperature, with the largest droplets in the distributions around twice that size, so within the range of the calculations. Since the mismatch is so large, it is unfeasible to convert the experimental distribution into a droplet size distribution via an interpolation of the calculated relationship.

I believe the current limitation in the determination of the droplet size distribution is the experimental resolution. As mentioned in Section 10.1.2, the resolution of v_x, determined from the ToF values, is at least an order of magnitude worse than the resolution of v_y and v_z. This most likely leads to a broadening of the deflection distributions. As a test, I ran the deflection analysis for I^+ fragments from Coulomb explosion of gas-phase I_2, and there a small distribution of deflection angles was also observed, even though the ions should eject back to back with perfect axial recoil. This corroborates that the resolution is too poor to conduct this experiment properly with the current experimental setup.

If the droplet sizes can eventually be recovered from the deflection angles it will also enable filtering of the Ak^+ ions based

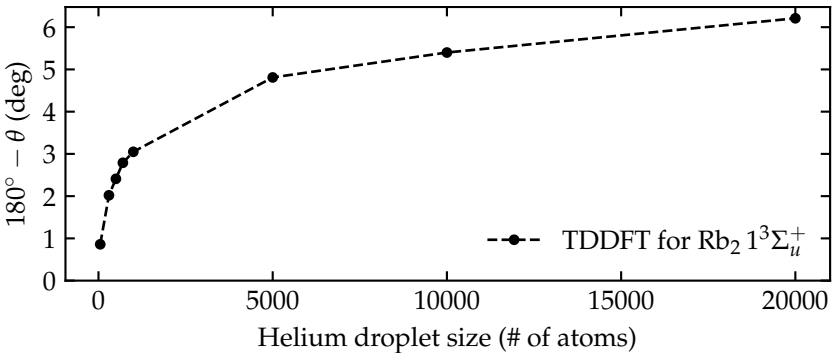

Figure 10.11: TDDFT calculated deflection angles for Rb^+ ions from Coulomb explosion of Rb_2 in the $1^3\Sigma_u^+$ state on helium droplets of various sizes. The helium density was kept frozen during the dynamics for calculations with more than 5000 He atoms. A black line is included to guide the eye. The calculations were done by Ernesto García-Alfonso, Nadine Halberstadt, Manuel Barranco, and Martí Pi (private communication).

on the droplet sizes, simply by discarding the pairs of Ak^+ ions that exhibit deflections that do not match the droplet sizes of interest. Doing so would enable direct studies of how dynamics, like the rotations and vibrations studied in Chapter 8 and Chapter 9, depend on the droplet size. This would be an improvement compared to the current approach of just regulating the expansion conditions for the droplet beam, which always produces a somewhat broad distribution of droplet sizes.

On a final note, the deflections must affect the observed degree of alignment found for the alkali dimers in Chapter 8. As long as both Ak^+ fragments from Coulomb explosion of an aligned dimer are deflected roughly the same amount, it should be possible to deconvolute the deflections and obtain a corrected value for the degree of alignment in future alignment experiments with the Tpx3Cam. Because this can be done individually for each dimer in the experiment, I expect that it would give better results than deconvolving the nonaxial recoil effect via information from the angular covariance maps as previously done for molecules in gas-phase and inside helium droplets [193].

10.3 Locating the parent Ak_2

The fact that the Ak^+ ions are deflected by the helium droplets during Coulomb explosion has an additional quite interesting potential application. No matter where the dimer resides on the droplet surface, the formed Ak^+ ions will always deflect toward the droplet. By determining which way in space the ions are deflected, one thus obtains information about the relative position of the droplet compared to the dimer. This should essentially make it possible to *pinpoint* the location where each parent dimer was residing on the droplet, by measurement of the 3D velocities of the Ak^+ fragments. Such information can be very useful, and for example make it possible to determine how the dimers are distributed across the droplet surfaces, potentially after manipulating them with an earlier laser pulse. A highly relevant possible application would be to combine it with the alignment experiments. This should make it possible to study whether the alignment dynamics depend on where on the droplets the dimers are located.

In the next section, I will show how the dimer locations can be pinpointed in practice and extract the distribution of locations for one of the data sets used to investigate the deflections in Section 10.2.

10.3.1 *The pinpointing method*

In the following, I will make two assumptions. The first assumption is that the pairs of Ak^+ fragments will experience symmetrical deflections, that is, that they both deviate the same amount from their original trajectories. This should be a quite good assumption for Rb_2 in the $1^3\Sigma_u^+$ state, again because it lies quite flat on the surface. The second assumption is that the helium droplets are completely spherical. For the droplet sizes used in my experiments, this should be a good approximation, in contrast to very large droplets on the order of 10^8–10^{11} helium atoms, where nonspherical droplets are sometimes observed due to large amounts of angular momentum leading to the formation of quantum vortices and distortion of the droplet shapes [77, 79, 80, 221].

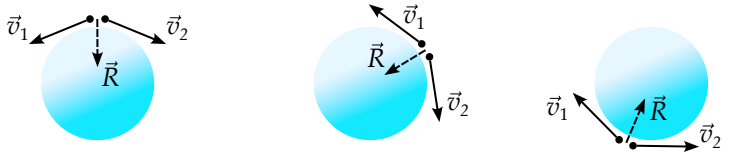

Figure 10.12: Illustration of the procedure used to pinpoint the location of Ak_2 on the droplet surface. No matter where on the droplet the dimer was residing, the sum of the 3D velocity vectors of the Ak^+ fragments will point to the droplet center. The location on the droplet can thus be retrieved.

To pinpoint the location of the parent dimers, the matching pairs of Ak^+ ions must again be determined. This is done in the same way as for the deflection analysis in Section 10.2. For each pair of Ak^+ ions, the 3D velocity vectors are added together, which under the assumed symmetry gives a vector $\vec{R}$ that points exactly to the droplet center, see Fig. 10.12. By flipping the sign and normalizing the length, a unit vector $\hat{P}$ is found, which points to the location of the parent dimer on a unit sphere that represents the droplet. Using this procedure I can now plot the found locations of all determined parent dimers in an experiment. As a demonstration, I will use the data from the measurement of Rb^+ deflections for $1^3\Sigma_u^+$ state Rb_2 on droplets created with a nozzle temperature of 14 K, presented in Section 10.2. The found locations are shown on a unit sphere in the lab frame in Fig. 10.13(a).

To investigate the distribution of locations further, the positions, represented by $\hat{P}$, can be converted to the corresponding pairs of Θ and φ values in spherical coordinates [see definition in Fig. 10.13(b)]. These can then be plotted as histograms, as shown in Fig. 10.14(a) and (b). Due to symmetry, there should be no preferred locations on the surface, so the true distribution of the dimers must be spherically uniform. In that case, the dimer locations should follow a $\sin(\Theta)/2$ distribution for the Θ-coordinate and a uniform distribution for the φ-coordinate, shown with red curves in Fig. 10.14(a) and (b). The agreement is fairly good but with some deviation for the distribution along Θ. More dimers are found to reside close to the poles ($\Theta = 0$ and π) compared to the expectation, while fewer are found close to the equator ($\Theta = \pi/2$).

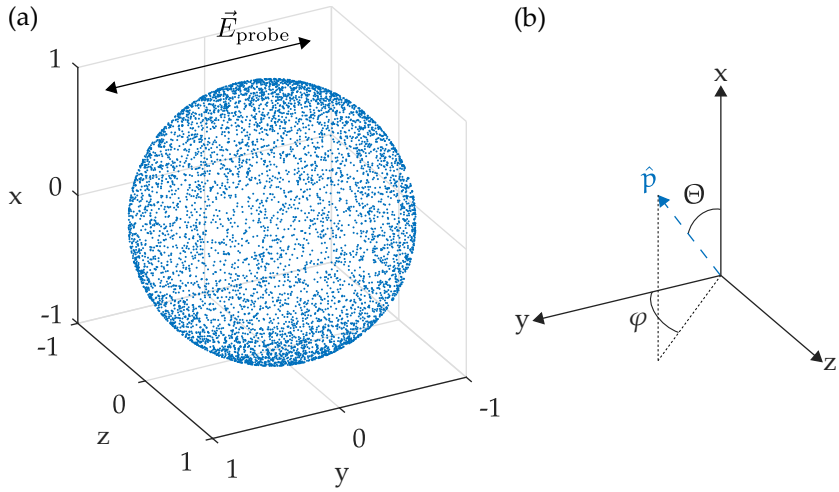

Figure 10.13: (a) Locations of $1^3\Sigma_u^+$ state Rb_2 on the helium droplets in the lab frame, visualized on a unit sphere. Only 25% of the dimer locations are plotted to avoid saturating the plot with data points. (b) Spherical coordinate system used for the description of locations on the helium droplets.

Two factors are likely to contribute to the observed experimental distribution of locations. The first factor is again the velocity resolution, in particular for the v_x component, for the Ak^+ ions used to calculate $\hat{p}$. This will most likely broaden the observed Θ and φ distributions, which can explain why more dimers are found to be located around the poles. Since the distribution along φ is already very uniform, the broadening will presumably not be visible there.

The second factor is the ionization probability. As addressed in Section B.1, the angular distribution of Rb^+ fragments should be anisotropic, due to resonances enhancing the ionization probability for Rb_2 oriented with the internuclear axis perpendicular to the polarization axis of the 800 nm pulse [see the polarization axis $\vec{E}_{\text{probe}}$ annotated in Fig. 10.13(a)]. Consider now that the possible orientations of the dimers are dictated by the droplet surface, restricting the orientation of the dimers along the direction perpendicular to the surface plane while the dimer can still rotate freely in the plane. Due to this restriction, the specific location on the droplet will affect the ionization probability, because it determines to what extent the dimers can lie parallel and perpen-

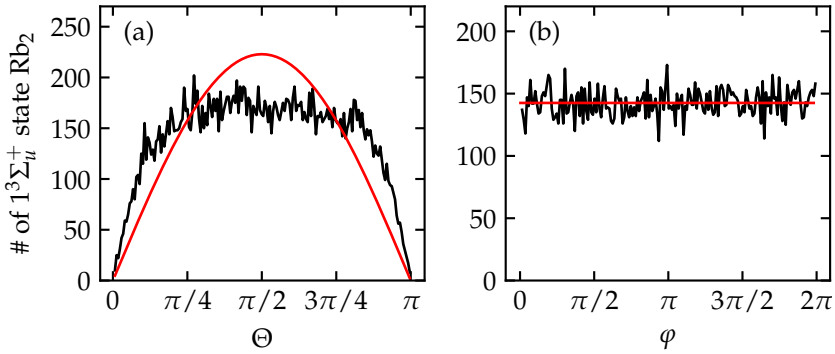

Figure 10.14: (a) Observed distribution of $1^3\Sigma_u^+$ state Rb_2 across the Θ-angle on the droplet surface. (b) Distribution of the positions of the dimers across the φ-angle. The red lines show the expectations for a spherically uniform distribution of points on a sphere. The binning is different in the two plots, resulting in different scales along the y-axis.

dicular to the polarization axis. As an example, a dimer residing at the equator ($\Theta = \pi/2$) will always lie perpendicular to the polarization axis if it lies at $\varphi = 0$ or π. In contrast, if the dimer is moved along the equator to $\varphi = \pi/2$ or $3\pi/2$ it can lie both parallel and perpendicular to the polarization axis, depending on how it is rotated in the surface plane. This argumentation can be repeated for all locations on the droplet surface. Ultimately, this creates a bias in which dimers are most likely to be probed, based on their location, which should affect the observed distributions of Θ and φ in Fig. 10.14(a) and (b). While not attempted, this can be studied further by varying the probe polarization and wavelength, changing which locations the dimers are most likely to be ionized at.

In future experiments, it should be possible to use the pinpointing method to isolate dimers from specific parts of the droplet in the data analysis. As briefly mentioned earlier, this opens the opportunity for studying the degree of alignment of alkali dimers based on their location on the droplet. I will present early results in Section 11.2, where I attempt to do exactly this for a new series of experiments where the alkali dimers are adiabatically aligned.

10.4 Conclusion

To conclude, I have shown that I can correct the data from the Tpx3Cam for the time-walk phenomenon via our implemented precorrection and postcorrection routine, thereby improving the ToF resolution enough to make 3D velocity map imaging achievable. I have then demonstrated that a calibration curve, which establishes a relationship between the ToF values and the v_x velocity, can be determined from a Coulomb explosion measurement of gas-phase I_2, making it possible to retrieve the full 3D velocity for other ion fragments. With this at hand, I investigated the deflection of Rb^+ and K^+ ions from Coulomb explosion of Rb_2 and K_2 on helium droplets, and found that the deflections especially appear to depend on the fragment velocities and the helium droplet size distribution. Unfortunately, the deflections currently cannot be used to retrieve the droplet sizes via comparison with TDDFT theory because the deflection angles are unreasonably large, most likely due to broadening caused by the current resolution of the experimental detection method. Finally, I demonstrated that the deflections can be used to pinpoint the location of Ak_2 on the droplets. The distribution of $1^3\Sigma_u^+$ state Rb_2 on the surface was found to be in fairly good agreement with a spherically uniform distribution, but with some deviation which can perhaps be explained by a location-dependent ionization probability. Also here, the resolution may be a limiting factor.

11

CONCLUSIONS AND OUTLOOK

The main research question during my PhD was if it is possible to rotate and align alkali dimers on the surface of helium droplets by irradiating them with a laser pulse in the nonadiabatic alignment regime. If successful, the next research questions were whether the alignment dynamics can be used to obtain insight into the rotational energy levels of the systems and the coupling between the alkali dimers and the helium droplet surface.

As a first step toward the goals, I demonstrated that laser-induced Coulomb explosion can be used to identify alkali dimers on helium droplets with quantum-state sensitivity. I then used this technique to probe the time-dependent alignment of Na_2, K_2, and Rb_2, on the surface of helium droplets, following irradiation by a nonresonant laser pulse with a duration of around 1 ps. The alkali dimers were observed to undergo rotation and align in periodically spaced, narrow time intervals. These observations answer the main research question.

Comparisons with theoretical calculations revealed that the observed rotational dynamics result from both the way the dimer responds to the dynamic Stark shift induced by the laser pulse and to the surface potential of the droplet. Particularly interesting, the rotational dynamics of Na_2 and K_2 in the $1^3\Sigma_u^+$ state and of K_2 and Rb_2 in the $1^1\Sigma_g^+$ state are very well described by a 2D rotor model. To my knowledge, these results are the first time-resolved experimental observations of 2D quantum rotation. For Na_2 in the $1^1\Sigma_g^+$ state, the rotations were also found to be modulated by the surface potential. However, the interaction is weaker and the laser-induced rotation is closer to that of the widely studies case of isolated gas-phase molecules. The theoretical modeling enabled the determination of the effective rotational constants of the dimers, but could not fully describe the gradual decay of the degree of alignment.

In contrast to the other dimers, Rb_2 in the $1^3\Sigma_u^+$ state exhibited no clear alignment dynamics after the initial response to

the laser pulse, perhaps because of interaction with the droplet. This inhibited comparisons with the theoretical model and the rotational dynamics of this dimer on the helium droplet surface are therefore still not fully understood.

Overall, the remaining research questions have thus also been quite successfully answered. However, more experimental and theoretical work is needed in the future to get a better understanding of the mechanisms that cause the gradual decay of the degree of alignment.

Several other experimental results have also been presented throughout the thesis. I have demonstrated that the structure sensitivity of the Coulomb explosion technique can be used to determine the distributions of internuclear separation for both homo- and heteronuclear alkali dimers on helium droplets and likewise for homonuclear alkali trimers. Overall, the central positions of the distributions agree well with the square of the ground state vibrational wave functions for the isolated dimers and trimers but the experimental widths were found to be larger, in part due to nonoptimal experimental conditions which can perhaps be remedied in future experiments.

I have also proved that the nonresonant alignment pulses used to set the alkali dimers into rotation can induce vibrational motion in Rb_2 in the $1^3\Sigma_u^+$ state residing on the droplet surface. The vibrations were tracked via timed Coulomb explosion and found to be essentially unaffected by the nearby helium droplet surface, in sharp contrast to what has been observed for the rotational motion of the alkali dimers. Furthermore, I found that the vibrations do not affect the rotational dynamics in any significant manner. While not shown in this thesis, experiments confirm that the alignment pulses also start vibrations in Na_2 and K_2 in the $1^3\Sigma_u^+$ state.

Lastly, I have shown that Coulomb explosion of the alkali dimers can be used to study the properties of the nearby helium droplet. I demonstrated that the droplets deflect the trajectories of the Ak^+ ions produced in the Coulomb explosions and that the deflection angles can be measured via 3D velocity map imaging and possibly be directly related to the size of the helium droplets. In addition, I suggested a way to determine the location of the alkali dimers on the helium droplets via the 3D velocities of the Ak^+ fragment ions.

The work presented in this thesis paves the way for many new experiments, particularly on alignment of alkali dimers on helium droplet surfaces. In the following, I will outline a few of such possible experiments.

11.1 Nonadiabatic alignment of Ak_2 using multiple laser pulses

A fundamental limitation in the nonadiabatic alignment experiment of the alkali dimers is that the intensity must be kept moderate to avoid ionization of the dimers. This limits the interaction strength and ultimately the degree of alignment that can be achieved. However, the issue can most likely be circumvented by using two alignment pulses with moderate intensity. The idea is to first prealign the dimers with one alignment pulse and then irradiate them with another alignment pulse when the degree of alignment peaks. The interaction with the second pulse should cause the angular distribution to narrow further, thereby increasing the degree of alignment beyond that obtained with only a single pulse. Previous works demonstrated that this approach works for molecules in both gas phase [24, 222, 223] and inside helium droplets [36]. In addition, it has also been demonstrated that one can use a train of synchronized pulses to repeat the process and thus obtain even stronger alignment [36, 224]. It would be interesting to extend such results to encompass molecules on a surface.

Another type of experiment using two alignment pulses was mentioned in Section 8.3. There I explained that a second alignment pulse can perhaps be used to create rotational echoes in the degree of alignment for the alkali dimers on the helium droplet surfaces. If it works, such echoes may be the key to understanding the broadening mechanisms that affect the alignment dynamics for the alkali dimers. The technique can perhaps also provide insight into the coupling between the rotations and the excitations of the helium droplet. Rotational echo experiments would therefore be exciting to attempt in the future.

11.2 Long-pulse alignment of Ak_2

Having demonstrated nonadiabatic alignment of the alkali dimers on helium droplet surfaces, it is interesting to show that the

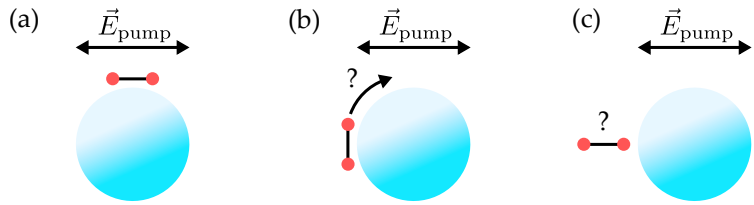

Figure 11.1: (a) On some parts of the helium droplets, alkali dimers can align themselves along the polarization axis $\vec{E}_{\text{pump}}$ of a long alignment pulse while still being parallel to the droplet surface. If the dimer cannot align along $\vec{E}_{\text{pump}}$ while staying parallel to the surface, will it then (b) minimize the energy of the interaction with the laser pulse by moving to a position where it can, or will it (c) remain in place and align despite the surface interaction?

dimers can also be aligned by much longer laser pulses. We therefore recently started doing experiments with the alignment pulses stretched to around 200 ps (obtained with the grating stretcher, see Section 4.4.1) in the group.

The preliminary results from the experiments show that the alkali dimers can be aligned strongly with such long pulses. For example, the peak degree of alignment reaches $\langle\cos^2\theta_{2D}\rangle = 0.78$ for Na_2 in the $1^3\Sigma_u^+$ state and $\langle\cos^2\theta_{2D}\rangle = 0.92$ for K_2 in the $1^3\Sigma_u^+$ state (Emil Hansen, private communication)[27]. This raises a question that has taken my interest toward the end of my studies. Consider an alkali dimer that lies flat on the surface of a helium droplet. If the dimer interacts with a 200 ps alignment pulse with the polarization axis parallel to the surface plane at the point where the dimer resides, then the alkali dimer should be able to align while still lying flat on the surface. This scenario is sketched in Fig. 11.1(a). The question is now, what would happen if the dimer is located at a position on the droplet, where the dimer cannot stay flat on the surface while also aligning along the polarization axis? In this case, the interaction with the laser pulse competes against the interaction with the droplet surface. Will the dimer respond by moving along the surface of the droplet until it reaches a position where it can align while staying flat on the surface, as sketched in Fig. 11.1(b)? By doing so, it would minimize the energies involved in both the interaction with the

27 These values are without any corrections for the nonaxial recoil.

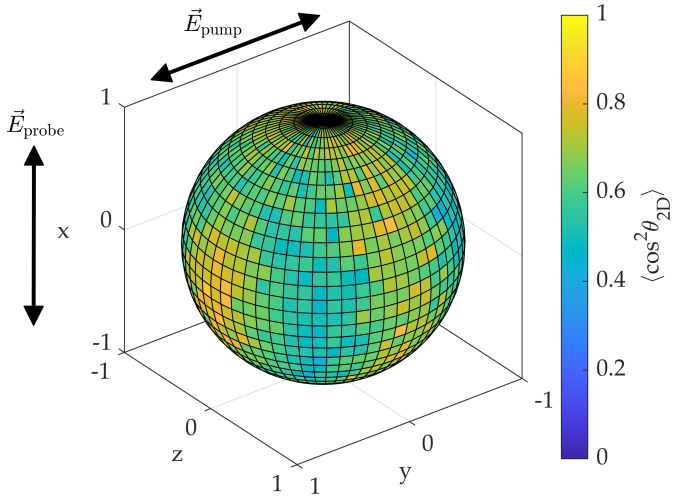

Figure 11.2: $\langle \cos^2 \theta_{2D} \rangle$ values for Na_2 in the $1^3\Sigma_u^+$ state for different zones on the helium droplet surfaces (visualized as a unit sphere). The data was collected at peak alignment.

laser pulse and the surface. It would take the dimer some time to move, and while it is certainly not possible during the interaction with the ~ 1 ps nonadiabatic alignment pulses, it can perhaps be achieved within a pulse duration of 200 ps. Alternatively, will the dimer remain in place at the same point on the droplet and align along the polarization axis even though it then no longer lies flat on the surface, as illustrated in Fig. 11.1(c)?

I have conducted a rudimentary analysis of the recently acquired data for Na_2 in the $1^3\Sigma_u^+$ state to begin the investigation of this question. In brief, I first used the pinpointing method presented in Section 10.3.1 to identify parent dimers from different zones on the droplet surface. Next, I calculated the average degree of alignment for the dimers in each zone. Figure 11.2 shows the results obtained when data is collected at the peak of alignment. It appears that the degree of alignment indeed depends on where the dimers are located on the surface. The underlying data also indicate that the dimers do remain in place during the interaction. When the experiment is done without the alignment pulse (not shown), the degree of alignment has the expected value of 0.5 in all zones on the droplet.

I am hesitant to conclude too much from the current results, in particular, because we know that the resolution of the detection setup can be improved. However, as soon as the data quality is

better, I believe it would be very interesting to continue these experiments, as it might provide more insight into the interaction between the alkali dimers and the helium droplet surfaces. Ideally, the experiment should be repeated for different alkali dimers, different pump-probe delays, and perhaps also with different alignment pulse durations, to more carefully assess how each dimer reacts to the alignment pulse. It will also be important to check if the pinpointing method can be reliably used in the analysis. If some dimers stand quite erect on the surface due to the alignment interaction [for example as illustrated in Fig. 11.1(c)], the pinpointing method will break down. The solution, in that case, might be to use a weaker alignment pulse such that the dimers stay flatter on the surface.

APPENDIX

A

VMI CALIBRATION

The VMI images must be calibrated to retrieve information about the velocity or, equivalently, the energy of the ions. One way to obtain such a calibration is to create ions with known kinetic energies and record a 2D velocity map image of them with the VMI spectrometer. With the image at hand, a relationship can be established between the radial position of the ions in the image and the energies.

Ions with well-defined energy can be created in a pump-probe experiment utilizing photodissociation of I_2. First, a molecular beam of gas-phase I_2 in the ground state is created via supersonic expansion with the Even-Lavie valve housed in the secondary source chamber (see details in Section 4.1.4). Inside the VMI spectrometer, the I_2 is pumped with a $\sim$ 50 fs laser pulse centered at 650 nm, obtained by frequency doubling the uncompressed 1300 nm output from the TOPAS. The pump pulse can excite the I_2 molecules to three different dissociative states. One state is accessed via a 1-photon transition and dissociates into two ground-state iodine atoms $I(^2P_{3/2})$+$I(^2P_{3/2})$ (labeled channel C1). The other two states are reached by 2-photon transitions and dissociate into either one ground-state atom and one excited-state atom $I(^2P_{3/2})$+$I(^2P_{1/2})$ (channel C2) or two ground-state atoms (channel C3).

The different dissociation channels give rise to iodine atoms with three different kinetic energies

$$E_{\text{kin}} = \frac{1}{2}(h\nu - D_0) \qquad \text{(C1)}, \tag{A.1}$$

$$E_{\text{kin}} = \frac{1}{2}(2h\nu - D_1) \qquad \text{(C2)}, \tag{A.2}$$

$$E_{\text{kin}} = \frac{1}{2}(2h\nu - D_0) \qquad \text{(C3)}. \tag{A.3}$$

Here, h is Planck's constant and ν is the frequency of the photons, while D_0 = 12441 cm^{-1} and D_1 = 20044 cm^{-1} are the dissociation

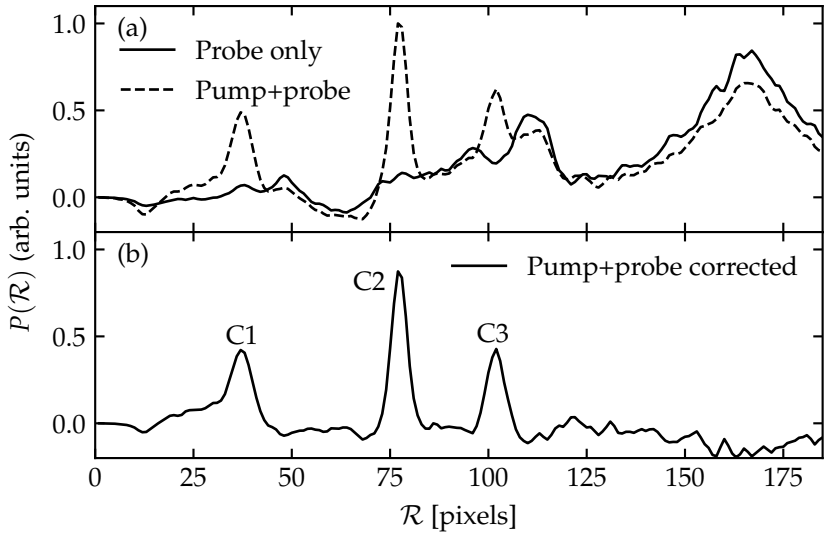

Figure A.1: (a) Radial distributions $P(\mathcal{R})$ of I^+ ions, after Abel inversion of the recorded 2D velocity map image, with the probe only (solid line) and with pump and probe (dashed line). (b) Radial distribution for pump and probe after subtracting the probe-only distribution. The dominant peaks have been assigned to the three dissociative channels C1, C2, and C3.

energies for the $I(^2P_{3/2})$+$I(^2P_{3/2})$ and $I(^2P_{3/2})$+$I(^2P_{1/2})$ atomic limits, respectively [225].

To measure the dissociation fragments it is necessary to turn them into ions. In practice, this is done by ionizing the iodine atom with an intense $\sim$ 50 fs laser pulse centered at 800 nm. To ensure ample time for the dissociation, the probe pulse is delayed by around 150 ps compared to the pump pulse. At this point, the dissociation fragments are so far apart that the Coulomb energy between the created ions is negligible. The ions, still having the energy released from the dissociation, are now projected onto the detector by the VMI spectrometer, and a 2D velocity map image is recorded.

Figure A.1(a) shows the radial distribution $P(\mathcal{R})$ of I^+ ions after Abel inverting the pump-probe image, as well as for an image recorded with the probe only. Three additional peaks are seen in the pump-probe radial distribution. To isolate the contribution from the pumped molecules, the pump-probe radial

distribution can be corrected by subtracting the probe-only radial distribution, see Fig. A.1(b). The peaks can now be paired up with the three different photodissociation channels as annotated in Fig. A.1(b).

We can now work out the energy calibration. A convenient way to do this is to utilize the fact that the energy difference between the ions in the C3 channel and the C2 channel must be given by $D_1 - D_0$. The benefit of using this relation is that it is independent of the wavelength used for the pump pulses. Now, as mentioned in Section 4.3 the kinetic energy scale as

$$E_{\text{kin}} = k\mathcal{R}^2. \tag{A.4}$$

Using this, we can calculate the calibration coefficient

$$k = \frac{E_{\text{kin,C3}} - E_{\text{kin,C2}}}{\mathcal{R}^2_{\text{C3}} - \mathcal{R}^2_{\text{C2}}} = \frac{D_1 - D_0}{\mathcal{R}^2_{\text{C3}} - \mathcal{R}^2_{\text{C2}}}. \tag{A.5}$$

Here, $\mathcal{R}_{C2}$ and $\mathcal{R}_{C3}$ are the central radial positions of the two channels in the radial distribution, see Fig. A.1(b), which can be determined by a fit.

B

SUPPLEMENTARY INFORMATION – CHAPTER 5

B.1 Angular anisotropies

Several of the ion images in Fig. 5.3(a1)–(e1) are anisotropic. This is supported by the angular distributions $P(\theta)$ shown in Fig. B.1, which I have obtained by integrating the ion yield in the channels along the radial axis. Figure B.1(a)–(c) reveal that Li^+ and Na^+ are more often ejected along the laser polarization axis, i. e., close to 0° and 180°, than perpendicular to the axis. In contrast, the Rb^+ ions are more likely to come out in a direction perpendicular to the polarization, as shown in Fig. B.1(f) and (g). For K^+ [Fig. B.1(d) and (e)] and Cs^+ [Fig. B.1(h) and (i)] the angular distributions are almost isotropic.

Angular anisotropies, such as the ones observed, can arise if one or multiple electronically excited states in the systems are resonant or close to resonant with the photons involved in the multiphoton ionization process. The resonances affect the transition probabilities according to the transition dipole moments associated with the involved states. As a result, it becomes easier for the probe to doubly ionize dimers with a specific orientation with respect to the probe polarization. This leads to the measured angular anisotropies since the emission directions of the fragments are governed by the orientation of the molecule being Coulomb exploded [5].

In the experiments, excited states in the alkali dimers can generally be reached already after absorption of one photon from the laser pulse (see the potential curve diagrams in Section B.3). Using Na_2 as an example, I will now show that resonant absorption of the first photon can explain the observed anisotropies in the ion images.

Figure B.4 show selected potential curves for Na_2. One photon at a wavelength of 800 nm can bring Na_2 in the $1^1\Sigma_g^+$ state close to the $1^1\Sigma_u^+$ state. Such a transition from $1^1\Sigma_g^+ \rightarrow 1^1\Sigma_u^+$ would be an allowed parallel transition, for which the absorption probability is

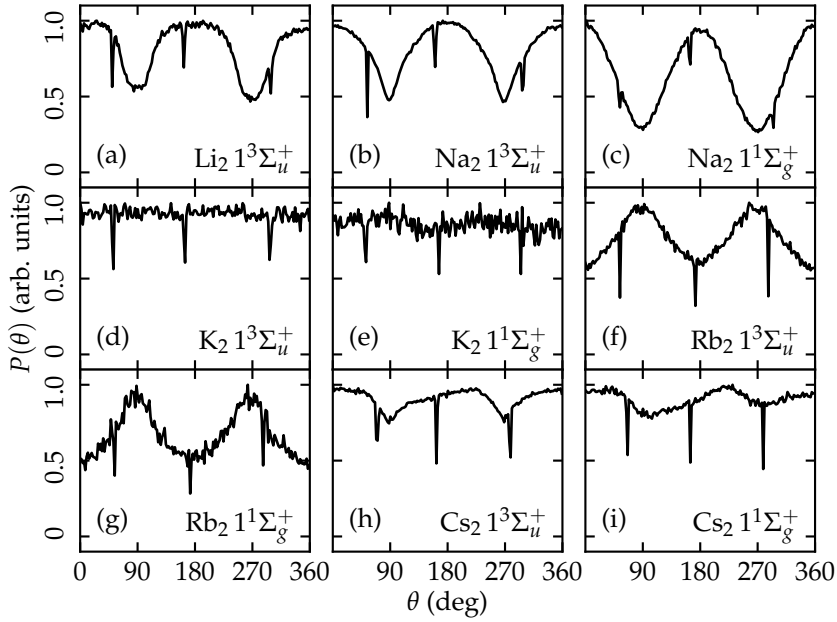

Figure B.1: $P(\theta)$ distributions for the Ak^+ ions in the $1^3\Sigma_u^+$ state and the $1^1\Sigma_g^+$ state channels in the velocity map images in Fig. 5.3(a1)–(e1). The definition for θ is annotated in Fig. 5.3(a1).

maximized for dimers with the internuclear axis oriented parallel to the laser polarization axis. This indicates that Na^+ ions from Coulomb explosion of Na_2 in the $1^1\Sigma_g^+$ state should preferentially come out in directions close to 0° and 180°. This agrees with the angular distribution obtained in the experiment, see Fig. B.1(c). Similarly, Na_2 starting in the $1^3\Sigma_u^+$ state can be brought close to the $1^3\Sigma_g^+$ state by a single photon, which is again an allowed parallel transition. Thus, the Na^+ ions from Coulomb explosion of Na_2 in the $1^3\Sigma_u^+$ state should also preferentially come out close to 0° and 180°, which again match the experimental observations, see Fig. B.1(b).

Higher-lying electronic states likely affect the absorption of the next photons. However, since the density of electronic states gets very high as the energy increases, it becomes difficult to determine which states may affect the multiphoton ionization process after the absorption of the first photon. For this reason, no such attempt has been made. It is however unlikely that the higher-lying states will lead to any significant anisotropy in the

ion images since both parallel and perpendicular transitions will most likely be available.

The fact that we observe vastly different angular anisotropies depending on the wavelength used to probe a given dimer strengthens the presented interpretation. In a different measurement where Na_2 was Coulomb exploded by a 400 nm probe pulse [see ion image in Fig. 7.3(a1)], the angular distributions for the ions in the $1^3\Sigma_u^+$ state and $1^1\Sigma_g^+$ state channels were only slightly anisotropic, with a small increase in the direction perpendicular to the probe pulse. The reason for that is most likely that many electronic states are accessible with one 400 nm photon, making both parallel and perpendicular transitions about equally probable. Similar has been observed for K_2 in the $1^3\Sigma_u^+$ state, which was also probed with 400 nm. The angular distribution in Fig. B.1(d) is essentially isotropic, while a measurement with an 800 nm probe (not shown) shows an increased likelihood for ionization of the dimers that lie perpendicular to the polarization axis.

B.2 Triplet-to-singlet ratios

The large presence of $1^3\Sigma_u^+$ state alkali dimers on helium droplets was clear from the very first experiments conducted with the dimers on the droplets. Much more unclear has been what the ratio of the $1^3\Sigma_u^+$ state dimers to the $1^1\Sigma_g^+$ state dimers are, that is, how many $1^1\Sigma_g^+$ state dimers are present on the droplets in the experiments? According to spin statistics, the triplet-to-singlet formation ratio should be 3:1 [99]. However, as mentioned in Section 2.3.1, the energy released during the formation of the dimers causes some of the $1^1\Sigma_g^+$ state dimers to desorb from the droplets. This should increase the observed triplet-to-singlet ratio. Surprisingly, a direct experimental determination of the ratios has been lacking, apart from a single measurement indicating a 50:1 triplet-to-singlet ratio for Na_2 on helium droplets with a mean size of $\sim$ 10000 He atoms [48, 102].

I have investigated the triplet-to-singlet ratios of the alkali dimers present in my experiments by analyzing the ion yield in the channels associated with Coulomb explosion of the $1^3\Sigma_u^+$ state and $1^1\Sigma_g^+$ state dimers. Specifically, I have done systematic

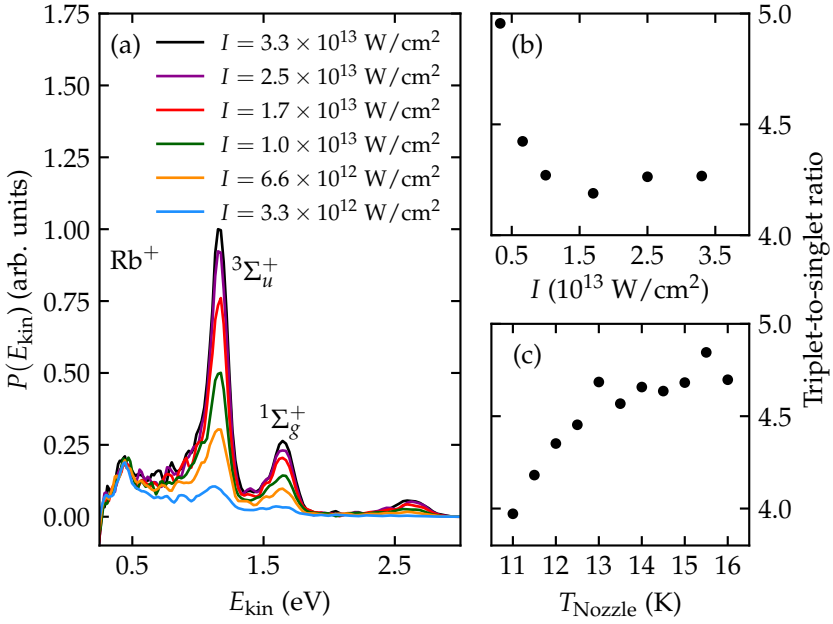

Figure B.2: (a) $P(E_{kin})$ distribution for Rb^+ ions formed in a series of Coulomb explosion measurements with Rb_2 on helium droplets using different probe intensities. (b) Triplet-to-singlet ratios at different probe intensities, obtained as the ratio of the areas of the peaks assigned to $1^3\Sigma_u^+$ state and $1^1\Sigma_g^+$ state Rb_2 in (a). (c) Rb_2 triplet-to-singlet ratios for different nozzle temperatures T_{nozzle}, and thus different droplet sizes, all recorded with a probe intensity of $I = 3.3{\times}10^{13}$ W/cm^2 ($P(E_{kin})$ distributions not shown). The data in (c) was previously shown in [124].

measurements with Rb_2. First, to ensure that I probe each spin state equally, I used the 800 nm probe beam with different intensities to record a series of VMI images of Rb^+ ions while keeping the nozzle temperature at 12 K. Figure B.2(a) shows the $P(E_{kin})$ distributions obtained for the various intensities. The triplet-to-singlet ratio has then been determined for each measurement as the ratio of the $1^3\Sigma_u^+$ peak area and the $1^1\Sigma_g^+$ peak area, calculated by numerical integration. The ratios are presented in Fig. B.2(c). For the lowest used intensity, the ratio is around 5:1. However, as the intensity is increased, the ratio drops to a lower threshold of around 4.2:1. From this I conclude that the double ionization done by the probe is saturated for both spin states

and that the triplet-to-singlet ratio extracted from the $P(E_{\mathrm{kin}})$ distribution reflects the actual ratios present in the experiment. Notice that the overall ion yield, see Fig. B.2(a), continues to rise as the intensity is increased. This is because the effective interaction volume in the experiment grows as the intensity in the wings of the laser spot becomes large enough to also start double ionizing the dimers.

I then made another series of measurements, this time keeping the intensity at $I = 3.3\times10^{13}$ W/cm^2, well within the saturation regime. This time the nozzle temperature, and thus the droplet size, is instead varied from T_{nozzle} = 11 K to 16 K. The triplet-to-singlet ratios obtained in those measurements are displayed in Fig. B.2(c). All data points lie within ratios of 4.0:1 and 4.8:1, with the smallest droplets having the largest ratios. Some uncertainty is expected to be present in the results, especially because the $1^3\Sigma_u^+$ state peaks in Fig. B.2(a) have large shoulders on the low-energy side. This makes it somewhat difficult to assign the area associated with ions from the $1^3\Sigma_u^+$ state dimers with any high degree of accuracy. Overall, the results are in good agreement with the tendency predicted by theoretical modeling, where the ratio is expected to drop closer and closer to the spin-statistics ratio of 3:1 as the droplet size increases [102]. My results are in stark contrast to the ratios of 50:1 and above mentioned in the literature, even when taking some uncertainty into account, and suggest that the amount of $1^1\Sigma_g^+$ state dimers desorbing from the droplet surface may be much smaller than previously expected.

I have not done a systematic droplet size scan for the other alkali dimers, but I expect the results to be similar for all of them. This is supported by the quite similar triplet-to-singlet ratios in the kinetic energy distributions in Fig. 5.3(a2)–(e2), which were recorded with nozzle temperatures T_{nozzle} = 11 K and 12 K and intensities that are expected to be in the saturation regime, or at least close to it. Furthermore, the ratios appear to be similar across experiments and tests carried out in the group over the years, including those carried out on the other helium droplet machine.

B.3 Selected potential curves for Ak_2

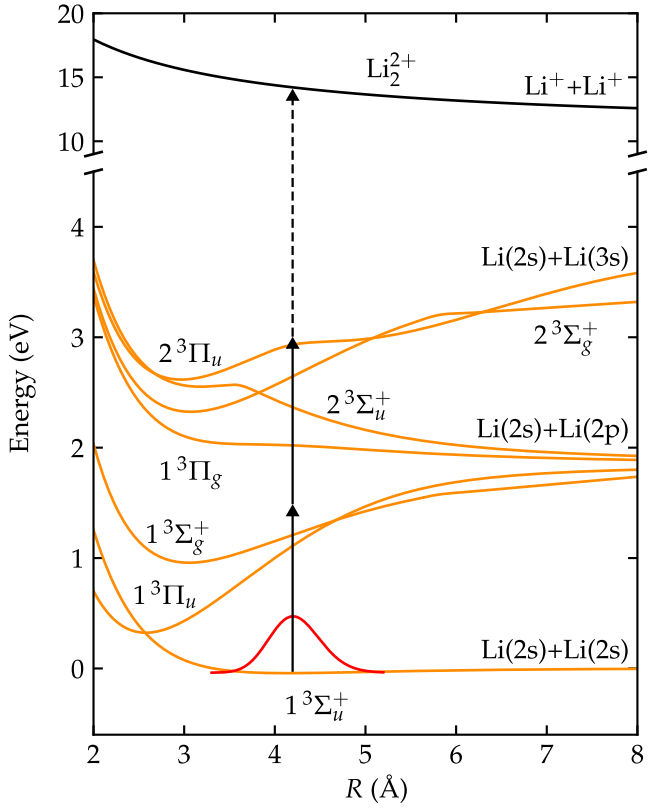

Figure B.3: Selected potential curves for Li_2 [141] and Li_2^{2+} [126]. The solid black arrows depict 800 nm photons, while the dashed black arrow illustrates the last 800 nm photons involved in the multiphoton ionization process leading to the formation of Li_2^{2+}.

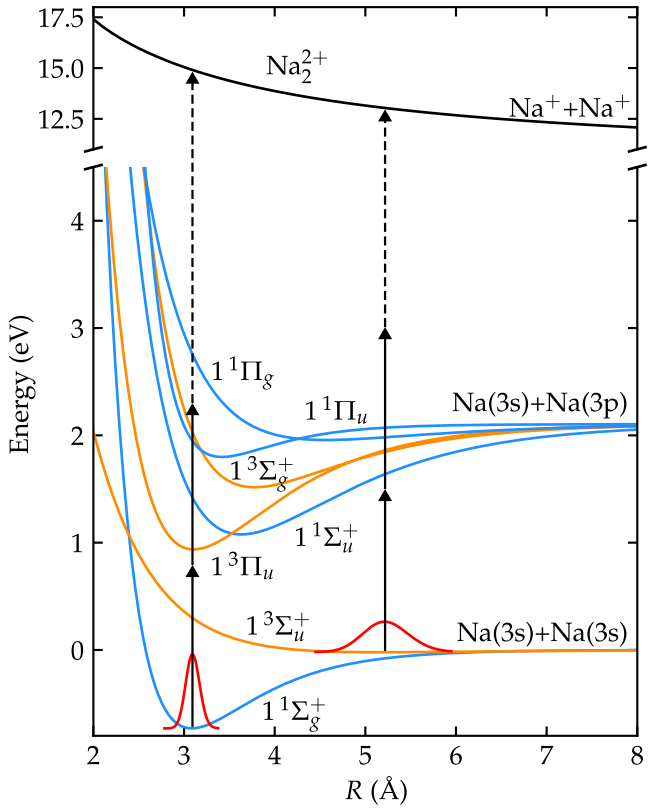

Figure B.4: Selected potential curves for Na_2 [107, 139] and Na_2^{2+} [126]. The solid black arrows depict 800 nm photons, while the dashed black arrows illustrate the last 800 nm photons involved in the multiphoton ionization processes leading to the formation of Na_2^{2+}.

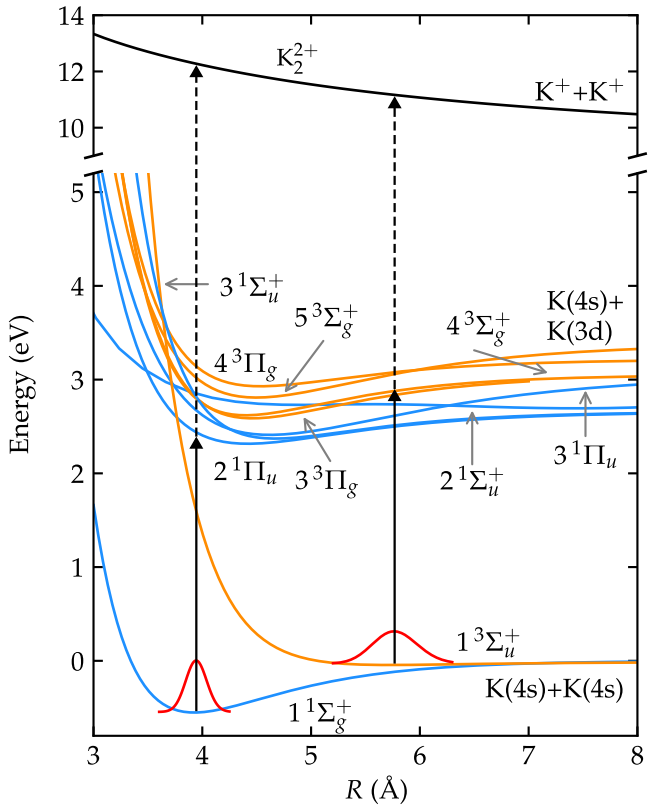

Figure B.5: Selected potential curves for K_2 [140] and K_2^{2+} [126]. The solid black arrows depict 400 nm photons, while the dashed black arrows illustrate the last 400 nm photons involved in the multiphoton ionization processes leading to the formation of K_2^{2+}.

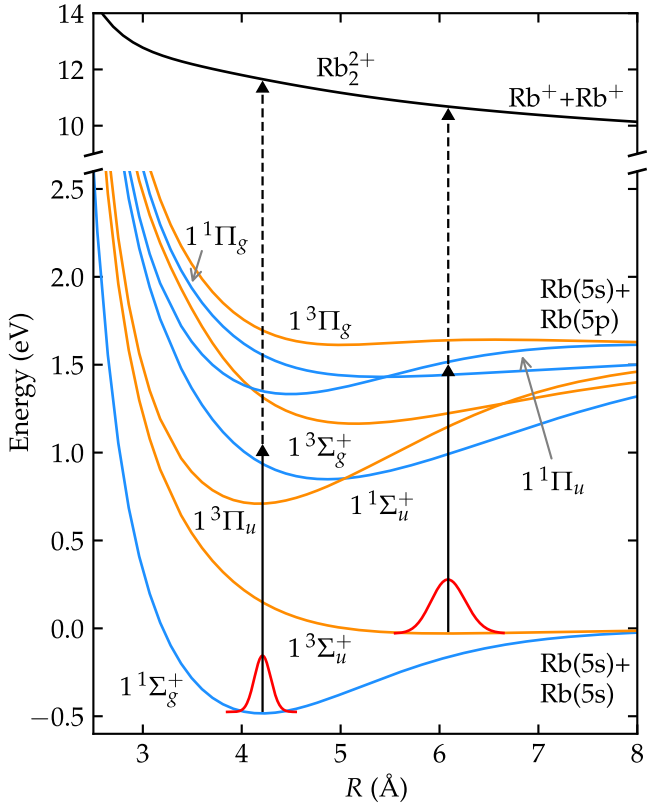

Figure B.6: Selected potential curves for Rb_2 [142] and Rb_2^{2+} [126]. The solid black arrows depict 800 nm photons, while the dashed black arrows illustrate the last 800 nm photons involved in the multiphoton ionization processes leading to the formation of Rb_2^{2+}.

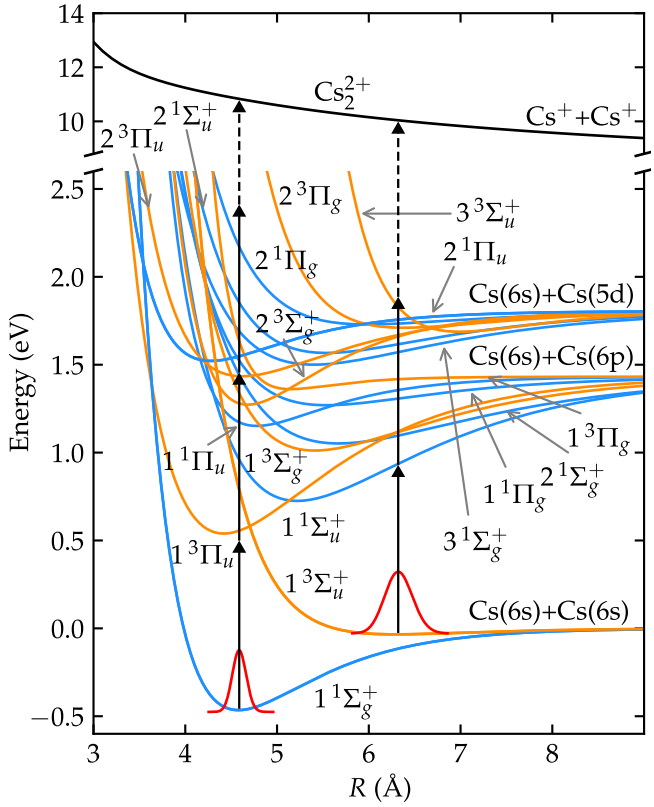

Figure B.7: Selected potential curves for Cs_2 [142] and Cs_2^{2+} [126]. The solid black arrows depict 1300 nm photons, while the dashed black arrows illustrate the last 1300 nm photons involved in the multiphoton ionization processes leading to the formation of Cs_2^{2+}.

C

SUPPLEMENTARY INFORMATION – CHAPTER 6

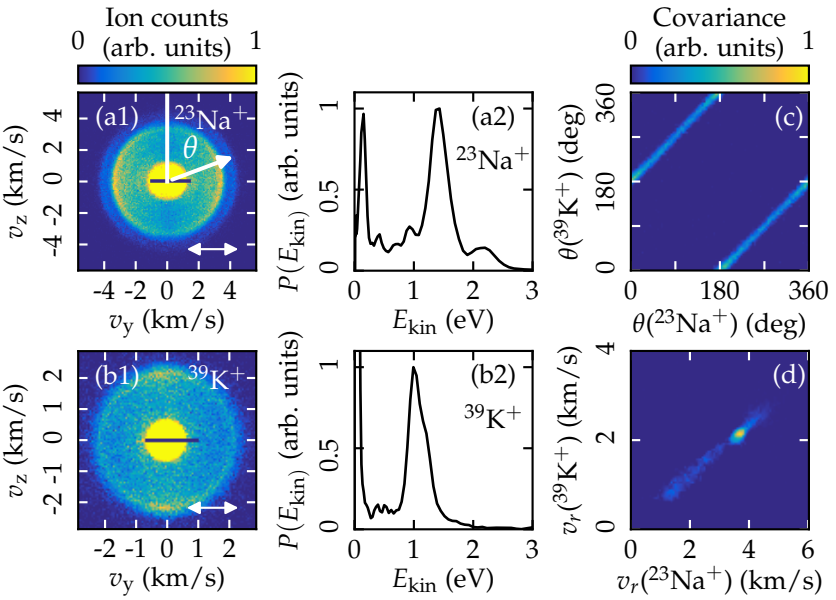

Figure C.1: Simultaneously recorded 2D velocity map images for $^{23}Na^+$ (a1) and $^{39}K^+$ (b1). The probe polarization axis is indicated by the white arrows in the lower right corners. The kinetic energy distribution is shown in (a2) for the $^{23}Na^+$ ions and in (b2) for the $^{39}K^+$ ions. (c) Angular covariance map between the $^{23}Na^+$ and $^{39}K^+$ ions in the kinetic energy ranges that correspond to Coulomb explosion of $1^3\Sigma^+$ state $^{23}Na^{39}K$. (d) Radial covariance map between the $^{23}Na^+$ and $^{39}K^+$ ions. Own work, inspired from [174].

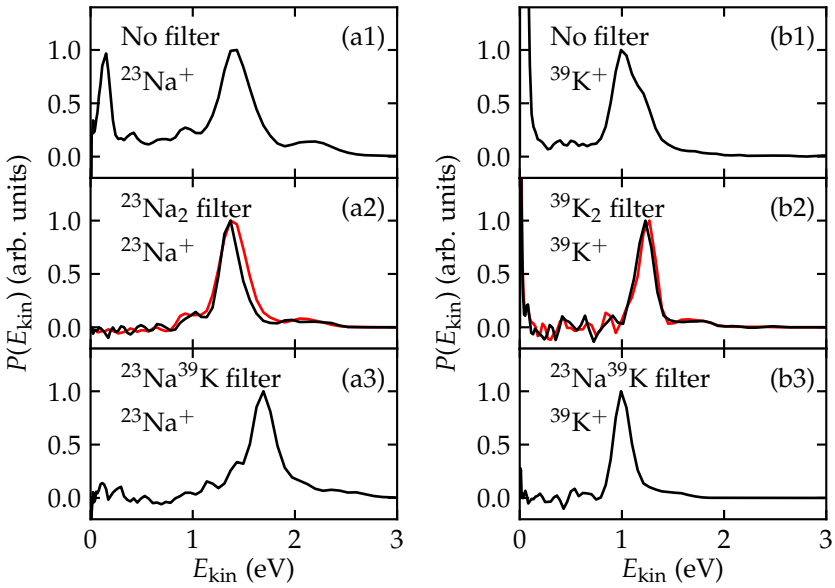

Figure C.2: Kinetic energy distribution $P(E_{kin})$ for $^{23}Na^+$ (a1) and $^{39}K^+$ (b1) ions extracted from the 2D velocity map images in Fig. C.1(a1) and (b1). (a2) and (a3) [(b2) and (b3)] $P(E_{kin})$ distributions for the $^{23}Na^+$ [$^{39}K^+$] ions after filtering the data with the homonuclear and heteronuclear dimer filters as annotated on the panels. The red curves in (a2) and (b2) show $P(E_{kin})$ distributions for $^{23}Na^+$ (a2) and $^{39}K_2$ (b2) obtained from a measurement series where only homodimers were formed on the droplets. Own work, inspired from [174].

D

SUPPLEMENTARY INFORMATION – CHAPTER 10

D.1 3D velocity map images for Coulomb explosion of I_2

In Section 10.1.2, I determined the calibration function needed to convert the individual ToF values of ions into their v_x velocity components. With the calibration at hand, it becomes possible to plot 3D velocity map images of ions. This is demonstrated here for the I_2 data sets used to make the calibration in the first place.

Figure D.1 shows the result for the measurement where the probe polarization was in the plane of the detector (along the y-axis). The amount of data points has been reduced by a factor of eight, such that the finer details become more pronounced. The illustrated projection in the x-y-plane corresponds to the ordinary 2D velocity map image, which was also shown in Fig. 10.4(a). Similarly, the measurement where the probe polarization was along the x-axis (the ToF-axis) is shown in Fig. D.2. With this polarization, only a quite isotropic round distribution of ions was observed in 2D [see the colored image in Fig. 10.4(b)]. In 3D, the clear lobes that were observed along the v_y-axis in Fig. D.1 are now observed along the v_x-axis as expected, demonstrating that the v_x velocity component has been retrieved.

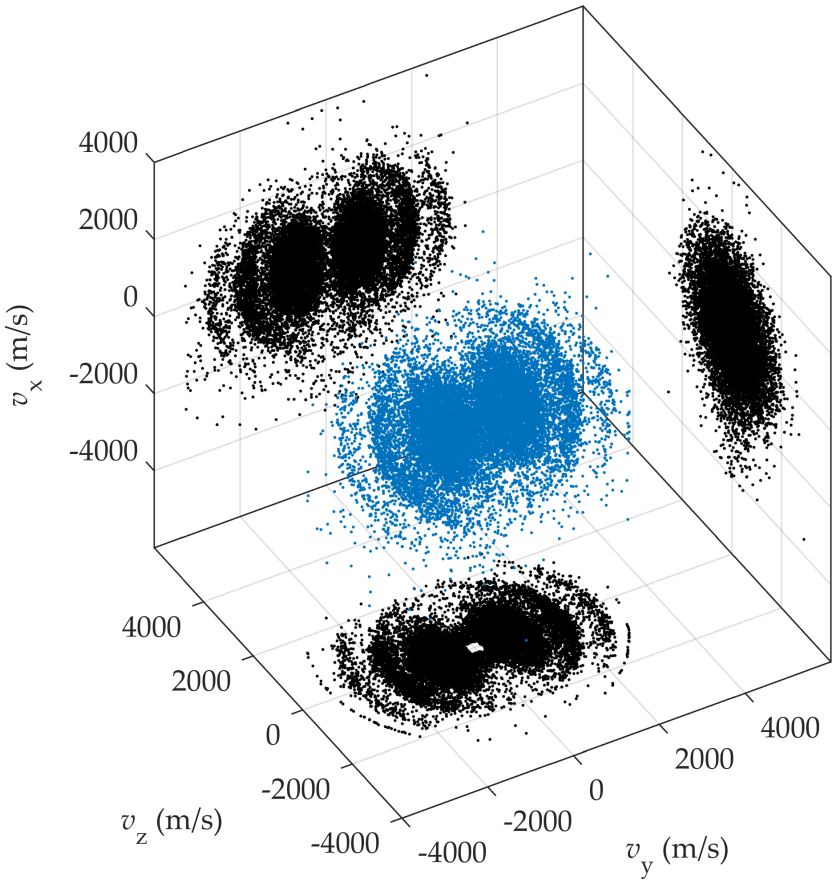

Figure D.1: 3D velocity map image of I^+ ion fragments from Coulomb explosion of I_2, shown in blue, recorded with a probe polarization along the y-axis. Projections onto the three planes are shown in black to help visualize the 3D image. The v_x velocity component was extracted from the ToF values of the ions.

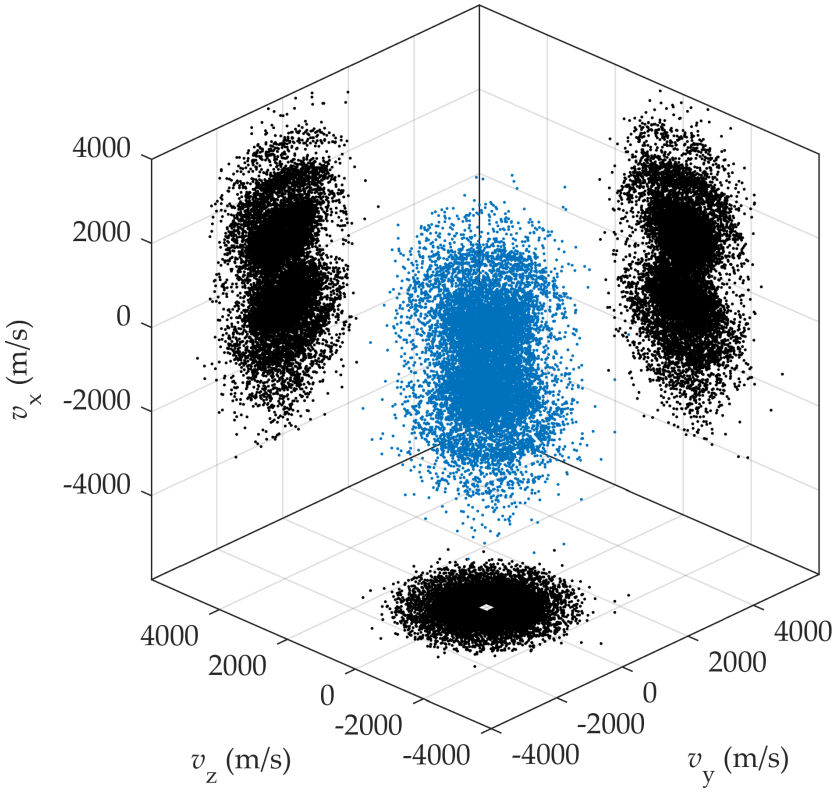

Figure D.2: 3D velocity map image of I^+ ion fragments from Coulomb explosion of I_2, shown in blue, recorded with a probe polarization along the x-axis. Projections onto the three planes are shown in black to help visualize the 3D image. The v_x velocity component was extracted from the ToF values of the ions.

D.2 Additional data for deflections of K^+

To investigate whether the vapor pressure of potassium in the doping oven influences the droplet size distributions and thus also the deflections, a series of measurements was done using a lower vapor pressure ($T_{\text{oven}} = 80$ °C) than that used for the results shown in Fig. 10.9 ($T_{\text{oven}} = 90$ °C). The found distributions of deflection angles are presented in Fig. D.3 for three different nozzle temperatures.

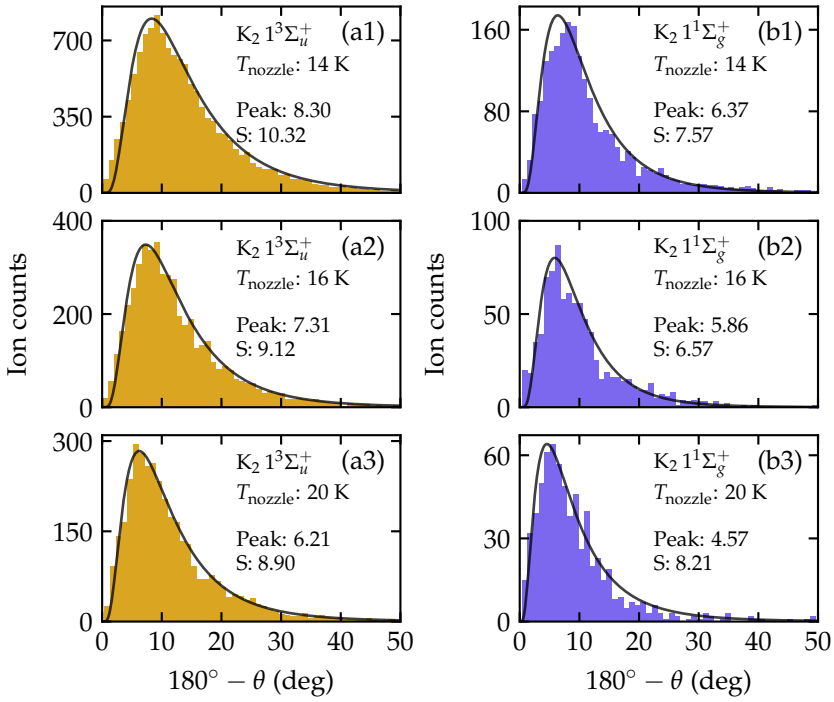

Figure D.3: (a1)–(a3) Distributions of the deflection angles, defined as $180° - \theta$, for pairs of K^+ ions from K_2 in the $1^3\Sigma_u^+$ state on droplets formed with various nozzle temperatures. The temperature of the doping oven was $T_{\text{oven}} = 80$ °C. (b1)–(b3) Same as for (a1)–(a3), but this time for K^+ ions from K_2 in the $1^1\Sigma_g^+$ state.

BIBLIOGRAPHY

[1] P. R. Brooks. "Reactions of Oriented Molecules." *Science* **193** (1976), 11.

[2] H. J. Loesch, and A. Remscheid. "Brute Force in Molecular Reaction Dynamics: A Novel Technique for Measuring Steric Effects." *J. Chem. Phys.* **93** (1990), 4779.

[3] R. N. Zare. "Laser Control of Chemical Reactions." *Science* **279** (1998), 1875.

[4] M. H. G. De Miranda, A. Chotia, B. Neyenhuis, D. Wang, G. Quéméner, S. Ospelkaus, J. L. Bohn, J. Ye, and D. S. Jin. "Controlling the Quantum Stereodynamics of Ultracold Bimolecular Reactions." *Nat. Phys.* **7** (2011), 502.

[5] R. N. Zare. "Photoejection Dynamics." *Mol. Photochem.* **4** (1972), 1.

[6] S. Selstø, M. Førre, J. P. Hansen, and L. B. Madsen. "Strong Orientation Effects in Ionization of H_2^+ by Short, Intense, High-Frequency Light Pulses." *Phys. Rev. Lett.* **95** (2005), 093002.

[7] L. Holmegaard, J. L. Hansen, L. Kalhoj, S. Louise Kragh, H. Stapelfeldt, F. Filsinger, J. Küpper, G. Meijer, D. Dimitrovski, M. Abu-samha, et al. "Photoelectron Angular Distributions from Strong-Field Ionization of Oriented Molecules." *Nat. Phys.* **6** (2010), 428.

[8] A. Barty, J. Küpper, and H. N. Chapman. "Molecular Imaging Using X-Ray Free-Electron Lasers." *Annu. Rev. Phys. Chem.* **64** (2013), 415.

[9] Z. Ma, X. Zou, L. Zhao, F. Qi, T. Jiang, P. Zhu, D. Xiang, and J. Zhang. "Ultrafast Isolated Molecule Imaging without Crystallization." *PNAS* **119** (2022), e2122793119.

[10] B. Friedrich, and D. Herschbach. "Alignment and Trapping of Molecules in Intense Laser Fields." *Phys. Rev. Lett.* **74** (1995), 4623.

[11] T. Seideman. "On the Dynamics of Rotationally Broad, Spatially Aligned Wave Packets." *J. Chem. Phys.* **115** (2001), 5965.

[12] H. Stapelfeldt, and T. Seideman. "Colloquium: Aligning Molecules with Strong Laser Pulses." *Rev. Mod. Phys.* **75** (2003), 543.

[13] T. Seideman, and E. Hamilton. "Nonadiabatic Alignment by Intense Pulses. Concepts, Theory, and Directions." *Adv. At. Mol. Opt. Phys* **52** (2005), 289.

[14] R. Torres, R. de Nalda, and J. P. Marangos. "Dynamics of Laser-Induced Molecular Alignment in the Impulsive and Adiabatic Regimes: A Direct Comparison." *Phys. Rev. A* **72** (2005), 023420.

[15] O. Ghafur, A. Rouzee, A. Gijsbertsen, W. K. Siu, S. Stolte, and M. J. J. Vrakking. "Impulsive Orientation and Alignment of Quantum-State-Selected NO Molecules." *Nat. Phys.* **5** (2009), 289.

[16] Y. Ohshima, and H. Hasegawa. "Coherent Rotational Excitation by Intense Nonresonant Laser Fields." *Int. Rev. Phys. Chem.* **29** (2010), 619.

[17] J. Wu, A. Vredenborg, B. Ulrich, L. P. H. Schmidt, M. Meckel, S. Voss, H. Sann, H. Kim, T. Jahnke, and R. Dörner. "Nonadiabatic Alignment of van Der Waals–force-bound Argon Dimers by Femtosecond Laser Pulses." *Phys. Rev. A* **83** (2011), 061403.

[18] D. Townsend, B. J. Sussman, and A. Stolow. "A Stark Future for Quantum Control." *J. Phys. Chem. A* **115** (2011), 357.

[19] N. Owschimikow, B. Schmidt, and N. Schwentner. "Laser-Induced Alignment and Anti-Alignment of Rotationally Excited Molecules." *Phys. Chem. Chem. Phys.* **13** (2011), 8671.

[20] S. Fleischer, Y. Khodorkovsky, E. Gershnabel, Y. Prior, and I. S. Averbukh. "Molecular Alignment Induced by Ultrashort Laser Pulses and Its Impact on Molecular Motion." *Isr. J. Chem.* **52** (2012), 414.

[21] J. Yang, and M. Centurion. "Gas-Phase Electron Diffraction from Laser-Aligned Molecules." *Struct. Chem.* **26** (2015), 1513.

[22] L. V. Thesing, A. Yachmenev, R. González-Férez, and J. Küpper. "Laser-Induced Alignment of Weakly Bound Molecular Aggregates." *Phys. Rev. A* **98** (2018), 053412.

[23] C. P. Koch, M. Lemeshko, and D. Sugny. "Quantum Control of Molecular Rotation." *Rev. Mod. Phys.* **91** (2019), 035005.

[24] E. T. Karamatskos, S. Raabe, T. Mullins, A. Trabattoni, P. Stammer, G. Goldsztejn, R. R. Johansen, K. Długołecki, H. Stapelfeldt, M. J. J. Vrakking, et al. "Molecular Movie of Ultrafast Coherent Rotational Dynamics of OCS." *Nat. Commun.* **10** (2019), 3364.

[25] A. S. Chatterley, M. O. Baatrup, C. A. Schouder, and H. Stapelfeldt. "Laser-Induced Alignment Dynamics of Gas Phase CS_2 Dimers." *Phys. Chem. Chem. Phys.* **22** (2020), 3245.

[26] C. A. Schouder, A. S. Chatterley, J. D. Pickering, and H. Stapelfeldt. "Laser-Induced Coulomb Explosion Imaging of Aligned Molecules and Molecular Dimers." *Annu. Rev. Phys. Chem.* **73** (2022), 323.

[27] M. Kunitski, Q. Guan, H. Maschkiwitz, J. Hahnenbruch, S. Eckart, S. Zeller, A. Kalinin, M. Schöffler, L. P. H. Schmidt, T. Jahnke, et al. "Ultrafast manipulation of the weakly bound helium dimer." *Nat. Phys.* **17** (2021), 174.

[28] J. H. Nielsen, D. Pentlehner, L. Christiansen, B. Shepperson, A. A. Søndergaard, A. S. Chatterley, J. D. Pickering, C. A. Schouder, A. V. Muñoz, L. Kranabetter, et al. "Laser-Induced Alignment of Molecules in Helium Nanodroplets." *In: Molecules in Superfluid Helium Nanodroplets. Topics in Applied Physics, vol. 145.* Ed. by A. Slenczka, and J. P. Toennies. Springer, Cham (2022), 381.

[29] P. W. Dooley, I. V. Litvinyuk, K. F. Lee, D. M. Rayner, M. Spanner, D. M. Villeneuve, and P. B. Corkum. "Direct Imaging of Rotational Wave-Packet Dynamics of Diatomic Molecules." *Phys. Rev. A* **68** (2003), 023406.

[30] C. Schröter, K. Kosma, and T. Schultz. "CRASY: Mass- or Electron-Correlated Rotational Alignment Spectroscopy." *Science* **333** (2011), 1011.

[31] G. Galinis, L. G. M. Luna, M. J. Watkins, A. M. Ellis, R. S. Minns, M. Mladenović, M. Lewerenz, R. T. Chapman, I. C. E. Turcu, C. Cacho, et al. "Formation of Coherent Rotational Wavepackets in Small Molecule-Helium Clusters Using Impulsive Alignment." *Faraday Discuss.* **171** (2014), 195.

[32] A. S. Chatterley, L. Christiansen, C. A. Schouder, A. V. Jørgensen, B. Shepperson, I. N. Cherepanov, G. Bighin, R. E. Zillich, M. Lemeshko, and H. Stapelfeldt. "Rotational Coherence Spectroscopy of Molecules in Helium Nanodroplets: Reconciling the Time and the Frequency Domains." *Phys. Rev. Lett.* **125** (2020), 013001.

[33] P. M. Felker. "Rotational Coherence Spectroscopy: Studies of the Geometries of Large Gas-Phase Species by Picosecond Time-Domain Methods." *J. Phys. Chem.* **96** (1992), 7844.

[34] C. Riehn. "High-Resolution Pump–Probe Rotational Coherence Spectroscopy – Rotational Constants and Structure of Ground and Electronically Excited States of Large Molecular Systems." *Chem. Phys.* **283** (2002), 297.

[35] D. Pentlehner, J. H. Nielsen, A. Slenczka, K. Mølmer, and H. Stapelfeldt. "Impulsive Laser Induced Alignment of Molecules Dissolved in Helium Nanodroplets." *Phys. Rev. Lett.* **110** (2013), 093002.

[36] L. Christiansen, J. H. Nielsen, D. Pentlehner, J. G. Underwood, and H. Stapelfeldt. "Alignment Enhancement of Molecules Embedded in Helium Nanodroplets by Multiple Laser Pulses." *Phys. Rev. A* **92** (2015), 053415.

[37] B. Shepperson, A. A. Søndergaard, L. Christiansen, J. Kaczmarczyk, R. E. Zillich, M. Lemeshko, and H. Stapelfeldt. "Laser-Induced Rotation of Iodine Molecules in Helium Nanodroplets: Revivals and Breaking Free." *Phys. Rev. Lett.* **118** (2017), 203203.

[38] B. Shepperson, A. S. Chatterley, L. Christiansen, A. A. Søndergaard, and H. Stapelfeldt. "Observation of Rotational Revivals for Iodine Molecules in Helium Droplets Using a Near-Adiabatic Laser Pulse." *Phys. Rev. A* **97** (2018), 013427.

[39] A. S. Chatterley, C. Schouder, L. Christiansen, B. Shepperson, M. H. Rasmussen, and H. Stapelfeldt. "Long-Lasting Field-Free Alignment of Large Molecules inside Helium Nanodroplets." *Nat. Commun.* **10** (2019), 133.

[40] J. Qiang, L. Zhou, P. Lu, K. Lin, Y. Ma, S. Pan, C. Lu, W. Jiang, F. Sun, W. Zhang, et al. "Femtosecond Rotational Dynamics of D_2 Molecules in Superfluid Helium Nanodroplets." *Phys. Rev. Lett.* **128** (2022), 243201.

[41] A. A. Milner, V. A. Apkarian, and V. Milner. "Dynamics of molecular rotors in bulk superfluid helium." *Sci. Adv.* **9** (2023), eadi2455.

[42] A. A. Milner, I. MacPhail-Bartley, K. Preocanin, S. Dasgupta, X. Peng, and V. Milner. "Coherent control of molecular rotation in superfluid helium." *Phys. Rev. A* **109** (2024), 013110.

[43] S. Grebenev, M. Hartmann, M. Havenith, B. Sartakov, J. P. Toennies, and A. F. Vilesov. "The Rotational Spectrum of Single OCS Molecules in Liquid ^{4}He Droplets." *J. Chem. Phys.* **112** (2000), 4485.

[44] Y. Kwon, P. Huang, M. V. Patel, D. Blume, and K. B. Whaley. "Quantum Solvation and Molecular Rotations in Superfluid Helium Clusters." *J. Chem. Phys.* **113** (2000), 6469.

[45] J. P. Toennies, and A. F. Vilesov. "Superfluid Helium Droplets: A Uniquely Cold Nanomatrix for Molecules and Molecular Complexes." *Angew. Chem. Int. Ed.* **43** (2004), 2622.

[46] M. Y. Choi, G. E. Douberly, T. M. Falconer, W. K. Lewis, C. M. Lindsay, J. M. Merritt, P. L. Stiles, and R. E. Miller. "Infrared Spectroscopy of Helium Nanodroplets: Novel Methods for Physics and Chemistry." *Int. Rev. Phys. Chem.* **25** (2006), 15.

[47] M. Lemeshko. "Quasiparticle Approach to Molecules Interacting with Quantum Solvents." *Phys. Rev. Lett.* **118** (2017), 095301.

[48] F. Stienkemeier, J. Higgins, W. E. Ernst, and G. Scoles. "Laser Spectroscopy of Alkali-Doped Helium Clusters." *Phys. Rev. Lett.* **74** (1995), 3592.

[49] J. Higgins, W. E. Ernst, C. Callegari, J. Reho, K. K. Lehmann, G. Scoles, and M. Gutowski. "Spin Polarized Alkali Clusters: Observation of Quartet States of the Sodium Trimer." *Phys. Rev. Lett.* **77** (1996), 4532.

[50] J. Higgins, C. Callegari, J. Reho, F. Stienkemeier, W. E. Ernst, K. K. Lehmann, M. Gutowski, and G. Scoles. "Photoinduced Chemical Dynamics of High-Spin Alkali Trimers." *Science* **273** (1996), 629.

[51] J. Higgins, T. Hollebeek, J. Reho, T.-S. Ho, K. K. Lehmann, H. Rabitz, G. Scoles, and M. Gutowski. "On the Importance of Exchange Effects in Three-Body Interactions: The Lowest Quartet State of Na_3." *J. Chem. Phys.* **112** (2000), 5751.

[52] J. H. Reho, J. Higgins, M. Nooijen, K. K. Lehmann, G. Scoles, and M. Gutowski. "Photoinduced Nonadiabatic Dynamics in Quartet Na_3 and K_3 Formed Using Helium Nanodroplet Isolation." *J. Chem. Phys.* **115** (2001), 10265.

[53] J. Nagl, G. Auböck, A. W. Hauser, O. Allard, C. Callegari, and W. E. Ernst. "High-Spin Alkali Trimers on Helium Nanodroplets: Spectral Separation and Analysis." *J. Chem. Phys.* **128** (2008), 154320.

[54] A. W. Hauser, G. Auböck, C. Callegari, and W. E. Ernst. "Relativistic Jahn–Teller Effects in the Quartet States of K_3 and Rb_3: A Vibronic Analysis of the $2\ ^4E' \leftarrow 1\ ^4A'_2$ Electronic Transitions Based on *Ab Initio* Calculations." *J. Chem. Phys.* **132** (2010), 164310.

[55] A. W. Hauser, and W. E. Ernst. "Homo- and Heteronuclear Alkali Metal Trimers Formed on Helium Nanodroplets. Part I. Vibronic Spectra Simulations Based on Ab Initio Calculations." *Phys. Chem. Chem. Phys.* **13** (2011), 18762.

[56] C. Giese, F. Stienkemeier, M. Mudrich, A. W. Hauser, and W. E. Ernst. "Homo- and Heteronuclear Alkali Metal Trimers Formed on Helium Nanodroplets. Part II. Femtosecond Spectroscopy and Spectra Assignments." *Phys. Chem. Chem. Phys.* **13** (2011), 18769.

[57] B. Grüner, M. Schlesinger, P. Heister, W. T. Strunz, F. Stienkemeier, and M. Mudrich. "Vibrational relaxation and dephasing of Rb_2 attached to helium nanodroplets." *Phys. Chem. Chem. Phys.* **13** (2011), 6816.

[58] G. Guillon, A. Zanchet, M. Leino, A. Viel, and R. E. Zillich. "Theoretical Study of Rb_2 in He_N: Potential Energy Surface and Monte Carlo Simulations." *J. Phys. Chem. A* **115** (2011), 6918.

[59] F. Rosca-Pruna, and M. J. J. Vrakking. "Revival Structures in Picosecond Laser-Induced Alignment of I_2 Molecules. I. Experimental Results." *J. Chem. Phys.* **116** (2002), 6567.

[60] V. Kumarappan, S. S. Viftrup, L. Holmegaard, C. Z. Bisgaard, and H. Stapelfeldt. "Aligning Molecules with Long or Short Laser Pulses." *Phys. Scr.* **76** (2007), C63.

[61] L. Holmegaard, J. H. Nielsen, I. Nevo, H. Stapelfeldt, F. Filsinger, J. Küpper, and G. Meijer. "Laser-Induced Alignment and Orientation of Quantum-State-Selected Large Molecules." *Phys. Rev. Lett.* **102** (2009), 023001.

[62] F. Stienkemeier, and A. F. Vilesov. "Electronic Spectroscopy in He Droplets." *J. Chem. Phys.* **115** (2001), 10119.

[63] M. Barranco, R. Guardiola, S. Hernández, R. Mayol, J. Navarro, and M. Pi. "Helium Nanodroplets: An Overview." *J. Low Temp. Phys.* **142** (2006), 1.

[64] F. Stienkemeier, and K. K. Lehmann. "Spectroscopy and Dynamics in Helium Nanodroplets." *J. Phys. B* **39** (2006), R127.

[65] S. Yang, and A. M. Ellis. "Helium Droplets: A Chemistry Perspective." *Chem. Soc. Rev.* **42** (2013), 472.

[66] M. Mudrich, and F. Stienkemeier. "Photoionisaton of Pure and Doped Helium Nanodroplets." *Int. Rev. Phys. Chem.* **33** (2014), 301.

[67] O. Gessner, and A. F. Vilesov. "Imaging Quantum Vortices in Superfluid Helium Droplets." *Annu. Rev. Phys. Chem.* **70** (2019), 173.

[68] S. Albertini, E. Gruber, F. Zappa, S. Krasnokutski, F. Laimer, and P. Scheier. "Chemistry and physics of dopants embedded in helium droplets." *Mass. Spec. Rev.* **41** (2022), 529.

[69] J. P. Toennies. "Helium Nanodroplets: Formation, Physical Properties and Superfluidity." *In: Molecules in Superfluid Helium Nanodroplets. Topics in Applied Physics, vol. 145.* Ed. by A. Slenczka, and J. P. Toennies. Springer, Cham (2022), 1.

[70] H. R. Glyde. "Excitations in the quantum liquid ^{4}He: A review." *Rep. Prog. Phys.* **81** (2018), 014501.

[71] S. Angus, K. M. de Reuck, and R. D. McCarty. "International Thermodynamic Tables of the Fluid State Helium-4." Pergamon Press (1977).

[72] L. Landau. "Theory of the Superfluidity of Helium II." *Phys. Rev.* **60** (1941), 356.

[73] D. R. Allum, P. V. E. McClintock, and A. Phillips. "The Breakdown of Superfluidity in Liquid ^{4}He: An Experimental Test of Landau's Theory." *Philos. Trans. R. Soc. A* **284** (1977), 179.

[74] A. Kramida, Yu. Ralchenko, J. Reader, and NIST ASD Team. NIST Atomic Spectra Database (ver. 5.11). Accessed March 28, 2024. https://physics.nist.gov/asd.

[75] M. Hartmann, R. E. Miller, J. P. Toennies, and A. Vilesov. "Rotationally Resolved Spectroscopy of SF_6 in Liquid Helium Clusters: A Molecular Probe of Cluster Temperature." *Phys. Rev. Lett.* **75** (1995), 1566.

[76] M. Lewerenz, B. Schilling, and J. P. Toennies. "A New Scattering Deflection Method for Determining and Selecting the Sizes of Large Liquid Clusters of ^{4}He." *Chem. Phys. Lett.* **206** (1993), 381.

[77] J. Harms, J. P. Toennies, and F. Dalfovo. "Density of Superfluid Helium Droplets." *Phys. Rev. B* **58** (1998), 3341.

[78] L. F. Gomez, E. Loginov, R. Sliter, and A. F. Vilesov. "Sizes of large He droplets." *J. Chem. Phys.* **135** (2011), 154201.

[79] L. F. Gomez, K. R. Ferguson, J. P. Cryan, C. Bacellar, R. M. P. Tanyag, C. Jones, S. Schorb, D. Anielski, A. Belkacem, C. Bernando, et al. "Shapes and Vorticities of Superfluid Helium Nanodroplets." *Science* **345** (2014), 906.

[80] B. Langbehn, K. Sander, Y. Ovcharenko, C. Peltz, A. Clark, M. Coreno, R. Cucini, M. Drabbels, P. Finetti, M. Di Fraia, et al. "Three-Dimensional Shapes of Spinning Helium Nanodroplets." *Phys. Rev. Lett.* **121** (2018), 255301.

[81] K. K. Lehmann. "Microcanonical thermodynamic properties of helium nanodroplets." *J. Chem. Phys.* **119** (2003), 3336.

[82] A. Scheidemann, J. P. Toennies, and J. A. Northby. "Capture of Neon Atoms by ^{4}He Clusters." *Phys. Rev. Lett.* **64** (1990), 1899.

[83] M. Lewerenz, B. Schilling, and J. P. Toennies. "Successive Capture and Coagulation of Atoms and Molecules to Small Clusters in Large Liquid Helium Clusters." *J. Chem. Phys.* **102** (1995), 8191.

[84] F. Ancilotto, G. DeToffol, and F. Toigo. "Sodium Dimers on the Surface of Liquid ^{4}He." *Phys. Rev. B* **52** (1995), 16125.

[85] F. Stienkemeier, J. Higgins, W. E. Ernst, and G. Scoles. "Spectroscopy of alkali atoms and molecules attached to liquid He clusters." *Z. Phys. B* **98** (1995), 413.

[86] F. Stienkemeier, J. Higgins, C. Callegari, S. I. Kanorsky, W. E. Ernst, and G. Scoles. "Spectroscopy of Alkali Atoms (Li, Na, K) Attached to Large Helium Clusters." *Z. Phys. D* **38** (1996), 253.

[87] J. H. Reho, J. P. Higgins, and K. K. Lehmann. "Dynamics of the $1^3\Pi_g$ state of K_2 on helium nanodroplets." *Faraday Discuss.* **118** (2001), 33.

[88] O. Bünermann, M. Mudrich, M. Weidemüller, and F. Stienkemeier. "Spectroscopy of Cs Attached to Helium Nanodroplets." *J. Chem. Phys.* **121** (2004), 8880.

[89] W. E. Ernst, R. Huber, S. Jiang, R. Beuc, M. Movre, and G. Pichler. "Cesium Dimer Spectroscopy on Helium Droplets." *J. Chem. Phys.* **124** (2006), 024313.

[90] P. Claas, G. Droppelmann, C. P. Schulz, M. Mudrich, and F. Stienkemeier. "Wave Packet Dynamics of K_2 Attached to Helium Nanodroplets." *J. Phys. B* **39** (2006), S1151.

[91] P. Claas, G. Droppelmann, C. P. Schulz, M. Mudrich, and F. Stienkemeier. "Wave Packet Dynamics in Triplet States of Na_2 Attached to Helium Nanodroplets." *J. Phys. Chem. A* **111** (2007), 7537.

[92] G. Auböck, J. Nagl, C. Callegari, and W. E. Ernst. "Triplet State Excitation of Alkali Molecules on Helium Droplets: Experiments and Theory." *J. Phys. Chem. A* **111** (2007), 7404.

[93] M. Theisen, F. Lackner, and W. E. Ernst. "Rb and Cs Oligomers in Different Spin Configurations on Helium Nanodroplets." *J. Phys. Chem. A* **115** (2011), 7005.

[94] M. Theisen, F. Lackner, and W. E. Ernst. "Cs Atoms on Helium Nanodroplets and the Immersion of Cs^+ into the Nanodroplet." *J. Chem. Phys.* **135** (2011), 074306.

[95] F. Lackner, J. Poms, G. Krois, J. V. Pototschnig, and W. E. Ernst. "Spectroscopy of Lithium Atoms and Molecules on Helium Nanodroplets." *J. Phys. Chem. A* **117** (2013), 11866.

[96] S. Bovino, E. Coccia, E. Bodo, D. Lopez-Durán, and F. A. Gianturco. "Spin-Driven Structural Effects in Alkali Doped ^{4}He Clusters from Quantum Calculations." *J. Chem. Phys.* **130** (2009), 224903.

[97] R. Zillich. *private communication* (2023).

[98] F. R. Brühl, R. A. Miron, and W. E. Ernst. "Triplet States of Rubidium Dimers on Helium Nanodroplets." *J. Chem. Phys.* **115** (2001), 10275.

[99] J. Higgins, C. Callegari, J. Reho, F. Stienkemeier, W. E. Ernst, M. Gutowski, and G. Scoles. "Helium Cluster Isolation Spectroscopy of Alkali Dimers in the Triplet Manifold." *J. Phys. Chem. A* **102** (1998), 4952.

[100] C. P. Schulz, P. Claas, D. Schumacher, and F. Stienkemeier. "Formation and Stability of High-Spin Alkali Clusters." *Phys. Rev. Lett.* **92** (2004), 013401.

[101] M. Mudrich, O. Bünermann, F. Stienkemeier, O. Dulieu, and M. Weidemüller. "Formation of Cold Bialkali Dimers on Helium Nanodroplets." *Eur. Phys. J. D* **31** (2004), 291.

[102] O. Bünermann, and F. Stienkemeier. "Modeling the Formation of Alkali Clusters Attached to Helium Nanodroplets and the Abundance of High-Spin States." *Eur. Phys. J. D* **61** (2011), 645.

[103] P. Atkins, and R. Friedman. "Molecular Quantum Mechanics." 5th ed. Oxford Univesity Press (2011).

[104] M. Leibscher, I. S. Averbukh, and H. Rabitz. "Enhanced Molecular Alignment by Short Laser Pulses." *Phys. Rev. A* **69** (2004), 013402.

[105] E. Hamilton, T. Seideman, T. Ejdrup, M. D. Poulsen, C. Z. Bisgaard, S. S. Viftrup, and H. Stapelfeldt. "Alignment of Symmetric Top Molecules by Short Laser Pulses." *Phys. Rev. A* **72** (2005), 043402.

[106] A. A. Søndergaard, B. Shepperson, and H. Stapelfeldt. "Nonadiabatic Laser-Induced Alignment of Molecules: Reconstructing $\langle\cos^2\theta\rangle$ Directly from $\langle\cos^2\theta_{2D}\rangle$ by Fourier Analysis." *J. Chem. Phys.* **147** (2017), 013905.

[107] J. B. Bauer, and J. P. Toennies. "An Accurate Semi-Empirical Potential Model for the a $^3\Sigma_u^+$ State of the Alkali Dimers Na_2, K_2, Rb_2, and Cs_2 Which Reproduces the Scattering Length." *J. Chem. Phys.* **150** (2019), 144310.

[108] J. Deiglmayr, M. Aymar, R. Wester, M. Weidemüller, and O. Dulieu. "Calculations of Static Dipole Polarizabilities of Alkali Dimers: Prospects for Alignment of Ultracold Molecules." *J. Chem. Phys.* **129** (2008), 064309.

[109] J. O. Smith. Spectral Audio Signal Processing. Accessed July 8, 2024. http://ccrma.stanford.edu/~jos/sasp/.

[110] J. Ortigoso, M. Rodríguez, M. Gupta, and B. Friedrich. "Time Evolution of Pendular States Created by the Interaction of Molecular Polarizability with a Pulsed Nonresonant Laser Field." *J. Chem. Phys.* **110** (1999), 3870.

[111] J. J. Larsen, H. Sakai, C. P. Safvan, I. Wendt-Larsen, and H. Stapelfeldt. "Aligning Molecules with Intense Nonresonant Laser Fields." *J. Chem. Phys.* **111** (1999), 7774.

[112] S. Trippel, M. Stei, C. Eichhorn, R. Otto, P. Hlavenka, M. Weidemüller, and R. Wester. "Nanosecond photofragment imaging of adiabatic molecular alignment." *J. Chem. Phys.* **134** (2011), 104306.

[113] S. Trippel, T. G. Mullins, N. L. Müller, J. S. Kienitz, K. Dlugolecki, and J. Küpper. "Strongly Aligned and Oriented Molecular Samples at a kHz Repetition Rate." *Mol. Phys.* **111** (2013), 1738.

[114] D. Pentlehner, J. H. Nielsen, L. Christiansen, A. Slenczka, and H. Stapelfeldt. "Laser-Induced Adiabatic Alignment of Molecules Dissolved in Helium Nanodroplets." *Phys. Rev. A* **87** (2013), 063401.

[115] S. Trippel, T. Mullins, N. L. M. Müller, J. S. Kienitz, J. J. Omiste, H. Stapelfeldt, R. González-Férez, and J. Küpper. "Strongly Driven Quantum Pendulum of the Carbonyl Sulfide Molecule." *Phys. Rev. A* **89** (2014), 051401.

[116] R. Boll, A. Rouzée, M. Adolph, D. Anielski, A. Aquila, S. Bari, C. Bomme, C. Bostedt, J. D. Bozek, H. N. Chapman, et al. "Imaging Molecular Structure through Femtosecond Photoelectron Diffraction on Aligned and Oriented Gas-Phase Molecules." *Faraday Discuss.* **171** (2014), 57.

[117] Z.-C. Yan, and T. Seideman. "Photomanipulation of External Molecular Modes: A Time-Dependent Self-Consistent-Field Approach." *J. Chem. Phys.* **111** (1999), 4113.

[118] J. G. Underwood, M. Spanner, M. Y. Ivanov, J. Mottershead, B. J. Sussman, and A. Stolow. "Switched Wave Packets: A Route to Nonperturbative Quantum Control." *Phys. Rev. Lett.* **90** (2003), 223001.

[119] B. J. Sussman, J. G. Underwood, R. Lausten, M. Y. Ivanov, and A. Stolow. "Quantum Control via the Dynamic Stark Effect: Application to Switched Rotational Wave Packets and Molecular Axis Alignment." *Phys. Rev. A* **73** (2006), 053403.

[120] A. Goban, S. Minemoto, and H. Sakai. "Laser-Field-Free Molecular Orientation." *Phys. Rev. Lett.* **101** (2008), 013001.

[121] J. H. Mun, D. Takei, S. Minemoto, and H. Sakai. "Laser-Field-Free Orientation of State-Selected Asymmetric Top Molecules." *Phys. Rev. A* **89** (2014), 051402.

[122] D. Takei, J. H. Mun, S. Minemoto, and H. Sakai. "Laser-Field-Free Three-Dimensional Molecular Orientation." *Phys. Rev. A* **94** (2016), 013401.

[123] A. S. Chatterley, E. T. Karamatskos, C. Schouder, L. Christiansen, A. V. Jørgensen, T. Mullins, J. Küpper, and H. Stapelfeldt. "Communication: Switched Wave Packets with Spectrally Truncated Chirped Pulses." *J. Chem. Phys.* **148** (2018), 221105.

[124] H. H. Kristensen, L. Kranabetter, C. A. Schouder, C. Stapper, J. Arlt, M. Mudrich, and H. Stapelfeldt. "Quantum-State-Sensitive Detection of Alkali Dimers on Helium Nanodroplets by Laser-Induced Coulomb Explosion." *Phys. Rev. Lett.* **128** (2022), 093201.

[125] B. Shepperson, A. S. Chatterley, A. A. Søndergaard, L. Christiansen, M. Lemeshko, and H. Stapelfeldt. "Strongly Aligned Molecules inside Helium Droplets in the Near-Adiabatic Regime." *J. Chem. Phys.* **147** (2017), 013946.

[126] H. H. Kristensen, L. Kranabetter, C. A. Schouder, J. Arlt, F. Jensen, and H. Stapelfeldt. "Laser-Induced Coulomb Explosion Imaging of Alkali-Metal Dimers on Helium Nanodroplets." *Phys. Rev. A* **107** (2023), 023104.

[127] "Printed instruction manual 09/2004." *ATMION* (2004).

[128] U. Even. "The Even-Lavie valve as a source for high intensity supersonic beam." *EPJ Techn. Instrum.* **2** (2015), 17.

[129] T. E. Wall. "Preparation of cold molecules for high-precision measurements." *J. Phys. B* **49** (2016), 243001.

[130] M. D. Morse. "Supersonic Beam Sources." *Exp. Meth. Phys. Sci.* **29** (1996), 21.

[131] P. E. Mason, F. Uhlig, V. Vaněk, T. Buttersack, S. Bauerecker, and P. Jungwirth. "Coulomb explosion during the early stages of the reaction of alkali metals with water." *Nat. Chem.* **7** (2015), 250.

[132] D. Blair, and S. Zimber. "Recognition and safe management of explosive chemicals." *Chem. Health Saf.* **7** (2000), 14.

[133] A. Grubelnik, V. R. Meyer, P. Bützer, and U. W. Schönenberger. "Potassium Metal Is Explosive — Do Not Use It!" *J. Chem. Educ.* **85** (2008), 634.

[134] A. T. J. B. Eppink, and D. H. Parker. "Velocity Map Imaging of Ions and Electrons Using Electrostatic Lenses: Application in Photoelectron and Photofragment Ion Imaging of Molecular Oxygen." *Rev. Sci. Instrum.* **68** (1997), 3477.

[135] G. M. Roberts, J. L. Nixon, J. Lecointre, E. Wrede, and J. R. R. Verlet. "Toward Real-Time Charged-Particle Image Reconstruction Using Polar Onion-Peeling." *Rev. Sci. Instrum.* **80** (2009), 053104.

[136] J. L. Wiza. "Microchannel plate detectors." *Nucl. Instrum. Methods* **162** (1979), 587.

[137] M. Ester, H.-P. Kriegel, J. Sander, and X. Xu. "A density-based algorithm for discovering clusters in large spatial databases with noise." *KDD-96 Proceedings* (1996), 226.

[138] A. Zhao, M. van Beuzekom, B. Bouwens, D. Byelov, I. Chakaberia, C. Cheng, E. Maddox, A. Nomerotski, P. Svihra, J. Visser, et al. "Coincidence Velocity Map Imaging Using Tpx3Cam, a Time Stamping Optical Camera with 1.5 ns Timing Resolution." *Rev. Sci. Instrum.* **88** (2017), 113104.

[139] S. Magnier, P. Millié, O. Dulieu, and F. Masnou-Seeuws. "Potential Curves for the Ground and Excited States of the Na_2 Molecule up to the (3s+5p) Dissociation Limit: Results of Two Different Effective Potential Calculations." *J. Chem. Phys.* **98** (1993), 7113.

[140] S. Magnier, M. Aubert-Frécon, and A. R. Allouche. "Theoretical Determination of Highly Excited States of K_2 Correlated Adiabatically above K(4p)+K(4p)." *J. Chem. Phys.* **121** (2004), 1771.

[141] P. Jasik, and J. Sienkiewicz. "Calculation of Adiabatic Potentials of Li_2." *Chem. Phys.* **323** (2006), 563.

[142] A.-R. Allouche, and M. Aubert-Frécon. "Transition Dipole Moments between the Low-Lying $\Omega_{g,u}^{(+/-)}$ States of the Rb_2 and Cs_2 Molecules." *J. Chem. Phys.* **136** (2012), 114302.

[143] U. Keller. "Ultrafast lasers." 1st ed. Springer (2022).

[144] W. Rudolph, and B. Wilhelmi. "Light Pulse Compression." 1st ed. Harwood Academic Publishers (1989).

[145] M. N. Polyanskiy. Refractive index database. Accessed March 12, 2024. https://refractiveindex.info.

[146] C. Rullière (editor). "Femtosecond laser pulses." 2nd ed. (ebook). Springer (2007).

[147] L. Holmegaard. "Laser-induced Alignment and Orientation: Photoelectron Angular Distributions from Strong Field Ionization." *PhD thesis, Aarhus University* (2010).

[148] T. Weber, A. O. Czasch, O. Jagutzki, A. K. Müller, V. Mergel, A. Kheifets, E. Rotenberg, G. Meigs, M. H. Prior, S. Daveau, et al. "Complete photo-fragmentation of the deuterium molecule." *Nature* **431** (2004), 437.

[149] T. Ergler, A. Rudenko, B. Feuerstein, K. Zrost, C. D. Schröter, R. Moshammer, and J. Ullrich. "Spatiotemporal Imaging of Ultrafast Molecular Motion: Collapse and Revival of the D_2^+ Nuclear Wave Packet." *Phys. Rev. Lett.* **97** (2006), 193001.

[150] B. Ulrich, A. Vredenborg, A. Malakzadeh, L. P. H. Schmidt, T. Havermeier, M. Meckel, K. Cole, M. Smolarski, Z. Chang, T. Jahnke, et al. "Imaging of the Structure of the Argon and Neon Dimer, Trimer, and Tetramer." *J. Phys. Chem. A* **115** (2011), 6936.

[151] S. Zeller, M. Kunitski, J. Voigtsberger, M. Waitz, F. Trinter, S. Eckart, A. Kalinin, A. Czasch, L. P. H. Schmidt, T. Weber, et al. "Determination of Interatomic Potentials of He_2, Ne_2, Ar_2, and H_2 by Wave Function Imaging." *Phys. Rev. Lett.* **121** (2018), 083002.

[152] C. A. Schouder, A. S. Chatterley, L. B. Madsen, F. Jensen, and H. Stapelfeldt. "Laser-Induced Coulomb-explosion Imaging of the CS_2 Dimer: The Effect of Non-Coulombic Interactions." *Phys. Rev. A* **102** (2020), 063125.

[153] F. Jensen. *private communication* (2023).

[154] X. Li, A. Rudenko, M. S. Schöffler, N. Anders, T. M. Baumann, S. Eckart, B. Erk, A. De Fanis, K. Fehre, R. Dörner, et al. "Coulomb Explosion Imaging of Small Polyatomic Molecules with Ultrashort X-Ray Pulses." *Phys. Rev. Res.* **4** (2022), 013029.

[155] P. G. Hoel, S. C. Port, and C. J. Stone. "Introduction to Probability Theory." Houghton Mifflin Company (1971).

[156] L. J. Frasinski, K. Codling, and P. A. Hatherly. "Covariance Mapping: A Correlation Method Applied to Multiphoton Multiple Ionization." *Science* **246** (1989), 1029.

[157] J. L. Hansen, J. H. Nielsen, C. B. Madsen, A. T. Lindhardt, M. P. Johansson, T. Skrydstrup, L. B. Madsen, and H. Stapelfeldt. "Control and Femtosecond Time-Resolved Imaging of Torsion in a Chiral Molecule." *J. Chem. Phys.* **136** (2012), 204310-204310.

[158] C. S. Slater, S. Blake, M. Brouard, A. Lauer, C. Vallance, J. J. John, R. Turchetta, A. Nomerotski, L. Christensen, J. H. Nielsen, et al. "Covariance Imaging Experiments Using a Pixel-Imaging Mass-Spectrometry Camera." *Phys. Rev. A* **89** (2014), 011401(R).

[159] C. S. Slater, S. Blake, M. Brouard, A. Lauer, C. Vallance, C. S. Bohun, L. Christensen, J. H. Nielsen, M. P. Johansson, and H. Stapelfeldt. "Coulomb-Explosion Imaging Using a Pixel-Imaging Mass-Spectrometry Camera." *Phys. Rev. A* **91** (2015), 053424.

[160] L. J. Frasinski. "Covariance Mapping Techniques." *J. Phys. B* **49** (2016), 152004.

[161] L. Christiansen, J. H. Nielsen, L. Christensen, B. Shepperson, D. Pentlehner, and H. Stapelfeldt. "Laser-Induced Coulomb Explosion of 1,4-Diiodobenzene Molecules: Studies of Isolated Molecules and Molecules in Helium Nanodroplets." *Phys. Rev. A* **93** (2016), 023411.

[162] F. Allum, M. Burt, K. Amini, R. Boll, H. Köckert, P. K. Olshin, S. Bari, C. Bomme, F. Braußе, B. Cunha De Miranda, et al. "Coulomb explosion imaging of CH_3I and CH_2ClI photodissociation dynamics." *J. Chem. Phys.* **149** (2018), 204313.

[163] C. Vallance, D. Heathcote, and J. W. L. Lee. "Covariance-Map Imaging: A Powerful Tool for Chemical Dynamics Studies." *J. Phys. Chem. A* **125** (2021), 1117.

[164] J. Unwin, F. Allum, M. Britton, I. Gabalski, H. Bromberger, M. Brouard, P. H. Bucksbaum, T. Driver, N. Ekanayake, D. Garg, et al. "X-ray induced Coulomb explosion imaging of transient excited-state structural rearrangements in CS_2." *Commun. Phys.* **6** (2023), 1.

[165] T. Walmsley, J. W. McManus, Y. Kumagai, K. Nagaya, J. Harries, H. Iwayama, M. N. R. Ashfold, M. Britton, P. H. Bucksbaum, B. Downes-Ward, et al. "The Role of Momentum Partitioning in Covariance Ion Imaging Analysis." *J. Phys. Chem. A* **128** (2024), 4548.

[166] J. D. Pickering, B. Shepperson, B. A. K. Hübschmann, F. Thorning, and H. Stapelfeldt. "Alignment and Imaging of the CS_2 Dimer Inside Helium Nanodroplets." *Phys. Rev. Lett.* **120** (2018), 113202.

[167] C. Schouder, A. S. Chatterley, F. Calvo, L. Christiansen, and H. Stapelfeldt. "Structure Determination of the Tetracene Dimer in Helium Nanodroplets Using Femtosecond Strong-Field Ionization." *Struct. Dyn.* **6** (2019), 044301.

[168] S. Zeller, M. Kunitski, J. Voigtsberger, A. Kalinin, A. Schottelius, C. Schober, M. Waitz, H. Sann, A. Hartung, T. Bauer, et al. "Imaging the He_2 Quantum Halo State Using a Free Electron Laser." *PNAS* **113** (2016), 14651.

[169] M. Berglund, and M. E. Wieser. "Isotopic compositions of the elements 2009 (IUPAC Technical Report)." *Pure Appl. Chem.* **83** (2011), 397.

[170] M. Fisher-Levine, R. Boll, F. Ziaee, C. Bomme, B. Erk, D. Rompotis, T. Marchenko, A. Nomerotski, and D. Rolles. "Time-resolved ion imaging at free-electron lasers using TimepixCam." *J. Synchrotron Radiat.* **25** (2018), 336.

[171] A. Nomerotski. "Imaging and Time Stamping of Photons with Nanosecond Resolution in Timepix Based Optical Cameras." *Nucl. Instrum. Methods Phys. Res. A* **937** (2019), 26.

[172] H. Bromberger, C. Passow, D. Pennicard, R. Boll, J. Correa, L. He, M. Johny, C. C. Papadopoulou, A. Tul-Noor, J. Wiese, et al. "Shot-by-shot 250 kHz 3D ion and MHz photoelectron imaging using Timepix3." *J. Phys. B* **55** (2022), 144001.

[173] S. Rousseau, A. Allouche, M. Aubert-Frécon, S. Magnier, P. Kowalczyk, and W. Jastrzebski. "Theoretical study of the electronic structure of KLi and comparison with experiments." *Chem. Phys.* **247** (1999), 193.

[174] S. H. Albrechtsen, J. K. Christensen, R. M. P. Tanyag, H. H. Kristensen, and H. Stapelfeldt. "Laser-induced Coulomb explosion of heteronuclear alkali-metal dimers on helium nanodroplets." *Phys. Rev. A* **109** (2024), 043112.

[175] M. Aymar, and O. Dulieu. "Calculations of transition and permanent dipole moments of heteronuclear alkali dimers NaK, NaRb and NaCs." *Mol. Phys.* **105** (2007), 1733.

[176] P. Soldán. "Lowest Quartet States of Heteronuclear Alkali-Metal Trimers." *Phys. Rev. A* **82** (2010), 034701.

[177] T. C. Thompson, G. Izmirlian, S. J. Lemon, D. G. Truhlar, and C. A. Mead. "Consistent analytic representation of the two lowest potential energy surfaces for Li_3, Na_3, and K_3." *J. Chem. Phys.* **82** (1985), 5597.

[178] L. Kranabetter, H. H. Kristensen, C. A. Schouder, and H. Stapelfeldt. "Structure Determination of Alkali Trimers on Helium Nanodroplets through Laser-Induced Coulomb Explosion." *J. Chem. Phys.* **160** (2024), 131101.

[179] G. Auböck, J. Nagl, C. Callegari, and W. E. Ernst. "Observation of relativistic E⊗e vibronic coupling in Rb_3 and K_3 quartet states on helium droplets." *J. Chem. Phys.* **129** (2008), 114501.

[180] L. Frasinski, P. Hatherly, and K. Codling. "Multiphoton Multiple Ionisation of N_2O Probed by Three-Dimensional Covariance Mapping." *Phys. Lett. A* **156** (1991), 227.

[181] J. D. Pickering, K. Amini, M. Brouard, M. Burt, I. J. Bush, L. Christensen, A. Lauer, J. H. Nielsen, C. S. Slater, and H. Stapelfeldt. "Communication: Three-fold Covariance Imaging of Laser-Induced Coulomb Explosions." *J. Chem. Phys.* **144** (2016), 161105.

[182] F. Allum, C. Cheng, A. J. Howard, P. H. Bucksbaum, M. Brouard, T. Weinacht, and R. Forbes. "Multi-Particle Three-Dimensional Covariance Imaging: "Coincidence" Insights into the Many-Body Fragmentation of Strong-Field Ionized D_2O." *J. Phys. Chem. Lett.* **12** (2021), 8302.

[183] V. Zhaunerchyk, L. J. Frasinski, J. H. D. Eland, and R. Feifel. "Theory and simulations of covariance mapping in multiple dimensions for data analysis in high-event-rate experiments." *Phys. Rev. A* **89** (2014), 053418.

[184] J. Schnabel, T. Kampschulte, S. Rupp, J. Hecker Denschlag, and A. Köhn. "Towards Photoassociation Processes of Ultracold Rubidium Trimers." *Phys. Rev. A* **103** (2021), 022820.

[185] P. Soldán. "Potential Energy Surface for Spin-Polarized Rubidium Trimer." *J. Chem. Phys.* **132** (2010), 234308.

[186] R. Guérout, P. Soldán, M. Aymar, J. Deiglmayr, and O. Dulieu. "Core Repulsion Effects in Alkali Trimers: Core Repulsion Effects in Alkali Trimers." *Int. J. Quantum Chem.* **109** (2009), 3387.

[187] A. Hauser. *private communication* (2023).

[188] L. Kranabetter, H. H. Kristensen, A. Ghazaryan, C. A. Schouder, A. S. Chatterley, P. Janssen, F. Jensen, R. E. Zillich, M. Lemeshko, and H. Stapelfeldt. "Nonadiabatic Laser-Induced Alignment Dynamics of Molecules on a Surface." *Phys. Rev. Lett.* **131** (2023), 053201.

[189] K. K. Lehmann. "Potential of a Neutral Impurity in a Large ^4He Cluster." *Mol. Phys.* **97** (1999), 645.

[190] K. K. Lehmann. "Lorentzian line shape due to an inhomogeneous size distribution without relaxation." *J. Chem. Phys.* **126** (2007), 024108.

[191] R. E. Zillich, K. B. Whaley, and K. von Haeften. "Lineshape of Rotational Spectrum of CO in ^{4}He Droplets." *J. Chem. Phys.* **128** (2008), 094303.

[192] A. A. Søndergaard. "Understanding Laser-Induced Alignment and Rotation of Molecules Embedded in Helium Nanodroplets." *PhD thesis, Aarhus University* (2016).

[193] L. Christensen, L. Christiansen, B. Shepperson, and H. Stapelfeldt. "Deconvoluting Nonaxial Recoil in Coulomb Explosion Measurements of Molecular Axis Alignment." *Phys. Rev. A* **94** (2016), 023410.

[194] M. Mirahmadi, B. Schmidt, and B. Friedrich. "Quantum Dynamics of a Planar Rotor Driven by Suddenly Switched Combined Aligning and Orienting Interactions." *New J. Phys.* **23** (2021), 063040.

[195] M. Blancafort-Jorquera, A. Vilà, and M. González. "Rotational Energy Relaxation Quantum Dynamics of a Diatomic Molecule in a Superfluid Helium Nanodroplet and Study of the Hydrogen Isotopes Case." *Phys. Chem. Chem. Phys.* **21** (2019), 21007.

[196] G. Karras, E. Hertz, F. Billard, B. Lavorel, J.-M. Hartmann, O. Faucher, E. Gershnabel, Y. Prior, and I. S. Averbukh. "Orientation and Alignment Echoes." *Phys. Rev. Lett.* **114** (2015), 153601.

[197] D. Rosenberg, R. Damari, S. Kallush, and S. Fleischer. "Rotational Echoes: Rephasing of Centrifugal Distortion in Laser-Induced Molecular Alignment." *J. Phys. Chem. Lett.* **8** (2017), 5128.

[198] J. Ma, H. Zhang, B. Lavorel, F. Billard, E. Hertz, J. Wu, C. Boulet, J.-M. Hartmann, and O. Faucher. "Observing Collisions beyond the Secular Approximation Limit." *Nat. Commun.* **10** (2019), 1.

[199] H. Zhang, B. Lavorel, F. Billard, J.-M. Hartmann, E. Hertz, O. Faucher, J. Ma, J. Wu, E. Gershnabel, Y. Prior, et al. "Rotational Echoes as a Tool for Investigating Ultrafast Collisional Dynamics of Molecules." *Phys. Rev. Lett.* **122** (2019), 193401.

[200] E. Krotscheck, and R. Zillich. "Dynamics of ^{4}He Droplets." *J. Chem. Phys.* **115** (2001), 10161.

[201] M. Mudrich, P. Heister, T. Hippler, C. Giese, O. Dulieu, and F. Stienkemeier. "Spectroscopy of Triplet States of Rb_2 by Femtosecond Pump-Probe Photoionization of Doped Helium Nanodroplets." *Phys. Rev. A* **80** (2009), 042512.

[202] M. Schlesinger, M. Mudrich, F. Stienkemeier, and W. T. Strunz. "Dissipative Vibrational Wave Packet Dynamics of Alkali Dimers Attached to Helium Nanodroplets." *Chem. Phys. Lett.* **490** (2010), 245.

[203] L. Bruder, M. Koch, M. Mudrich, and F. Stienkemeier. "Ultrafast Dynamics in Helium Droplets." *In: Molecules in Superfluid Helium Nanodroplets. Topics in Applied Physics, vol. 145.* Ed. by A. Slenczka, and J. P. Toennies. Springer, Cham (2022), 447.

[204] C.-C. Shu, E. F. Thomas, and N. E. Henriksen. "Femtochemistry in the Electronic Ground State: Dynamic Stark Control of Vibrational Dynamics." *Chem. Phys. Lett.* **683** (2017), 234.

[205] H. Niikura, P. B. Corkum, and D. M. Villeneuve. "Controlling Vibrational Wave Packet Motion with Intense Modulated Laser Fields." *Phys. Rev. Lett.* **90** (2003), 203601.

[206] A. Rudenko, T. Ergler, B. Feuerstein, K. Zrost, C. Schröter, R. Moshammer, and J. Ullrich. "Real-time observation of vibrational revival in the fastest molecular system." *Chem. Phys.* **329** (2006), 193.

[207] J. Yang, M. Guehr, X. Shen, R. Li, T. Vecchione, R. Coffee, J. Corbett, A. Fry, N. Hartmann, C. Hast, et al. "Diffractive Imaging of Coherent Nuclear Motion in Isolated Molecules." *Phys. Rev. Lett.* **117** (2016), 153002.

[208] C. Vallance, M. Brouard, A. Lauer, C. S. Slater, E. Halford, B. Winter, S. J. King, J. W. L. Lee, D. E. Pooley, I. Sedgwick, et al. "Fast Sensors for Time-of-Flight Imaging Applications." *Phys. Chem. Chem. Phys.* **16** (2014), 383.

[209] C. Cheng, R. Forbes, A. J. Howard, M. Spanner, P. H. Bucksbaum, and T. Weinacht. "Momentum-resolved above-threshold ionization of deuterated water." *Phys. Rev. A* **102** (2020), 052813.

[210] C. Cheng, L. J. Frasinski, G. Moǧol, F. Allum, A. J. Howard, D. Rolles, P. H. Bucksbaum, M. Brouard, R. Forbes, and T. Weinacht. "Multiparticle Cumulant Mapping for Coulomb Explosion Imaging." *Phys. Rev. Lett.* **130** (2023), 093001.

[211] C. Cheng, G. Moǧol, T. Weinacht, A. Nomerotski, and C. Trallero-Herrero. "3D velocity map imaging of electrons with Tpx3Cam." *Rev. Sci. Instrum.* **93** (2022), 013003.

[212] M. Davino, E. McManus, N. G. Helming, C. Cheng, G. Moǧol, Z. Rodnova, G. Harrison, K. Watson, T. Weinacht, G. N. Gibson, et al. "A plano–convex thick-lens velocity map imaging apparatus for direct, high resolution 3D momentum measurements of

photoelectrons with ion time-of-flight coincidence." *Rev. Sci. Instrum.* **94** (2023), 013303.

[213] F. Pitters, N. A. Tehrani, D. Dannheim, A. Fiergolski, D. Hynds, W. Klempt, X. Llopart, M. Munker, A. Nürnberg, S. Spannagel, et al. "Time Resolution Studies of Timepix3 Assemblies with Thin Silicon Pixel Sensors." *J. Inst.* **14** (2019), P05022.

[214] J. H. Posthumus, A. J. Giles, M. R. Thompson, W. Shaikh, A. J. Langley, L. J. Frasinski, and K. Codling. "The Dissociation Dynamics of Diatomic Molecules in Intense Laser Fields." *J. Phys. B* **29** (1996), L525.

[215] S. Müller, M. Mudrich, and F. Stienkemeier. "Alkali-Helium Snowball Complexes Formed on Helium Nanodroplets." *J. Chem. Phys.* **131** (2009), 044319.

[216] M. Theisen, F. Lackner, and W. E. Ernst. "Forming Rb^+ Snowballs in the Center of He Nanodroplets." *Phys. Chem. Chem. Phys.* **12** (2010), 14861.

[217] L. An der Lan, P. Bartl, C. Leidlmair, R. Jochum, S. Denifl, O. Echt, and P. Scheier. "Solvation of Na^+, K^+, and Their Dimers in Helium." *Chem. Eur. J.* **18** (2012), 4411.

[218] E. García-Alfonso, M. Barranco, N. Halberstadt, and M. Pi. "Time-Resolved Solvation of Alkali Ions in Superfluid Helium Nanodroplets." *J. Chem. Phys.* **160** (2024), 164308.

[219] S. H. Albrechtsen, C. A. Schouder, A. V. Muñoz, J. K. Christensen, C. E. Petersen, M. Pi, M. Barranco, and H. Stapelfeldt. "Observing the primary steps of ion solvation in helium droplets." *Nature* **623** (2023), 319.

[220] A. Braun. "Photodissociation studies of CH_3I and CF_3I in fluid ^{4}helium nanodroplets." *PhD thesis, Lausanne EPFL* (2004).

[221] D. Verma, S. M. O. O'Connell, A. J. Feinberg, S. Erukala, R. M. P. Tanyag, C. Bernando, W. Pang, C. A. Saladrigas, B. W. Toulson, M. Borgwardt, et al. "Shapes of rotating normal fluid ^{3}He versus superfluid ^{4}He droplets in molecular beams." *Phys. Rev. B* **102** (2020), 014504.

[222] C. Z. Bisgaard, M. D. Poulsen, E. Péronne, S. S. Viftrup, and H. Stapelfeldt. "Observation of Enhanced Field-Free Molecular Alignment by Two Laser Pulses." *Phys. Rev. Lett.* **92** (2004), 173004.

[223] K. F. Lee, I. V. Litvinyuk, P. W. Dooley, M. Spanner, D. M. Villeneuve, and P. B. Corkum. "Two-Pulse Alignment of Molecules." *J. Phys. B* **37** (2004), L43.

[224] J. P. Cryan, P. H. Bucksbaum, and R. N. Coffee. "Field-Free Alignment in Repetitively Kicked Nitrogen Gas." *Phys. Rev. A* **80** (2009), 063412.

[225] R. J. LeRoy. "Spectroscopic Reassignment and Ground-State Dissociation Energy of Molecular Iodine." *J. Chem. Phys.* **52** (1970), 2678.